ANATOMY AND BIOMECHANICS OF THE PIA-ARACHNOID COMPLEX

by

Gregory George Scott

A thesis submitted to the faculty of
The University of Utah
in partial fulfillment of the requirements for the degree of

Master of Science

Department of Mechanical Engineering

The University of Utah

August 2014

The University of Utah Graduate School

STATEMENT OF THESIS APPROVAL

The thesis of **Gregory George Scott**

has been approved by the following supervisory committee members:

Brittany Coats	, Chair	**06/06/2014** Date Approved
Kenneth Monson	, Member	**06/06/2014** Date Approved
Gary Hedlund	, Member	**06/09/2014** Date Approved

and by **Tim Ameel**, Chair of

the Department of **Mechanical Engineering**

and by David B. Kieda, Dean of The Graduate School.

ABSTRACT

Traumatic brain injury (TBI) is a leading cause of death and disability in the U.S.A. In mild cases, common etiologies of TBI (i.e., hemorrhage or edema) are not readily apparent during medical examination. We propose that the pia-arachnoid complex (PAC) contributes to the brain's response in TBI. The PAC is the only layer of tissue between the brain and dura (a tough membrane tightly adhered to the skull), and acts as a mechanical tether between the brain and skull. If the fine structures of the PAC are damaged during TBI, they likely go undiagnosed due to their small size and difficulty to image.

To better understand the mechanics of PAC injury, several experimental and computational studies were conducted. First, a novel application of optical coherence tomography (OCT) was utilized to acquire microscale images of the *in-situ* porcine PAC and measure the amount of arachnoid trabeculae (AT) present. Next, two parametric studies were conducted on a microscale model of the PAC which evaluated its sensitivity to variable substructure moduli and AT volume fraction (VF). Afterwards, the microscale PAC model was paired with a macroscale head model to determine the effect of a non-uniform AT VF on whole-head mechanics. Finally, an immature porcine model of mild TBI was used to investigate PAC damage following head rotation, and identify clinically relevant MRI biomarkers indicative of PAC damage.

The OCT imaging of the PAC revealed high variability of VF within each head,

but low variability between brain regions and between animals. The microscale parametric studies showed high sensitivity to changes in substructure moduli and VF. The macroscale model studies showed improvement of intracranial hemorrhage prediction when variable VF was introduced into the models. Clinically relevant biomarkers of PAC damage were not able to be confidently developed, but increased sample size and improved resolution may lead to innovative biomarkers for TBI.

The work presented here addresses a significant lack of data on the PAC, and presents new insights into its anatomy and biomechanics. Many of the studies presented here are the first of their kind, opening up many new paths of TBI research opportunities.

TABLE OF CONTENTS

ACKNOWLEDGEMENTS

I would like to thank my advisor, Dr. Brittany Coats, for her constant support and guidance throughout my degree. Without her, none of the work you see presented here would have been possible. I would also like to thank my committee members, Dr. Ken Monson and Dr. Gary Hedlund, for lending their professional expertise and insight on my work here.

Many thanks go out to my fellow lab mates: Jami Saffioti, Shaun Evans, Daniel Shedd, Jourdan Colter, Justin Jones, Alex Williams, Kiffer Creveling, John Muhs, and McKenna Heninger. You all kept me sane during this whole process.

I would like to thank Dr. Ed Hsu and his dedicated team at the UofU Small Animal Imaging Core. Without their expertise, our MRI studies would have never come to fruition. Special thanks to Osama Abdullah, A. David Gomez, Samer Merchant, and Boston Terry for the abundance of shared codes, knowledge, and imaging help.

I would also like to thank the dedicated staff at the UofU Comparative Medicine center for working with us every step of the way during our animal studies. Special thanks go out to Jackie Brown, Yunuen Coria, Liana Roberson, Rochelle Moore, Misti Seppi, and Reesha Dennis for their constant help with our studies.

I would also like to thank the Primary Children's Medical Center Foundation Early Career Grant for funding and supporting this and other projects within our lab.

Last but not least, I would like to thank my parents Ronald and Marian Scott, my siblings Jeffrey and Crystal Scott, and my girlfriend Harvest Montemayor for their never-ending support throughout all of my life's endeavors.

INTRODUCTION

Traumatic brain injury (TBI) is a leading cause of death and disability, contributing to nearly a third (30.5%) of all injury-related deaths in the United States. According to a recent report published by the CDC, an estimated 1.7 million people sustain a TBI annually. Of these cases, 52,000 result in death, 275,000 result in hospitalization, and 1.365 million result in treatment and release from an emergency department [1]. This same report also noted that children aged 0 to 4 years are one of the most likely groups to sustain a TBI (in addition to adolescents and the elderly) and that nearly a half-million children (473,947) visit the emergency department for TBI annually in the United States.

Although falls are the leading cause of TBI in children aged 0 to 4 years, a large amount of these injuries are due to inflicted injury in the form of abuse [2]. The etiologies diagnosed in children who have experienced accidental TBI (by way of falls or motor-vehicle related incidents) do not show readily apparent differences from etiologies in children who experience abusive head trauma (such as being struck by an adult, struck against another surface, or shaken by an adult [3]). This places a large burden on clinicians who must determine causes of injury based on reported medical histories, which can often times be inaccurate, incomplete, and/or fabricated. Diagnosing AHT in children is especially challenging due to their inability to communicate the history of their injury (in infants) or choose not to communicate their histories due to intimidation

by the abuser (in older children).

In severe cases of TBI, injury is readily apparent due to signs such as open-skull injury, skull fracture, and contusion/bleeding of the head and neck. In addition to readily apparent etiologies, computed tomography (CT) and magnetic resonance imaging (MRI) can elucidate subdural or subarachnoid hemorrhage, inflammatory responses in brain tissue (edema), and diffuse axonal injury (DAI) in white matter tracts. These biomarkers all allow the clinician to determine the severity of TBI and develop appropriate recovery measures in the child. However, in cases involving mild TBI (mTBI), especially in non-contact injury (i.e., shaking) very few or none of these etiologies may be present. This can often times cause under-diagnoses of the injury at hand, leading to unattended-to detrimental effects on the patient's nervous system.

It is our hypothesis that the pia-arachnoid complex (PAC) plays a large role in mTBI injuries. The PAC (also known as the leptomeninges) is a series of collagen-based membranous structures that serve as one of two layers between the brain and skull. The only other tissue layer is the dura, a rigid membrane tightly adhered to the skull. The PAC lies just beneath the dura, and consists of cerebral spinal fluid (CSF), arachnoid trabeculae (AT), and subarachnoid vasculature (SAV) sandwiched between the arachnoid and pia membranes (Figure 1). It serves a critical function of protecting the brain from insult by acting as a mechanical tether between the brain and skull, and absorbing energy upon impact. The overall mechanical response of the PAC, as well as the interweaving of cortical vessels within the PAC suggest that this complex structure will influence cortical vessel strain and/or rupture during TBI. In cases in which no hemorrhage has occurred, and thus no blood can be visualized, we believe that the fine structures of the AT may be

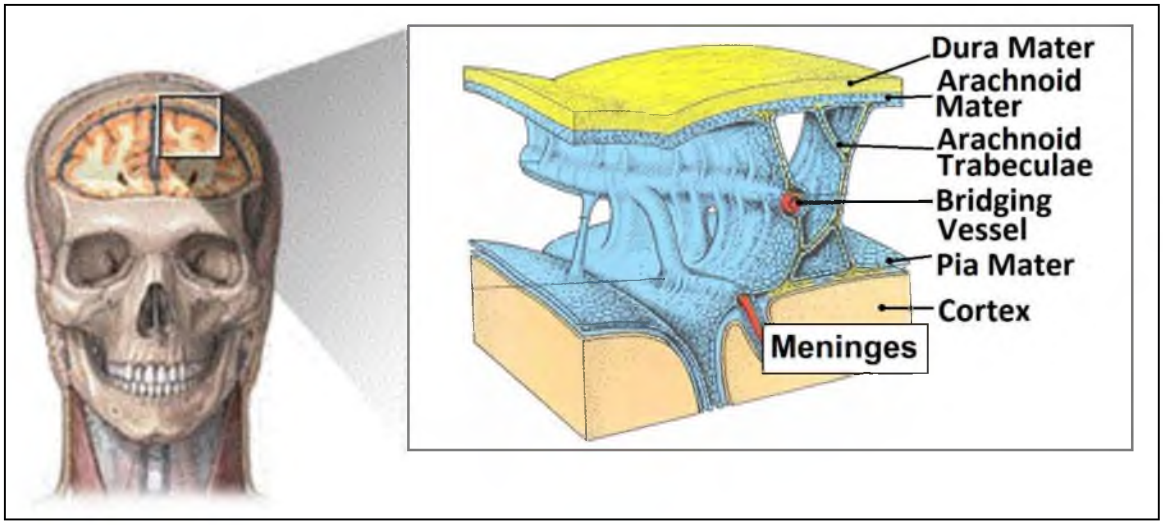

Figure 1: Anatomical diagram of a section of the PAC. Adapted from [4] & [5].

damaged, yet undetectable to modern medical imaging technologies. This damage would leave the patient more susceptible to injury during potential future TBI events.

There exists a large body of literature investigating TBI from a biomechanics standpoint, including finite element (FE) studies [6-13] animal models [14-23], and kinematic models in instrumented surrogate dummies [24-25]. The body of FE literature fails to accurately represent the PAC with the exception of a few studies which simplify the PAC as a solid element, fluid element, or prescribed mechanical boundary condition [26-30]. There are a few studies that have modeled the PAC on a microscale level. The first by Ma et al. [31] represents the AT as a repeated structure of elastic connectors, and is not very anatomically realistic. The second by Zoghi-Moghadam et al. [32] is based on anatomical drawings but does not account for variable amounts of AT present. Existing animal models of TBI have been accurate at identifying TBI in postmortem examination, and in some cases *in-vivo* via MRI and CT imaging; however, none of these studies have directly focused on the PAC. Surrogate simulations provide very useful information for

boundary conditions, applied loads, and other kinematic information in TBI accident recreation. Unfortunately, they do not provide very useful output information (i.e., tissue strains, injury predictors, and other biological indicators).

The overall goal of the work contained in this thesis was to investigate the PAC in a variety of methods, including medical imaging and finite element modeling, in order to learn more about its biomechanical response to TBI.

Chapter 1 details our first foray into exploring the PAC by finding a way to better visualize its fine structure. This was achieved with a novel application of optical coherence tomography (OCT) in which the surfaces of exposed immature porcine brains were imaged after craniotomy. Images obtained from this analysis were analyzed for amount of AT structures present via manual image segmentation (referred to as volume fraction (VF) in this paper). The results from these analyses were then compared statistically for any differences in AT structure population across regions of the brain or across different animals.

In Chapter 2, finite element modeling was utilized to create a microscale model of the PAC. This model discretized the PAC into its constitutive components (pia, upper arachnoid (UA), subarachnoid vasculature (SAV), and arachnoid trabeculae (AT)). Aside from one other study [32], this is the most physiologically detailed model of the PAC currently available. A novel method of populating the model with SAV and AT structures to different levels of VF, while maintaining a randomized distribution was created. Then, two parametric studies were conducted, one evaluating the role of AT VF on brain-skull displacement and SAV strain, and the other evaluating the role of differing moduli of the substructures within the PAC on the same metrics.

Chapter 3 was motivated by the findings of Chapter 1, which indicated high variability of VF within brains, and the findings of Chapter 2, which indicated that VF had a significant effect on injury metrics. Since it was now established that the VF of the PAC had a significant effect on the injury metrics established in our microscale model, it was desired to extend these predictions to a macroscale model utilizing a multiscale modeling approach. The microscale PAC model was rebuilt to contain immature porcine properties and dimensions. This model was subjected to tensile tests in and out of plane, for different VFs, in order to establish material properties dependent on VF. These material properties were then imported into a macroscale model of an immature piglet undergoing a rapid rotational deceleration injury (similar to that experienced during shaken baby syndrome), which had been previously created by Coats et al. [23]. The macroscale model was built such that the imported PAC properties were varied according to the measured VF in two piglet brains studies in Chapter 1. This allowed a look into the effects of the highly variable VF of the PAC on whole-brain mechanics.

Ultimately, the invasive OCT imaging would not be a viable tool for identifying PAC damage clinically. Therefore, in Chapter 4, we expanded upon an animal model of 3-5 day old piglets which undergo shaking representative of that incurred by human children during shaken baby syndrome [33-34]. Previously, the animals were only examined for brain injury upon postmortem dissection and histological review. For the present study, *in-vivo* imaging of injured and uninjured animals was conducted with an MRI machine to elucidate clinically relevant biomarkers of PAC damage. Multiple MRI modalities were evaluated for their abilities to provide useful biomarkers relating to PAC damage. These clinically relevant, *in-vivo* biomarkers were to be correlated to the

previously mentioned *ex-vivo* and simulated biomarkers. Additionally, postmortem OCT imaging was conducted as in Chapter 1, allowing for direct comparison of injured and uninjured animals.

These studies address a significant lack of data in the literature surrounding the PAC, a structure that may largely affect the brain's response during injury. The studies presented here provide a solid groundwork for continuing investigations of the PAC's contribution to the brain's behavior during TBI.

CHAPTER 1

CHARACTERIZATION AND QUANTIFICATION OF THE PIA-ARACHNOID COMPLEX

1.1 Introduction

Traumatic brain injury (TBI) is one of the leading causes of death and disability in the world, and is often identified by the presence of subdural and/or subarachnoid hemorrhages that develop from ruptured cortical vessels during brain-skull displacement. The pia-arachnoid complex (PAC), also known as the leptomeninges, lies just beneath the dura, and consists of cerebral spinal fluid (CSF), arachnoid trabeculae (AT), and subarachnoid vasculature (SAV) sandwiched between the arachnoid and pia membranes. It serves a critical function of protecting the brain from insult by acting as a mechanical tether between the brain and skull, and absorbing energy upon impact. The overall mechanical response of the PAC, as well as the interweaving of cortical vessels within the PAC, suggest that this complex structure influences cortical vessel strain and/or rupture during head trauma.

Traditionally, imaging of brain anatomy is performed with magnetic resonance imaging (MRI), computed tomography (CT), or nuclear medicine techniques such as positron emission tomography (PET). Each of these techniques are very robust in imaging many of the gross structures of the *in-vivo* brain; however, none of them possess

a fine-enough resolution to capture the microscale structures of the PAC. In order to image the PAC substructures, microscopy methods can be employed, but only at the risk of potentially damaging the structures during brain removal and tissue preparation. Transmission election microscopy (TEM) and scanning electron microscopy (SEM) have been used to obtain extremely detailed images of the PAC in cranial [35-37], spinal [38], and optic nerve [39] regions in humans. While these images are certainly detailed, they are not representative of the *in-vivo* state of the tissue, as TEM and SEM usually require extensive preparation methods including drying, freezing, staining, and/or coating.

Another alternative, however, is optical coherence tomography (OCT). OCT is a relatively new imaging modality primarily used in ophthalmology to image the structures of the eye [40]. Secondary biomedical uses for OCT include dermatology [41], gastro-intestinal imaging [42], and intravascular imaging [43]. OCT is an interferometry based imaging technique which uses backscattered near-infrared light to construct images of the scattering media. The method typically results in micrometer and sub-micrometer resolution, three-dimensional images, and can obtain a much larger penetration depth than standard microscopy techniques. This penetration depth, however, is still only a few millimeters and is best suited for imaging surface structures or tissues prepared in dissected slices. A major drawback of this method compared to clinical imaging modalities, such as MRI and CT, is its reduced imaging window (usually a volume only a few millimeters in size, as compared to the entire brain via MRI/CT methods). Another limitation of OCT is its sensitivity to IR-opaque materials (e.g., bone and blood) which can cause severe signal attenuation loss.

Despite the stated limitations, the very high resolution of OCT is still appealing to

many neuroanatomical researchers. Multiple early studies used OCT to differentiate between gray and white matter and visualize the general neural morphology of brain tissue by identifying differences in light attenuation in each tissue type [44-45]. Srinivasan et al. have studied cerebrovascular physiology in rats with alternative forms of OCT such as Doppler OCT and OCT angiography [46-47]. Studies have also recently been conducted using Multi-Contrast OCT to visualize tractography in *ex-vivo* slices of the brain [48] and identify tumorous cortical tissue [49]. Attempts have also been made to alleviate the skull's presence as a barrier to *in-vivo* brain imaging by implementing transparent skull substitutes [50], or skull-thinning techniques [51]. To eliminate the limitation of the small-field-of-view of OCT, Finke et al. presented a method of meshing together OCT images and creating large field-of-view images of resection cavities in neurosurgical applications [52]. Lastly, OCT has also found its way into being utilized as an optical elastography tool for viscoelastic material property testing in the brain [53] [54]. These forays into brain imaging with OCT indicate that it is a viable method of obtaining high resolution images of various structures of the brain, both *ex-vivo* and in some cases *in-situ*.

To date, no studies have been performed in which OCT is utilized to image the PAC. The goal of this study was to quantify the regional variability in the amount of AT and SAV present in the PAC (reported as volume fraction). Brain-to-brain variability and within-brain variability of volume fraction in the PAC may provide insight into brains and regions within a brain that have increased vulnerability to subdural and subarachnoid hemorrhage associated with head trauma.

1.2 Methods

1.2.1 Optical Coherence Tomography Imaging Protocol Development

All OCT imaging was performed using a Bioptigen R2200 OCT scanner. The Bioptigen InVivoVue software was used to specify scan settings best suited for imaging the PAC. In OCT imaging, volume acquisitions are characterized by three main parameters: number of A-scans per B-scan (1-D lines into tissue per 2-D slices), number of B-scans (2-D slices across the volume), and number of C-scans (repetitions of the same volume) (Figure 2). Additional controls are available to alter the A-scan depth, scan volume size, scan angle offset, and many other ophthalmological parameters not needed for our study. In addition to scan settings, scan resolutions depend on the light source and lens used when scanning. Our setup consisted of an ultra-high-resolution (UHR) light source and a 12 mm telecentric lens. This resulted in a maximum attainable resolution of 1.6 µm (axially in A-scans) and 2 µm (within B-scan frames), and a maximum field of view of 8 mm by 8 mm with a 1.7 mm depth.

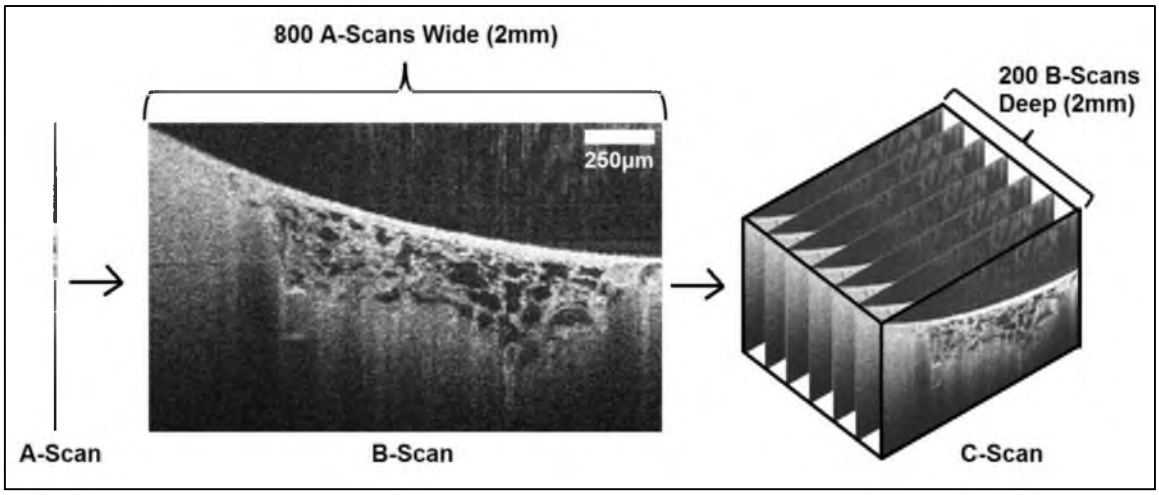

Figure 2: Schematic showcasing the final chosen scan parameters: 800 A-scans per B-scan, 200 B-scans, resulting in 1 C-scan (no averaging). Voxel resolution was 2 µm x 3.125 µm x 10 µm.

The maximum values of the system, however, are theoretical and not practical for the current application. In typical OCT examinations of the eye, only a few B-scans are needed, as the ophthalmologist is generally only interested in a single "slice" view of the internal ocular structures. In this study, we wanted to attain high-resolution in all three dimensions of our scan, which meant including a large number of B-scans. This increased number of B-scans increases the virtual memory requirements of the scanning program, and eventually supersedes the capacity of the computer running the scanner. Because of this, a balancing act was necessary to maximize A-per-B scans (in-slice resolution) and number of B-scans (out-of-slice resolution). To identify the best imaging protocol and scan settings for the PAC, preliminary test scans were performed on *ex-vivo*, fixed brains. Settings were iteratively varied and different combinations of A, B, and C-scans were evaluated. The final scan settings for the PAC were: 800 A-scans per B-Scan, 200 B-scans, and 1 C-scan (no averaging) over a field of view of 2 mm by 2 mm by 1.2 mm (Figure 2). These settings resulted in volume acquisitions with a voxel resolution of 2 μm (axially in A-scans), 3.125 μm (within B-scan frames), and 10 μm (spacing between B-scans).

1.2.2 In-Situ Tissue Preparation

Immature piglets (aged 3-5 days old, female, n=7) were euthanized and perfusion fixed with 10% unbuffered formalin in order to remove all blood from the brain. This allotted for longer imaging time (circumventing tissue degradation), and improved image quality as blood causes signal loss and shadowing due to hemoglobin's high levels of near infra-red light absorption. Once perfusion was complete, the animal was placed in a

prone position and a craniotomy was performed (Figure 3). A small hand drill was used to create a series of holes around the edges of the upper hemisphere. Pointed rongeurs were then used to carefully crack the skull away, without damaging the underlying dura. Once the skull cap was fully separated from the basal skull, it was gently pulled away from the dura. Taking care not to puncture the arachnoid, tweezers were used to pull up a small section of dura while puncturing it with curved scissors. The curved scissors were inserted through the hole and slid along the interface of the dura and arachnoid, cutting the dura as the membranes were separated. In order to not disturb the bridging vessels entering the superior sagittal sinus, the dura was not removed from the midline. This resulted in only the left and right hemispheres being exposed (Figure 3E).

1.2.3 Imaging Procedure

Optical coherence tomography imaging was performed on each brain with a custom stereotactic device that allowed precise imaging around a spherical coordinate system (Figure 4). The device features a linear positioning stage which allows high-precision control in the r-direction, a circular stage in the horizontal plane which provides rotation in the ϕ-direction, and custom-built hoop shaped bearing tracks which provide motion in the third (θ) direction. The OCT aiming probe was firmly attached to the holster, which could be held in a stable position at any user-determined r-depth and θ or ϕ angle. When equipped with a 12 mm telecentric lens, the positioning device has a 0-85 mm radius of travel and could accommodate brains as small as rat to as large as adult human.

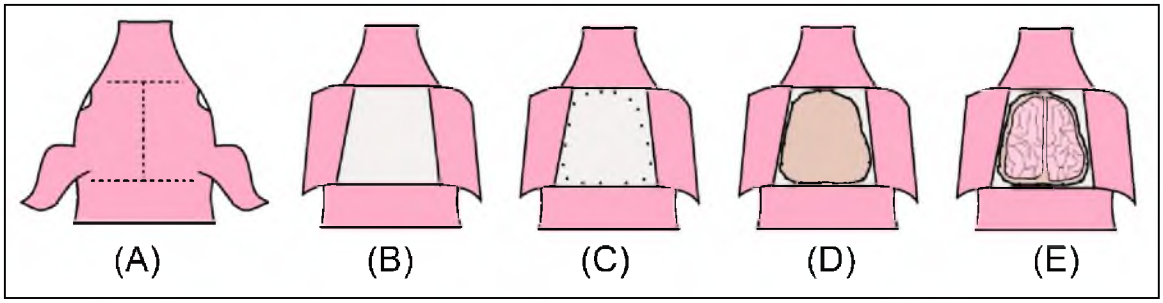

Figure 3: Craniotomy procedure: Scalpel was used to cut the scalp (A), and reflect the scalp back to reveal the skull (B). Holes are drilled through the skull (C) to better control facture lines as rongeurs chipped away the skull (D). The dura was carefully removed from the cortical surface, except over the superior saggital sinus (E).

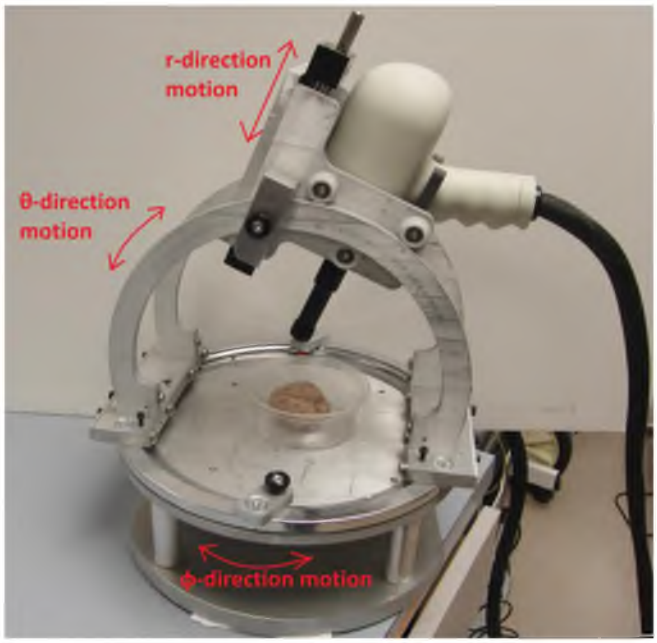

Figure 4: Custom-built stereotactic device for imaging of brains or any other pseudo-spherical tissue.

To image the brain, the piglet's head was placed under the OCT aiming probe in the stereotactic device. Image volumes were acquired with the settings described earlier (Section 1.2.1). The medial frontmost portion of the brain was imaged first, and then the aiming probe was moved back sequentially to the backmost portion of the brain. The probe was then moved laterally and scans were obtained sequentially moving forward until the front of the brain was reached. This was performed on both hemispheres, as

shown in Figure 5. The volumetric images were categorized as: left or right hemisphere (L/R), medial or lateral (M/L), and frontal, parietal, or occipital lobe (F/P/O). The combination of these categories resulted in 12 total regions of interest.

It was noticed that during these imaging sequences, the PAC appeared to be slightly collapsed, as only images in the sulci of the brain were achievable, and the upper arachnoid (UA) membrane was in contact with the cortex over the gyri (deflating the PAC and making AT impossible to image). A remedy to this was implemented on the last 2 brains, in which a syringe pump was utilized to pump saline into the subarachnoid space and re-inflate the PAC. This inflation was not easy, and in many cases had to be abandoned due to the inability to cause substantial inflation. Issues included: saline flushing back out of the injection site, microscopic puncture holes in the UA letting saline leak out, and saline leaking into other CSF spaces in the piglet's anatomy.

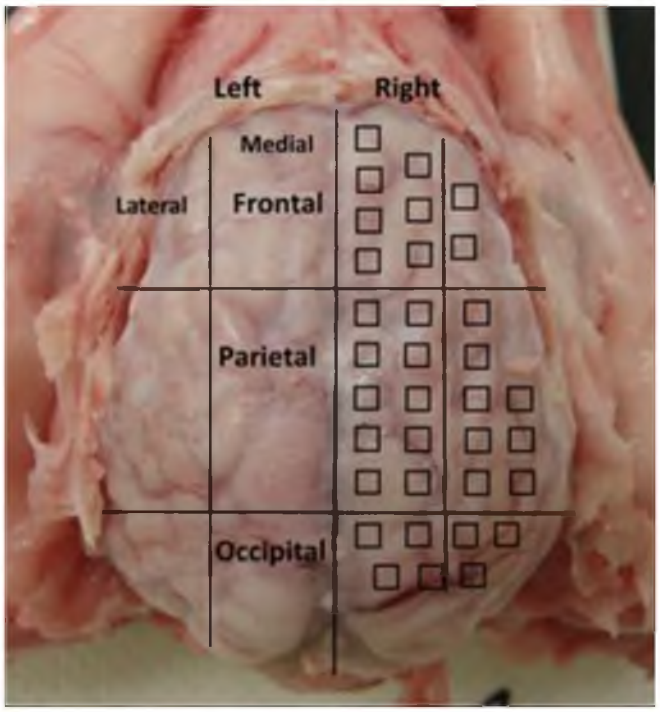

Figure 5: Locations for volumetric OCT imaging of PAC substructures on porcine brain

Of the 2 brains that were inflated, there was no way of knowing how close the inflation was to the *in-vivo* state of the PAC. Additionally, there was no way of guaranteeing that each brain was inflated to the same level aside from the fact that the syringe pump was always set to the same volumetric flow rate (8 ml/min). The resulting volume fraction values would be dependent on both of these factors, so these brains were excluded from the data set. It was then assumed that relative changes in volume fraction between brains and between regions in the same brain would be captured with the relative changes in the sulci.

1.2.4 B-Scan Image Processing Protocol

Each volumetric scan contained 200 B-scans. Approximately 30 volumes were obtained from each brain, and 7 brains were analyzed. This resulted in over 42,000 2D images collected during our study. An automated image processing algorithm would be ideal to process this large magnitude of images. However, automated segmentation was impractical due to the complexity of the structures in the images, the amount of noise in all images, and the occasional occurrence of image artifacts. Therefore, volume fraction (VF) was obtained through manual segmentation using Adobe Photoshop (CS5, Adobe Systems Incorporated). Analyzing over 42,000 images with manual segmentation would be an extremely arduous process. As such, only one frame per volume (Figure 6A) was analyzed with the assumption that the area fraction of a single frame from the 200-frame volume was representative of the VF of the whole volume. In each image, the AT and SAV were manually selected in the subarachnoid space, taking care not to include the UA membrane or cortex of the brain (Figure 6B). The entire subarachnoid space was then

selected (Figure 6C), and the area fraction was calculated as the number of pixels of AT/SAV divided by the total number of pixels in the subarachnoid space (Figure 6D). Images were scaled from their skewed display aspect ratio (640 by 480) to the true anatomical aspect ratio (640 by 384, or 2 mm by 1.2 mm) prior to the area fraction calculation. One-way ANOVA analyses were conducted on the collected data, to see if there were any significant differences across lobes of the brain, animal, or any of the 12 subregions. The means and p-values of these analyses are presented in Appendix A.3.

1.2.5 Whole Volume Processing Protocol

To validate the assumption that area fraction in a single 2D frame is representative of the entire 3D volume fraction, three entire volumes were segmented and analyzed in Seg3D [55]. Seg3D automates the volumetric image segmentation process as much as possible, but still requires the user to manually trace the regions of interest in each frame. Similar to the 2D manual segmentation, each image in a volume is manually segmented by highlighting AT, SAV, and subarachnoid space. The program then renders an isosurface from the series of 2-D images (Figure 7) and calculates multiple geometric properties, including volume. The 3D volume of the AT/SAV structures was divided by the volume of the entire subarachnoid space, to estimate a volume fraction. The 3D volume fraction was then compared to the 2D-slice it corresponded to, and a percent difference between the VF and area fraction (AF) was calculated. It was assumed that the true 3D VF could be compared to the 2D AF directly, since multiplying the AF by volume thickness would scale both the denominator and numerator, resulting in the same value.

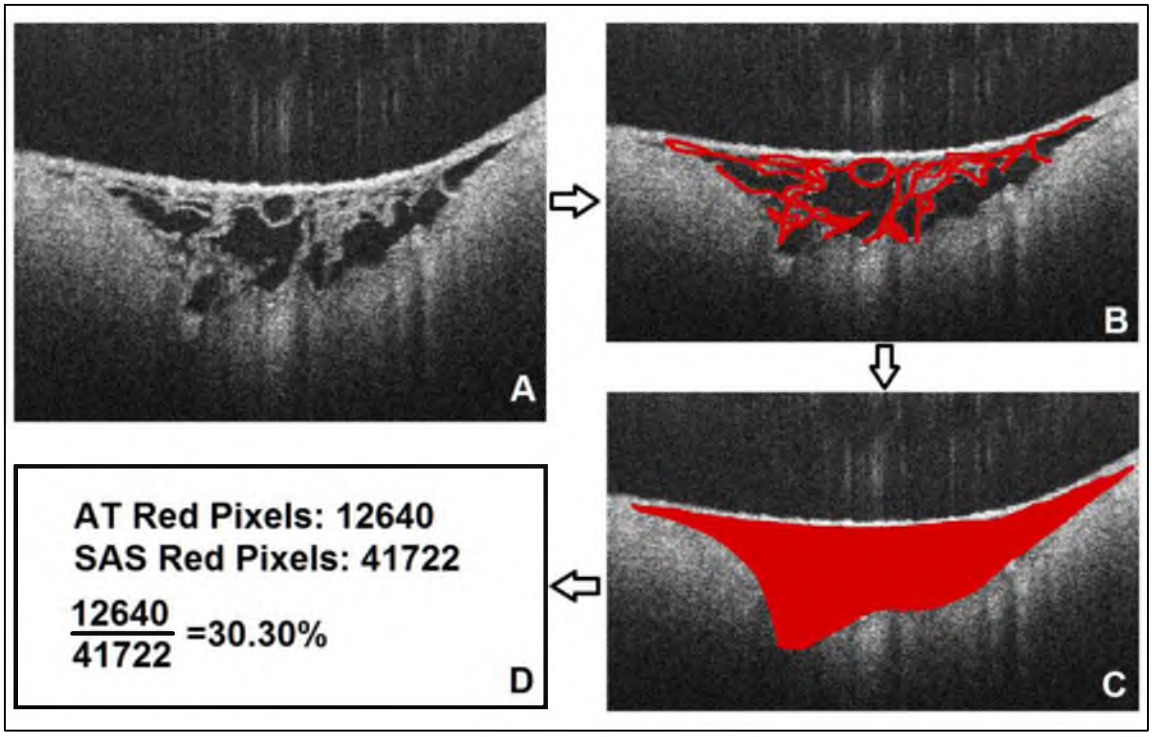

Figure 6: Representative OCT image before scaling (A). Area fraction was calculated by first scaling the images, then highlighting the AT & SAV (B) and subarachnoid space (C) manually, and calculating the ratio between the two (D).

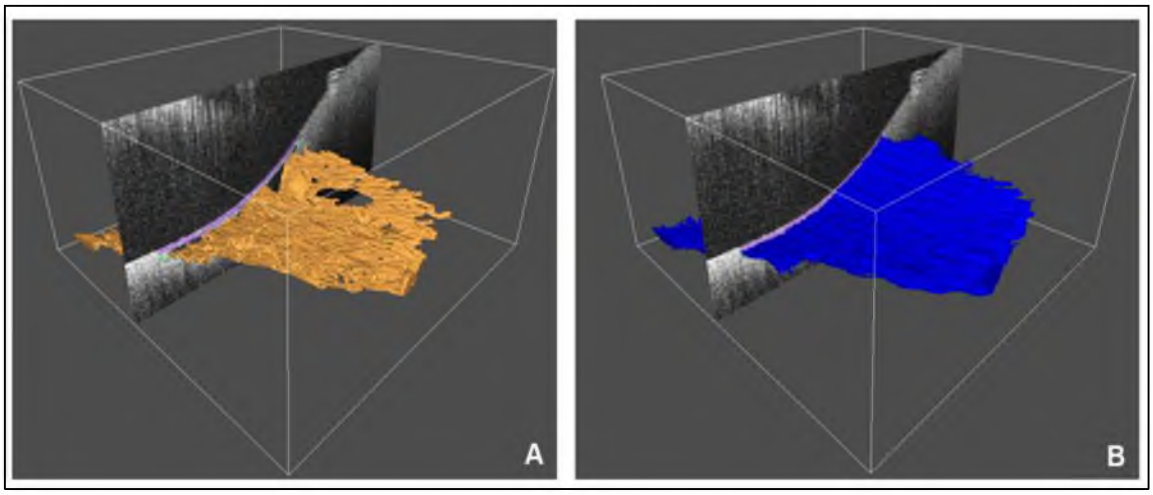

Figure 7: Rendered 3D isosurface of AT & SAV (A) and the associated subarachnoid space (B) used to calculate volume fraction from an OCT volume scan.

1.3 Results

The maximum difference between the volume fractions calculated in Seg3D and their corresponding 2D image area fraction was 7.5% (Table 1). No clear bias in the measurements was seen when comparing the two methods (as some results were lower and some were higher than the expected value). This suggests that the manual 2D image processing method is a reasonable approximation of volume fraction.

The 2D estimates of volume fraction were categorized by anatomical subregion (n=12) and animal number (n=5). Two animals (P13-121, P13-122) were excluded from these analyses, because the SAS of these animals was manually inflated with saline. This caused the mean of the VF measurements to be approximately 9.2% lower than the others and not is directly comparable. The average (±standard deviation) volume fraction of AT measured across all 5 uninflated brains was 32.26% (±7.2%). AT volume fraction across all brains ranged from 13.8-53.0%. Because of the large variability, no significant differences in AT volume fraction were found among the lobes, subregions, or animals (Figures 8-10 respectively).

The average volume fraction (averaged over the entire brain) differed between animals by a maximum of 4.8%, but differences in averaged volume fraction between subregions within a single brain ranged 20.1 - 38.4%. This suggests there is a much larger variability within a brain than between the brains of two animals. Despite the lack of statistical significance, a specific trend can be seen for the majority of the brains. Commonly, the highest VF values were measured at the most caudal portion of the occipital lobes and the most rostral portions of the frontal lobes. This seems to indicate there may be a trend near the edges of our craniotomy opening of higher VF values. This

Table 1: Comparison of 2D area fraction values to 3D volume fraction values.

Animal	Location of scan	2D AF	3D VF	Difference
P13-110	Right, Lateral, Frontal	29.3%	33.9%	-4.60%
P13-098	Left, Medial, Frontal	31.4%	25.2%	6.21%
P13-110	Right, Medial, Frontal	26.6%	34.1%	-7.51%
P13-102	Left, Medial, Parietal	23.4%	19.9%	-3.55%

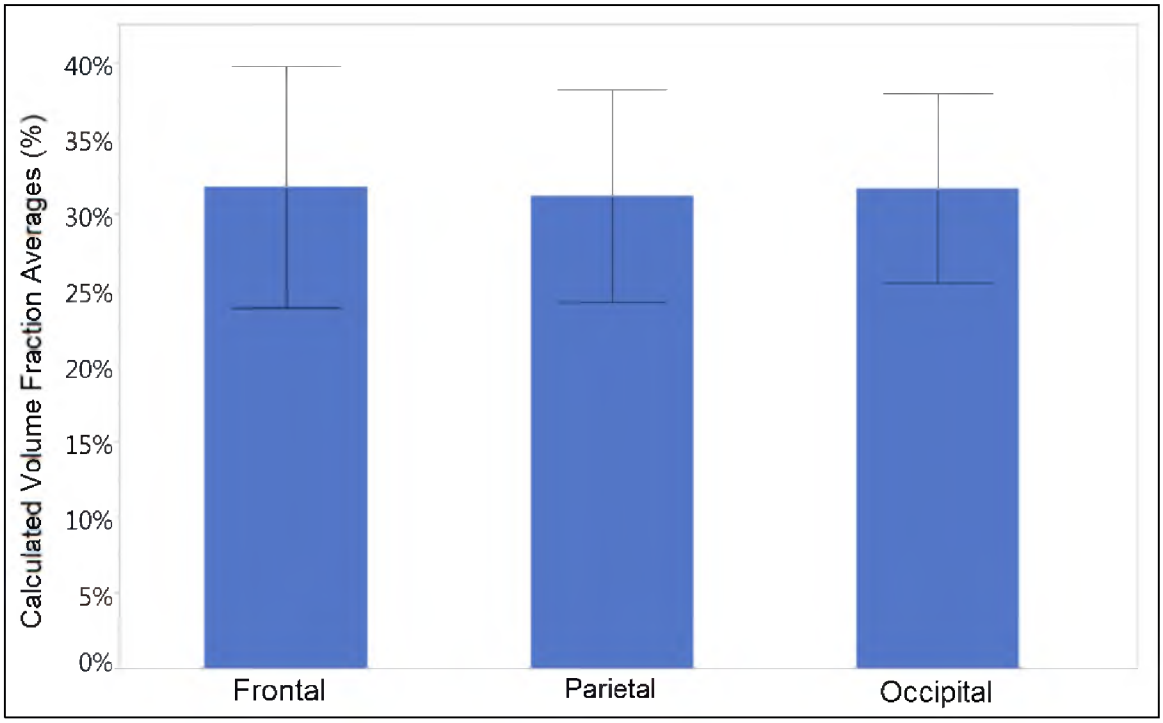

Figure 8: Means (with standard deviation) of the measured volume fractions in all uninflated brains (N=5), categorized by 3 major lobes of the brain.

could potentially mean higher VF on more ventral portions of the frontal lobes and rostral portions of occipital lobes of the brain, which lie just outside our imaging window. The lowest values of each brain did not appear to have an obvious regional trend. There was also a large amount of cases where our highest values were immediately adjacent to our lowest values. These large jumps highlight the extremely variable anatomy of the PAC, as the transitions from low to high values are not smooth. A color map of the measured VF values is presented in Figure 11 for the five uninflated brains.

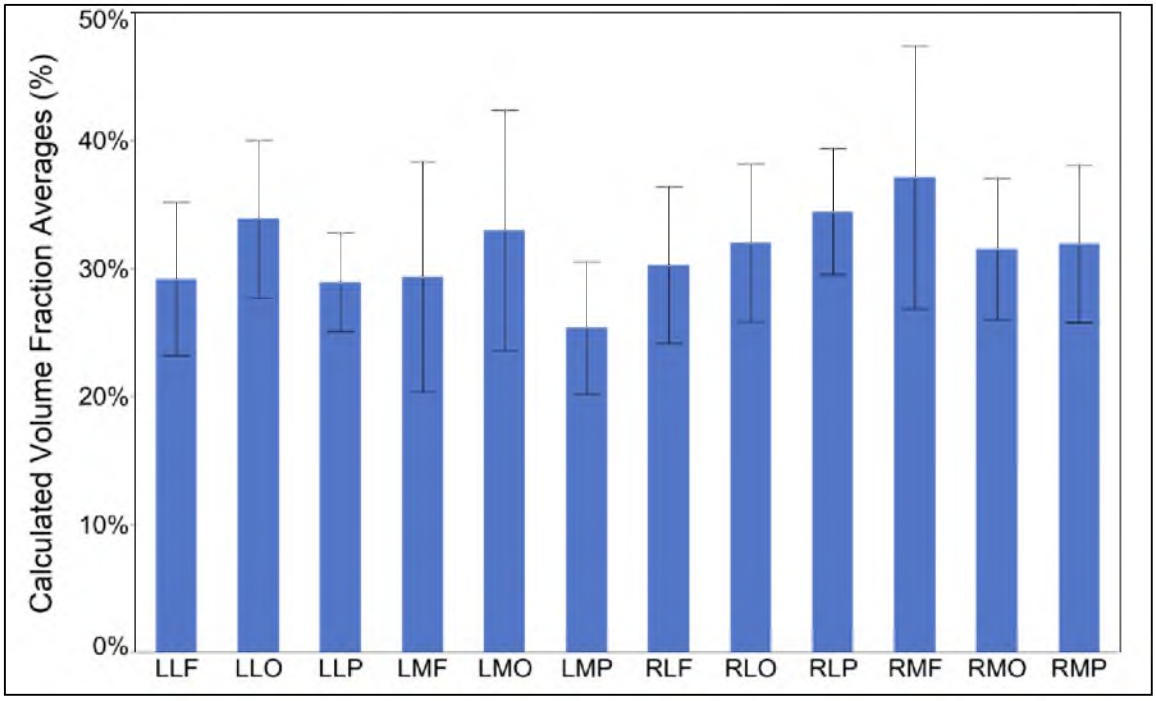

Figure 9: Means (with standard deviation) of the calculated volume fractions in all uninflated brains (N=5), categorized by 12 anatomical subregions (1st letter: left or right, 2nd letter: lateral or medial, 3rd letter: frontal, parietal or occipital).

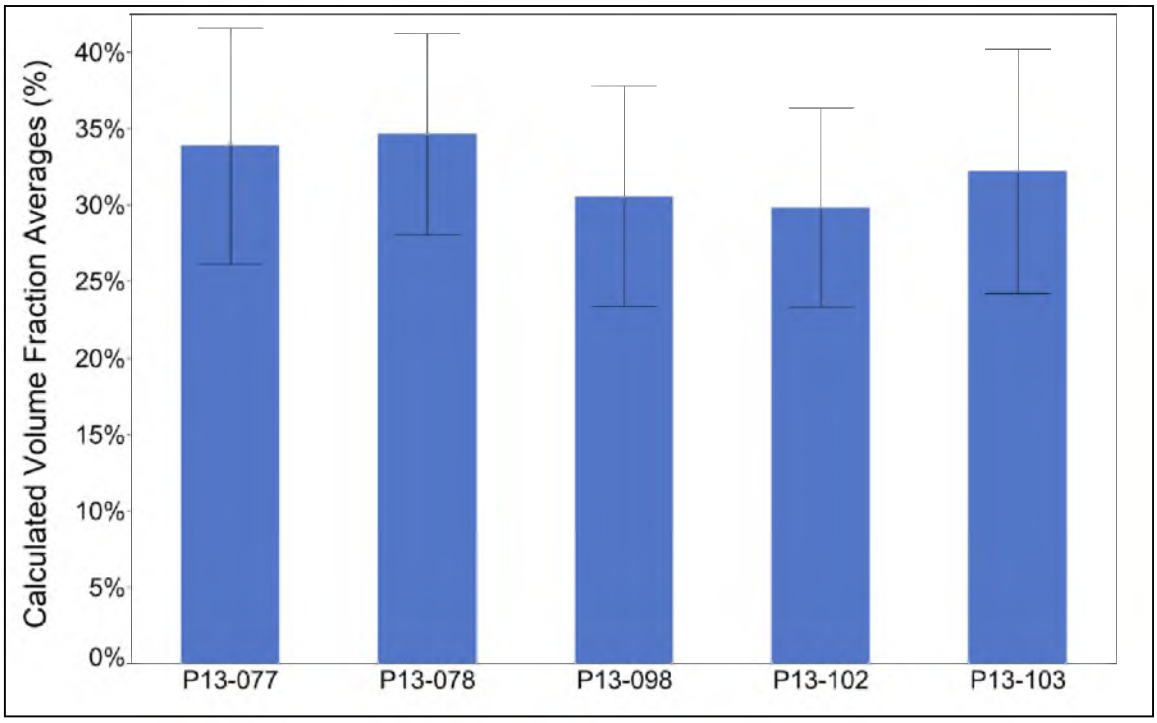

Figure 10: Means (with standard deviations) of the calculated volume fractions in all uninflated brains (N=5), categorized by each separate animal.

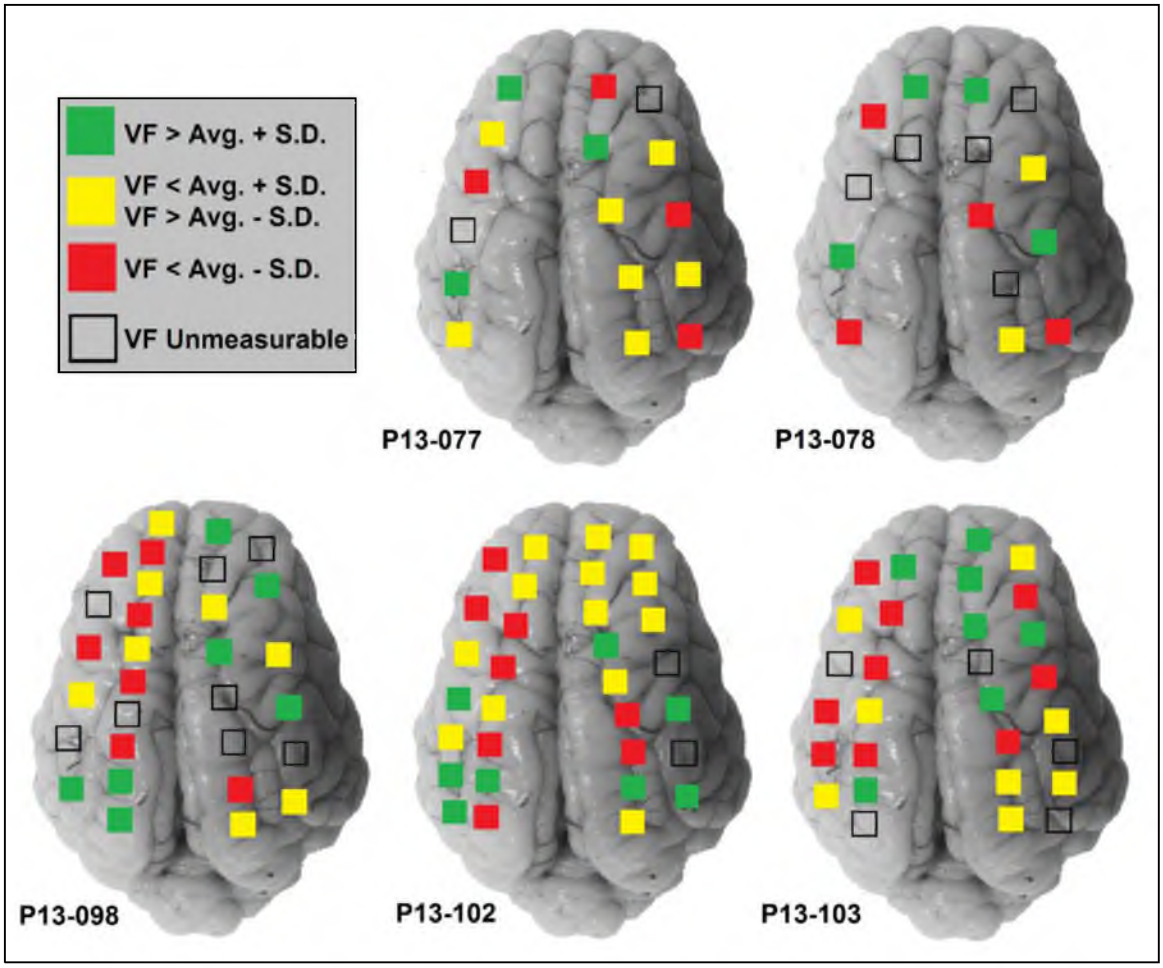

Figure 11: Color map of VF distributions across the five uninflated brains. Averages and standard deviations are calculated for each brain separately. Note that positions are approximate and based on notes collected from the operator during the imaging session.

1.4 Discussion

In this study, we demonstrate that OCT imaging is a viable alternative to traditional microscopy methods to obtain high-resolution volumetric images of the PAC. Optical coherence tomography is a new and evolving imaging field, and as such, the quality of images obtained with it will only improve over time. Our preliminary study was able to identify AT and SAV structures, allowing accurate (albeit manual) measurement of these structures across the cortical surface. If OCT imaging continues to

evolve at its current rate, automated scans of entire brain surfaces, followed by automated processing of the substructures found in the scans would not be farfetched.

The data presented seem to indicate that there are no large regional differences in AT volume fraction, nor does it indicate large animal to animal variability. The results do indicate a large variability within each animal, however, which is an intriguing finding. The various regions of high and low VF may exhibit a stronger or weaker tethering effect on the brain. When coupled with the large variability of bridging veins [56] and other subarachnoid vasculature, many different levels of susceptibility to subdural or subarachnoid hemorrhages (SDH or SAH) are present across the brain. The fact that there was a low brain-to-brain variability shows that our findings are not unique to specific patients, but rather apply to the whole population. The implications of these findings provide a difficult to handle problem in terms of clinical TBI diagnosis. The clinician must treat every patient as susceptible to SDH or SAH, yet has no way of knowing what regions of the PAC to target. Additionally, due to the exhibiting high variability, it is difficult to diagnose if degradation of the PAC has occurred after injury, or if the targeted region simply had low VF to start with. With increased sample size, potential regional trends such as the ones observed in the rostral frontal and caudal occipital regions could become more apparent. These trends could then direct researchers to focus their efforts on these specific regions when studying TBI.

Due to the fact that the brains were deflated during imaging, the absolute values of volume fraction reported are not representative of the *in-vivo* state of PAC. Relative differences can still be utilized to compare all brains, however, which is why each brain was compared to its own mean in the previous section. Normalization of the data (in

which each measurement in a brain is divided by the overall mean of the brain) may provide a way to allow comparison across deflated and artificially inflated brains (which had average volume fractions roughly 9.2% less than the deflated brains). This normalization method should not yield any scaling errors. The vacant space scales linearly with the VF in inflated brains, and the occupied space (AT & SAV) stays constant. However, at low levels of inflation, more AT & SAV structures will be folded in onto each other, and some blurring of the boundaries in the images may occur. This could result in over prediction of VF when the images are processed. Until a method measuring the true *in-vivo* state of the PAC is found, there is no way to accurately correlate the deflated and artificially inflated VF findings to *in-vivo* levels.

Extreme care should be taken when interpreting these findings, as the small sample size (N=5) does not give the study a significant amount of power. This small sample size significantly reduces our ability to discern regional trends of VF. Future studies are currently planned (N=24) which will hopefully shed some light on trends that may have been too subtle for the current study to discern.

The quality of the OCT images was also a limiting factor in the research. Noise and image artifacts prevented an automated image processing algorithm from being implemented to measure VF. Due to this, human bias may have been introduced into the findings. Although the manual segmentation of images proved to be fairly accurate, the calculated volume fractions are still dependent on image quality. If a structure is diffuse or hard to identify, a user may not see it as an AT/SAV structure, and classify it as an artifact or noise. Additionally, frame spacing was low, resulting in a 4 times reduction in resolution of our out-of-frame axis. Window size was limited to 2 mm by 2 mm, which

only allows for the viewing of one sulci at a time. If upgrades to our current computer system were made, scan window size could be increased and our number of B-scans could be increased. An increased number of B-scans would allow for equal out-of-plane and in-plane resolution, resulting in AT structures traveling in the out-of-plane direction to be better imaged. Full resolution volumes could then be obtained, allowing structures to be properly imaged in and out of plane. Additionally larger window sizes could allow for more efficient processing of the entire brain's surface, and not only select regions. The light source could also be upgraded, allowing for deeper A-scan penetration depths, lower signal-to-noise ratio, and higher resolution images. Future studies may incorporate these upgrades, potentially allowing for the re-evaluation of using an automated image processing algorithm.

1.5 Conclusion

A novel method of imaging PAC microstructures with optical coherence tomography has been presented and has proven to be quite useful in determining the distribution of AT/SAV microstructures across the brain's surface. To the author's knowledge, no study has been performed to date which provides quantifiable values on the distribution of AT/SAV in the brain. In the form of our reported volume fraction, we now provide researchers with preliminary scalable values of AT/SAV distribution and variability on the brain. Large variability of AT/SAV volume fraction was found, indicating a potential for random localized weak points on the brain to SDH and SAH. A quantifiable set of numbers dictating the amount of AT present in the PAC will allow traumatic brain injury researchers to construct more realistic FE models of the PAC and

more accurately predict head injury. The presented work is a first step towards a comprehensive data set of such values, and has great potential to become a useful tool for the TBI research community.

CHAPTER 2

MICROSCALE FINITE ELEMENT MODEL OF THE PIA-ARACHNOID COMPLEX

2.1 Introduction

A powerful tool commonly used in the investigation of traumatic brain injury (TBI) is finite element (FE) modeling. Researchers have developed comprehensive whole-head models of head injury which take into account many of the biological complexities of the head including scalp, skull, meninges, brain (with gray/white matter differentiation), and vasculature [6-13]. However, these studies fall short in how they represent the pia arachnoid complex (PAC) and its interaction between the brain and the skull. Most commonly, the PAC is modeled as either a solid element or a fluid element, which allows for accurate stress/strain matching, but falls short in terms of injury prediction. Coats et al. compared elastic spring connectors to the previous interface modalities and compared brain/skull displacement and brain strain predictions to experimental animal data [23]. The elastic connectors were found to be an improvement over the solid elements because the sensitivity and specificity of intracranial hemorrhage predictions occurring anywhere in the brain were 80 and 85%, respectively. However, regional predictions of hemorrhage did not perform as well and resulted in sensitivity and specificity values as low as 63% and 76%, respectively. Other studies have evaluated

how boundary conditions at the brain/skull interface influence predictions of brain injury and agree that the accurate representation of the PAC is critical to the accurate prediction of head injury [26-30]. Despite this agreement, a sufficient simplified representation of the PAC has not been found to date. Recently, one research group has developed a microscale model of the PAC based on anatomical drawings and paired it with a whole-head model in a multiscale approach to simulating head injury [32]. Their model appears to be an improvement in the qualitative sense, but their conclusions were limited due to the lack of experimental data to compare to. Additionally, they assumed that the distribution of the microstructures was uniform across the brain, but our data in Chapter 1 show that there is a large variation (13.8% - 53.0%) in the volume fraction of PAC substructures throughout the brain.

In this study, we generated a new microscale model of the PAC. This microscale model was not created based on qualitative anatomical drawings and images. Rather, a more systematic approach was taken, in which simplified structures representative of the arachnoid trabeculae (AT) were distributed in a randomized fashion. These randomized models were utilized in a parametric study to evaluate the effect of differing material properties of the PAC substructures, as well as differing population densities (volume fractions) of AT present in the PAC. The microscale model will then be used in conjunction with a whole-head FE model, in Chapter 3, to simulate rapid head rotation and determine the effects PAC variation has on overall predictions of TBI.

2.2 Methods

2.2.1 Geometry

The PAC model consists of a 4 mm by 4 mm square slice of dura membrane, upper-arachnoid membrane, arachnoid trabeculae, subarachnoid vasculature, and pia membrane. Dimensions of the entire PAC model were based on average dimensions reported for bovine/porcine and adult human PAC. The parametric study detailed in this chapter explores stiffness values ranging from animal to human values, and it was desired to create a model at a midline size to best incorporate this large range of moduli [57-63]. When constructing this midline model, it was important that no structures were scaled too large or small, and that the model appeared realistic when compared to anatomical diagrams. Therefore, the dimensions of PAC substructures are not all true mathematical averages or medians, but rather close approximations of those averages. This resulted in a more anatomically accurate model.

Membrane thicknesses were based off of estimated midline sizes between bovine and human measurements. Bovine PAC thicknesses reported by Jin et al. [57] were 23.6 μm on average (in a collapsed state, without the subarachnoid space). The subarachnoid space thickness was estimated between reported values measured in bovine brains *in-vivo* (~0.5mm) [64] and the thickness used in an adult human FE model (2.5mm) [32]. Dimensions of the AT structures were estimated from traditional optical microscopy and electron microscopy images presented in the literature [35-36,39] as well as the aforementioned in-house OCT imaging. Dimensions of subarachnoid vessels were scaled down from adult human data reported by Monson et al. to have the same size relative to other structures in the model [62]. See Table 2 for a complete listing of all important

Table 2: Dimensions of all substructures in the microscale model of the PAC

Structure	Parameter	Dimension (mm)	References
Entire PAC	Slice Area	4 x 4	[65] [57] [58] [59]
	SAS Thickness (Gap)	0.8	[32] [66] [67] [68] [69]
Dura Membrane	Thickness	0.1	[32] [57] [58] [59]
Pia Membrane	Thickness	0.1	
Arachnoid Membrane	Thickness	0.05	
Arachnoid Trabeculae	Diameter of chords & sheet-end radii	0.05	[35] [39] [36] & In-House OCT Data
	Length of short sheet	0.4	
	Length of long sheet & sheet with SAV	1.2	
Subarachnoid Vessels	Outer diameter	0.3	[62] & In-House OCT Data
	Wall thickness	0.05	

dimensions along with their corresponding references.

In its *in-vivo* state, the SAS contains cerebrospinal fluid (CSF). CSF was excluded from this simulation (and the space it usually filled was left empty) due to the difficulty of including fluid (which requires an eulerian solver) in an otherwise solid simulation (which uses lagrangian solvers). This exclusion would have a significant effect on dynamic simulations as the CSF would exhibit damping behavior and cushion brain-skull displacement. For our microscale PAC model, which will be used in parametric studies evaluating the effects of relative substructure stiffnesses and volume fraction variance on brain mechanics, we elected to use nondynamic, implicit-solution FE methods. Therefore, the dynamic effects of the CSF are negligible.

In addition to the membranes, the microscale PAC model consists of 4 basic AT substructures, a chord, a short sheet, a long sheet, and a sheet encompassing a sub-arachnoid vessel. These structures are placed between flat sheets representing the pia, arachnoid, and dura (Figure 12). Since the focus of this study was of the overall mechanical behavior of the PAC model, detailed anatomical morphology was not pertinent. The simplified chord and sheet shapes are able to act as tethers between the upper and lower membranes in much the same way as the true anatomical structures do. By this logic, we can be confident that our geometrical simplifications do not affect our model results in any significant manner.

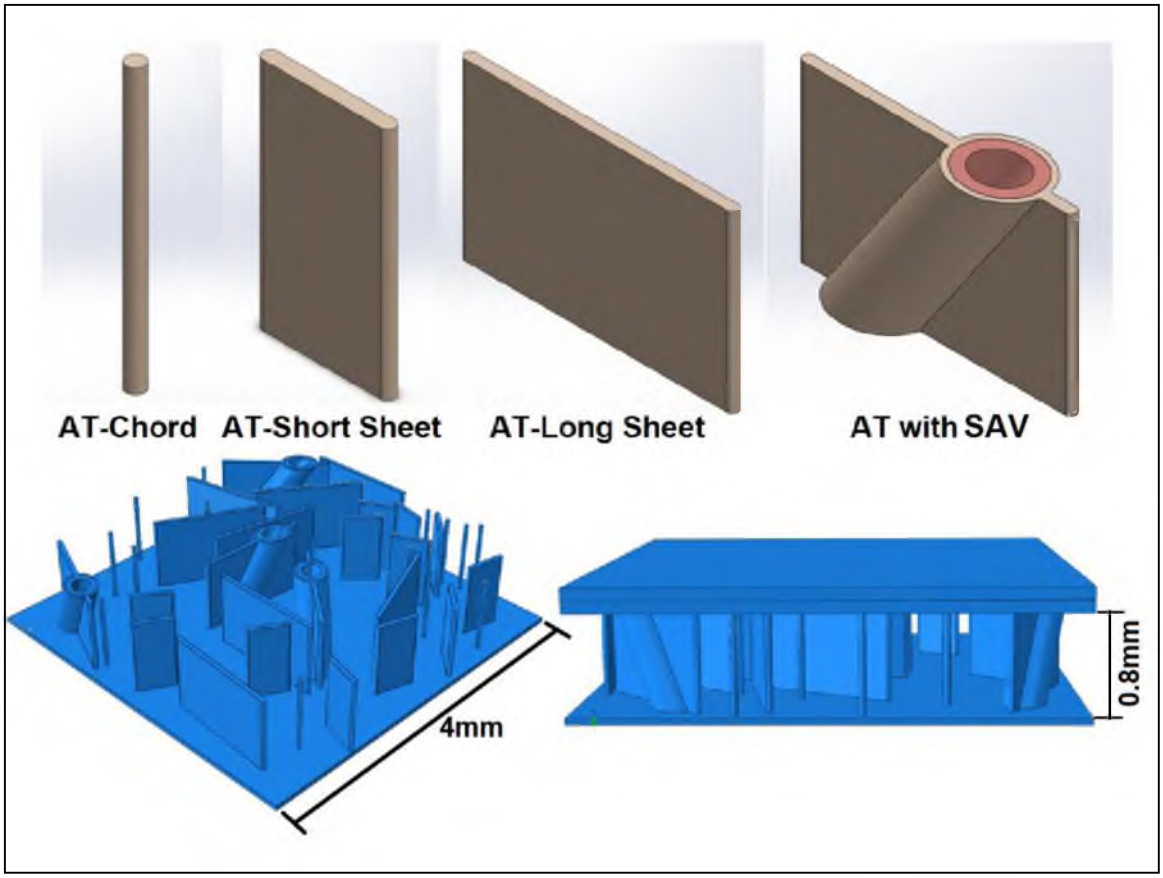

Figure 12: Simplified AT substructures along with an example of a final randomly populated model.

The substructures in the model were not populated equally, but rather they were populated based off of observations made during the OCT imaging studies. In general, more small spindly chord-like structures were observed than longer large sheets or SAV when viewing the PAC structures with OCT. As such, the PAC model was populated by defining a base set of structures, and multiplying this set to attain different volume fractions. This base set consisted of 10 structures: 4 chords, 3 short sheets, 2 long sheets, and 1 sheet with SAV. The volume fraction of the model was calculated as the ratio of the sum of cross-sectional areas of each structure over the total cross-sectional area of the subarachnoid space. Presented in Table 3 is an example of how VF is calculated for a model with an 8% VF. In order to prevent human bias when placing the substructures in the PAC model, substructure placement was randomized using a custom code written in MATLAB (2011b, The MathWorks Inc.) (Appendix B.1). This script generates positions for the AT chord shapes by picking random values within the boundaries of the microscale model. Each time it chooses a new point, it tests that point's coordinates against all previous points and ensures no two points are too close to cause intersections of substructures. After all chords are placed, the code then repeats this process in choosing the end points of the sheet shapes. The code rotates each sheet shape by a random angle, thus randomizing any directionality in the sheets. The code then generated a Python (v3.3.0, Python Software Foundation) macro which automated the model building process in ABAQUS (v6.12, Dassault Systèmes) (Appendix B.2). A plot of a typical output of this code is shown in Figure 13. The code does not account for overlap during the rotation stage (i.e., two sheets could cross each-other like an "X"); therefore, any overlapping structures were manually corrected later in ABAQUS.

Table 3: Example calculation of volume fraction by multiplying each structure's cross sectional area by the base unit and multiplier.

Shape	Cross-sectional area (mm^2)	# of parts per base unit	Multiplier to create desired VF	Aggregate cross-sectional area (mm^2)
Chord	7.854×10^{-3}	4	4	0.1257
Short Sheet	27.854×10^{-3}	3	4	0.3342
Long Sheet	67.854×10^{-3}	2	4	0.5428
Sheet /w/ SAV	$\sim 67.854 \times 10^{-3}$	1	4	0.2714
Total Cross-Sectional Area of PAC				16.0
Ratio of aggregate AT area divided by area of PAC				1.274/16 = 7.96%
Resulting Rounded VF				**8%**

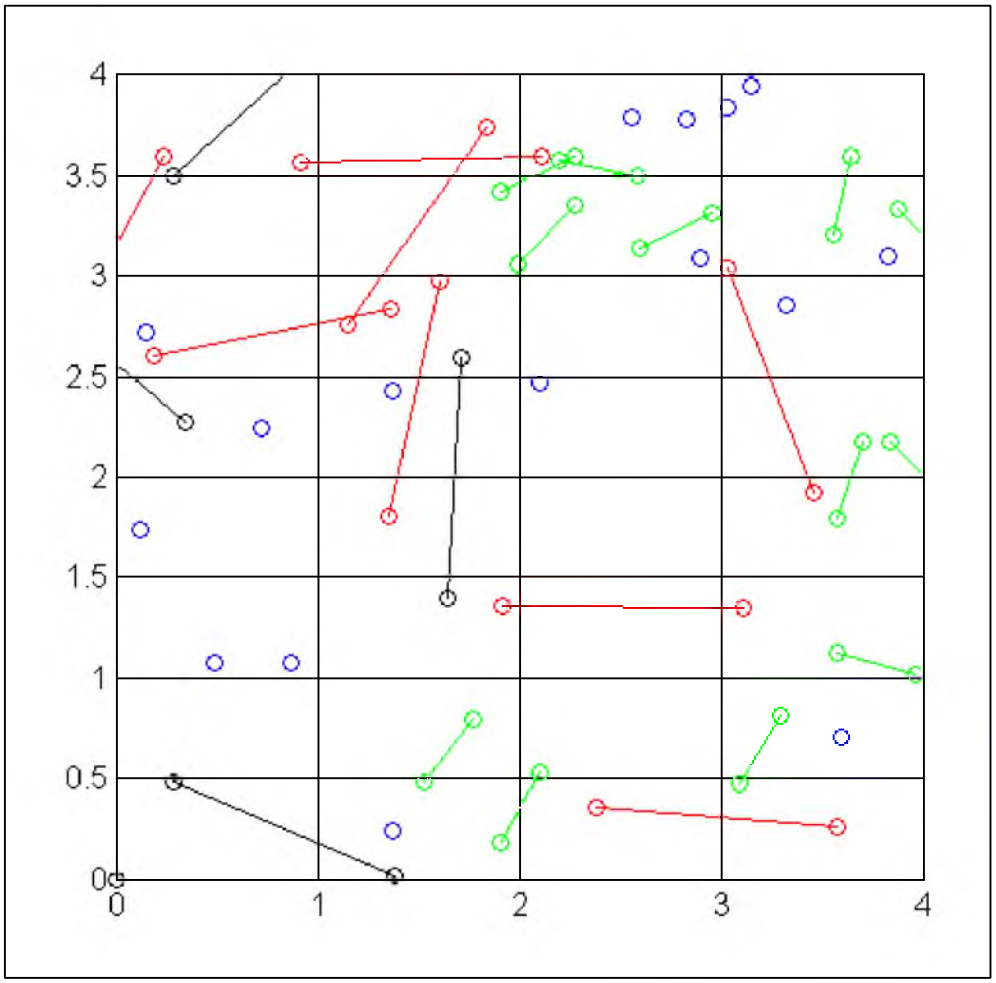

Figure 13: Example output of the randomized structure locations output by the MATLAB code. Blue = chords, green = short sheets, red = long sheets, black = sheets with subarachnoid vasculature (axis scale = mm)

2.2.2 Meshing

A comprehensive convergence study was conducted for all components within the PAC model. Each arachnoid trabeculae (AT) substructure was subjected to simple shear (4 kPa) and the maximum end deflection of the structure was recorded (Figure 14). For the AT with SAV structures, maximum SAV strain was also recorded as a convergence parameter. The mesh size was refined iteratively until the change in end deflection and/or vessel strain had reached 0.5% of an acceptable value. The accepted value was defined as the value the convergence graph approaches asymptotically. Mesh densities were also chosen with the knowledge that substructures would be repeated many times in the model, and minimum mesh densities were desired for reasonable simulation run times. A convergence graph for one of the substructures (the AT chord) is presented in Figure 15.

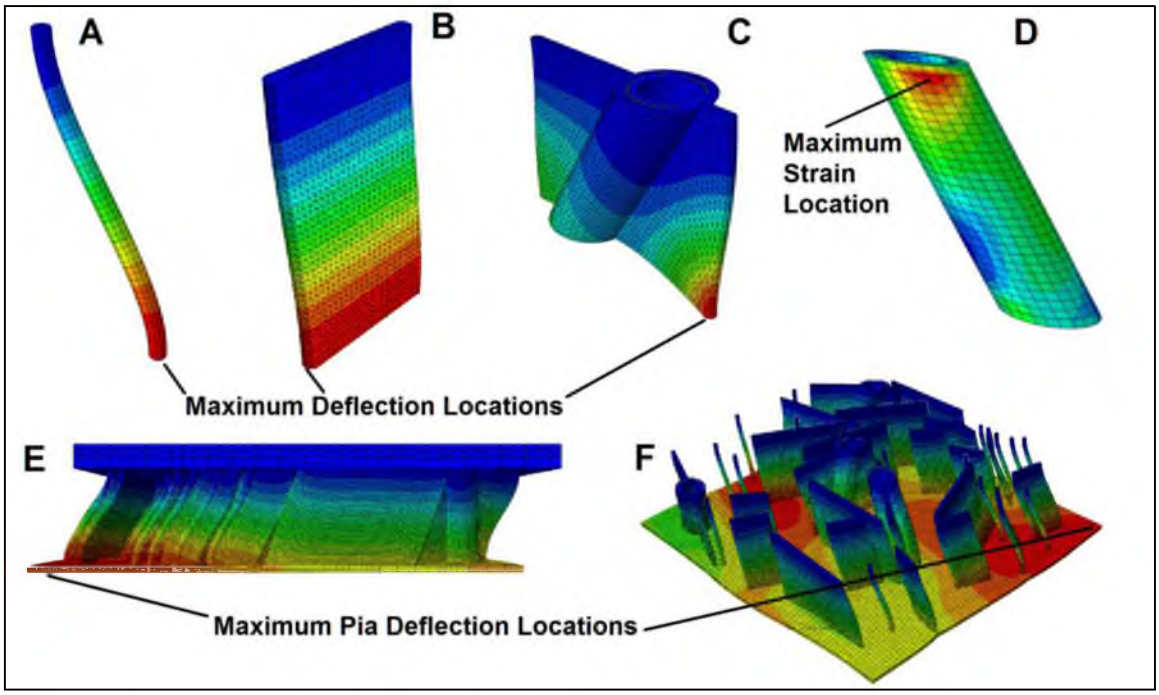

Figure 14: Representative images of deformed structures and their convergence variables: A) AT chord, B) AT sheet, C) SAV-enveloping AT sheet, D) SAV, E) whole model (side view), F) whole model (isometric view, dura and UA removed). Note color maps correspond to individual, unrelated scales.

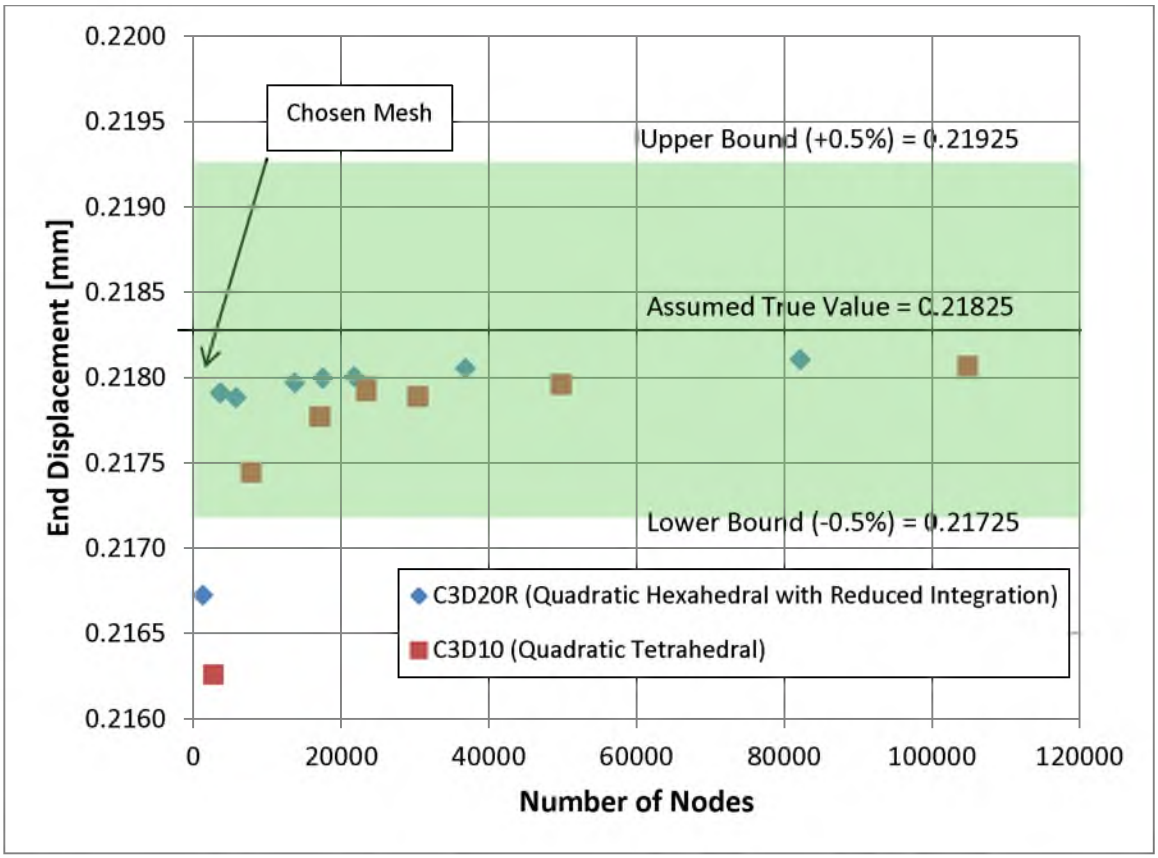

Figure 15: Example of typical convergence study graph. Increasing mesh densities (represented by number of nodes) are plotted versus end tip displacement of the substructure. The minimum value within 0.5% of the assumed true value is chosen.

Once acceptable meshes were reached for all substructures, a shearing pressure was applied to the entire assembly (membranes and trabeculae) and the mesh density of the dura, UA, and pia membranes was increased until converged as defined above. The convergence variables for the entire assembly were maximum SAV strain and maximum pia deflection. The final element types, mesh densities, and element qualities resulting from the convergence study are provided in Table 4. The final meshes for each structure are illustrated in Figure 16. The results of each substructure's convergence study, including individual convergence graphs and element selection criterion, are presented in detail in Appendix C.

Table 4: Final mesh parameters in microscale PAC model (values for 8% VF baseline model shown)

Structure	Element Type	Avg. Aspect Ratio	Avg. Shape Factor	Elements	Nodes	# in Model	Total Nodes
AT-Chord	Quadratic Hexahedral	1.79	n/a	816	4,190	16	67,040
AT-Short Sheet	Quadratic Tetrahedral	1.54	0.701	16,693	26,814	12	321,768
AT-Long Sheet	Quadratic Tetrahedral	1.43	0.757	19,578	33,588	8	268,704
AT-w-SAV	Quadratic Tetrahedral	1.41	0.784	17,110	30,993	4	123,972
SAV	Quadratic Hexahedral	1.25	n/a	6,336	32,164	4	128,656
Dura & UA	Linear Hexahedral	2.0	n/a	816	3,200	2	6,400
Pia	Linear Hexahedral	3.0	n/a	16,693	26,244	1	26,244
					Total Nodes in Entire Model:		942,784

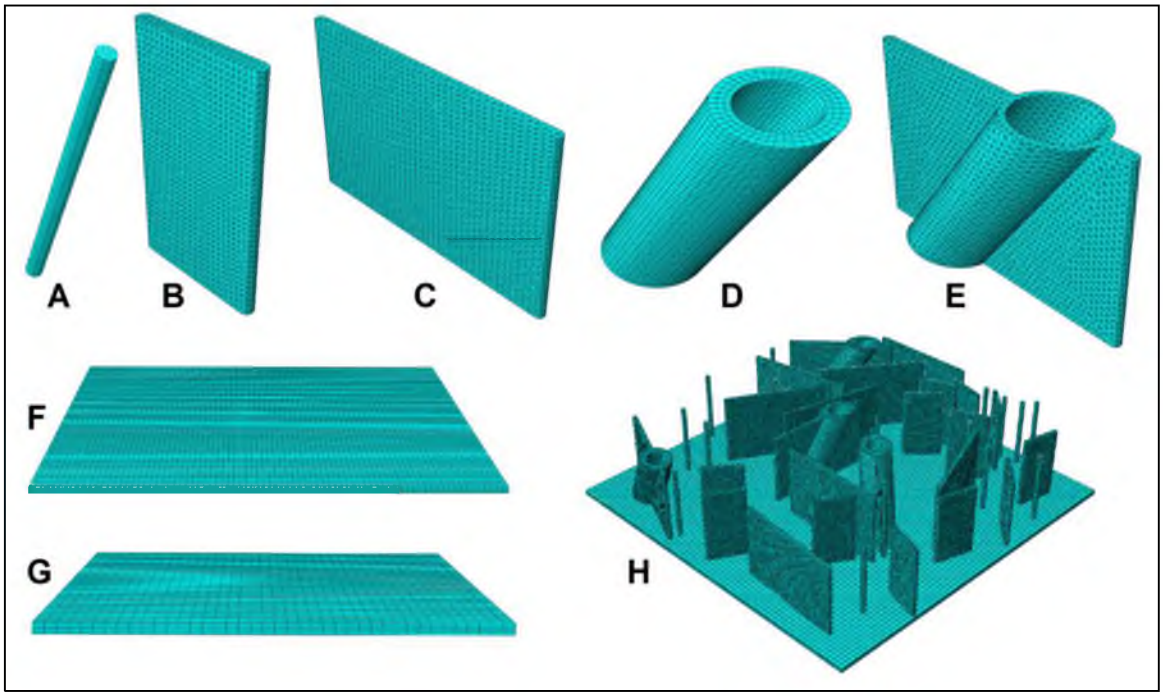

Figure 16: Final meshes: A) AT chord, B) AT short sheet, C) AT long sheet, D) SAV, E) SAV-enveloping AT sheet, F) pia, G) dura/UA, H) whole model (dura and upper arachnoid hidden)

2.2.3 Material Properties

The pia, UA, and AT have not been well characterized in the literature and pose a challenge for accurately implementing them into the PAC model. The behavior of the bovine PAC as a whole has been classified by Jin et al. in tension [57], normal traction [58], and shear [59] tests. A study by Aimedieu and Grebe claims to have tested bovine pia in tension; however upon review of their dissection procedure, these tests were likely testing the entire PAC [70]. One other study exists in which spinal canine pia mater is tested in uniaxial tension [71], however, caution should be used when extracting cranial pia values from spinal pia tests. Aside from the data from these few studies, little to no material data have been collected on the material properties of the substructures of the PAC. To identify the contribution of these properties on the mechanical response of the PAC model, a parametric study was performed. Data from the literature were used to guide the baseline values for the study.

The tests by Jin et al. may be used to infer information about the behavior of the pia, UA and AT. When testing the PAC in tension, the pia and UA membranes are being directly loaded while the AT structures likely contribute very little to the response. Based on this logic, we can assume the data reported from these tests were representative of moduli for the pia and UA membranes. Midline moduli reported by Jin et al. (Table 5) were used as guiding values for ranges utilized in the parametric studies. Jin's results showed a strain-dependent "bi-linear" response (a linear toe region, followed by a stiffer linear working range). Only a linear response was used for the parametric simulations. The normal traction tests conducted by Jin et al. likely passed most of the load to the AT structures, and the pia and UA likely contributed very little to the material response. As

Table 5: Summary of meningeal material property data for dura, pia, upper arachnoid (UA), and subarachnoid vasculature (SAV). Only values pertinent to the PAC microscale model are shown.

Tissue	Species, Age, Sample Size	Reported or Calculated Elastic Moduli ($E_{\text{strain-rate in s^-1}}$)	Ref.
Dura	Human, Adult, n=133	$E_{0.0666}$ = 6027 ± 3138 psi (41.55 ± 21.64 MPa) $E_{0.666}$ = 6430 ± 3238 psi (44.33 ± 22.33 MPa) $E_{6.66}$ = 8799 ± 3720 psi (60.67 ± 25.65 MPa)	[60]
Dura	Porcine, Adult, n=unknown	E_{max} = 66.50 MPa E_{min} = 13.00 MPa E_{avg} = 31.14 MPa *Biaxial inflation tests were varied with different inflation pressures, strain rate is unknown.	[61]
Pia & UA	Bovine, 17-20 weeks, n=10	Strain-dependent behavior reported, moduli values are for linear region on a "bi-linear" curve. $E_{0.05}$ = 6.75 ± 0.75 MPa $E_{0.5}$ = 7.52 ± 0.59 MPa $E_{5.0}$ = 10.78 ± 0.58 MPa E_{100} = 40.19 ± 3.54 MPa	[57]
Pia & UA	Bovine, 45 ± 29 months, n=9	Stiffness reported from linear region on a nonlinear curve. Modulus not reported, but is calculated assuming the same thickness as reported in [57]. Stiffness = 0.019 N/mm $E_{calculated}$ = 8.05 MPa	[70]
AT	Bovine, 17-20 weeks, n=40	$E_{0.36}$ = 30.92 ± 1.27 kPa $E_{2.0}$ = 31.45 ± 1.27 kPa $E_{20.5}$ = 35.02 ± 1.41 kPa $E_{116.3}$ = 59.81 ± 1.41 kPa	[58]
SAV	Human, 38-80 years, n=11	Strain-dependent behavior shown, modulus of linear working region reported: E = 6.43 ± 3.44 MPa	[62]
SAV	Porcine, Adult, n=15	Nonlinear stress-strain response reported, linear elastic moduli curve-fit in-house: $E_{circumferential}$ = 48.1 kPa $E_{longitudinal}$ = 27.3 kPa	[63]

such, the data from these tests were used as nominal values for AT moduli in the parametric simulations (Table 5). These studies showed a linear response, potentially signifying that the AT behave linearly when loaded in tension. These structures were therefore modeled as linear elastic.

The material behavior of dura has been well characterized in the literature for adult monkey and human [60, 72-76], fetal human [77-78], and adult porcine [61] samples. The general consensus of these tests is that the dura can be modeled as a linear material; however, some studies [77-78] argue in favor of a strain-dependent nonlinear behavior. There does appear to be a good consensus, however, on the fact that the dura is rate-dependent, and is well modeled by viscoelasticity. Since the current study was not dynamic, a linear elastic model was selected for the parametric study. The baseline value selected for the parametric simulations was 20 MPa, which represented a low-range value for both human and porcine values from the literature. This low value was selected to evaluate dura in a worst-case scenario (maximal potential deflection).

It is common knowledge within the neurosurgical community that the dura is the toughest of the meningeal membranes, the UA membrane is much more compliant and weak, and the arachnoid trabeculae and pia are the weakest structures. A series of comprehensive literature reviews by Adeeb et al. exist on the topic for the interested reader [79-81]. Due to these qualitative relations, for our baseline model, the dura was assumed twice as stiff at the UA membrane, which itself was twice as stiff as the pia and AT. During the parametric studies, each structure's modulus was varied within a reasonable range guided by these qualitative restrictions of relative stiffness.

The material behavior of subarachnoid vasculature (SAV) has been reported in

humans by Monson et al. [62, 72-73], and in porcine subjects by Pang et al. [63]. In these studies, both research groups did not find any significant rate-dependence of the vessels, but did find strain-dependent nonlinear behavior. Both teams also report different moduli between longitudinal and circumferential tests, signifying anisotropic behavior. A value of 6.43 MPa was chosen as the value to be used in all of our studies, which modeled the SAV as linear-elastic, isotropic structures. This value represented the average modulus reported by Monson et al. for human bridging veins collected after autopsy. The value fit well with the various moduli utilized for the PAC structures, as it was not drastically higher or lower, so no scaling was deemed necessary for this qualitative study.

Near incompressibility was assumed for all materials in this study, and as such a Poisson's ratio of 0.45 was used for all material definitions. Density of all structures was assumed to be 1130 kg/m^3, based on data reported for human and monkey dura, pia, and venous sinus [84].

2.2.4 Parametric Study Design

Two parametric studies were conducted with the microscale model. The first was a study on the sensitivity of each PAC substructure's stiffness to the overall response of the model. This first study involved a series of models that held all moduli constant except one structural group of interest (either the pia, AT and UA, or dura) which had its moduli varied with the ranges described in Section 2.2.3 (Table 6). In the pia and dura stiffness studies, the moduli of the pia and dura were each varied (respectively). However, in the arachnoid stiffness study, two structures were varied; the UA and AT. Based on general anatomical knowledge, it is known that the cellular structure is more

tightly packed in the UA near the dural border cell interface than in the AT in the subarachnoid space [79, 81]. Because of this, it was assumed that the UA was always two times stiffer than the AT (which has a lower collagen content is and is less stiff).

The second parametric study investigated the sensitivity of AT population density (volume fraction) of AT on the biomechanical response of the PAC. The substructure moduli for this study were those of the midline values for each structure (Table 5). The volume fraction (VF) of AT were varied from 4% to 12% (Table 6). These VF values were chosen based on visual estimates from drawings and microscopy images of the PAC in the literature [35-39]. The OCT findings in Chapter 1 had not been completed at the time of this study. The differences between the actual measured VF values and our assume VF values will be discussed in Section 2.4.

The boundary conditions and loading of our model were created to represent a common case of loading that the PAC may experience during head injury. This case is of shear during head impact, in which the skull is suddenly arrested, and the brain continues to move relative to the brain. To create shear, the upper surface of the dura was fixed (no translation in all three directions) and a shear traction load of 12 kPa was applied to the pia in the x-direction (Figure 17). The pia was restricted from movement in the y direction (which kept the membrane parallel to the dura). The magnitude of the applied load (12 kPa) was based on PAC shear test data reported by Jin et al. [59]. For both parametric studies, pia-dura deflection (which is an approximation of brain-skull displacement) was evaluated. The nodal deflection within the entire pia structure was sampled and the maximum value was utilized as our metric for the stiffness studies. In the volume fraction study, each VF model had different AT distributions and orientations,

Table 6: Parametric study design. Note that for all values, density was assumed 1.13 x 10^{-6} kg/mm^3 and Poisson's ratio was assumed 0.45.

	Pia	UA	AT	Dura	SAV	VF
Stiffness Study (Pia)	**1-10 MPa**	10 MPa	5 MPa	20 MPa	6.43 MPa	8%
Stiffness Study (Arachnoid)	5 MPa	**2-20 MPa**	**1-10 MPa**	20 MPa	6.43 MPa	8%
		UA always 2X AT Stiffness				
Stiffness Study (Dura)	5 MPa	10 MPa	5 MPa	**4-20 MPa**	6.43 MPa	8%
Volume Fraction Study	5 MPa	10 MPa	5 MPa	20 MPa	6.43 MPa	**4 – 12%**

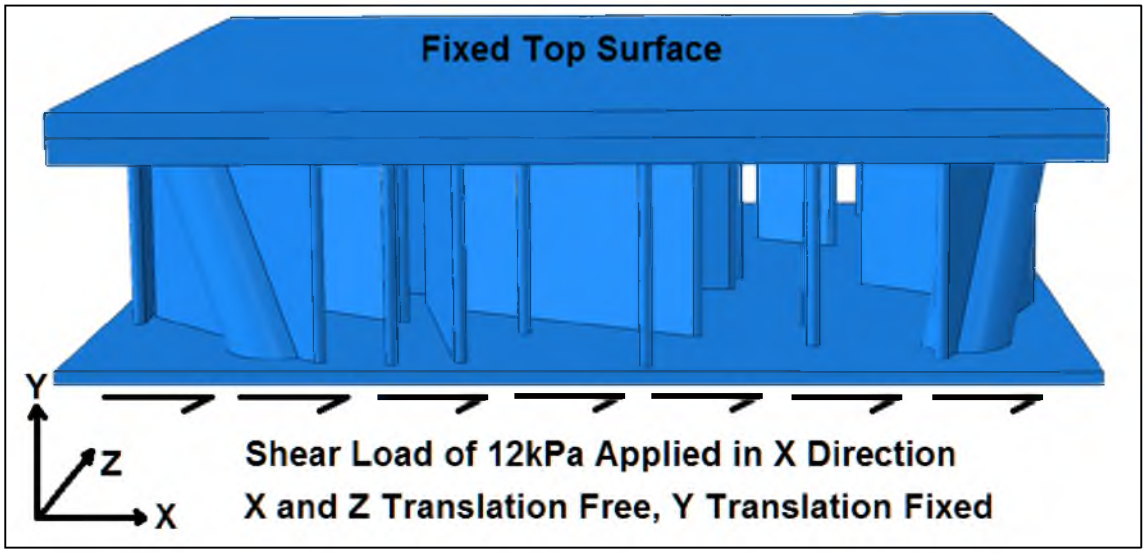

Figure 17: Boundary conditions and loads for the applied shear in the parametric studies.

because of this, pial deflection had very sporadic and varied local maxima. To account for this, the average pial deflection was used as our variable instead of maximum pial deflection. The second variable evaluated for our parametric studies was SAV strain, which is relevant to prediction of intracranial hemorrhages in TBI. Since multiple SAV structures were present in the models, an average of each of the maximum strain values in each SAV was calculated and used as our metric. This allowed comparison of SAV strain across models with differing VF.

2.3 Results

Presented in Figure 18A is a typical strain map within the SAV structures, and in Figure 18B is a typical strain map of the whole model (dura and UA excluded). Figure 18C showcases a typical deflection map of the whole model (dura and UA excluded) and Figure 18D showcases deflection map from a bottom view of the pia.

2.3.1 Material Stiffness Study

Increasing the stiffness of the pia and arachnoid membranes resulted in a non-linear decrease in maximum vessel strain (Figure 19) and pial deflection (Figure 20). Further increases in pia stiffness appear to converge to a minimal vessel strain of 0.12 - 0.13 and a minimal pial deflection of 0.2 - 0.3 mm. However, a further increase in arachnoid stiffness continues to decrease both variables. Dura stiffness had no effect on vessel strain or pial deflection.

2.3.2 Arachnoid Volume Fraction Study

For each volume fraction, the location and orientation of the substructures in the PAC model were different due to the randomization program. The response of maximum vessel strain to VF was concave-up and nonlinear, similar to the stiffness studies (Figure 21 - red). As the volume fraction decreased, vessel strain increased, since there were less AT structures helping to tether the membranes together, and the SAV had more load. Average pial deflection had a similar response, signifying that there is more pial deflection when less AT structures were present (Figure 21 - blue).

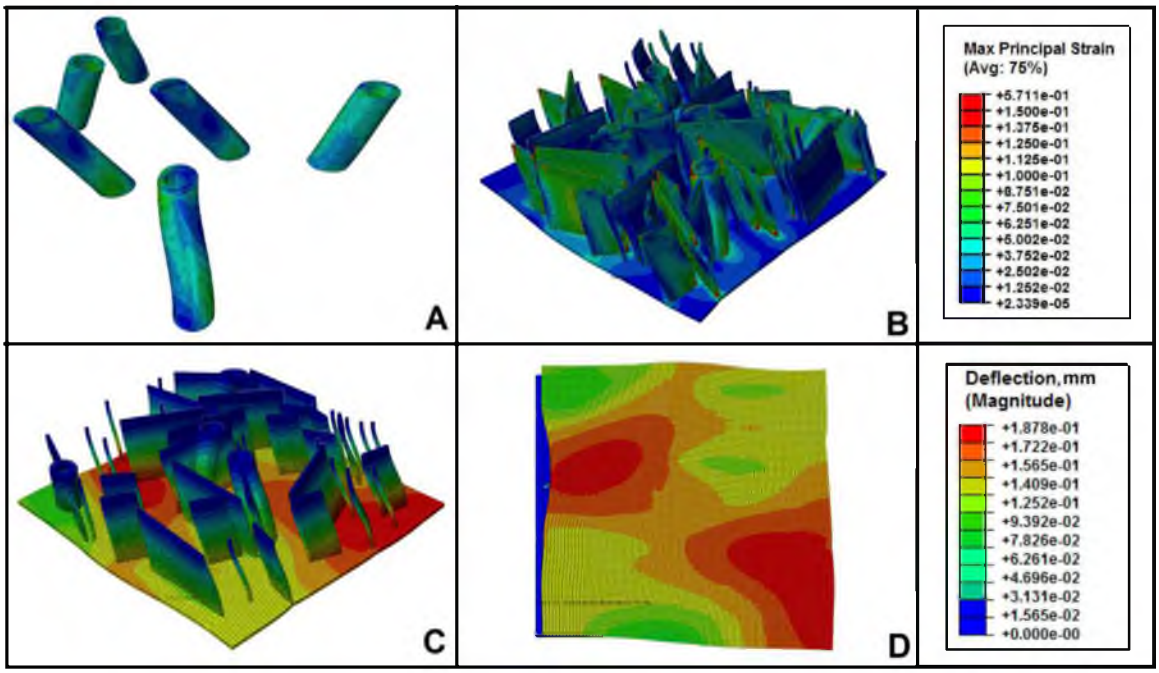

Figure 18: Typical results; A) strain map: vessels only, B) strain map: whole model (dura/upper arachnoid removed for clarity), C) deflection map: whole model (dura/upper arachnoid removed), D) deflection map: bottom view of pial surface.

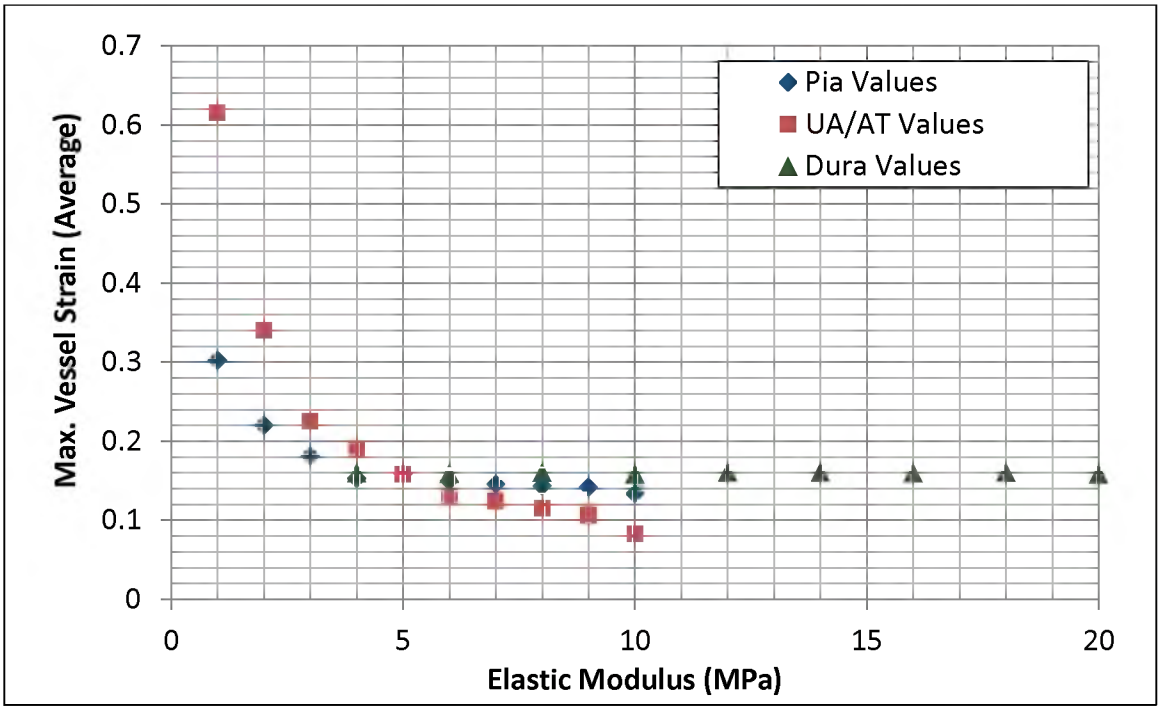

Figure 19: Increasing pia and UA/AT moduli nonlinearly decreased average maximum vessel strain. Increasing dura moduli had little effect. Note that AT values are plotted for the UA/AT dataset.

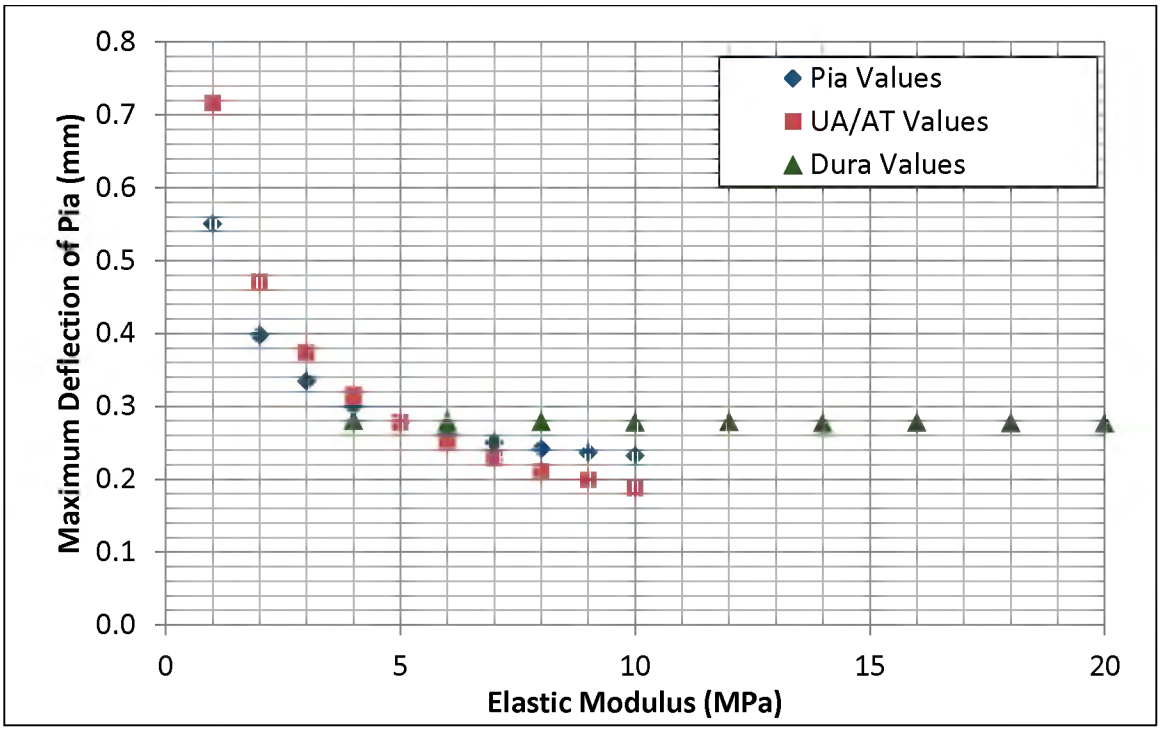

Figure 20: Increasing pia and UA/AT moduli nonlinearly decreased maximum pial deflection. Increasing dura moduli had little effect. Note that AT values are plotted for the UA/AT dataset.

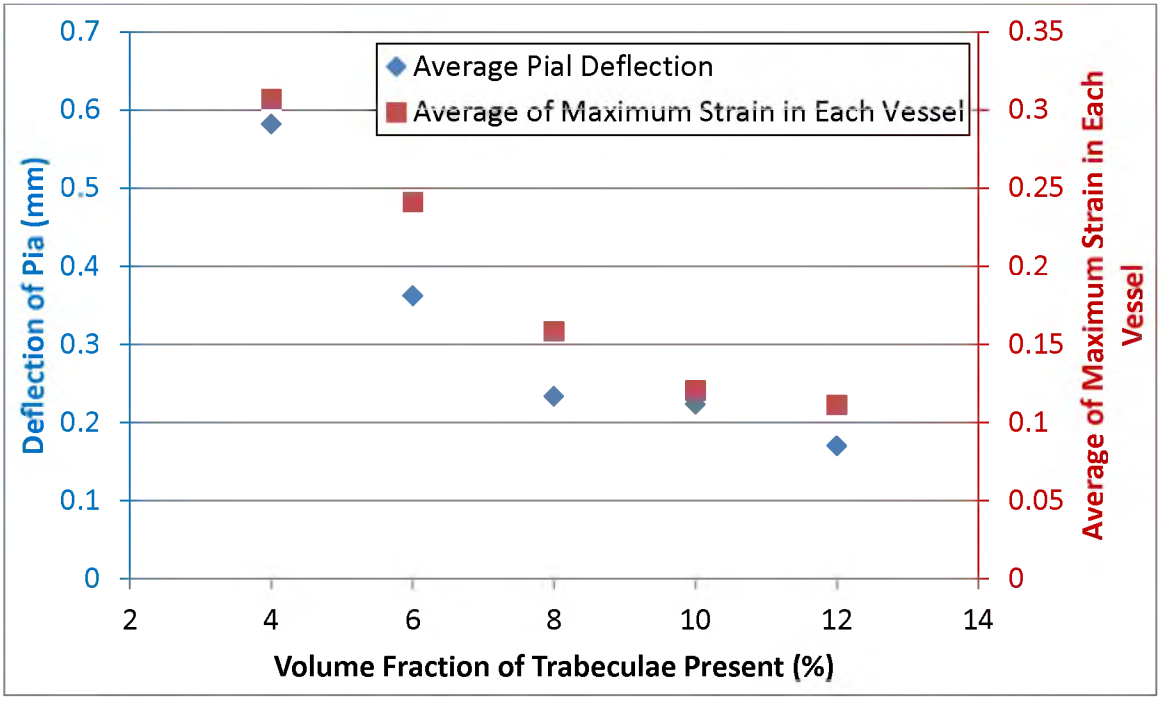

Figure 21: Increasing volume fraction (VF) of arachnoid trabeculae (AT) decreased average pial deflection and average maximum vessel strain nonlinearly.

2.4 Discussion

When looking at the strain in our subarachnoid vasculature, we tend to see hot spots near the top or bottom, where the vessel connects to the membranes. This makes sense mechanically as the vessels are being pulled on by a much stiffer membrane. In a physiological sense, this could mean that vessel rupture is more likely to occur at membrane interfaces. Not surprisingly, the highest regions of strain in the pia and upper arachnoid membranes are at the interfaces between AT and SAV structures. We see a general increase in deflection near the bottom of the model (as expected in simple shear), but we also see minute differences along the surfaces of the pia due to the random nature of the tethers.

There were two major observations from the PAC substructure stiffness sensitivity study. The first was that the pia and arachnoid membranes have a significant effect on both vessel strain and pial deflection. This relationship was nonlinear, with very large increases in strains and deflections occurring from small initial decreases in pia and UA/AT moduli. This makes sense since both of these structures are known to be the weakest points in the PAC. Their moduli likely drive most of the PAC's mechanical interactions, so slight changes to the moduli are expected to cause large changes in the mechanical response. When looking at the tests conducted by Jin et al., we saw that the normal traction tests reported moduli values in the 30-60 kPa range, and the tensile tests reported moduli values in the 0.5-4 MPa range. If we were to have incorporated this large of a difference in the PAC model, and weakened the AT structures by an entire order of magnitude, they would have undoubtedly shown a huge influence on pial deflection and SAV strain. This change would also likely reduce the influence of pial stiffness on the

overall interactions of the PAC

The second finding of the stiffness sensitivity study was that the dura does not have a large effect on either pial deflection or vessel strain when varying its modulus within physiologically relevant limits. This makes sense as well, since the dura is the most exterior membrane, furthest away from the majority of the deformation in the PAC. In addition to the geometric constraint, the dura is also the stiffest structure in the PAC, so it is unlikely to influence pial deflection, which is driven by the weaker structures. One caveat to this statement would be that at the regions of the falx and tentorium, the dura folds in and interacts with the arachnoid granulations and bridging vessels of the region. These regions would require their own specific models and the results presented here are not indicative of these obviously different geometric and mechanical interactions. In this study, the values of the dura were varied down to values much lower than expected physiologically, and even then no effects were seen on pial deflection and SAV strain. Therefore, the most important meningeal structures to accurately model across the cortical surface (except near the falx and tentorium) are the pia and arachnoid. Unfortunately, these structures are the least characterized of the meninges in the literature.

Similar to the parametric stiffness study, pial deflection and SAV strain were very sensitive to volume fraction and exhibited similar nonlinear behavior. This highlights the importance of quantifying volume fraction data in order to more accurately model head injury. To the authors best knowledge, no quantitative studies have characterized the volume fraction of AT in any species.

The VF values calculated in the FE model contain some error due to the sheet

with SAV structure containing off-axis geometry. SAV volume calculated via CAD software contained about 50% more volume than was estimated with the cross-sectional area (Table 3). When taken into context of the total PAC model, the overall volume fraction increased roughly 2%, and the true simulated range was 6-12%. For simplicity's sake, the values in this study were not corrected for this error, because it would not alter any of the results or conclusions, which were driven by relative differences.

The volume fraction of AT measured in the immature piglet in Chapter 1 using optical coherence tomography shows that volume fraction ranged from 13.8-53.0%. At first glance, this would appear to mean that our simulated volume fraction values do not correlate to physiological values at all. However, it is important to note that the values reported in Chapter 1 were of the collapsed, deflated PAC. The simulations presented in this chapter were intended to represent an *in-vivo* inflated PAC. In order to correlate the two properly, one would need to know the difference in VF values between inflated and deflated PAC. The two brains that were imaged in an inflated state had VF averages roughly 9% below the uninflated brains and ranged from 7.91-44.93%. If we assume that these inflated brains were inflated to *in-vivo* state, and consider the true VF values evaluated by the PAC model (6-12%), we see there is some overlap with physiological values, albeit only at the low end. The change in response at higher VFs was minimal (Figure 21). Therefore, it is anticipated that these higher VFs (>12%) will not significantly affect brain mechanics. This cutoff threshold (>12%) is somewhat dependent on the current model's geometry and will be verified on a porcine sized model in Chapter 3. The assumption that the inflated brains were representative of *in-vivo* brains, however, is suspect. There is no guarantee whether or not the inflation method

truly yielded *in-vivo* inflation states, or rather just a partially inflated state, as discussed in Chapter 1. The true *in-vivo* VFs would then be even lower.

Overall, the results in this study reinforce the notion that the AT directly affect the mechanical response of the PAC in shear loading. One acknowledged limitation of this study was the lack of strain-dependent material properties in the pia, UA and SAV, as well as the lack of rate-dependent properties in all structures. While the magnitudes and nonlinear relationships may vary by implementing more advanced material models, the qualitative results and conclusions of this study would likely not change.

Another potential limitation of the study is the use of a static simulation. In real life, the shearing motion in the PAC would be caused by a dynamic event, such as a head impact or rapid head rotation. Implementing time-dependent material properties and applying dynamic loads would definitely change magnitudes of deflection and strain measured in the model. Additionally, the interactions between some substructures may alter slightly, as some exhibit larger changes in moduli at higher strain rates than others. Despite this, the qualitative conclusions of the study would still likely remain unchanged in a dynamic setting, with the pia and arachnoid structures dominating our response.

A third potential limitation of the study was the exclusion of anisotropic material properties in the SAV. Incorporation of different moduli for the axial and circumferential directions within the SAV would result in more physiologically accurate strain maps. Again, the qualitative results of the study would likely remain unchanged with this implementation. Implementation of strain and rate-dependent material models and/or anisotropy into future simulations would allow for more accurate quantitative results, and should be seen as an absolute must if one were to attempt to predict injury with a

microscale model of the PAC.

Aside from material property limitations, one geometric limitation may be present in our model as well. In the present model, the PAC cross-sectional area was 4 by 4 mm. In the Jin et al. studies [57-59], a testing size of 12.7 by 12.7 mm was utilized. This size was dictated by the continuum assumption proposed by Harrigan et al. for trabecular bone testing [65]. Harrigan's assumption stated that in order for trabecular bone to be accurately modeled as a continuum (and not model each trabeculae as a singular structure); the sample size must include at least 5 trabeculae along its length. In our model, this requirement is generally met, but occasionally falls short in the lower VF models. This would explain the slight deviations from our standard nonlinear curves seen in Figure 21. These slight deviations only caused minor errors in the PAC simulations, and again would not have affected the qualitative results. If future models were to be constructed in which physiologically relevant data was to be extracted, a larger cross-sectional area may be desired.

2.5 Conclusion

These preliminary studies have shown that the arachnoid trabeculae, although commonly overlooked, play a large role in the mechanical interactions of the brain and skull. A refined microscale model, scaled to match known test data or *in-vivo* measurements in animals or humans, could become a very valuable tool in accurately predicting injury in TBI. Predictions of commonly seen etiologies of TBI (such as subdural or subarachnoid hemorrhaging) could be more easily pinpointed and predicted with a refined model of the PAC. Brain-skull deformation could also be more accurately

predicted if a refined microscale model of the PAC were to be paired with a macroscale whole-head model of TBI, leading to more accurate predictions of brain strain and axonal injury.

CHAPTER 3

IMPLEMENTATION OF A MULTISCALE FINITE ELEMENT MODEL OF MILD TRAUMATIC BRAIN INJURY

3.1 Introduction

Traumatic brain injury research has greatly benefitted from finite element simulations of the head and its constitutive tissues. As described in Chapter 2, multiple whole-head simulations of brain injury have been presented in the literature which exhibit varying levels of detail for many of the substructures of the head [6-13]. These studies are all limited, however, by lack of detail of the pia arachnoid complex (PAC) and its interactions with the brain and skull. Other studies in the literature have addressed these limitations by studying the effect brain-skull boundary conditions had on brain injury prediction [23, 26-30].

In order to facilitate more accurate injury prediction, researchers need to delve into the tissue level and cellular level interactions of brain tissues. Whole head FE models have not yet reached a level of resolution or complexity fine enough to elucidate microscale injury metrics such as axonal injury or localized hemorrhage and contusion. A few teams have turned to multiscale simulations to allow for microscale injury predictors to be measured in macroscale injury simulations. Studies by Cloots et al. have demonstrated a multiscale modeling approach with whole head, tissue, and cell level

models of deep brain tissue coupled together to predict axonal injury at the cellular level based on inputs applied to the whole head [85-87]

In terms of modeling more accurate interactions of the PAC, only two models exist. A simple microscale model of the PAC has been demonstrated by Ma et al. who modeled the PAC as either a series of solid elements or beam elements sandwiched between two plates [31]. No macroscale model was directly coupled with this model, although it was stated the results from the microscale simulations could be implemented into a macroscale model. A second team has developed a microscale model of the PAC based on anatomical drawings and paired it with a whole-head model in a multiscale approach to simulating head injury [32]. As stated in Chapter 2, this model appears to be an improvement in the qualitative sense, but their conclusions were limited due to the lack of experimental data to compare to, and because they assumed that the distribution of the PAC microstructures was uniform across the brain.

In this study, we aimed to develop the framework for a multiscale modeling approach to predict mild TBI in the immature piglet. This framework involves two models; the first model is a refined version of the microscale PAC model discussed in Chapter 2. The microscale PAC model was simulated multiple times with different volume fractions (VF) of arachnoid trabeculae (AT). The results from these simulations were used to create representative solid elements (RSE) which could be placed in the macroscale whole-head model and act as a more realistic representation of the PAC.

The second model utilized is a whole-head model of an immature piglet which included skull, brain, dura (including falx/tentorium), and CSF (which represented the whole PAC). As discussed in Chapter 2, this whole-head model was previously utilized

in studies by Coats et al. to evaluate the effects of different brain/skull boundary conditions on brain strain and intracranial hemorrhage predictions [23]. This model had a 80% sensitivity and 85% specificity when predicting the overall presence of hemorrhage in the brain, but it fell short when attempting to predict hemorrhage specific to regions of the brain, with sensitivity and specificity values as low as 63% and 76%. The new RSEs exhibit different material properties dictated by the different VFs present in each correlated microscale model. Two subject-specific whole head models were populated with their respective VFs and simulations of rapid sagittal head rotations were run. The results from these studies will help infer what role differing VF of AT across the brain surface has on brain mechanics and predictions of intracranial hemorrhage.

3.2 Methods

3.2.1 Microscale Model Geometry

The new microscale PAC was constructed to represent the immature porcine anatomy and material properties as best as possible. Anatomical measurements of the upper arachnoid (UA), subarachnoid vasculature (SAV), and subarachnoid space (SAS) were measured directly from the optical coherence tomography (OCT) scans obtained in Chapter 1. These measurements were taken from the scans of the two re-inflated brains (P13-121, P13-122). The inflated brains were selected because they most closely represented the *in-vivo* state of the PAC, which is what this model would be simulating. Since this model would be paired with a macroscale model with the dura already represented, the dura was excluded from the microscale PAC model.

From OCT images, UA thickness was measured in a randomly selected location

that appeared typical (Figure 22A). SAS thickness was also measured from OCT images in two locations from each image. The first location was the "minimum" or smallest gap where AT structures were present. The second was the "maximum" or largest SAS gap where AT structures were present (Figure 22B-C). Gaps were not measured where there were no AT structures, or where the pia extended below the image window (in the case of a deep sulcus). The average of these two measurements was taken and used to represent an average SAS thickness. Since the PAC model assumed the UA and pia membranes were perfectly parallel, and the SAS did not vary like the real-life measurements, this average gap measurement was applied. Measurements were taken on all of the same B-scans analyzed in the VF study (Chapter 1) for the two animals. Raw measurement data are presented in Appendix A.1 for reference.

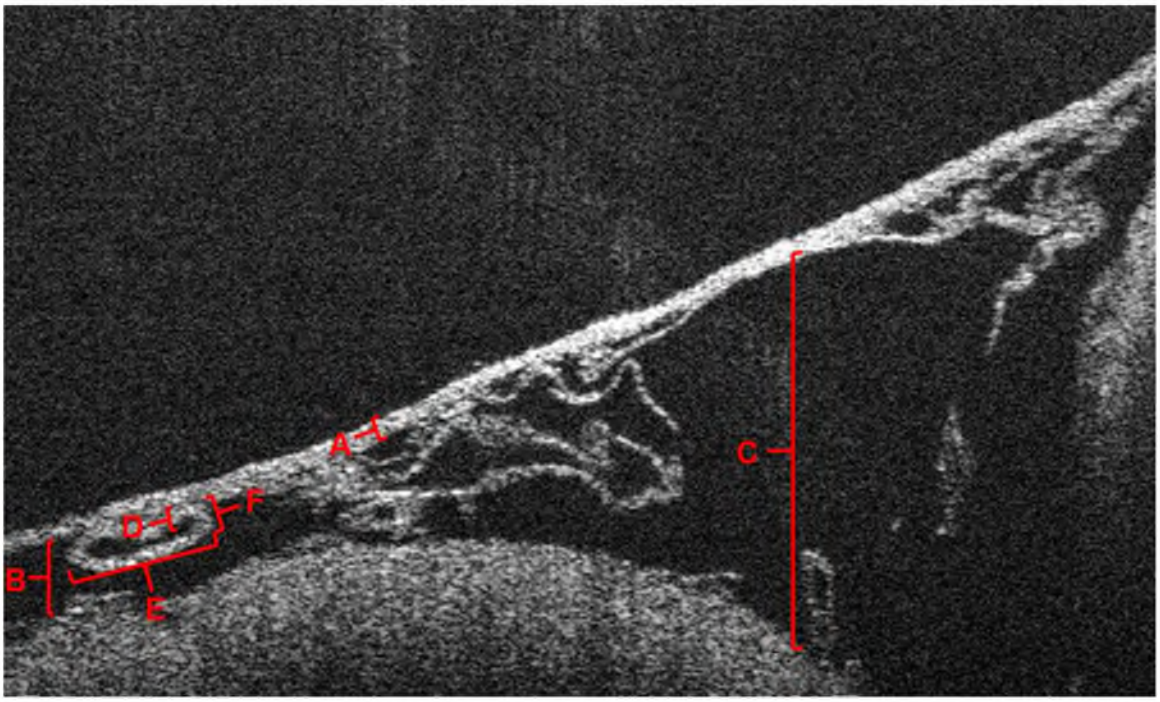

Figure 22: Example OCT image with relevant measurements labeled: UA thickness (A), minimum SAS thickness (B), maximum SAS thickness (C), SAV lumen thickness (D), SAV major diameter (E), SAV minor diameter (F).

Three measurements were taken to evaluate the dimensions of the SAV. The first measurement was the lumen (or wall) thickness of the vessels. A single area of the vessel was selected that appeared to be a good average representation of the vessel's wall thickness (Figure 22D). In addition to wall thickness, vessel diameter was measured. Most vessels were not circular in the images, so the major and minor axes were measured. These dimensions were then averaged to approximate a representative diameter (Figure 22E-F). Some images contained no SAV, and no measurements were taken. Conversely, some images contained multiple vessels, and multiple separate measurements were taken.

The dimensions of the AT and SAV structures in the PAC model developed in Chapter 2 were scaled down to fit within the newly established subarachnoid space dimensions. The same relative dimensions (i.e., same length to diameter ratio) were preserved. The only dimension not perfectly preserved from the microscale model in Chapter 2 was the diameter and angle of approach of the SAV. These dimensions had to be adjusted to better match the average measurements obtained from the OCT scans, which had larger diameters and thicker lumens. These diameters and wall thicknesses were averaged across all measured vessels. Table 7 presents all pertinent dimensions of the refined microscale model.

Based on observations made while obtaining the VF of AT in immature piglet brains with OCT (Chapter 1), it was observed that the amount of blood vessels present in the scans were generally much less than the amount represented in the PAC microscale model. The images analyzed for VF in Chapter 1 were re-evaluated for SAV presence, and the amount of vessels was counted in each image (Appendix A.1). The average

Table 7: Dimensions of the Microscale Model of the Immature Piglet PAC.

Structure	Parameter	Dimension (μm)
Entire PAC	Slice Area	1500 x 1500
	SAS Thickness (Gap)	300
Pia Membrane	Thickness	15
Arachnoid Membrane	Thickness	30
Arachnoid Trabeculae	Diameter of chords & sheet-end radii	18
	Length of short sheet	150
	Length of long sheet & sheet with SAV	450
Subarachnoid Vessels	Outer diameter	112.5
	Wall thickness	18.75

amount of vessels per image for the inflated images was 1.35. This average value did not drastically fluctuate for higher or lower VFs of AT. This indicated that the old method of multiplying a 10-structure set (4 AT chords, 3 AT short sheets, 2 AT long sheets, and 1 AT with SAV) to achieve higher VF was not very physiologically accurate, as it introduced far too many SAV structures at higher VFs.

As such, the base set of structures was altered to only include AT structures, and the number of SAV structures was set slightly above average to 2 for each model (regardless of VF). The ratio of AT structures in the base set was also altered to contain 10 AT chords, 6 AT short sheets, and 3 AT long sheets per base set. This allowed the thinner, chord-like structures to dominate the model, and better match what was seen physiologically during the OCT examinations. The same MATLAB (Version 2011b, The Mathworks Inc.) randomization code described in Chapter 1 was utilized to create all of the varied VF models. Figure 23 shows the final geometry and all of the different VF microscale models created for this study. Table 8 presents an example of the VF calculation for the 21% VF model.

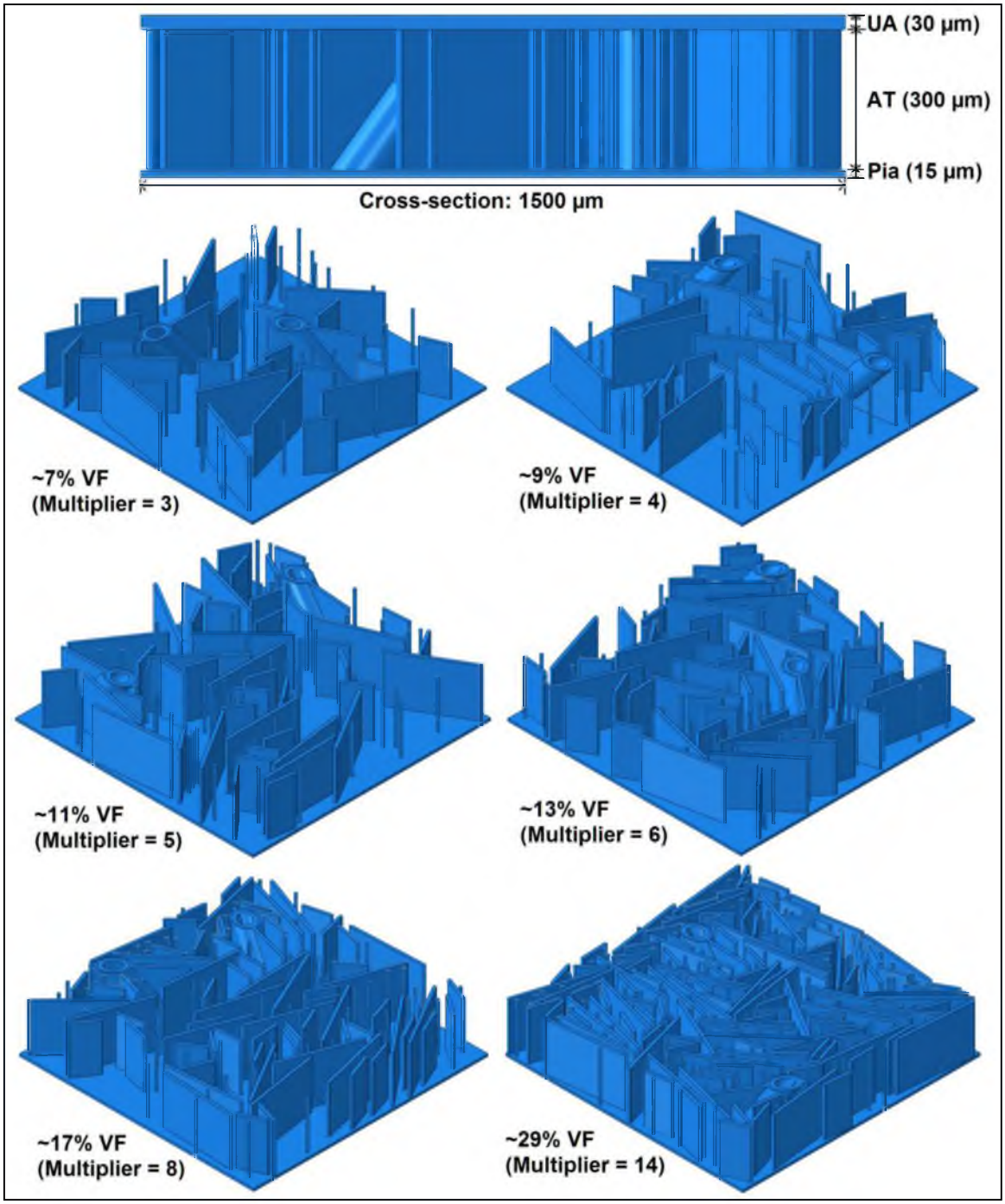

Figure 23: Final microscale models: side view showcasing geometry of model (top), and isometric views with UA removed to show each models differing VF of AT structures.

Table 8: Example calculation of volume fraction of the immature porcine microscale PAC model.

Shape	**Volume (mm^3)**	**# of parts per base unit**	**Multiplier to create desired VF**	**Aggregate volume (mm^3)**
Chord	7.634×10^{-5}	10	10	7.634×10^{-3}
Short Sheet	8.863×10^{-4}	6	10	5.318×10^{-2}
Long Sheet	2.506×10^{-3}	3	10	7.519×10^{-1}
Sheet /w/ SAV	5.074×10^{-3}	2	1 (not multiplied)	1.015×10^{-2}
			Total volume of PAC	0.675
			Ratio of aggregate AT volume divided by volume of PAC	0.146/0.675 = 21.16%
			Resulting Rounded VF	**21%**

3.2.2 Microscale Model Meshing

The meshing of this resized porcine model did not have to be changed drastically due to the fact that most structures kept the same relative aspect ratios and the general geometry of the model was unchanged. As such, no convergence study was performed on this model; instead, the previous convergence study conducted in Chapter 2 was used to inform our meshing decisions. The mesh element types were all kept the same, however, the mesh size had to be scaled down such that our structures contained roughly the same number of nodes as in the previous model. Table 9 presents the final mesh parameters for the 21% VF model and Figure 24 provides a visual of each meshed part.

Table 9: Final mesh parameters for the porcine microscale PAC model

Structure	Element Type	Avg. Aspect Ratio	Avg. Shape Factor	Elements	Nodes	# in Model	Total Nodes
AT-Chord	C3D20R	1.79	n/a	848	4352	100	435,200
AT-Short	C3D10	1.57	0.6894	15758	25480	60	1,528,800
AT-Long	C3D10	1.8	0.6467	19417	33757	30	1,012,710
AT-w-SAV	C3D10	1.43	0.7881	17480	31825	2	63,650
SAV	C3D20R	1.29	n/a	6336	32164	2	64,328
Pia	C3D4	3	n/a	30000	40804	1	40,804
UA	C3D4	3	n/a	60000	71407	1	71,407
						Total Nodes in Entire Model:	3,255,562

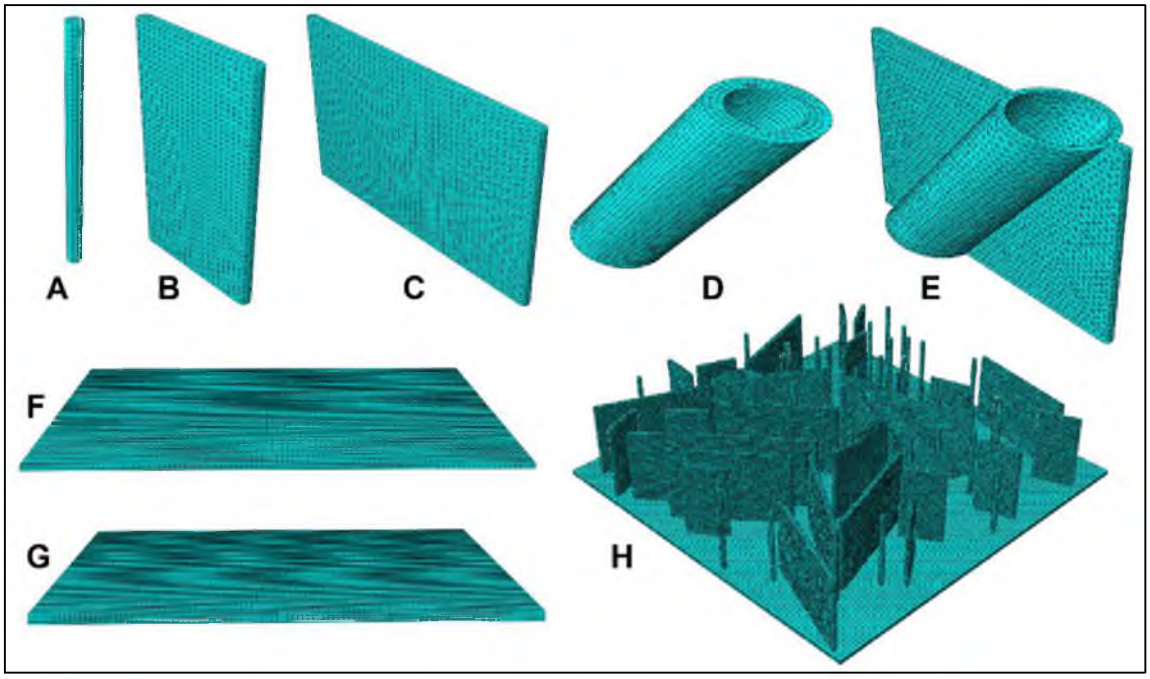

Figure 24: Final meshes for porcine microscale model: A) AT chord, B) AT short sheet, C) AT long sheet, D) SAV, E) SAV-enveloping AT sheet, F) pia, G) dura/UA, H) whole model (dura and upper arachnoid hidden)

3.2.3 Microscale Model Material Properties

The material properties for this model were chosen to be as close to actual porcine values as possible. As stated in Chapter 2, material data for the PAC are limited to a handful of studies, four of which were used to inform our material property selections in this study. The first three studies utilized were those conducted by Jin et al. on bovine PAC in tension [57], normal traction [58], and shear [59]. The fourth study utilized was the one by Aimedieu and Grebe on bovine PAC in tension [70]. The material properties of the SAV structures were based on the biaxial tests on porcine bridging veins conducted by Pang et al. [63]. Since the whole-head model that these microscale PAC models would be coupled to is subjected to a dynamic load, the material properties from the highest strain rate tests were used for all PAC tissues except the SAV which only had quasistatic

test results available. Additionally, Monson et al. observed no rate dependence in human cortical arteries and veins during tensile tests at strain rates of 0.01- $500s^{-1}$ [82].

As described in detail in Chapter 2, the normal traction test data from Jin et al. [58] can be used to infer the material properties of the AT structures, since they are the structures likely bearing the large majority of the load. However, one issue arose when correlating the reported moduli from the normal traction tests and applying these moduli to the individual AT structures. In the calculation of elastic modulus, Jin et al. treated the entire PAC as a single solid continuum; that is, they divided their measured loads by the cross-sectional area of the whole rectangular specimen when calculating stress. Our microscale model is small enough that the continuum assumption does not apply to the entire PAC, and it must be analyzed as a system of different components. If the modulus reported by Jin et al. (of an entire solid continuum) was used as the modulus of the AT components (which only make up approximately 8 to 45% of the space) the response of the PAC would be too compliant. This is because we are applying the same strength to less load-bearing volume in the region, and it is weakened by the void space. To account for this, it was assumed that the data reported by Jin et al. were those of an average VF specimen (21% VF) and the modulus of the continuum (59.81 kPa) was scaled up by the inverse of the VF, resulting in an AT modulus of 284.81 kPa.

Similarly, the tensile elastic moduli of the pia and UA membranes can be inferred from the tensile tests conducted by Jin et al. [57]. In this case, the cross-sectional area used for stress calculations in the Jin et al. results was that of the collapsed PAC. This majority of this cross-sectional area was made up of the pia and UA membranes, with very small contribution from the AT, which were collapsed and smashed between the pia

and UA. No scaling was performed on these data, and the reported stress-strain curves were fit to a linear function which estimated an elastic modulus of 15.814 MPa. This modulus was applied to the pia and UA without further scaling, since their dimensions were directly based on the Jin et al. measurements.

The elastic modulus of the SAV was calculated by fitting a linear curve to the reported data (despite the fact that it exhibited a slight nonlinear response). The curve-fit was conducted on the longitudinal direction tests (which have been shown in some studies to be more compliant than circumferential tests [62, 83]) resulting in a "worst-case" scenario of low moduli vessels allowing more brain-skull displacement. The linear elastic modulus used in this fit was 27.30 kPa. Density and Poisson's ratio was assumed the same as in the previous studies from Chapter 2, as 1130 kg/m^3 and 0.45, respectively [84]. Table 10 presents the material properties used for all structures in this study.

3.2.4 Development of a Representative Solid Element

In order to implement the microscale model's behavior into the macroscale model's CSF element layer, a representative solid element (RSE) was developed. This material behavior of this RSE was dictated by two simulations of material property tests conducted in ABAQUS on the microscale model. These simulations were designed to be very similar to the material tests conducted by Jin et al. in tension and normal traction. The tension studies would characterize the in-plane (tangent to brain surface) material properties, and the normal traction studies would characterize the out-of-plane (perpendicular to the brain surface) material properties. These tests were repeated for each varying volume fraction, resulting in a characterization of in-plane and out-of-plane

Table 10: Material properties utilized in microscale model of Porcine PAC. Note that density was assumed as 1130 kg/m^3 and Poisson's ratio of 0.45.

Structure	Modulus (E)	Source
AT structures	284.8095 kPa	[58]
SAV	27.30 kPa	[63]
Pia & UA	15.814 MPa	[57]

moduli for each VF. These values were then fit to a curve which correlated VF to modulus, resulting in a function that could define the material properties of an RSE representing the PAC for any VF.

The tension test simulations were conducted by fixing the pia and UA on one side, and applying a prescribed displacement to the other end (Figure 25). This prescribed displacement was 0.225mm, which resulted in 15% strain. This was chosen since it resulted in a moderate value of extension but did not exceed the level of strain that the weakest samples failed at in the Jin et al. studies [57]. The reaction force at the end with the prescribed displacement was collected, and along with the cross-sectional area, was used to calculate the stress-strain response of the simulated material test. The cross-sectional area was calculated from the pia and UA only (i.e., not including the SAS). This is because the load in these simulations is carried almost entirely by the pia and UA, which is evident when viewing the stress map of the deformed PAC model.

The normal traction test simulations were conducted by fixing the bottom surface of the pia and prescribing a displacement of 0.15mm to the top surface of the UA (Figure 26). This displacement was chosen as it would result in a 50% strain of the 0.300mm tall AT structures (or, if considering the entire 0.345mm tall PAC, a 43.47% strain). These levels of strain were chosen since they represented a moderate level of stretch without

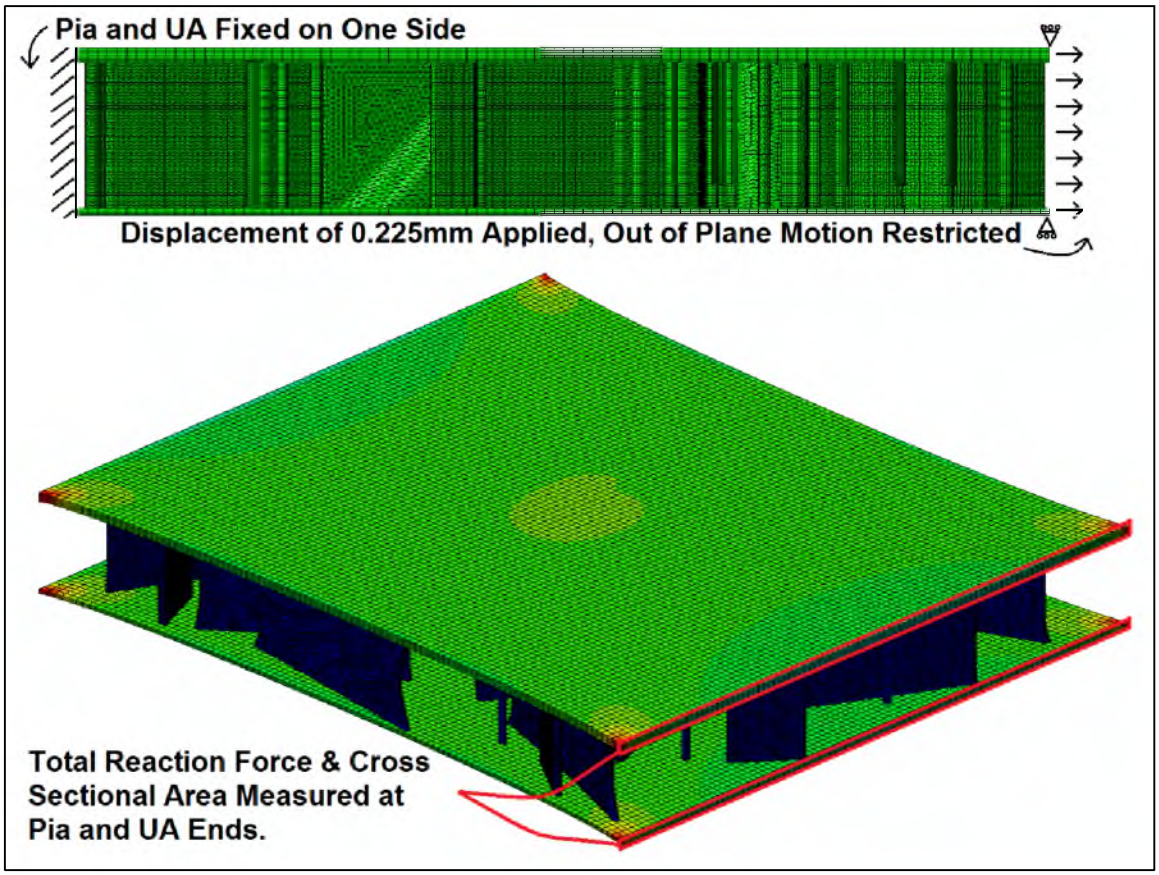

Figure 25: Boundary conditions and loading for the tensile test simulations and post-deformation stress map showcasing the pia and UA surfaces used to collect reaction force and cross-sectional area used to calculate stress in the RSE.

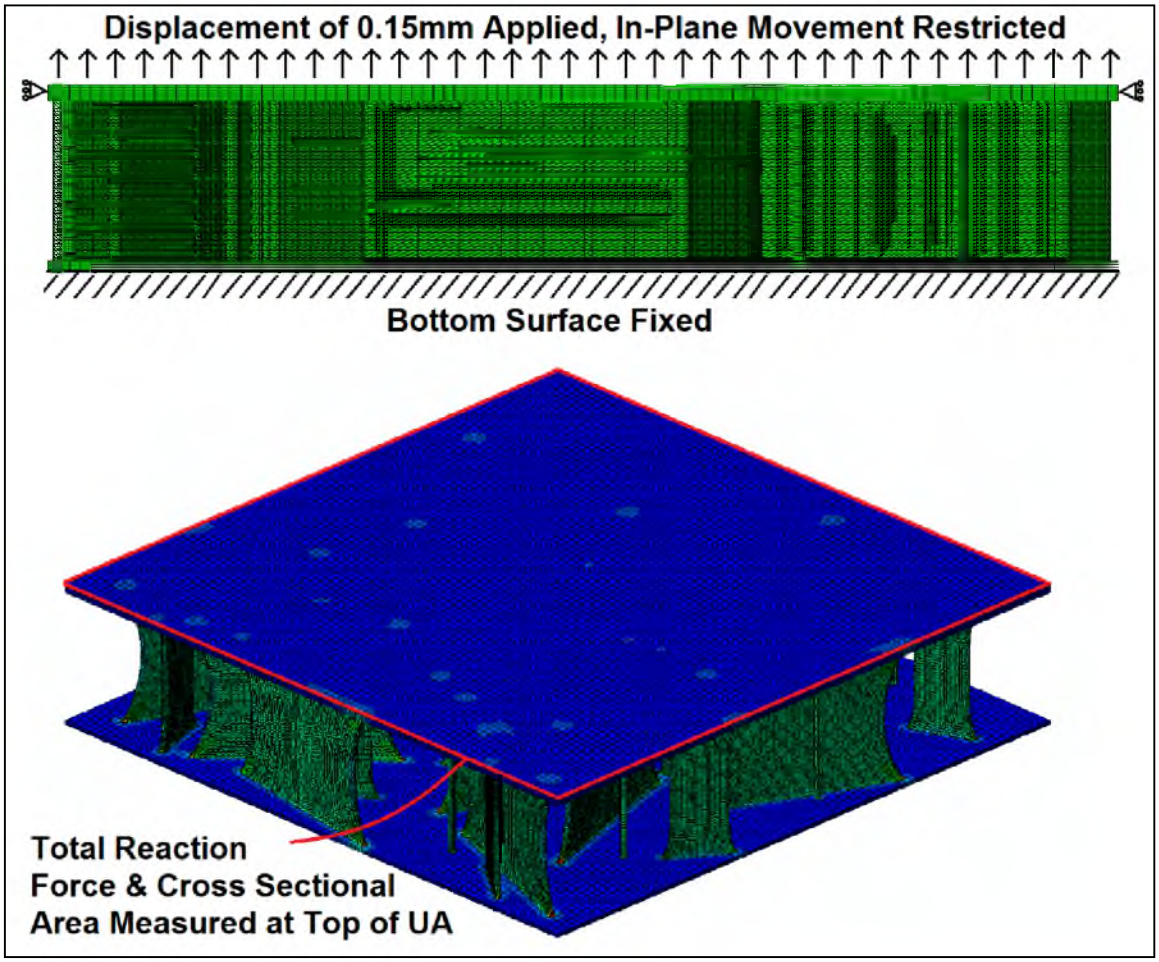

Figure 26: Boundary conditions and loading for the normal traction test simulations and postdeformation stress map showcasing the pia and UA surfaces used to collect reaction force and cross-sectional area used to calculate stress in the RSE

going above the failure points of some of the weakest tests reported by Jin et al. [58]. Additionally, since the tests by Jin et al. showed linear stress-strain responses, we did not expect any strain nonlinearities and values of stress at larger strains could easily be extrapolated if needed.

The stress-strain responses of each microscale tension test were extracted from each different VF model and plotted in order to visualize trends. Since the tensile tests were largely dominated by the pia and UA, VF did not influence the results very much (Figure 27A).

Several tests were conducted to see if any bias was introduced into the PAC models from the randomization procedure. For this assessment, the lowest VF model (7%, which had the least AT structures and would be most influenced by directionality of such structures) was tested in both in-plane directions (x and y). In addition, an entirely new model was built with a new randomized set of structures, still with a 7% VF. This model was also subjected to tensile tests in two in-plane directions. The four results of these tests showed no significant differences, with a maximum error of 0.006% occurring at the maximum stress point (Figure 27B).

The stress-strain responses of each microscale normal traction test were also plotted for each different VF model (Figure 28). In this case, large differences were seen between models, which were expected since the AT dominates the material response for these normal traction tests. When viewing these results, it was found that the difference in modulus was directly proportional to the change in VF on a linear scale, and this relationship could be used to predict the RSE modulus for VF models which we did not simulate.

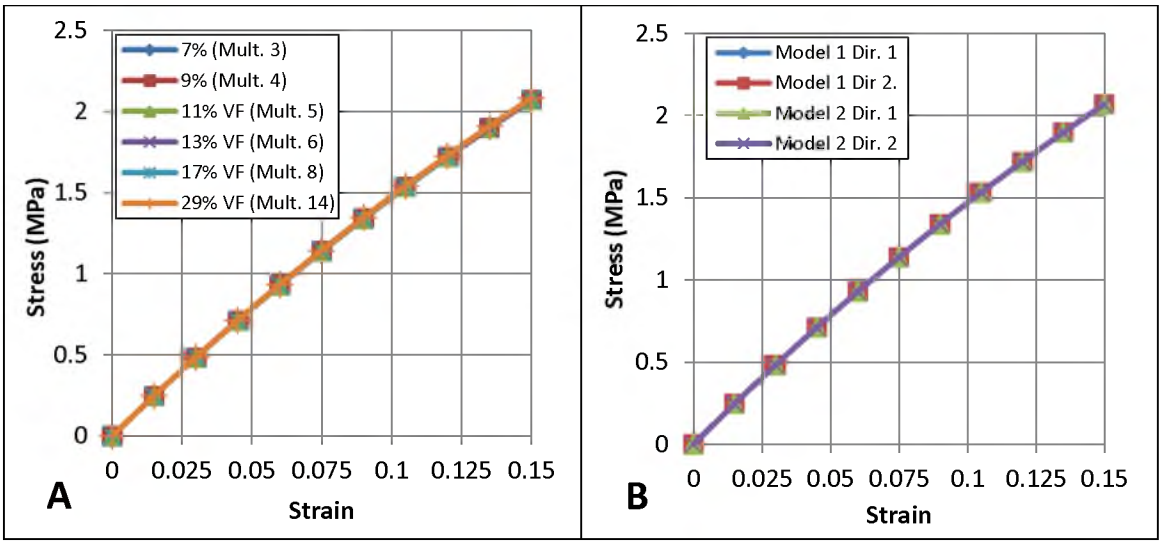

Figure 27: In-plane tensile test simulation results: stress-strain curves for all VFs (A), and stress-strain curves for randomization tests on 7% VF model (B).

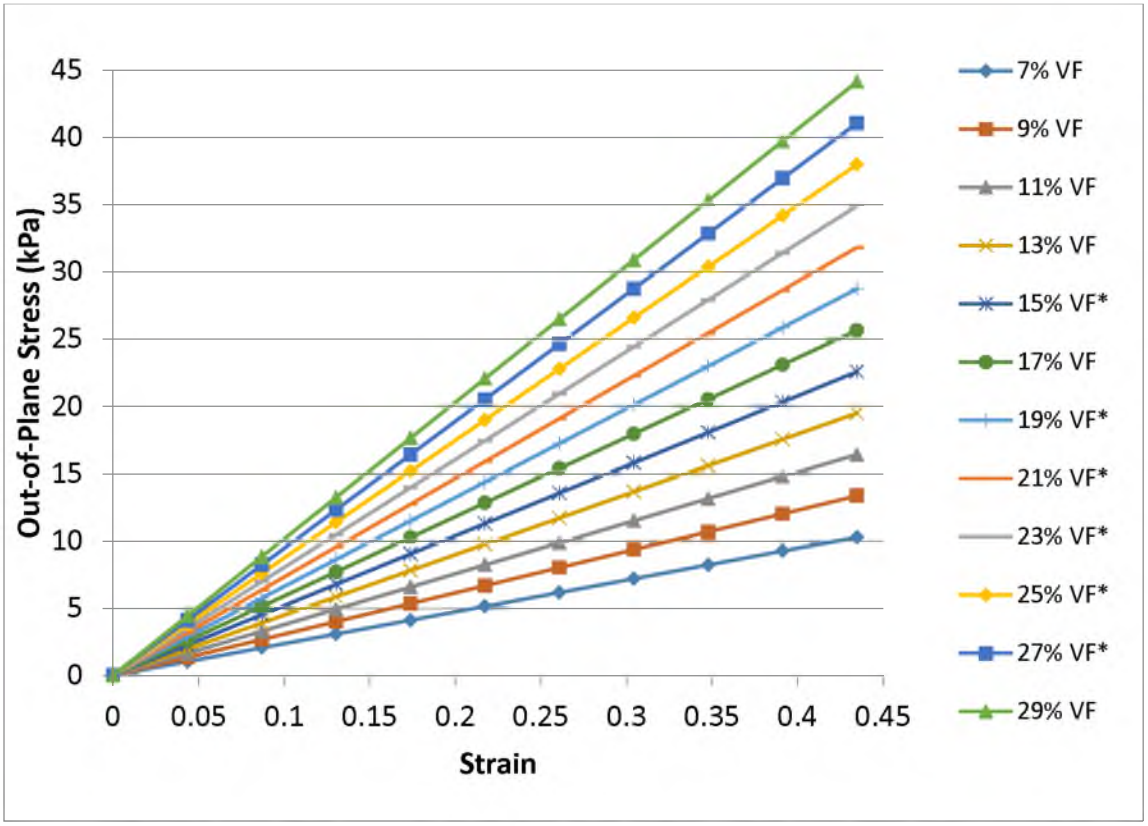

Figure 28: Stress-strain curve results from the microscale normal traction test (out-of-plane tension) simulations. Note that values with "*" denote an interpolated curve, and were not actually simulated.

Each stress strain curve presented in Figure 27 and Figure 28 was fit to a linear regression trend line, and the resulting linear slope in the regression equation was used as the modulus. For the tensile tests, it is acknowledged that there are slight nonlinearities present due to slight contributions from the AT to the stress-strain response at higher strains (or potentially due to computational errors inherent to the FE program). However, a linear fit still represented the data the best. Each modulus was then plotted against its corresponding VF for the two types of tests. When viewing the tensile test results, there appears to be slight increases in stiffness of the RSE for increases in VF; however, the changes are very small and outweighed by the inherent error between models (likely caused by FE stability controls adjusting elements slightly and altering forces). When applying a linear fit to the data points, the coefficient of determination was only 0.4479, and thus it was not trusted. Instead, an average of all of the moduli was chosen as the final modulus to be used in every RSE. When viewing the normal traction test results, a clear linear increase in modulus is seen for increasing VF.

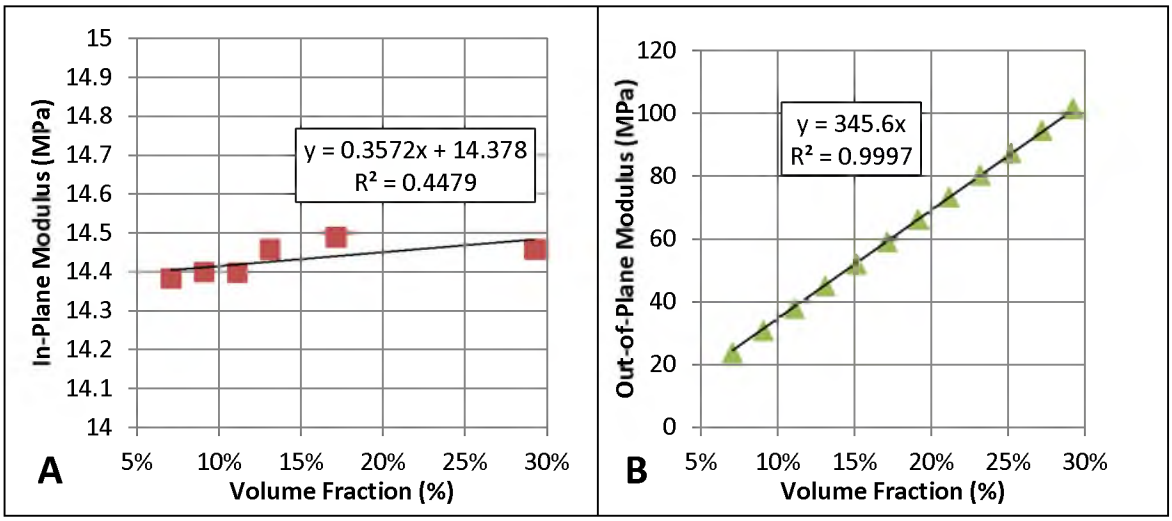

Figure 29: Results of the microscale model tension (A) and normal traction (B) tests. Note that for the normal traction tests, additional interpolated values are also plotted. Also note that for the normal traction tests, a y-intercept of 0 was enforced.

The moduli found from the microscale simulation studies were used to define the material properties of the RSE for any physiologically relevant volume fraction. As will be explained in Section 3.2.6, the RSEs will be implemented into the macroscale model as transversely isotropic elements. As such, the reported in-plane modulus (E_P) and transverse modulus (E_T) had to be supplemented with data from the literature in order to form a complete material definition for use within ABAQUS. The in-plane Poisson's ratio (ν_P), out-of-plane (transverse) Poisson's ratio (ν_{TP}), in-plane shear modulus (G_P), and transverse shear modulus (G_{TP}) all had to be defined. Note that for the differing VF models, only the transverse modulus (E_T) and transverse Poisson's ratio (ν_{TP}) were varied (Table 11). All other values were kept constant and are based on the assumptions and equations detailed next (Table 12).

The in-plane Poisson's ratio would be almost entirely governed by the pia and UA moduli, so a Poisson's ratio of these tissues was to be used. However, no literature exists which reports this value, and all material studies of the PAC were conducted without an additional strain measurement device monitoring the secondary axes, preventing any indirect calculation of VF. Persson et al. report the Poisson's ratio for spinal dura however, which can be compared to cranial dura if one considers the circumferential direction measurements (as the longitudinal measurements contained much higher collagen fiber directionality than cranial dura, and could not be used) [88]. Based on these reported data, the estimated in-plane Poisson's ratio was 0.45.

For transversely isotropic materials, the out-of-plane Poisson's ratio is generally not equivalent to the in-plane Poisson's ratio. Therefore, the assumption of 0.45 could not be utilized. Instead, the Poisson's ratio was calculated based on a ratio of the in-plane and

Table 11: Transverse modulus and transverse Poisson's ratio for the RSEs across a range of VFs.

VF	E_T (kPa)	ν_{TP}		VF	E_T (kPa)	ν_{TP}
7.059%	24.398	0.000761		25.193%	87.069	0.002715
9.074%	31.361	0.000978		27.208%	94.032	0.002932
11.089%	38.324	0.001195		29.223%	100.995	0.003150
13.104%	45.288	0.001412		31.238%	107.959	0.003367
15.119%	52.251	0.001629		33.253%	114.922	0.003584
17.134%	59.215	0.001847		35.268%	121.886	0.003801
19.149%	66.178	0.002064		37.283%	128.849	0.004018
21.164%	73.142	0.002281		39.298%	135.813	0.004235
23.179%	80.105	0.002498		41.313%	142.776	0.004452

Table 12: Constant material properties for all RSEs regardless of VF.

	Property	Value
	In-Plane Modulus (E_P)	14.43 MPa
	In-Plane Poisson's Ratio (ν_P)	0.45
	In-Plane Shear Modulus (G_P)	4.976 MPa
	Transverse Shear Modulus (G_{TP})	22.37 kPa

transverse moduli reported in the ABAQUS to ensure model stability (Equation 1) [89]. This calculation resulted in very low values of ν_{TP} (Table 11). When stretching or compressing the AT, there is likely very little contribution to changes in pia and UA shape, thus a low ν_{TP} makes logical sense. The in-plane shear modulus (G_P) was calculated based on the classical mechanics relation between shear modulus, elastic modulus, and Poisson's ratio (Equation 2). The in-plane elastic modulus (14.43 MPa) and assumed in-plane Poisson's ratio of 0.45 were utilized since the pia and UA largely dominate this shear response. The transverse shear modulus (G_T) was assumed based on shear moduli reported by Jin et al. who reported multiple shear moduli across different strain rates. The moduli from the highest strain rate test (22.37 kPa) was chosen since the whole-head model is subjected to high rate dynamic loading.

$$\nu_{TP} \leq \left(\frac{E_T}{E_P}\right)^{1/2} \quad \text{[Eq. 1]}$$

$$G_P = \frac{E_P}{2(1+\nu_P)} = \frac{14.43\ MPa}{2(1+0.45)} = 4.976\ MPa \quad \text{[Eq. 2]}$$

3.2.5 Macroscale Porcine Model Parameters

The macroscale model utilized in this study is one that has already been verified and validated in an FE study on nonimpact rapid head rotations in the immature piglet by Coats et al. [23]. The geometry of this model was created by segmenting a sequence of coronal computed tomography (CT) images of a 4-week-old pig brain, and scaling the dimension of that brain to that of an average 3-5-day-old piglet brain (Figure 30). The skull geometry was then created by extending the brain's outer surface outwards by 1mm, and smoothing to remove gyral morphology. The falx was created based on measurements obtained in-house with calipers *in-vivo* and *ex-vivo*. The model consisted of 17,587 elements (13,018 brain and brainstem hexahedral elements, 1891 falx tetrahedral elements, and 2678 skull rigid elements). An additional 2678 solid hexahedral elements were later added for one of the brain-skull boundary conditions, explained next.

The PAC was represented with 5 different boundary conditions. The first tied the brain and skull together (no-slip), the second allowed slip between the brain and skull with a coefficient of friction of 0.2, the third allowed slip between the brain and skull with no friction (pure slip). The fourth condition involved tying each brain surface node to its nearest inner skull surface node with an elastic connector. These connectors represented the tethering provided by the cortical vasculature in the brain and had their

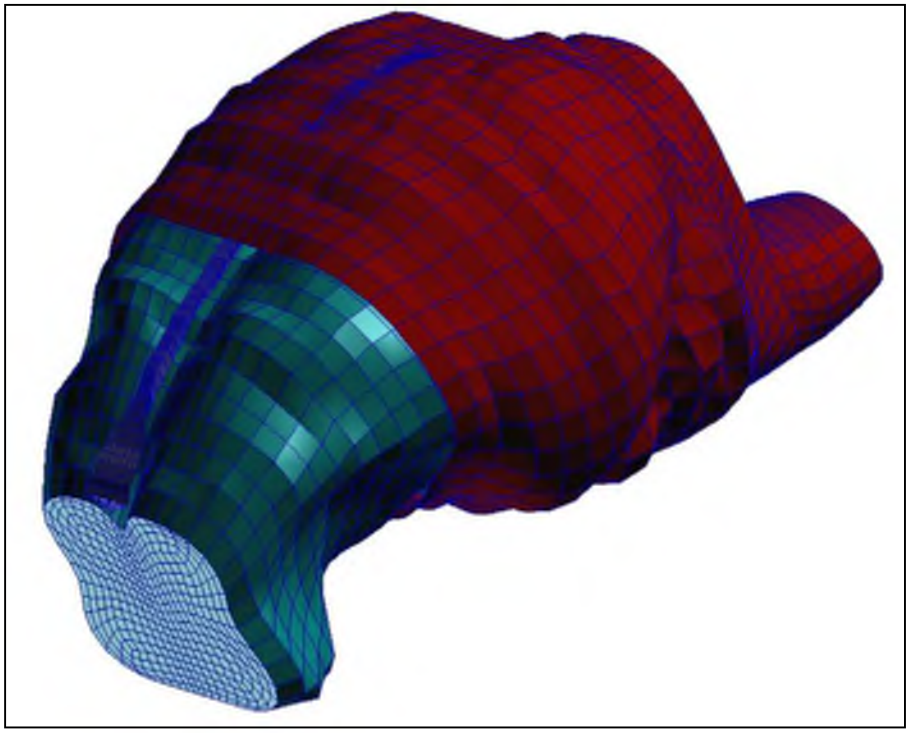

Figure 30: Macroscale finite element model of a 3-5 day old piglet brain and skull. Components include brain (green), brainstem, falx (blue), and skull (red). Reproduced with permission from Coats et al. [23].

properties defined by the values reported for cortical veins from autopsy by Monson et al. [62]. The fifth interaction represented the PAC with solid hexahedral elements. These elements represented the CSF with a fluid-like response. This response was governed by the Mie-Gruneisen equations of state as described by Meyers et al. [90].

For our study, only the last two interactions were utilized. The connector model (fourth interaction type) was utilized as the baseline model, as it was the one with the highest predictive capability of subdural and subarachnoid hemorrhage reported by Coats et al. The CSF model (fifth interaction type) was utilized for its geometry, as the material properties of the CSF elements could easily be replaced with those defined by the RSE for each regional PAC model. The new models with the RSE-defined elements could then be directly compared to the connector model.

The material properties of the model were chosen to best represent a 3-5-day-old piglet. The brain's material properties were determined from data presented on 5-day-old porcine samples [91]. The falx material properties were scaled down two-fold from Galford and McElhaney's reported values [72], based on a ratio of adult to fetal dural stiffness calculated from data by Bylski et al. [78]. Connector stiffness was defined as that of cortical veins [62]. Table 13 presents a summary of all of the material properties utilized in the macroscale model.

During the studies conducted by Coats et al. [23], the model was subjected to rapid head rotations in the axial, coronal, and sagittal planes which replicated animal experiments conducted by Eucker et al. [34]. These head rotations exhibited angular accelerations of 26 to 85 krad/s^2 and angular velocities of 130 to 220 rad/s, which produced a range of traumatic brain injury etiologies, including diffuse axonal injury and subdural and subarachnoid hemorrhage in the more extreme cases. For the multiscale study, only one head rotation was simulated. The selected velocity profile rotated the pigs head 60° in the sagittal direction reaching a maximum angular velocity of 161.29 rad/s (Figure 31). This velocity profile corresponds to model 24 in Coats et al. [23].

Table 13: Material properties utilized in the macroscale whole-head model. Adapted with permission from Coats et al. [23].

Structure	Material Property	Source
Brain/Brainstem	μ = 526.9 Pa τ_1 = 2.96 s α = 0.01 τ_2 = 0.181 s C1 = 0.332 ν = 0.49999 C2 = 0.389	[91]
Falx	ρ = 1.13 g/cm^3 E = 16 MPa ν = 0.45	[72]
Connectors	k = 3460 N/m	[62]

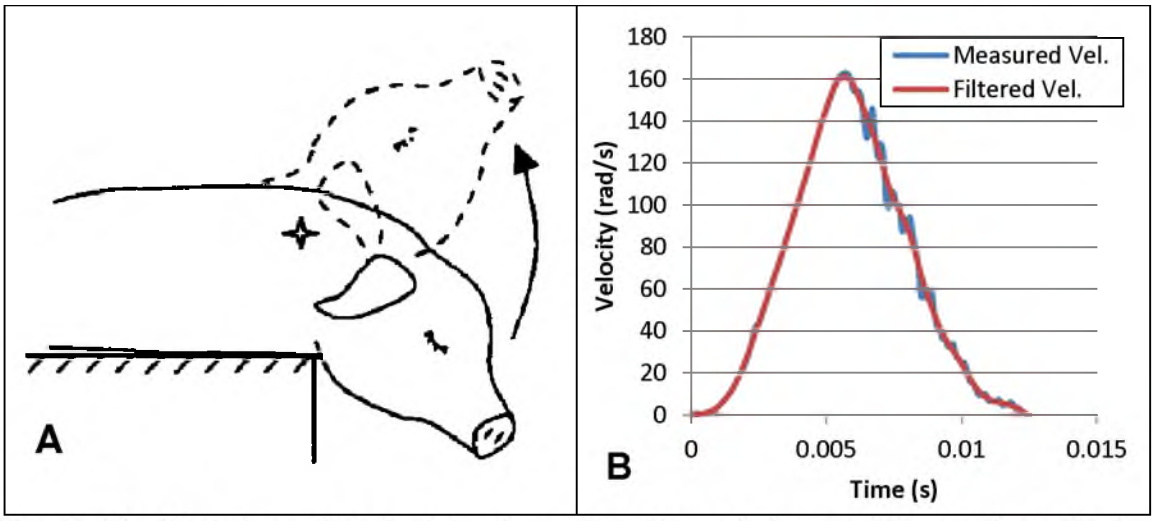

Figure 31: Depiction of sagittal head rotation (A) and the specific angular velocity loading behavior for the simulated experiment (B), the filtered velocity trace was used in the simulations.

3.2.6 Implementing the Representative Solid Element into Macroscale Models

The CSF elements from the whole-head model (5th boundary condition) were isolated and segmented into the 12 scanned regions used for the OCT imaging studies in Chapter 1. A 13th region was created that represented all the unscanned areas (Figure 32) Each of the 12 scanned regions were populated with the material properties of the RSE that represented the average VF found in that region. Two separate models were created. One represented the VF averages from animal P13-121 and the other represented the VF averages from animal P13-122. The brains of these animals had their subarachnoid space inflated with a syringe pump during imaging, and represented the closest representation of an *in-vivo* scan of the PAC. Table 14 provides the averages of the 12 subregions used to populate the FE models and Figure 33 presents a color map of the two brains. The unscanned region of both models was populated with RSE's which represented the brain's overall average VF for each animal.

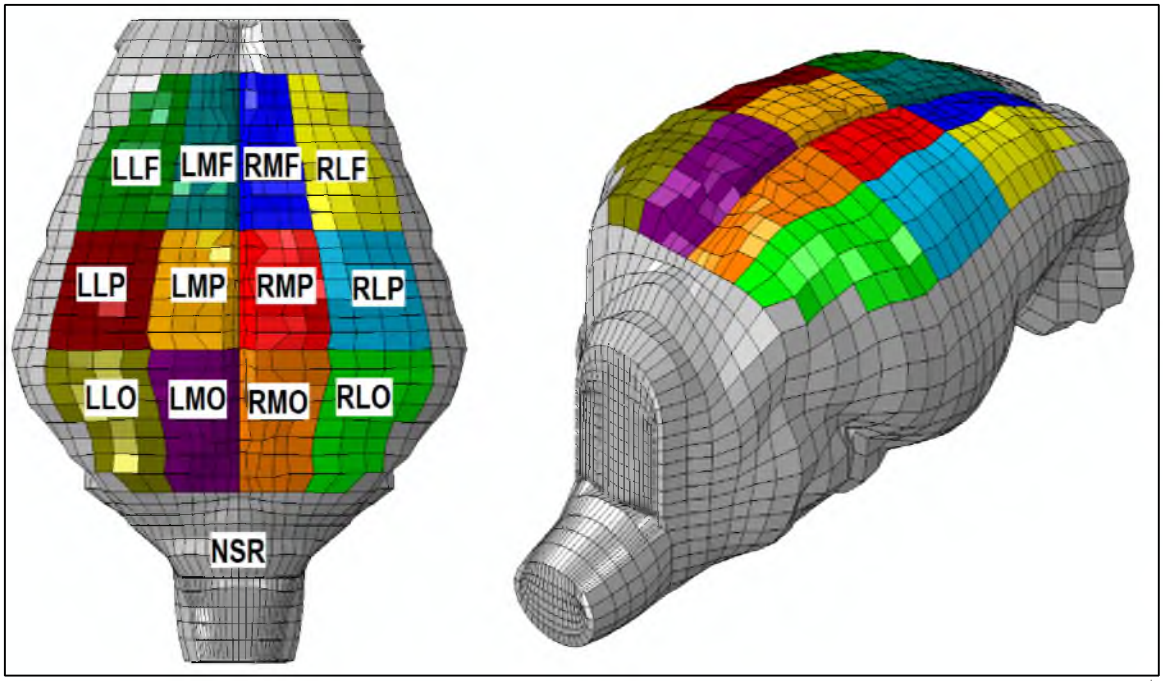

Figure 32: Modified CSF elements of whole-head model. For the 12 scanned regions: 1st letter indicates left or right, 2nd letter indicates medial or lateral, 3rd letter indicates frontal, parietal, or occipital. NSR indicates the not scanned region.

Table 14: Average VF values for each anatomical subregion of the two inflated brains. 1st letter indicates left or right, 2nd letter indicates medial or lateral, 3rd letter indicates frontal, parietal, or occipital.

Subregion	P13-121 Average	P13-122 Average
LLF	14.05%	29.06%
LLP	17.17%	16.55%
LLO	23.10%	37.15%
LMF	11.00%	24.08%
LMP	21.97%	23.12%
LMO	15.09%	20.40%
RLF	29.17%	24.36%
RLP	18.86%	26.29%
RMO	26.32%	34.79%
RMF	22.65%	11.15%
RMP	33.25%	32.77%
RMO	14.99%	27.81%
Entire Brain	20.29%	25.83%

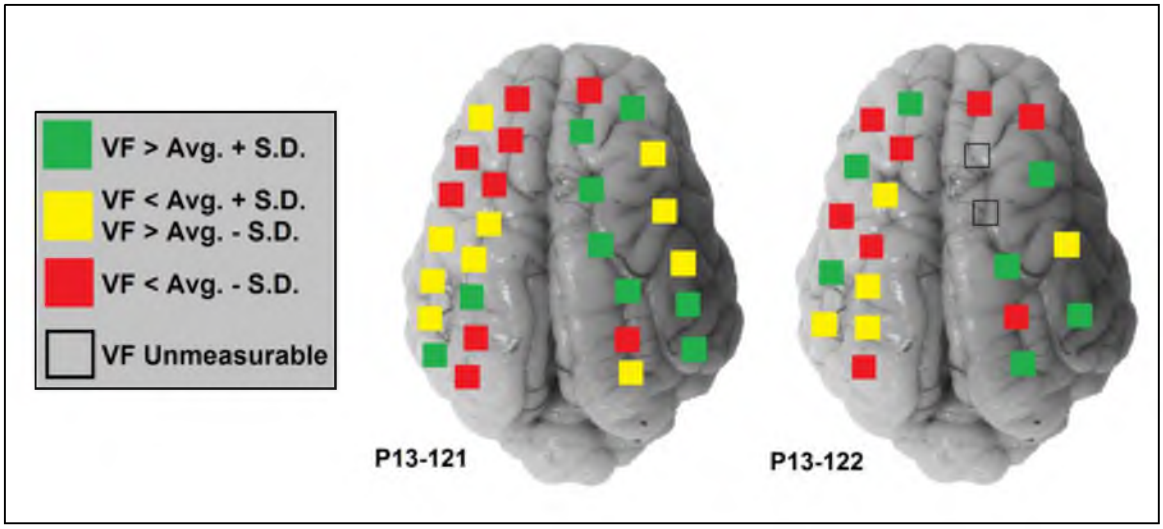

Figure 33: Color map of VF distributions across the two inflated brains. Averages and standard deviations are calculated for each brain separately. Note that positions are approximate and based on notes collected from the operator during the imaging session.

The material properties of the CSF elements were replaced with a transversely isotropic, linear elastic material model. The in-plane directions (the two directions with identical moduli) were the two tangent to the brain's surface, dictated by the pia and UA's response. The out of plane direction was perpendicular to the brain's surface (dictated by the AT response). To properly apply transverse isotropy, a local coordinate system was established in ABAQUS, in which the z direction (out of plane) for all elements was always perpendicular to the brain's surface. The input files for the final models are provided in Appendix D.1.

3.2.7 Macroscale Model Postprocessing

The coordinates of all the outer surface nodes of the brain and inner surface nodes of the skull were extracted at all time-points. These node sets were imported into a MATLAB code adapted from previous work by Coats et al. [23] (Appendix D.2).

This code subtracted the values of the skull's overall deflection from the values of the brain's overall deflection for each adjacent node pair, resulting in brain-skull displacement. The brain-skull displacement for each node pair over all time points was extracted and plotted against the fraction of elements in the model which experienced that displacement (or greater). This created distribution plots of peak brain-skull displacement (presented in Section 3.3.2). Distribution plots were created for 5 regions within the model which mimicked the 5 regions used to categorize intracranial hemorrhage prediction (IHP) scores in previously published animal experiments [34].

The distribution plots were utilized to assess whether there were significant differences in the simulations of animals P13-121 and P13-122. This significance was evaluated with a two-sample Kolmogorov-Smirnov goodness-of-fit test for continuous distributions [92] (Appendix D.3) A p-value <0.05 was used to indicate statistically significant differences between the distributions.

In addition to comparing the two simulations to each other, they were compared with the previously described macroscale simulations presented by Coats et al. [23]. In Coats et al., the model that best predicted intracranial hemorrhage utilized cortical spring connectors to represent the PAC boundary. The top 1% of its peak connector strain was used as the predictor with 0.31 mm/mm as the threshold for predicting injury. Coats et al. treated any regional percentage of hemorrhage found in the animal model above 25% as positive for hemorrhage, and any regional percentage of hemorrhage below 25% as negative for hemorrhage. Based on this criterion, the animal model simulated in the current work predicted hemorrhage with a 100% accuracy (i.e., it predicted all positive/negative results properly).

For our study, it was desired to evaluate the predictive capability of the multiscale models not only on how well they could predict the presence of hemorrhage (binary all or none value), but how well the brain-skull displacements correlated with gradients of hemorrhage (continuous severity variable). In order to do this, the IHP score provided by Coats et al. for each region was plotted against the 1%, 5%, 10%, and 50% fractions of peak brain-skull displacement extracted from each regional distribution plot. Linear regression fit lines were fit to each fraction data set, and the value with the highest coefficient of determination was selected as the best biomechanical parameter for predicting hemorrhage. For both of the multiscale simulations, the 50% fraction performed the best, and as such it was chosen as the best predictor of IHP. The linear regressions of IHP with 50% brain-skull displacement from the multiscale models and the 1% connector strain from the Coats et al. model were compared to see if the multiscale models had increased predictive capability of regional IHP.

3.3 Results

3.3.1 Qualitative Behavior

The multiscale simulations exhibit more discontinuous stress surfaces with small, localized hot spots of stress than the connector model. The connector model has homogenous stress contours due to the homogenous nature of the spring connectors. Two major kinematic events were observed to create local peaks of stress. The first is when the skull is leading the brain and the PAC is in tension (Figure 32). This occurs at the same time for the multiscale models, but slightly earlier for the connector model. At this time point, there is a large concentration of stress in the midline regions of the multiscale

models with some "fingers" of stress across various regions of the brain. In the connector model, there is only one large concentration of stress that spans the occipital and parietal lobes.

The second major kinematic event is when the brain "catches up" to the skull and is now leading, causing compression of the PAC elements (bottom row of Figure 32). During this stage, there is a hot spot of stress in the midline at the intersection of the frontal and parietal lobes in the multiscale models, but there is a much higher level of stress and more discontinuity in the connector model.

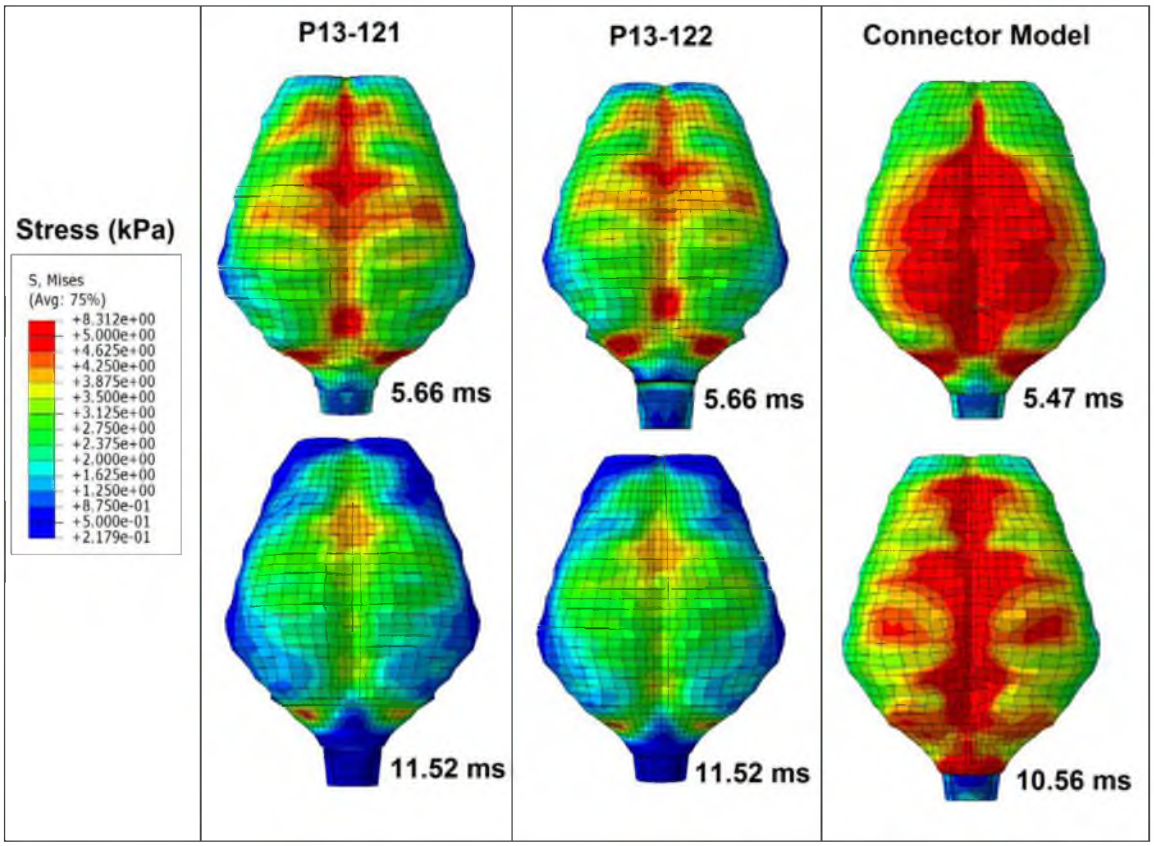

Figure 32: Stress maps of the top surface of the brain in all three simulations. In the top row, the skull is leading the brain and the PAC is in tension. In the bottom row, the brain has caught up with the skull motion. The brain is now leading and the PAC is in compression.

3.3.2 Comparison of Two Subject-Specific Multiscale Models

The Kolmogorov-Smirnov goodness-of-fit tests resulted in p-values of <<0.0001 for all 5 regions, indicating that the distributions in each of the two animal simulations were significantly different (Table 15). Figure 33 presents the distribution curves across all 5 regions for the two multiscale models. Animal P13-121 exhibited a higher levels of brain-skull displacement, which was expected, as it had lower overall VF levels than animal P13-122.

3.3.3 Injury Prediction Capabilities

The brain-skull displacement (multiscale models) and connector strain (connector model) experienced by 1%, 5%, 10%, and 50% of the elements, and the corresponding IHP scores, are presented in Table 16. Both the displacement and strain values trend upward as IHP score increases, with the exception of the midline data. Linear regression plots are presented for data including the midline values, as well as data excluding the midline values (Figure 34). In both cases and in both animals, the multiscale models exhibit better curve-fits and higher R^2 values, outperforming the cortical connector model. However, for the fits which include the midline values, the multiscale model regression lines slope backwards, which invalidates any comparison to the other model.

Table 15: Results of the two-sample Kolmogorov-Smirnov goodness-of-fit test for brains P13-121 and P13-122. (n=185)

	Anterior Left	Anterior Right	Posterior Left	Posterior Right	Midline
D-Value	0.39946	0.32520	0.17724	0.20217	0.46233
P-Value	4.56×10^{-26}	2.03×10^{-17}	1.79×10^{-5}	5.41×10^{-7}	8.99×10^{-35}

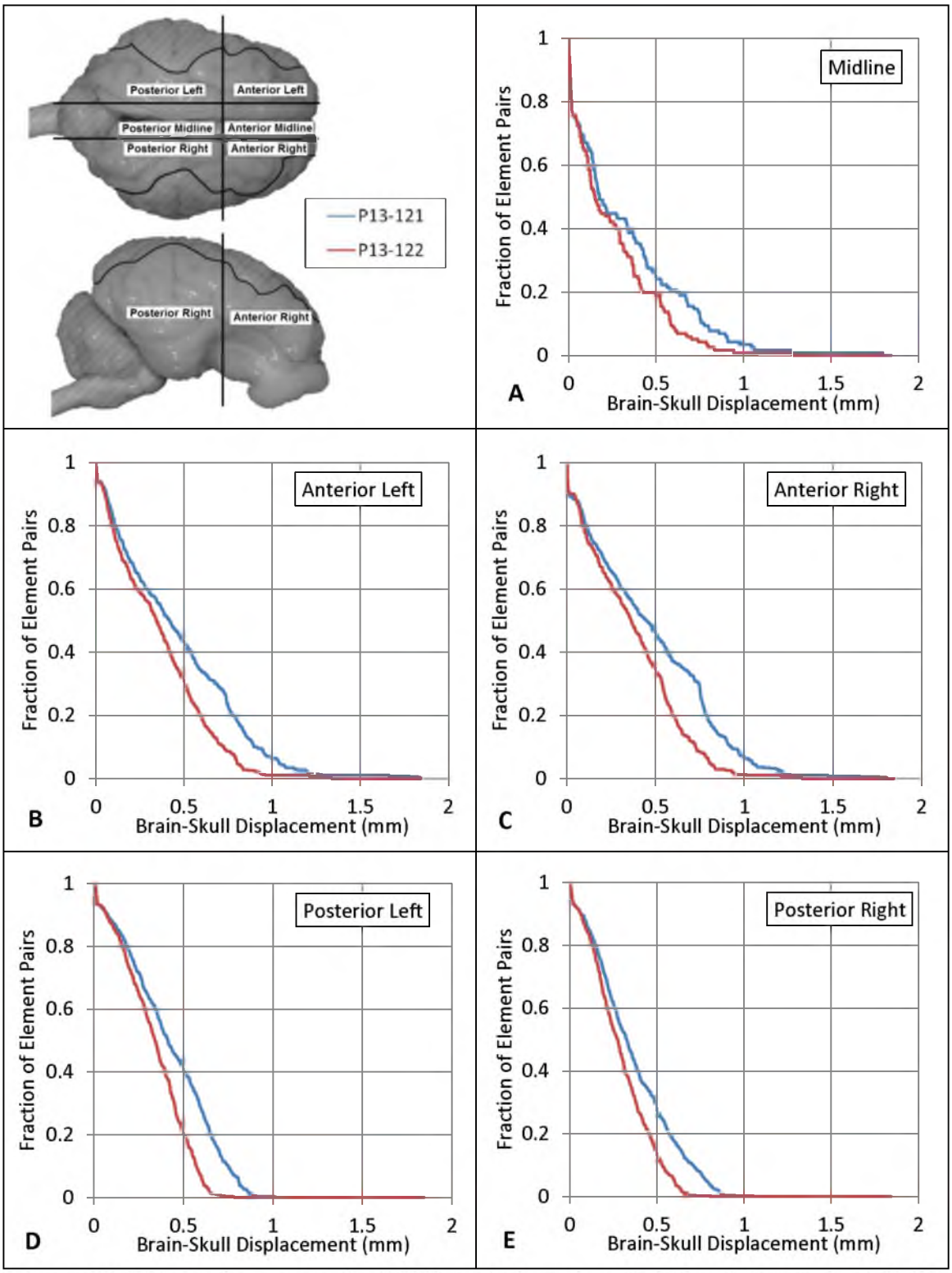

Figure 33: Distribution curves for 5 IHP analysis regions (midline (A), anterior left (B), anterior right (C), posterior left (D), posterior right (E)). Legend is adapted from images presented by Coats et al. [23].

Table 16: Peak values of brain-skull displacement or connector strain for the three macroscale models along with their corresponding IHP scores.

P13-121 Peak Brain-Skull Displacement Values					
	IHP Score	50%	10%	5%	1%
Posterior Right	11%	0.329	0.7095	0.7885	0.8775
Anterior Right	25%	0.45	0.9265	1.0455	1.4715
Posterior Left	25%	0.414	0.7505	0.8105	0.8875
Anterior Right	27%	0.421	0.9125	1.0375	1.6615
Midline	66%	0.1775	0.7755	0.9115	1.2755
P13-122 Peak Brain-Skull Displacement Values					
	IHP Score	50%	10%	5%	1%
Posterior Right	11%	0.2755	0.5345	0.6005	0.6805
Anterior Right	25%	0.3645	0.7275	0.8055	1.2065
Posterior Left	25%	0.341	0.5705	0.6085	0.6925
Anterior Right	27%	0.3435	0.7275	0.8005	1.2095
Midline	66%	0.152	0.5855	0.7415	0.9445
Cortical Connector Model Peak Connector Strain Values					
	IHP Score	50%	10%	5%	1%
Posterior Right	11%	0.0358	0.08945	0.10315	0.16445
Anterior Right	25%	0.0869	0.25895	0.33305	0.69415
Posterior Left	25%	0.03145	0.09095	0.12235	0.24325
Anterior Right	27%	0.08085	0.28265	0.38865	0.81435
Midline	66%	0.06485	0.22255	0.38815	0.69605

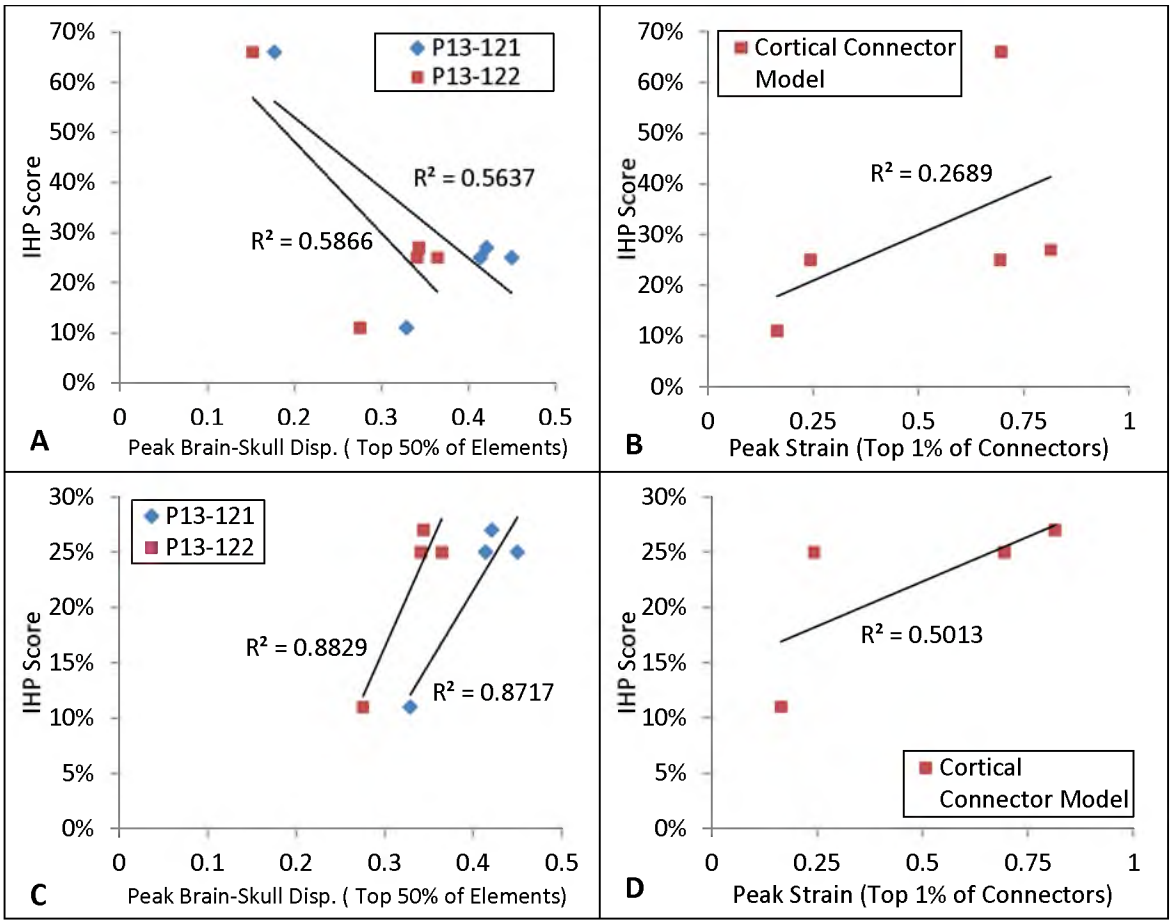

Figure 34: Linear regression fits of the best IHP predictors; top 50% displacement values for variable VF models and top 1% connector strain for spring connector model. Results are presented with the midline data included (A,B) and excluded (C,D).

3.4 Discussion

In this study, a robust microscale model of the porcine PAC was developed and utilized to develop a set of material properties which took into account the effects of the different microstructural components of the PAC. These material properties allowed the creation of a set of representative solid elements (RSEs) that could be implemented into a whole-head model of injury, allowing more accurate representation of the PAC in a computationally inexpensive manner. As in Chapter 2, a major limitation of this model was the use of linear-elastic material properties. Inclusion of strain- and rate-dependent

material models would allow more physiologically realistic RSEs to be developed. However, inclusion of more advanced material models would be at the expense of computational time. If nonlinear strain- and rate-dependent properties were to be applied in different material directions, a user-defined material definition may need to be created and tested. In addition to these properties, some observed phenomena of the PAC may not be easily represented by standard material definitions. For example, with the current material definitions, the PAC behaves the same in compression as it does in tension. We know this is not true in either the in-plane or out-of-plane directions, as the compliant pia, UA, and AT structures would simply buckle in this loading configuration. Physiologically, the compression response of the PAC is actually dominated by the fluid buoyancy of the CSF, which as previously mentioned, was excluded from this current model. Inclusion of CSF or loading-direction specific material parameters would result in more physiologically relevant simulations.

Regardless of this limitation, the results showing the effects of VF variability on a whole-head model of TBI were informative. There was an increase in localized variability, and "hot spots" of stress along the brain were found. This is an intriguing finding, as it may hold the key to increasing simulation accuracy when trying to predict local hemorrhage locations.

Two subject-specific models of VF variance were simulated to evaluate the effect of subject-specific variation on brain mechanics. There were statistically significant differences in brain-skull displacement between the two subjects. This makes sense intuitively, since not only did the models have variable VF applied to 12 different regions, but animal P13-122 also had higher VF overall by about 5%. This higher VF led

to a distinct trend of lower brain-skull displacement across all regions, due to the higher tethering action present. This trend was larger at intermediate values and not as prevalent near the upper and lower limits of the distribution curves. Considering that the brain-skull displacement experienced by 50% of the elements was the best at correlating with hemorrhage scores, the effect of different volume fractions in this region is important. This suggests that two subjects subjected to the same loading could experience different levels of injury. They could also experience different locations of injury, due to the different distributions of VF. In general, the hypothesis that lower levels of VF allow for higher brain-skull displacements (and thus higher risk of injury) held true throughout all regional comparisons.

The two multiscale models showed an increased ability to correlate with the severity of regional intracranial hemorrhage when compared to the existing cortical connector model for most regions. All models (multiscale and connector) fell short on their correlation with hemorrhage in the midline region. This region exhibited very high levels of IHP scoring when evaluated in a physical animal model. This is due to the large amounts of bridging vessels leading into the superior sagittal sinus which are more prone to injury than cortical vessels on more lateral brain surfaces. The multiscale and connector models do not account for vascular anatomy, and essentially treat all regions as having the same chance of injury. This lack of bias towards cardiovascular anatomy may explain why all the FE models do not accurately predict IHP in this region. Additionally, we did not image the microstructures in the midline region in Chapter 1. During OCT imaging, the superior sagittal sinus was left intact, and the dura over the midline was not removed to prevent tearing of bridging vessels and potential tearing of the PAC

structures. This prevented imaging from being conducted in the most medial regions of the brain, thus the midline regions were assumed to have the same values of VF in the multiscale model. It is likely that imaging these structures and creating PAC models specific for this region would enhance the prediction of hemorrhage in this region.

Removing the midline from the analysis, the multiscale models correlated extremely well with the IHP scores and performed much better than the connector model. The R^2 values were 0.8829 and 0.8717 for the multiscale models and 0.5013 for the connector model. More impressive was the tight grouping of the brain-skull displacements that correlated with 25-27% hemorrhage in the animal model. The connector model does not have this regional accuracy. This is a powerful finding because it suggests the multiscale model may have a direct relationship between brain-skull displacement and hemorrhage severity in all regions but the midline. This analysis was only performed on the simulation of one animal study, however. Simulation of all 24 animal experiments in Coats et al. [23] is required to truly evaluate the predictive capabilities of the multiscale model.

Despite the apparent improvements in the present model over the previous connector model, the RSE elements implemented into the macroscale model carried with them the limitations of their microscale model parents. Despite the fact that the nonlinear strain and rate responses of brain tissue were well represented with hyperelastic and viscoelastic properties in the whole-head model, the linear elastic nature of the RSE elements may have limited the accuracy of the injury predictions. Incorporation of strain and rate-dependent material models into our RSEs would allow for more physiologically realistic predictions of IHP.

Due to the preliminary nature of this study, it was never planned to test a large number of subject-specific models, nor was it possible since only two trustworthy measurement sets from the inflated brains were available. The sample size of two was still able to make some fairly strong observations about the effects of VF variability on whole-head biomechanics in general. However, to truly understand trends in VF and variability among subjects, much larger sample size is required. As with most scientific studies, the trends observed in this study will only become stronger with increasing sample sizes.

3.5 Conclusion

In this study, a computationally efficient method of implementing microscale level details of the PAC into a macroscale whole-head model was developed. The macroscale simulations showed a significant correlation between VF variability and potential brain injury. A specific microscale model of the sagittal sinus needs to be created, however, before predictive capabilities are improved for all regions of the brain. Regardless, these simulations also showed a marked improvement in predicting IHP when using variable VF models (as compared to a strictly homogenous model). These data suggest that the PAC does have a significant effect on brain biomechanics. To drive more accurate injury prediction in FE models of brain injury, more personalized, patient-specific models may need to be developed with the knowledge that no two brains have the same PAC distributions.

CHAPTER 4

INVESTIGATION OF PIA-ARACHNOID COMPLEX DAMAGE FROM REPETITIVE HEAD ROTATION

4.1 Introduction

Physical models have long been a well-accepted way to study the biomechanics of traumatic brain injury, and have included cadaveric as well as *in-vivo* human and animal studies. One phenomenon under heavy study is that of brain-skull displacement during TBI, with early studies using gel phantoms in human skulls [93-94] or monkeys with Lucite calvarium prosthetics to directly view brain-skull displacement [95]. More recently, some studies have leveraged medical imaging technology to provide researchers brain-skull displacement values. Some studies utilized x-ray cinematography to track relative movements between brain and skull in dogs and monkeys [96-97]. Other studies measured relative brain-skull movement by the injection of intravenous contrast agents and/or radiopaque marker implantation [98-99]. These studies provided researchers general translation/rotation values between the brain and skull; however, they fell short in their inability to measure deep brain deformation and brain strain. One study did provide information on deep brain movement during impact by implanting neutral density targets into deep brain regions of adult cadaver heads and imaging those targets with X-radiography [100].

In order to address injury predictions to deep brain structures, some research groups have turned to magnetic resonance imaging (MRI) to track strains in the entire brain. One team has developed tagged MRI and magnetic resonance elastography methods which evaluate the mechanical behavior and material properties of the mouse, rat, and ferret brain when subjected to rapid deformations [101-104]. The same team has also utilized tagged MRI sequences to measure brain strains during mild linear accelerations [105-106], and mild rotational accelerations [107] in human subjects. Many more studies exist which capitalize on noninvasive medical imaging technologies to study the behavior of the brain during injury [108].

The goal of this study was to evaluate a number of MRI methods for their feasibility as a means to predict mechanical damage to the pia arachnoid complex (PAC) and subsequent mechanical changes to the brain as a whole. Utilizing the findings from this study, clinically relevant imaging biomarkers that relate to PAC damage can be developed. MRI imaging and our previously established OCT imaging protocol were both utilized to assess PAC damage in brains 24 hours after a repetitive head rotation.

4.2 Methods

4.2.1 Study Procedure and Animal Care Protocols

Piglets were housed in pairs at the University of Utah Comparative Medicine Center (CMC) according to all pertinent regulations set forth by the USDA (U.S. Department of Agriculture) and IACUC (Institutional Animal Care and Use Committee). On study dates, the piglets were transported to the University of Utah Small Animal Imaging Facility (where all imaging was performed) by CMC personnel. At all time-

points during the study, strict adherence to IACUC guidelines was observed.

The piglets were anesthetized with 5% isoflurane via a snout mask, intubated, and then maintained on 1-3% isoflurane. Once the animals had reached a stable level of anesthesia, they were loaded onto a custom MRI bed (detailed in Section 4.2.4). The intubation tube was connected to the anesthesia airline of a MRI compatible ventilator. Vital monitoring probes (rectal temperature, PulseOX monitor, ECG, and respiration transducer) were attached to the piglet, and the piglet was loaded into the MRI. Multiple imaging modalities (described in subsequent sections) were performed to investigate their potential to act as a biomarker for PAC damage. Imaging was conducted for no more than 3 hours due to the animal's sensitivity to prolonged anesthesia after that time point.

After MRI imaging, the animal was kept under anesthesia and transferred to a procedure room where it was attached to a cyclic shaking device known to produce mild injury in 3-5-day-old piglets [33]. A picture and schematic drawing of the device, as well as an illustration of the head rotation, are presented in Figure 35.

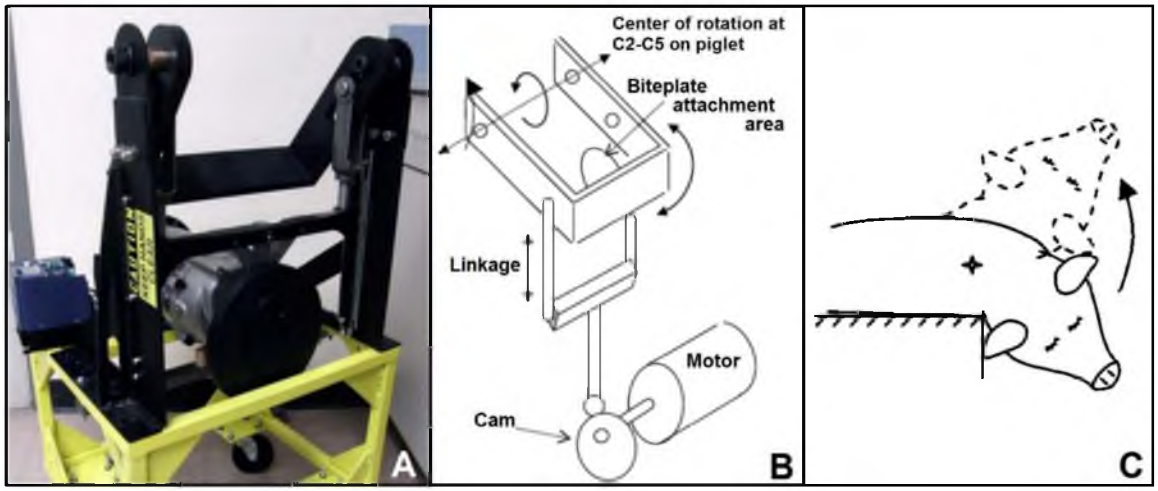

Figure 35: Custom cyclic device capable of inducing mild TBI from nonimpact head rotation in an immature piglet (A & B) and schematic of axial head rotation induced with the device during the studies (C).

The cyclic device repeatedly rotated the piglet's head from -50° to 50° in the axial plane resulting in an overall 100° head rotation. The center of rotation was located approximately at the C2-C3 spinal segment. After completion of one 100° rotation, the device reversed direction and the rotation was repeated, creating a consistent cyclic back and forth rotation of the head. Cyclic rotations occurred at a frequency of 3 Hz for a duration of 20 seconds.

Angular velocity of the cyclic motion was captured with an angular velocity transducer (DTS ARS 8K, Seal Beach, CA) and angular acceleration was calculated from these measurements via numerical differentiation. Typical results for these measurements are presented in Figure 38. A summary of the means and standard deviations of these measurements is provided in Table 17. After these rotations, the animal was transported back to the CMC, for recovery and monitoring. Animals were typically back to normal activity within 2 hours postinjury.

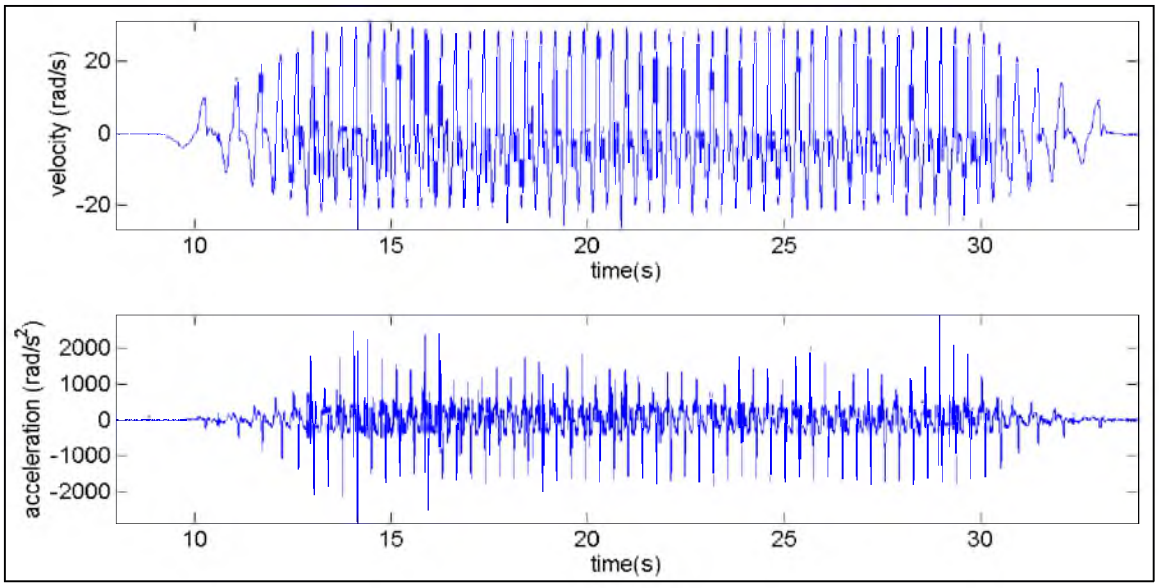

Figure 36: Typical measurements from the angular velocity transducer taken during the cyclic shaking of each animal (top), and the resulting calculated angular acceleration response (bottom).

Table 17: Averages and standard deviations of angular displacement, angular velocity, and angular acceleration data collected on three of the five injury animals. Animals P13-110 and P14-002 were excluded due to bad measurement data.

	Displacement (Degrees)	Angular Velocity (rad/s)	Angular Acceleration (rad/s^2)	Frequency (Hz)
P14-001	103.60 ± 20.45	48.032 ± 4.811	1206.2 ± 803.81	3.0158
P14-006	102.98 ± 8.466	41.147 ± 13.40	1372.2 ± 609.35	2.9666
P14-007	109.47 ± 9.033	50.629 ± 2.458	1593.3 ± 561.97	2.9608

4.2.2 T2-Weighted Imaging

MRI has been shown to be an efficient means of detecting small hemorrhage, contusion, and cellular swelling in TBI patients [109]. It is common clinical practice to utilize T2 to visualize cerebrospinal fluid (CSF), which appears hyperintense (white). This is largely driven by the well-accepted Monro-Kellie hypothesis [110], which states that the skull is a rigid container and all intracranial contents (CSF, intracranial blood, brain tissue) are incompressible and must maintain a constant volume balance. Therefore, many neurological pathologies can be diagnosed by evaluating changes in CSF volume.

The use of T2 imaging was motivated by the theory that if PAC microstructures were damaged during mild TBI, mechanical tethering in the SAS would be lessened, and the SAS would more readily be filled with CSF. Additionally, the T2 images would serve as a "gold standard" view of the brains, and allow for a standard clinical examination of the brains for any signs of injury.

Scan quality was limited by the amount of time the animals could safely be kept under anesthesia. Therefore, scan parameters were iteratively changed until an optimum balance of image quality and scan time was reached. Table 18 presents the scan parameters for the 5 animals which experienced the repetitive head rotation. All scans were T2 RARE sequences with a repetition time (T_R) of 5133.587 ms, echo time of (T_E)

50 ms, and flip angle (FA) of 180° with the exception of animal P13-110 (which had T_R = 3000 ms, T_E = 50 ms, and FA of 130°).

The images acquired during this study were analyzed in two ways. First, all images were reviewed by the MRI engineer and a pediatric radiologist for any qualitative clinical findings. Second, the T2 images were quantitatively analyzed for CSF volume changes before and after injury. In order to reduce error in the quantitative study, it was desired to remove as much noise from the images as possible and enhance the spatial resolution. This enhancement was done with ImageJ (v1.47, National Institutes of Health, Besthesda, MD). First, the images were all cropped to 190 by 170 pixels to remove as much extraneous tissue as possible, and focus only on the brain. Second, the images were scaled up by 200% (resulting in 380 by 340 pixel images). Third, a denoising algorithm was run on the images to improve the signal to noise ratio [111]. The denoising algorithm features 2 adjustable parameters. The first is number of cycle spins (of which we chose the maximum, 10, which achieves the best signal to noise ratio, at the expense of the worst computational time). The second is number of frames for multiframe averaging; we chose 5, which allowed 2 frames before and after the current frame to contribute to its noise parameter estimation. Last, after the denoising algorithm had completed, the images were then scaled up by 200% again, resulting in a final denoised image with 760 by 680 pixels (Figure 37).

The denoised and scaled images were analyzed by implementing a MATLAB algorithm (Appendix E.1) which enhanced the contrast of the images and thresholded the images such that only the most hyperintense range of pixel intensities (which represent CSF) remained as white in a binary black and white image. Contrast enhancement

parameters and threshold cutoff values were changed for each animal due to the different inherent contrast levels of the input images. The individual parameters for each image volume were selected with repeatability between frames in mind such that each image showed the same amount of CSF hyperintensity, with minimized hyperintensity of other structures and noise. The user then drew a freehand selection around a region of interest (ROI) and the program reported how many white "CSF" pixels were in that ROI. Four anatomical ROIs were analyzed. These ROIs were selected because they could be reproducibly identified on all animals and were typically filled with measurable amounts of CSF (Table 19). The entire amount of CSF in the brain was also analyzed by having the user circle the entire brain as a ROI across each frame. Care was taken to not include ocular, skull, and cochlear structures which typically were of high enough hypointensity that they were not removed by the thresholding. When measuring the CSF in the whole brain, measurements were always taken from the backmost portion of the cerebellum to the frontmost portion of the olfactory bulbs. This ensured the entire brain was sampled for CSF. Position of the animals was not exact for each scan, so in order to adhere to the same measurement protocol across brains, some frames at the beginning and end of the images were ignored. Animal P13-110 had to be excluded from the analysis due to the field of view not encompassing the entire brain and too low of a resolution for direct comparisons. Figure 38 shows representative images of each ROI being captured and Figure 39 shows a sampling of representative frames from the whole brain analysis which typically consisted of 24-28 frames total. The collected pixel values for each ROI and the whole brain were tabulated. Pre- and postinjury CSF volumes were compared for each animal.

Table 18: T2 RARE scan parameters for each animal.

Animal #	Pre/Post Injury	Matrix size, # of averages, Frame spacing (mm)	Field of View (mm)	Voxel Size (mm)
P13-110	Pre	128 x 128, 4, 3	90 x 90 x 30	0.7 x 0.7 x 3
P13-110	Post	128 x 128, 4, 3	90 x 90 x 30	0.7 x 0.7 x 3
P14-001	Pre	256 x 256, 2, 2	70 x 70 x 64	0.27 x 0.27 x 2
P14-001	Post	256 x 256, 6, 2	70 x 70 x 64	0.27 x 0.27 x 2
P14-002	Pre	256 x 256, 2, 2	70 x 70 x 64	0.27 x 0.27 x 2
P14-002	Post	256 x 256, 6, 2	70 x 70 x 64	0.27 x 0.27 x 2
P14-006	Pre	256 x 256, 6, 2	80 x 80 x 64	0.31 x 0.31 x 2
P14-006	Post	256 x 256, 6, 2	80 x 80 x 64	0.31 x 0.31 x 2
P14-007	Pre	256 x 256, 6, 2	70 x 70 x 64	0.27 x 0.27 x 2
P14-007	Post	256 x 256, 6, 2	70 x 70 x 64	0.27 x 0.27 x 2

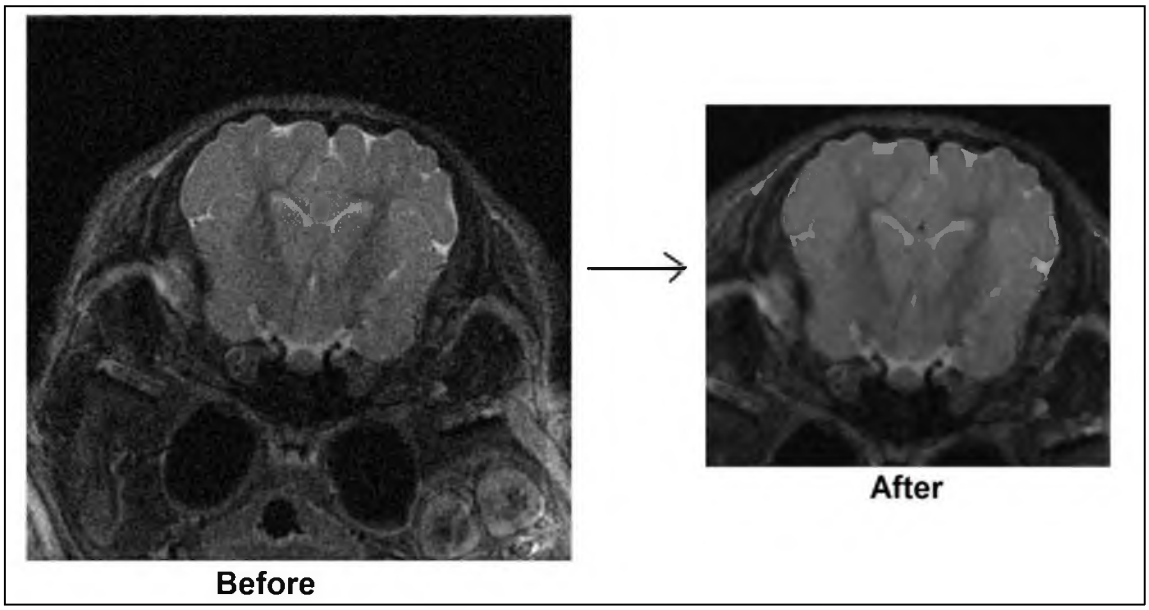

Figure 37: A representative frame of a T2-RARE image before and after the scaling and denoising protocol was performed.

Table 19: Anatomical locations of the four user-selected regions of interest as well as the whole-brain analysis region.

Region	Anatomical Description
I	Occipital meeting of the tentorial and falcine sinuses near the cerebellum.
II	Lateral cerebral fissures at the level of the internal capsule.
III	Parafalcine sulci just lateral to the falx. At a level just caudal to the ocular orbit.
IV	Parafalcine sulcus at the level of the eyes.
Whole Brain	Starting from the most caudal frame of the cerebellum, the entire brain is circled up to the most rostral frame of the frontal lobes/olfactory bulbs is reached.

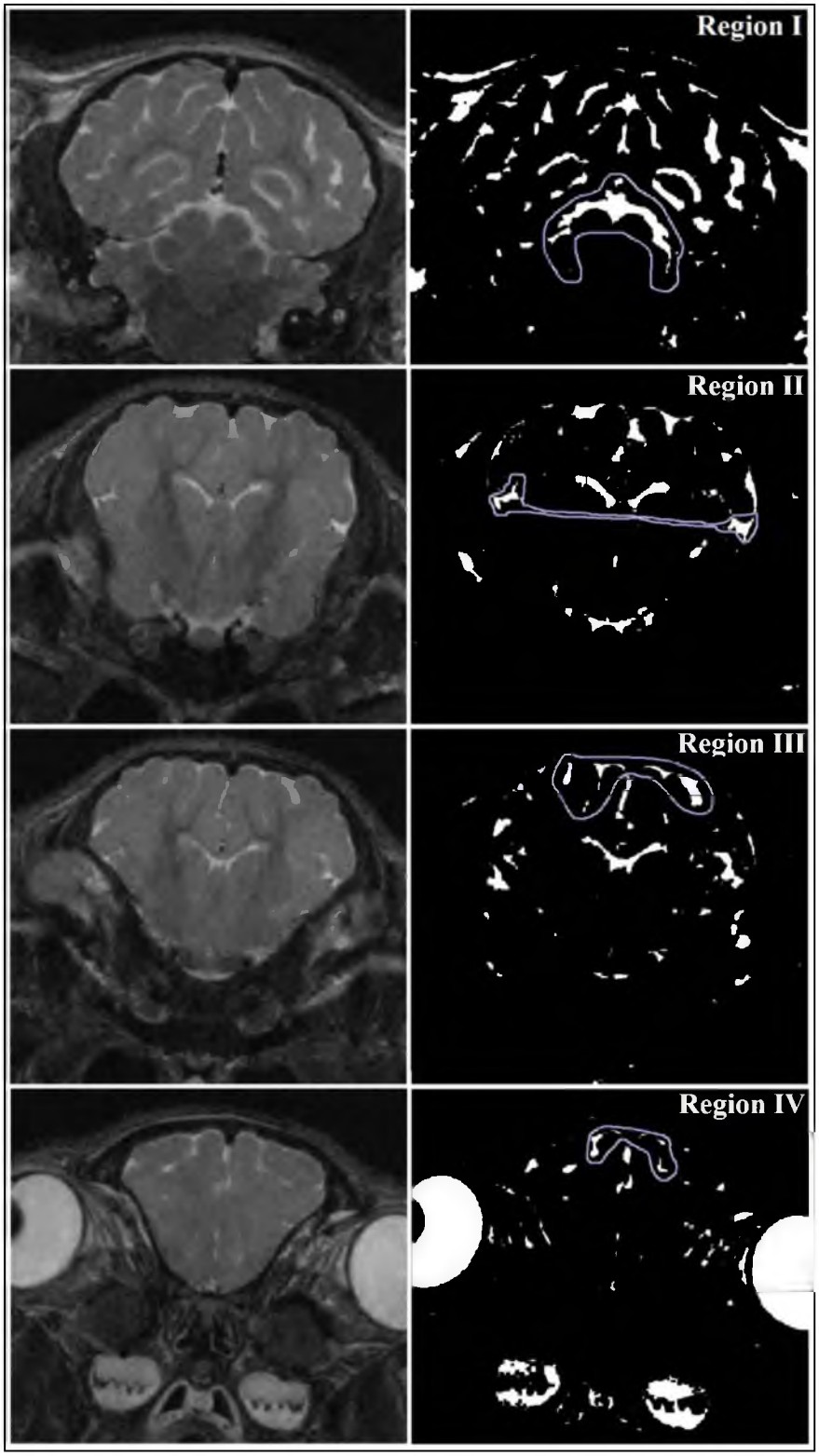

Figure 38: User-selected regions of interest: Region I – occipital meeting of the tentorial and falcine sinus, Region II – Lateral cerebral fissures at the level of the internal capsule, Region III – Parafalcine sulci at just caudal to ocular orbit, Region IV – parafalcine sulci at the level of the eyes.

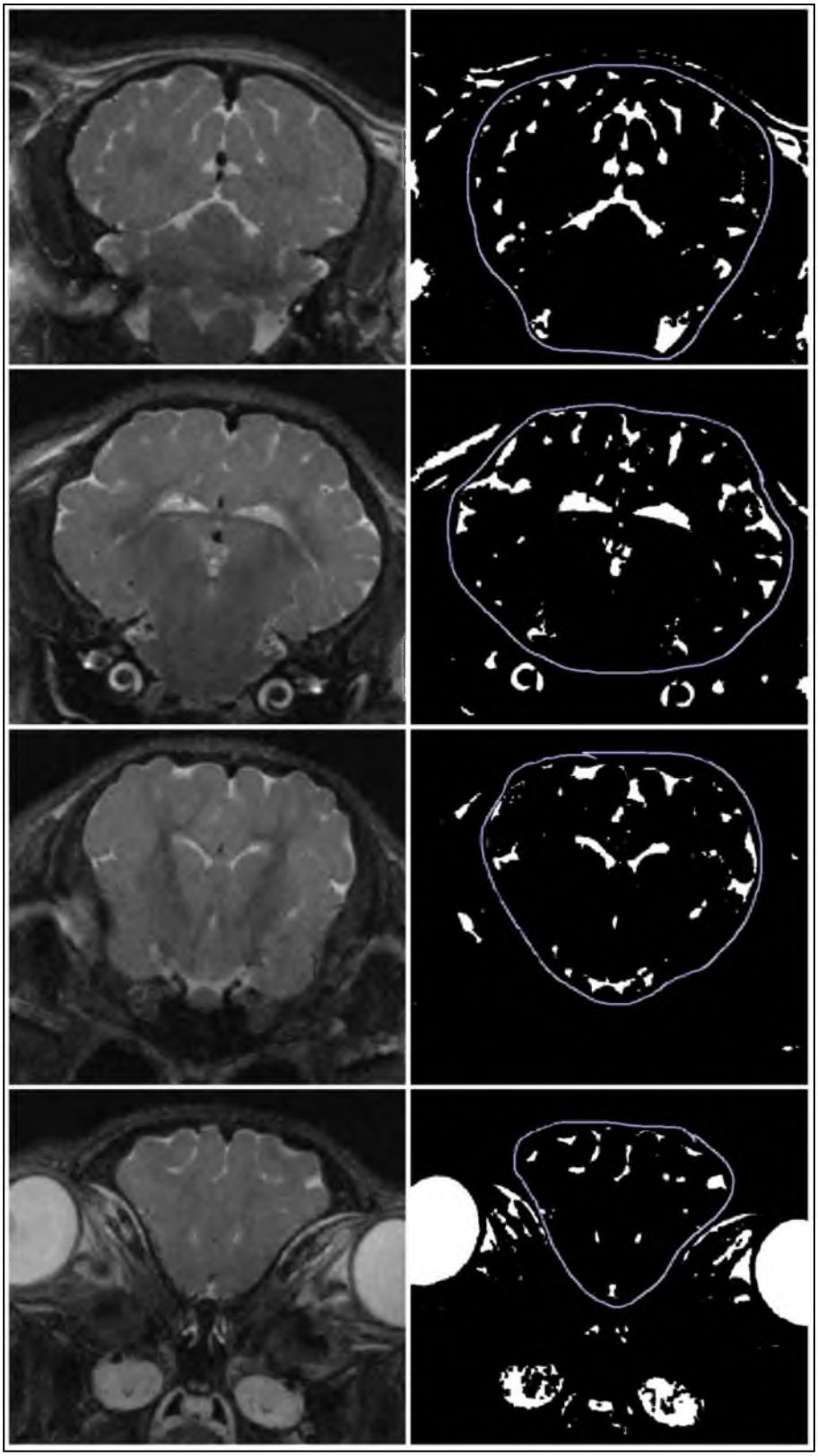

Figure 39: Four representative frames (rostral to caudal) of the whole-brain T2 analysis. The entire analyzed volume generally consisted of 24-28 total frames.

4.2.3 Phase Contrast Velocity Imaging of Cerebrospinal Fluid

Phase contrast velocity MRI has been proven as a robust method of measuring CSF velocity in cerebral aqueducts and ventricular cavities (see review by Wagshul et al. [112]). Traditionally, CSF flow studies have focused on two aspects, the total flow volume through the ROI (commonly termed stroke volume) and the CSF flow waveform (amplitude and phase are commonly discussed parameters). For our study, stroke volume and maximum stroke velocity amplitude were analyzed in lateral ventricles and subarachnoid space to see if PAC damage caused any changes in flow dynamics of the CSF.

To quantify CSF flow parameters, a MATLAB algorithm was employed which allowed the user to view the magnitude images of the phase contrast scans and trace over them (Appendix E.2). The user was instructed to trace a known piece of static "no flow" tissue (in our case the thalamic region of the brain) and then trace a ROI of CSF. Four total ROIs were analyzed: the left and right lateral ventricles, and the left and right subarachnoid space from the level of the lateral fissures to the superior sagittal sinus. The program then averaged the velocities contained within the static tissue (noise), and subtracted it from the velocities in the ROI. The stroke volume was defined as the sum of the velocities in the ROI over time, multiplied by the area of the ROI. The aggregate velocity waveform for the ROI was also plotted. Figure 40 shows an example of the measurement regions overlayed on the magnitude image of the scan (left), as well as a typical graph of the aggregate sum of velocities in the ROI (right).

MRI scans required identical resolution in order to be compared because the calculation of stroke volume and velocity is dependent on the dynamic range of the scan

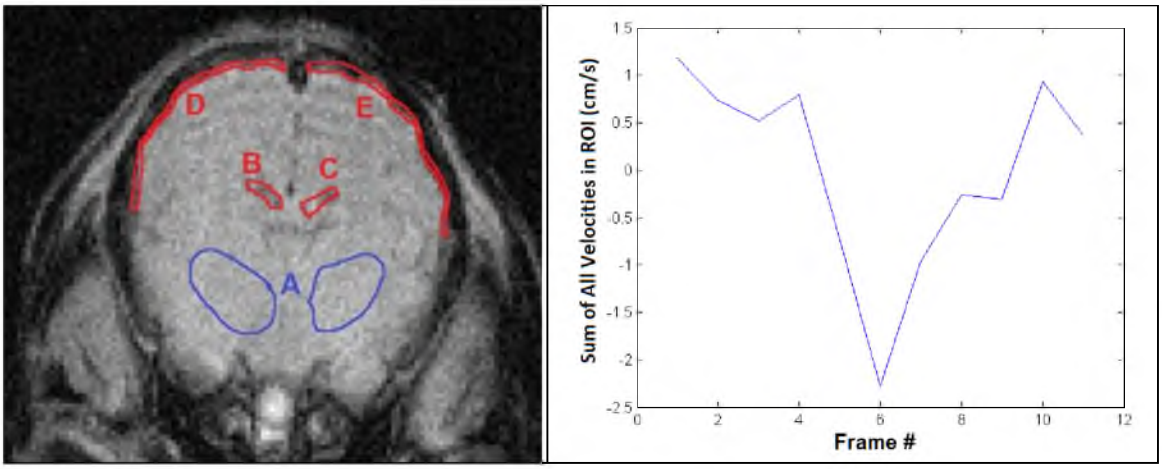

Figure 40: Measurement regions for CSF flow analysis (left). The user first selects a static region of tissue (A), then selects one of 4 regions of interest: left lateral ventricle (B), right lateral ventricle (C), left subarachnoid space (D), right subarachnoid space (E). The analysis program outputs the stroke volume and the aggregate velocity waveform of all sampled velocities in the ROI (right).

Table 20: Phase Contrast Velocity Imaging Scan Settings

Parameter	***Value***
T_R (Repetition Time, ms)	7
T_E (Echo Time, ms)	14.8150
Acquisition Size (pixels)	128 by 128
Number of Spatial Frames	11
Resolution (mm/pixel)	0.1953 by 0.2734
Dynamic Range (V_{enc}, cm/s)	0.5915

(known as V_{enc} in most MRI machines). The six best quality scans (representing animals P14-001, P14-002, and P14-007 pre- and postinjury) with identical dynamic ranges were chosen for the analysis (Scan parameters presented in Table 20).

Two separate operators measured each region of interest in each animal, before and after injury. The images obtained were substantially affected by noise, so measurements taken were highly variable. Therefore, each operator would measure the same area three separate times, and an average of the measurements was treated as the true value.

The regions of interest were selected with a freeform drawing tool and the relative size of the regions changed between operator and between measurements. To obtain consistent and comparable measures across operators, the stroke volumes were normalized by the selected area. Since the velocity waveform plotted by the program output an aggregate velocity of each pixel in the ROI, this value had to be divided by the selected area as well, resulting in an averaged peak velocity value. Paired student's t-tests were performed to identify significant differences between operators. These paired t-tests showed a significant difference as discussed in Section 4.3.2, as such further statistical analyses were conducted on each operator's dataset separately. A two-way ANOVA separated by operator was then performed to determine if there was symmetry between the results in the left and right hemispheres and if there was differences between pre- and postinjury.

4.2.4 FLASH MRI Cine Scans of Coronal Head Rotations

FLASH (Fast Low Angle SHot) MRI cine scans are able to reconstruct multiple frames captured of a periodic repeatable motion (such as a cardiac cycle) [113] similar to the Tagged MRI imaging studies conducted in humans [106]. We aimed to utilize these FLASH cine scans to visualize the motion of the porcine brain during a noninjurious, angular deceleration in the coronal plane. These decelerations were used as an evaluation tool for brain-skull displacement and should not be confused with the injurious, axial rotations described previously in section 4.2.1. This imaging sequence would test the hypothesis that damage to the PAC would decrease the tethering of the brain to the skull and result in more brain-skull displacement upon impact than without the damage.

A repeatable angular deceleration of the head needed to be produced for the FLASH cine scan imaging sequences to be performed and brain/skull displacements to be measured. Drawing inspiration from similar devices built for human studies of linear and angular deceleration of the head [105-107], a custom bed was designed (Figure 41 and Figure 42). The bed's overall dimensions were designed to fit a Bruker BioSpec 7.1T MRI equipped with a 150mm volume coil. Generally, the smaller the volume coil used in MRI, the better the signal-to-noise ratio, which results in better resolution. This volume coil was the smallest available coil that still allowed for a piglet's body to fit into the MRI. All components were machined out of MR-Safe plastics. Care was taken to only use new tooling or tooling which had not been previously used on metallic materials, in order to ensure MR-unsafe materials were not embedded in the components during machining. Complex geometries unable to be machined were manufactured with a 3D printer out of ABS plastic.

Repeatable coronal head rotations were achieved via pneumatic actuation of an air-piston driven rack and pinion device (Figure 41). As one piston is pressurized (A), the rack turns the pinion gear (B), which is rigidly attached to a shaft (C) supported by a ball-bearing (D). On the other side of this bearing, the shaft is rigidly coupled with a biteplate (E). The animal's snout was securely attached to the biteplate via over-the-snout clamps (F). During actuation, the shaft is free to rotate until the biteplate comes into contact with a stopper (G), which arrests the motion and causes a rapid angular deceleration of the head. This stopper was padded with foam to allow for the rapid deceleration of motion to lie beneath injury thresholds. During the other imaging sequences, the biteplate was simply a stationary restraint, with no actuation. The pneumatic actuation was controlled

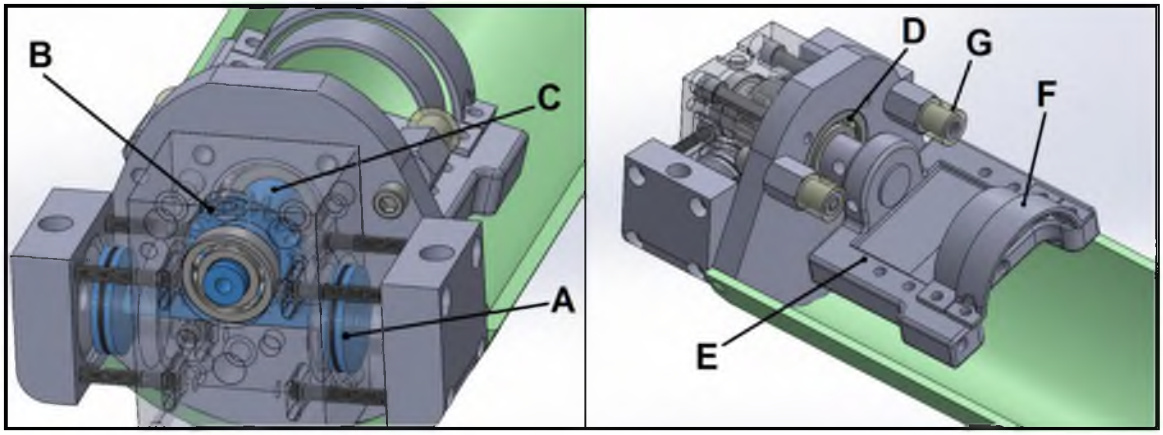

Figure 41: CAD model rendering of the custom MRI bed. As one piston (A) is pressurized, the rack turns the pinion gear (B), which is rigidly attached to a shaft (C) supported by a ball-bearing (D). The shaft is rigidly coupled with a biteplate (E) to which the animal is attached with over-the-snout clamps (F). Motion is arrested with the stopper (G), creating angular deceleration.

with a dual-action pneumatic solenoid and triggered by an Arduino Uno R3 micro-controller (Figure 42). Pressure was regulated with a 0-120 psi rated pressure regulator.

Actuation pressure and timing, as well as compliance of the foam stoppers, were iteratively changed until an acceptable level of head deceleration was obtained. The target levels of deceleration were based on studies which measured angular head accelerations during heading of a soccer ball (978-1754 rad/s^2) [114]. These levels of acceleration were reported to be subinjurious, although there is some dispute over multiple repeated occurrences potentially having some mild effects. Applying the same angular acceleration as these studies would not produce similar brain deformation in piglets due to the smaller brains. It has been established in the literature that in order to produce comparable injury in an animal, the applied acceleration must be multiplied by a mass-scaling factor to account for the smaller mass (and subsequently, less inertia) of the animal's brain [93-94, 115-116]. The equations of scaling rotational acceleration are supplied in Equation 3 below, where α is rotational acceleration and m is brain mass.

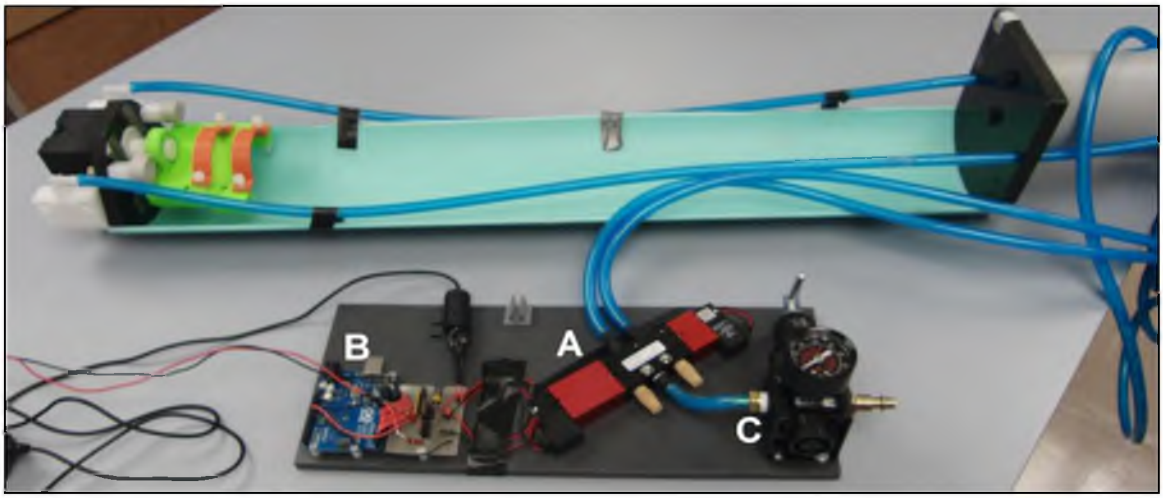

Figure 42: The completed custom MRI bed with pneumatic control panel. The pneumatic actuation was controlled with a dual-action pneumatic solenoid (A), triggered by an Arduino Uno R3 micro-controller (B). Pressure was regulated with a 0-120psi range pressure regulator (C).

$$\alpha_{piglet} = (\alpha_{human})\left(\frac{m_{human}}{m_{piglet}}\right)^{\frac{2}{3}} \quad \text{Eq. [3]}$$

For our calculations, we assumed a human brain mass of 1300g (the low end of the commonly accepted 1300-1400g range, [117]), and a piglet brain mass of 51.21g (the maximum weight of a series of 3-5-day-old piglet brains measured in lab). These assumptions would result in the most conservative estimate of angular acceleration needed to result in injury. Applying these masses, and a target human angular acceleration of 1000 rad/s^2, an angular acceleration of 8,637 rad/s^2 was desired for the piglets. Multiple pressures and stopper materials were evaluated with a 400g mass (representative of an immature piglet head) attached to the biteplate to determine which configuration best matched our parameters. A pressure of 15 psi and a foam stopper approximately ¼" thick best approximated our target values with resulting maximum

angular velocities of ~30 rad/s and angular accelerations of ~8000 rad/s^2 (Figure 43).

In order to capture the rapid deceleration of the brain, temporal resolution of the scans had to be maximized. This is partly why FLASH cine scans were chosen over traditional tagged MRI. The temporal resolution was able to be as fine as 7.6 ms between frames, whereas a tagged MRI sequence with an x and y axis tagging grid only allowed as fine as 25 ms. Tagged MRI scans also could not track the entire coronal rotation (1.5 s) before the tags faded (at approximately 200 ms). Only one coronal slice of the brain was captured at the level of the ventricular horns. The addition of multiple slices of the brain would have decreased the temporal resolution (i.e., a 2-slice acquisition would have had a resolution of 14ms). The location of the slice was selected based on the direction of rotation of the animals head (coronal) and the presence of a fairly large and visible subarachnoid space, and that it was closer to the application of the deceleration (the biteplate). Additional parameters were iteratively refined by the MRI engineer over the course of the study. A summary of the final parameters used in the two animals discussed in this section (P14-006, P14-007) is presented in Table 21.

In order to extract displacement data from the images, some postprocessing and image registration was required. Utilizing in-house protocols already developed by the University of Utah Small Animal Imaging Core, the scans were cropped spatially and temporally, denoised, and had imaging artifacts removed when possible. Afterwards, the scans were registered utilizing a nonrigid registration algorithm known as the "Demons Algorithm" first proposed by Thirion [118]. The algorithm is computationally fast and allows for more accurate measurement of large deformations. The algorithm introduces forces (demons) that push the points according to the behavior of fluid diffusion [119].

The algorithm falls short, however, in images with materials with large differences in stiffness, as it applies the same diffusion parameters to all tissues. This would over predict deformations in stiffer materials (bone) and under predict in softer materials brain). Nonetheless, the algorithm provides a quick and robust method for measuring the motion of any point within our scans in an automated fashion. The user's only input is that of selecting the starting points for the program to track.

Since the target result of this imaging modality was brain-skull displacement, tracking points were placed on the skull and brain in pairs. Each pair would have its displacement extracted, and the skull displacement would be subtracted from the brain displacement, leaving only the relative displacement between the two. Seven total pairs were seeded onto the images; these pairs were easily identified by anatomical features, ensuring repeatability between scans. The pairs were located at the following locations: the leftmost and rightmost lateral point of the brain/skull (1 & 5), the maximum point of curvature on a gyrus halfway between the previous points and the center axis of the brain (2 & 4), the superior sagittal sinus (3), and the left and right basilar surfaces of the brain, just medial to the brainstem (6 & 7) (Figure 44).

After the points were selected, the program was allowed to run across all time frames. The program output a trace over the image of the incremental displacements between each frame (Figure 45) and saved them to a data table, these displacements were collected and analyzed in an Excel (2013, Microsoft Corporation) spreadsheet. At this point, the incremental displacements were added together to create absolute displacements, and the brain and skull displacements were subtracted to yield relative brain-skull displacement.

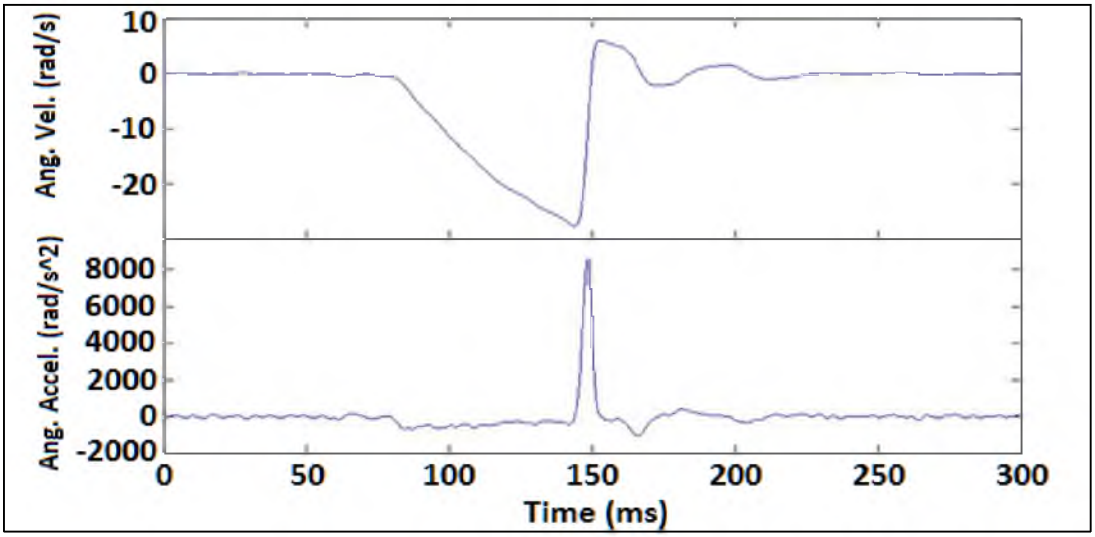

Figure 43: Example of an angular velocity and acceleration curve measured from the device when driven by 15 psi and utilizing ¼" thick foam stopper.

Table 21: FLASH Cine Scan Imaging Parameters

Parameter	***Value***
T_R (Repetition Time, ms)	7.59964 (temporal resolution)
T_E (Echo Time, ms)	2.94012
Acquisition Size (pixels)	128x128
Spatial Resolution (mm/pixel)	0.7x0.7
Slice Thickness (mm)	4
Number of Averages	6
Flip Angle (FA)	20°

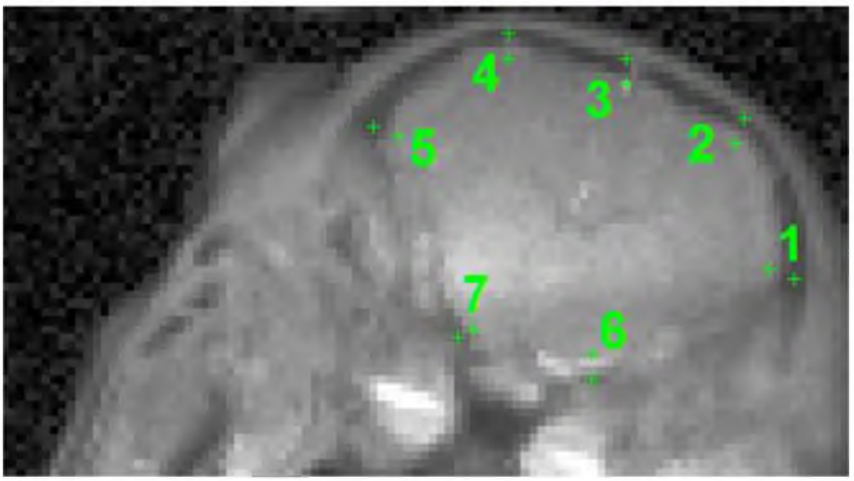

Figure 44: First frame of a representative FLASH cine scan with the 7 paired brain and skull seed points for deformation analysis.

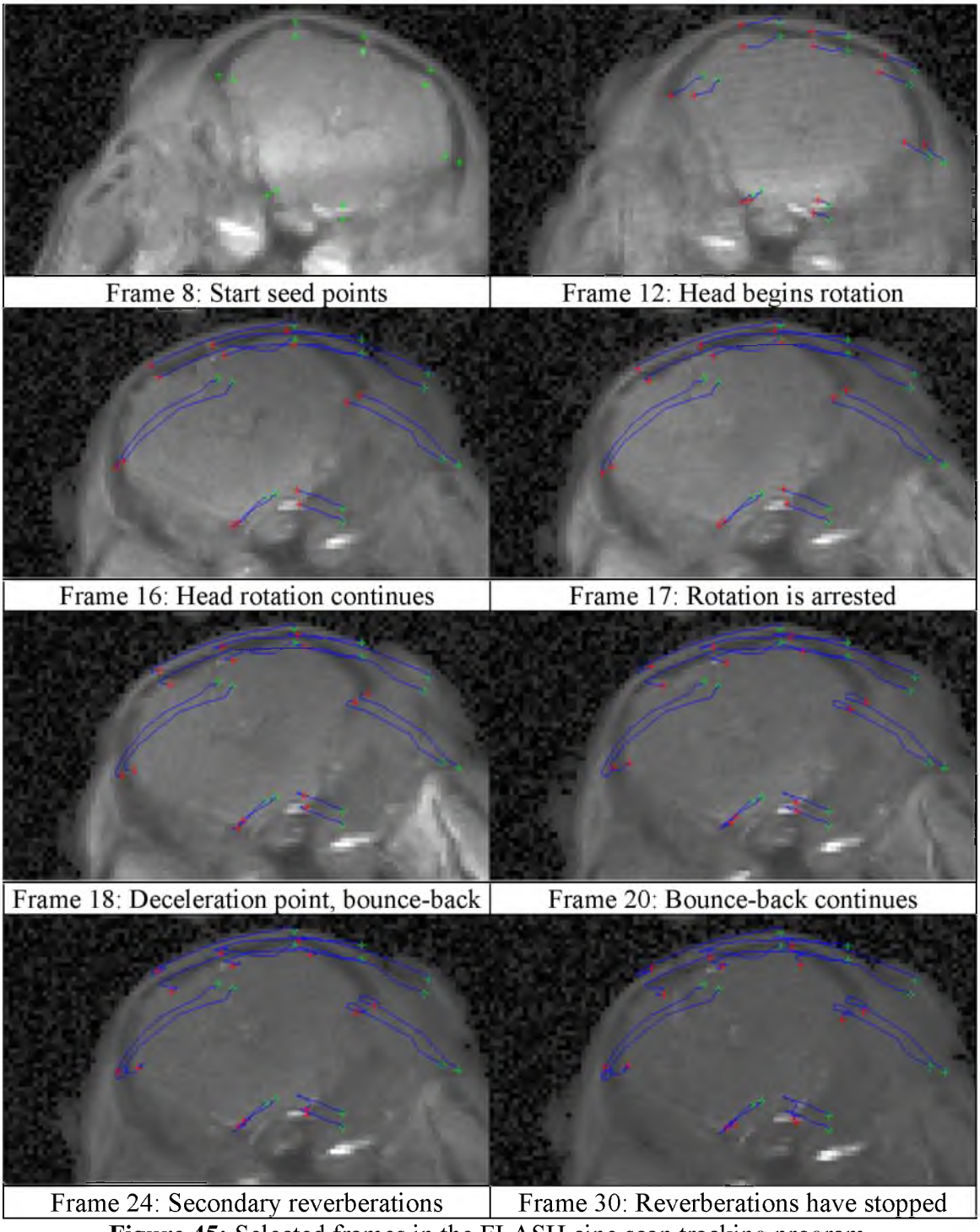

Figure 45: Selected frames in the FLASH cine scan tracking program.

4.2.5 Postmortem Optical Coherence Tomography Imaging

Twenty-four hours after injury, all animals were euthanized and perfusion fixed according to the same methods utilized on our noninjury animals in Chapter 1, and optical coherence tomography of the PAC was performed. The imaging and postprocessing was performed following the exact same protocol detailed in Chapter 1. A one-way ANOVA was conducted comparing the injured animals and control animals to see if any differences in PAC volume fraction were observed. Two of the animals analyzed had the PAC reinflated successfully, while no inflation was attempted in the others. Comparisons were primarily made among uninflated brains; however, if inflated brains were included, the comparison was only made on normalized volume fractions.

4.3 Results

4.3.1 T2-Weighted Imaging

No signs of gross injury were found after qualitative visual examination of all image volumes for four of the five piglets (animal P13-110 was excluded due to low scan resolution). The comparative study of CSF volume did not exhibit any clear statistically significant trends, indicating there was an increase or decrease in CSF volume in any of the subregions or of the whole brain (Figure 46). If one were to look at the individual results for each region, they can see that for region I, three of the four animals exhibit a clear increase in CSF volume postinjury. If one were to consider P14-007 as an outlier, this may highlight a trend potentially hidden by the currently low sample sizes.

Figure 47 shows the whole brain measurements across all frames, allowing a better view of any form of systematic trends along the rostral-caudal direction of the

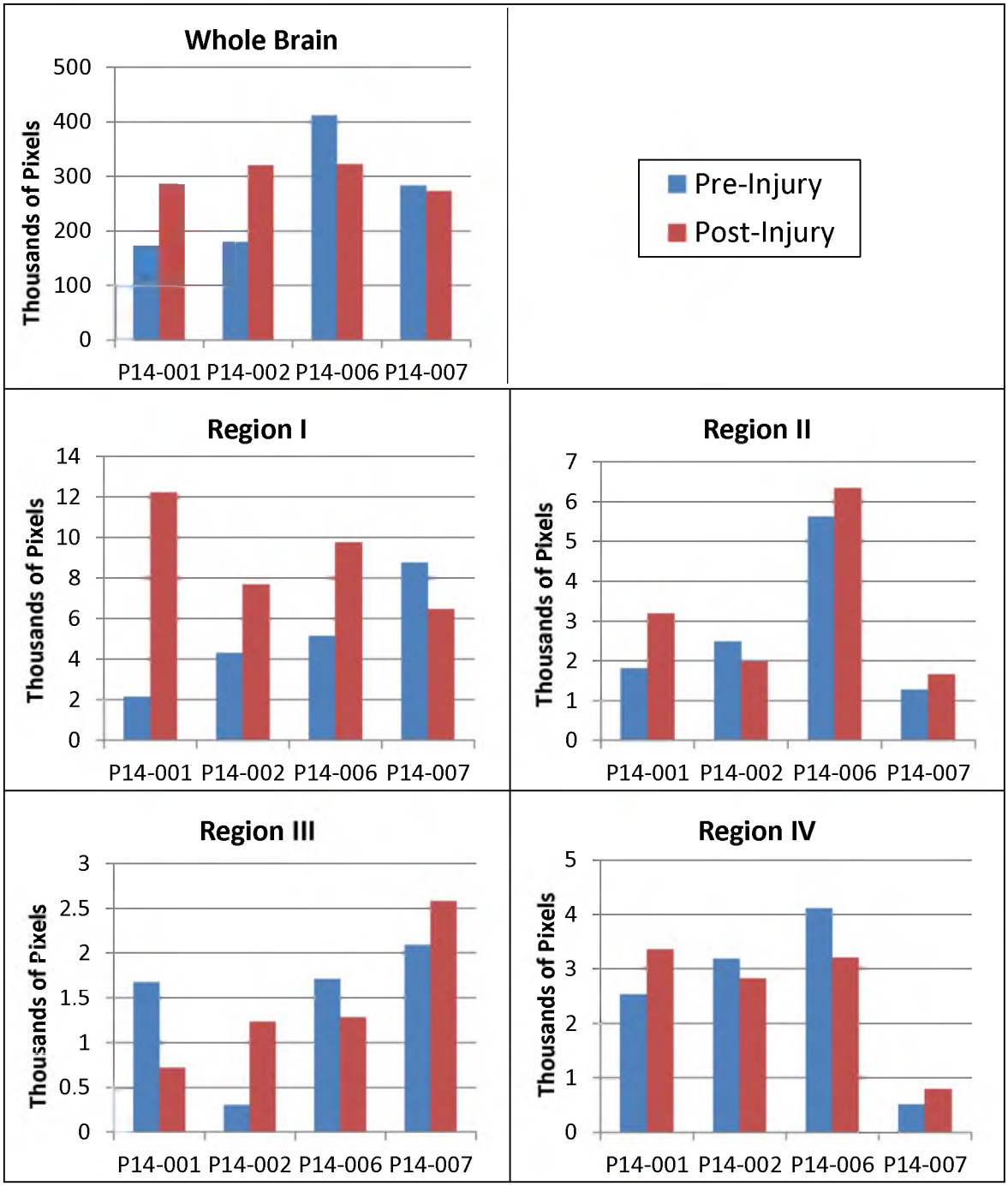

Figure 46: CSF pixel counts from quantitative T2 analysis

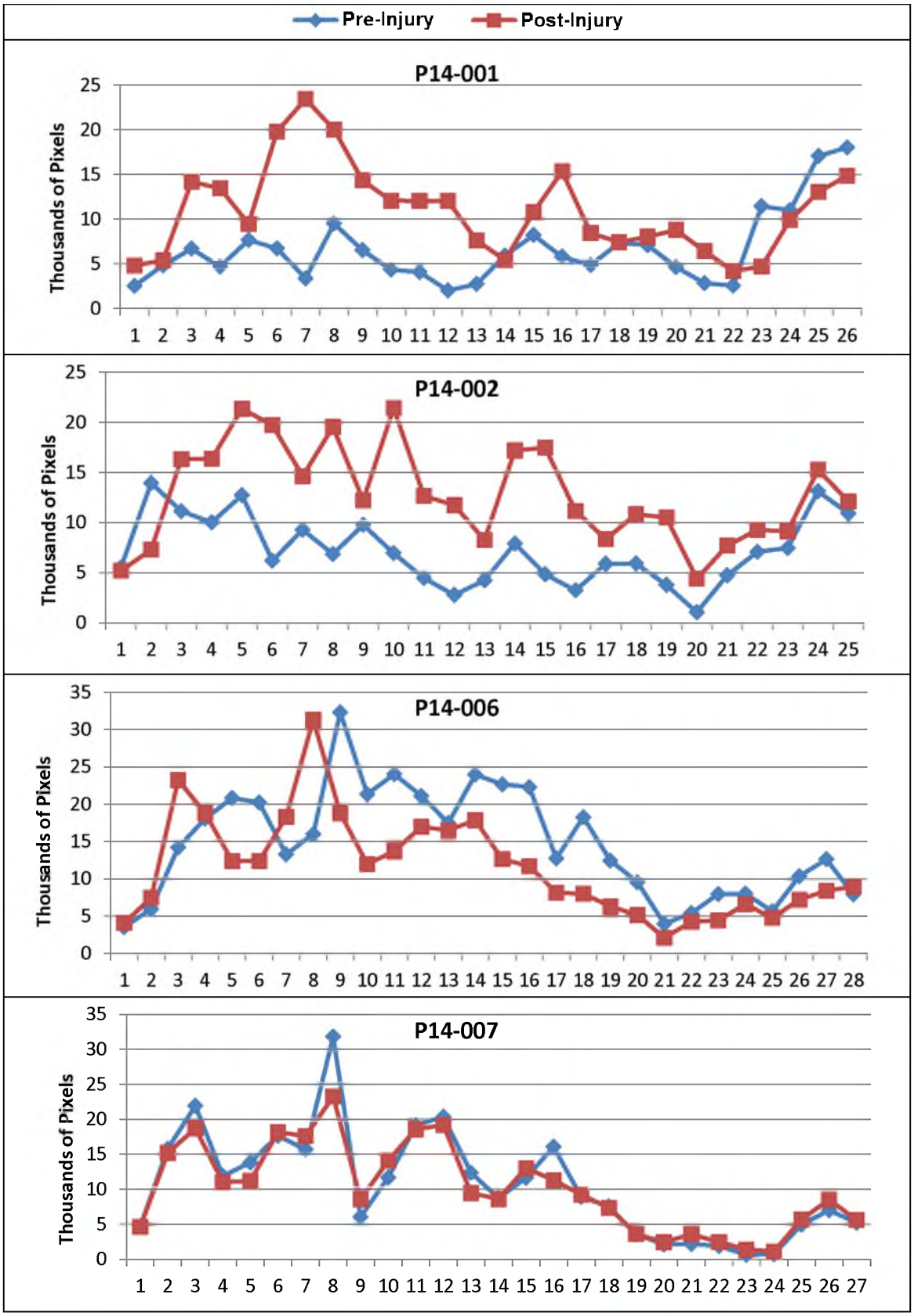

Figure 47: Frame by frame CSF pixel measurements across each brain (caudal to rostral)

brain. There is a clear increase in postinjury CSF volume in animals P14-001 and P14-002, but this may be an artifact of the scan resolution. Pre-injury scans in both of these animals were only averaged twice and the postinjury scans were averaged 6 times. The lower averaging results in a loss of fine detail, and the smaller CSF spaces were likely missed. Animals P14-006 and P14-007 had identical scan parameters and did not exhibit any clear trends.

4.3.2 Phase Contrast Velocity Imaging of Cerebrospinal Fluid

The paired t-test comparing means across operator showed significant differences in 2 of our 4 measured values, with operator 1 consistently measuring higher values than operator 2 in three of those values (Table 22). Due to the knowledge that there was significant difference between operators, subsequent statistics were performed on pre- and postinjury data but only within each operator's data set. A two-way ANOVA was conducted on the data, blocking by operator and comparing all possible pairings (pre- and postinjury, left and right, as well as the cross of these two). Table 23 presents the means and F-statistic for these tests, which showed no significant p-values for any pairings (with two exceptions). These exceptions were operator 2's lateral ventricle and subarachnoid space stroke volume measurements, which showed significant differences between left and right means.

Presented in Figures 50-53 are plots of the pre- and postinjury data collected for all animals. The data are separated by operator and hemisphere due to the findings of the previous statistical tests. Looking at the data on a case-by-case basis, a few potential trends appear. Across both operators, for both animals P14-001 and P14-002, the right

Table 22: Paired Student's t-test results for CSF flow measurement metrics.

Pairing	Measurement	Operator 1 Mean	Operator 2 Mean	P-Value
Op. 1/2	L.V. Stroke Vol.	5.56165	3.39952	0.0002*
Op. 1/2	SAS Stroke Vol.	1.53339	1.31703	0.2941
Op. 1/2	L.V. Avg. Vel.	0.29734	0.19401	0.0100*
Op. 1/2	SAS Avg. Vel.	0.07106	0.07575	0.4970

Table 23: Two-way ANOVA results for CSF flow measurement metrics. Asterisk indicates significant differences were found between left and right means, but no others.

Op	Measurement	Pre-injury Mean	Postinjury Mean	Left Mean	Right Mean	Prob. > F
Op. 1	L.V. Stroke Vol.	5.10192	6.02139	4.87875	6.24456	0.3595
Op. 1	SAS Stroke Vol.	1.22638	1.40768	1.41287	1.22119	0.5167
Op. 1	L.V. Avg. Vel.	0.27979	0.31488	0.26070	0.33399	0.6482
Op. 1	SAS Avg. Vel.	0.07196	0.07017	0.06611	0.07601	0.8188
Op. 2	L.V. Stroke Vol.	2.97599	3.82304	2.83459	3.96444	0.0997*
Op. 2	SAS Stroke Vol.	1.55323	1.51355	1.99057	1.07621	0.0420*
Op. 2	L.V. Avg. Vel.	0.21865	0.16937	0.16983	0.21818	0.5844
Op. 2	SAS Avg. Vel.	0.07025	0.08126	0.08422	0.06729	0.1098

side SAS stroke volume always increases postinjury. If P14-007 was an outlier, this could be a trend that may become amplified with the addition of more tests. When looking at lateral ventricle stroke volume, 9 of 12 of the comparisons show an increase after injury. For the lateral ventricle averaged peak velocity, all cases except the left hemisphere of P14-001 showed an increase in velocity. These two findings could also signify the beginning of a trend hidden by the currently small sample size. Small trends like these support the possibility that differences will be able to be seen in the data with larger sample sizes.

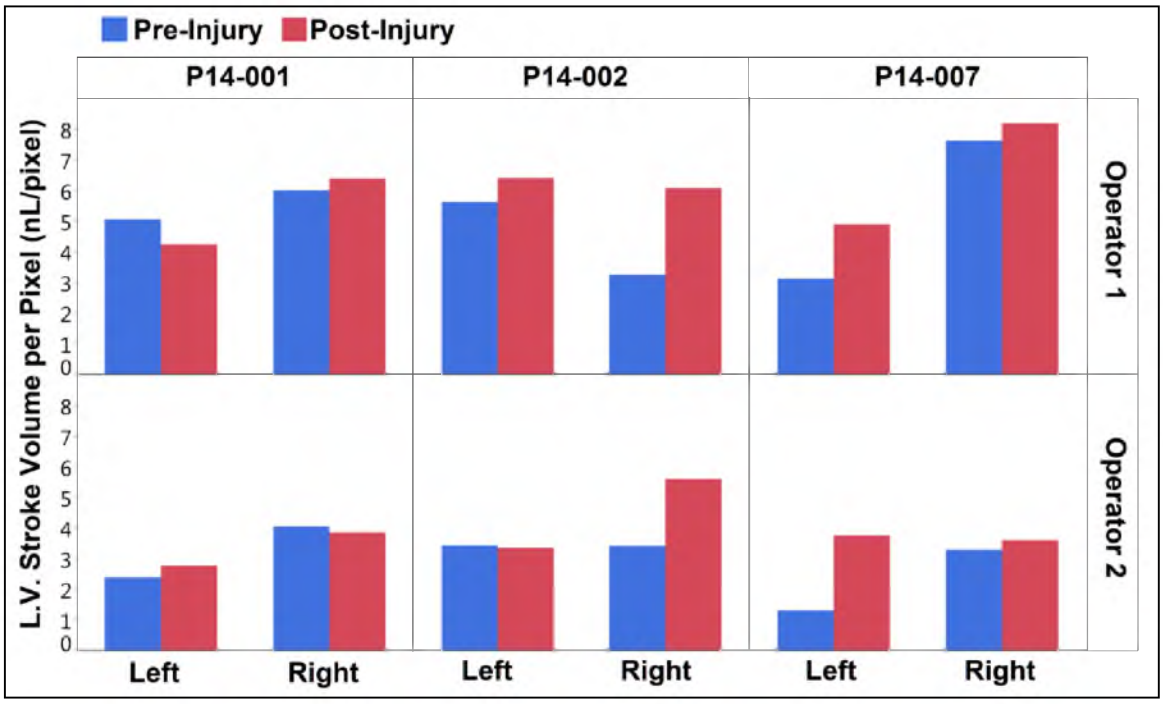

Figure 48: Lateral ventricle (LV) normalized stroke volume per pixel, pre- and postinjury.

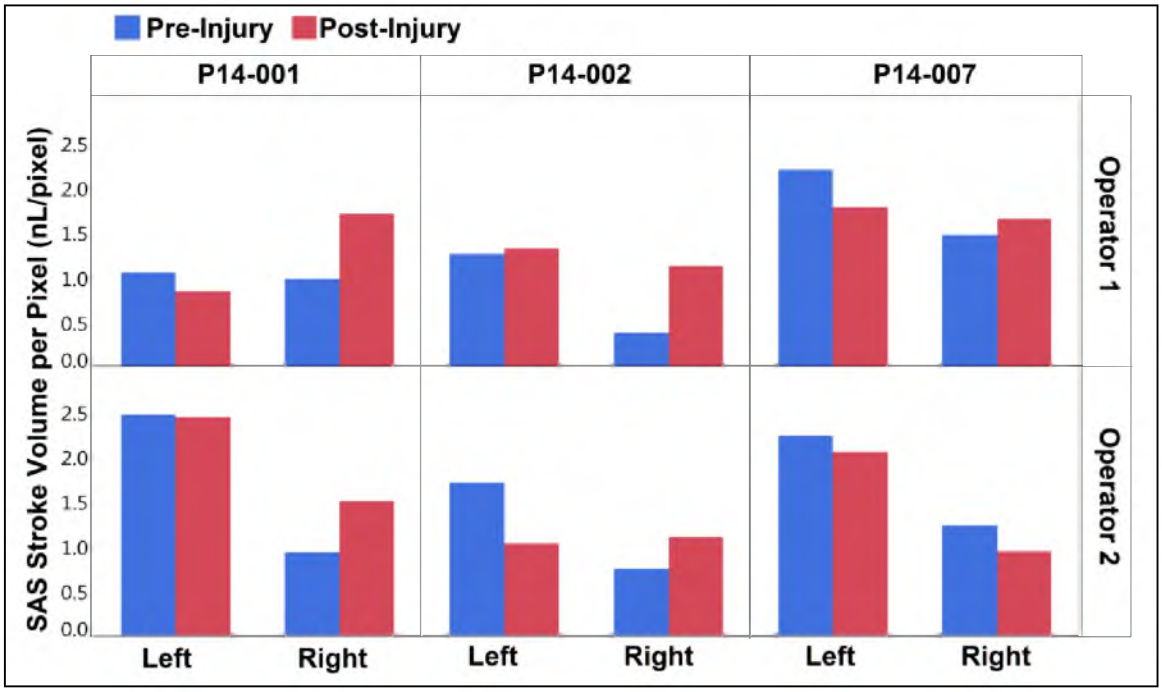

Figure 49: Subarachnoid space (SAS) normalized stroke volume per pixel, pre- and postinjury.

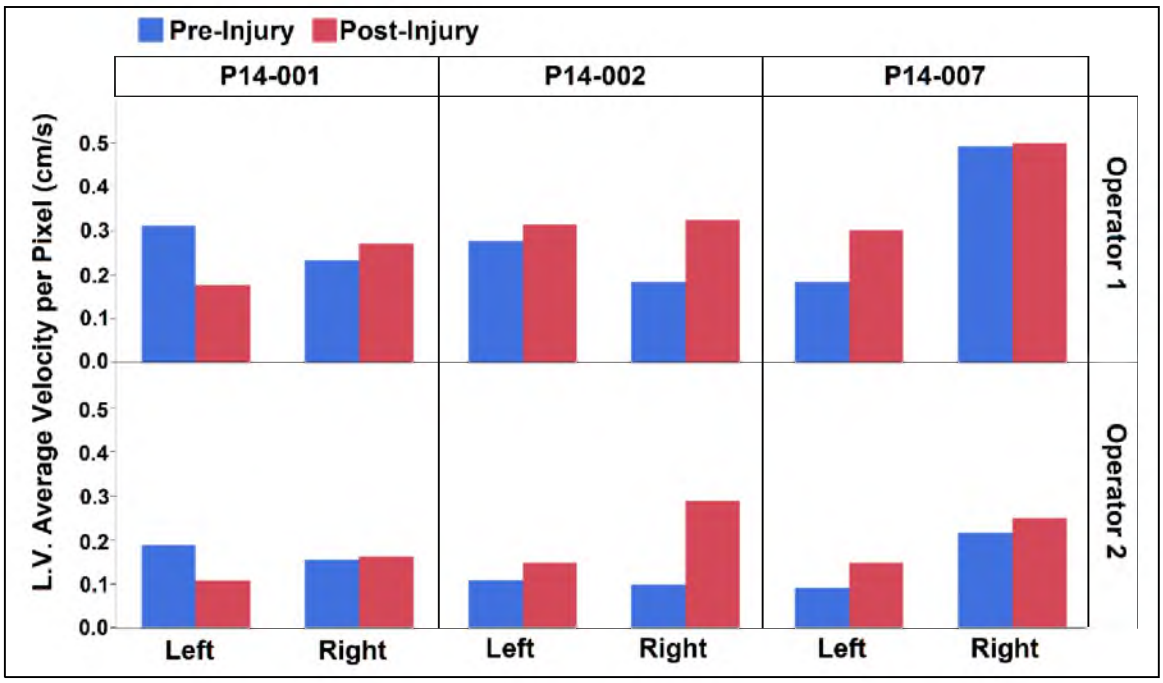

Figure 50: Lateral ventricle (LV) averaged peak velocity per pixel, pre- and postinjury.

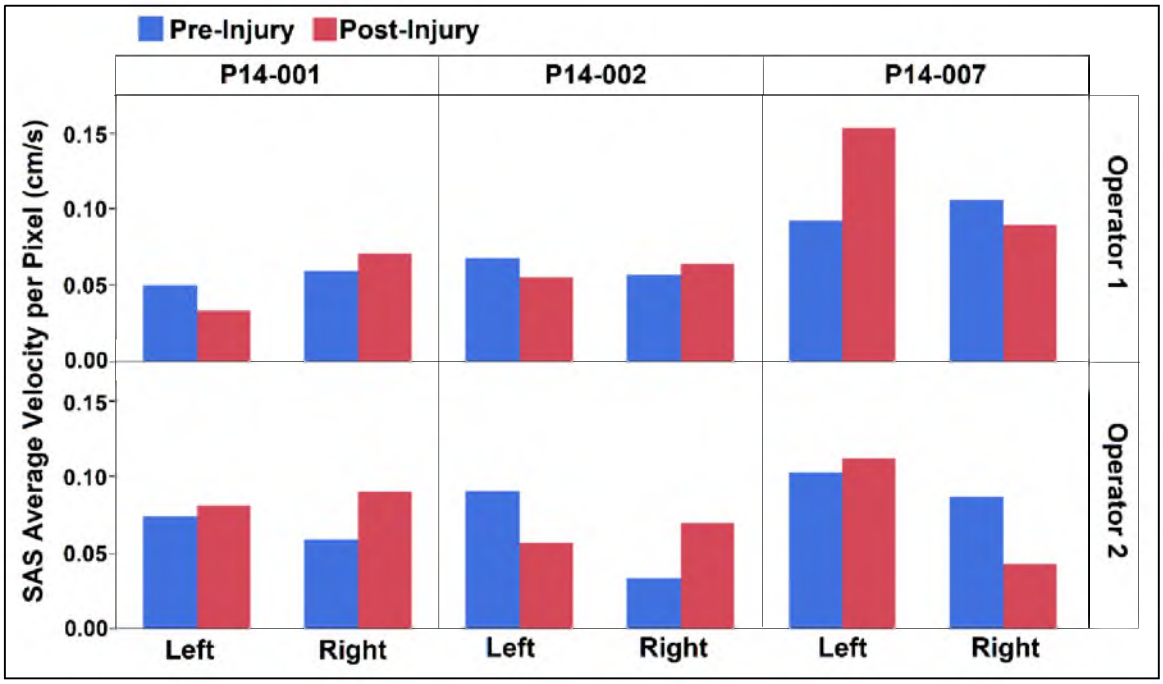

Figure 51: Subarachnoid space (SAS) averaged peak velocity per pixel, pre- and postinjury.

4.3.3 FLASH MRI Cine Scans of Coronal Head Rotations

The Demon's tracking algorithm was able to track the gross motion of the majority of the points seeded on the cortical surface of the brain, as well as the adjacent points on the skull (Figure 45). Some points on the brain drifted from their intended position due to motion blurring and noise. Since deleting these frames would remove all other good points, and corrupt their signal, the tracking was left unchanged and it was accepted that these few points would have inherent error.

The linear velocities of the skull nodes were extracted from this dataset in order to ensure the rotational device was indeed producing the intended rotational velocities and accelerations demonstrated during its tuning (Section 4.2.4). A peak linear velocity of 276 mm/s was measured at the skull point which experienced the maximum velocity values (in this case the point above the superior sagittal sinus). The distance to the center of rotation (just inferior to the brainstem/spinal cord) was estimated as 20.65mm by utilizing on-screen calipers within ImageJ (1.47v, National Institutes of Health, USA). These two values were utilized to calculate the angular velocity and acceleration profiles seen in Figure 52. The angular velocity data match our tuning data fairly well (with a similar peak of ~30 rad/s). However, the angular acceleration trace does not reach as high of a value as our tuning data (only ~3000 rad/s^2 of the expected ~8000 rad/s^2). It is suspected this is likely due to the much smaller temporal sampling of data points in these MRI images (7.6ms per frame) causing the peak deceleration point to be missed, resulting in a perceived lower value. Errors inherent to numerical differentiation may also be influencing this lower value. Additionally, the angular velocity curve reaches its maximum value (and hits the stopper) slightly sooner in the MRI measured data set than

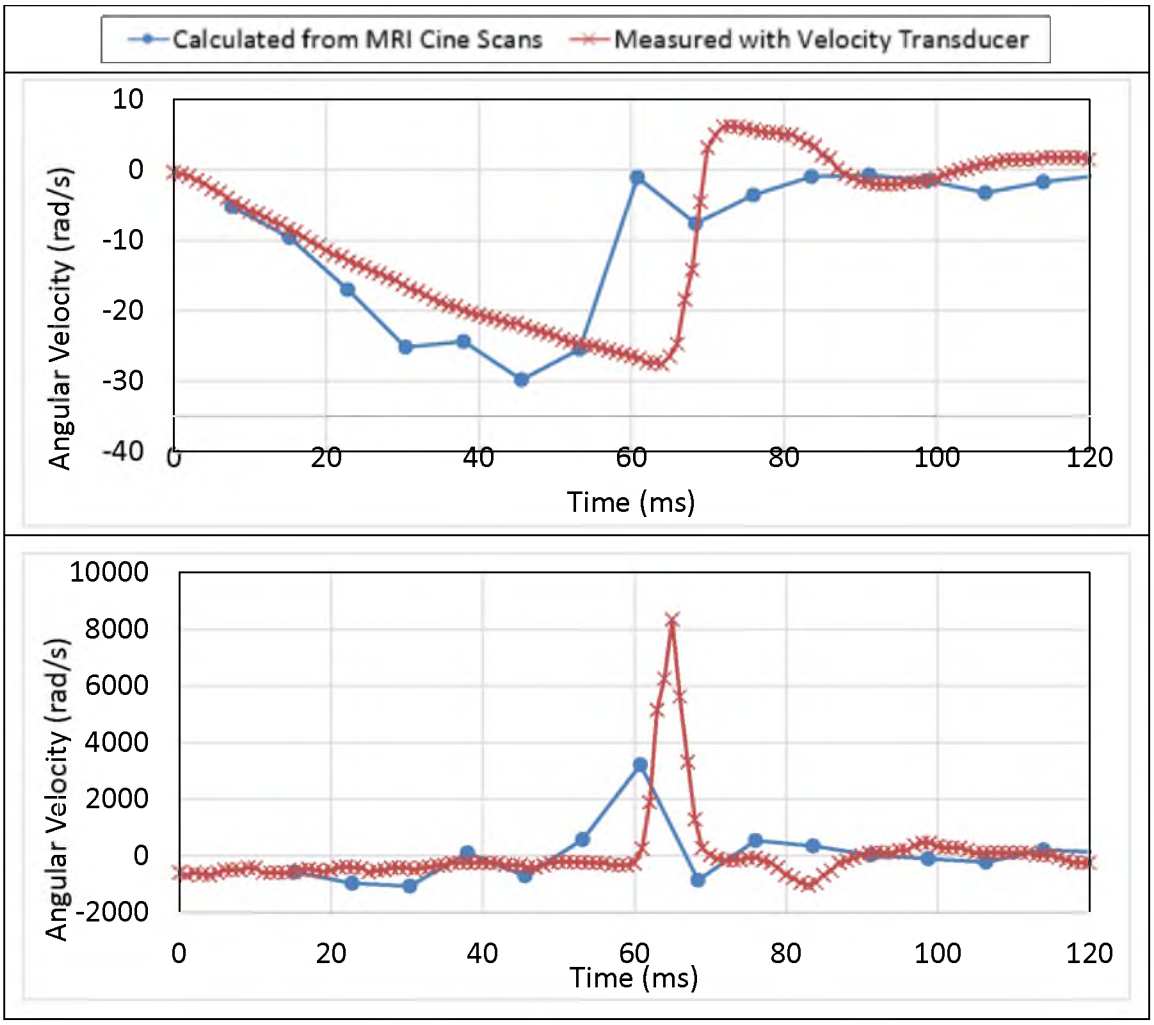

Figure 52: Angular velocity (top) and angular acceleration (bottom) curves calculated from linear velocity measurements taken from FLASH MRI Cine scans (blue) and measured directly when testing the device (red).

in the test with a static mass attached to the biteplate. This could be due to variations in air pressure from when the device was tuned and actually utilized, and due to the different weights and loading forces on the bite plate when actuating the device with a live animal versus a static mass. Regardless of these discrepancies, the overall trends of both curves and the durations of the deceleration impulses (~10 ms) match fairly well and indicate that the device appeared to be generating the proper applied angular velocities and accelerations as previously described in Section 4.2.4.

The behavior of all tracked points was as expected (Figure 53), with large displacements during the initial rotation, and a reversal of direction upon the point of impact (and thus deceleration). After the impact, there are subtle reverberations, which are either damped vibrations resulting from the impulsive deceleration, or noise. Some points exhibited some minor drift (i.e., the right lateral skull's Y-position in Figure 53), because the tracking algorithm falsely predicted motion after the system had come to rest.

Relative displacement between the brain and skull was calculated by subtracting the skull displacement from brain displacement within each paired point. The x and y data were then converted into a single magnitude of relative displacement per frame. The relative brain-skull displacement measured in animal P14-007 before injury is plotted in Figure 54, separated into left, right, and midline regions of the brain for better plot clarity. The same data are plotted for the animal after injury in Figure 55. Only one additional animal was processed (animal P14-006). The results are not presented because the dataset contained a lot of noise and resulted in artificial tracking of most of the points.

The largest brain-skull displacement in the pre-injury data occurred before impact, which is quite counter-intuitive. These peaks may be due to motion blurring during the pre-impact phases of motion. There are some peaks during the impact, but these peaks are near our resolution limits (all under 1 pixel, where each pixel represents 0.7mm). These peaks may therefore be influenced by noise or tracking issues. More definitive peaks were seen during impact for the postinjury scans. These peaks ranged from 0.535 - 1.260 mm with an average ± standard deviation of 0.853 ± 0.260 mm. These values are still close to the resolution limits. The gross deformation of the brain was as high as 30 pixels (~21 mm). This tells us that the images were of high enough quality to

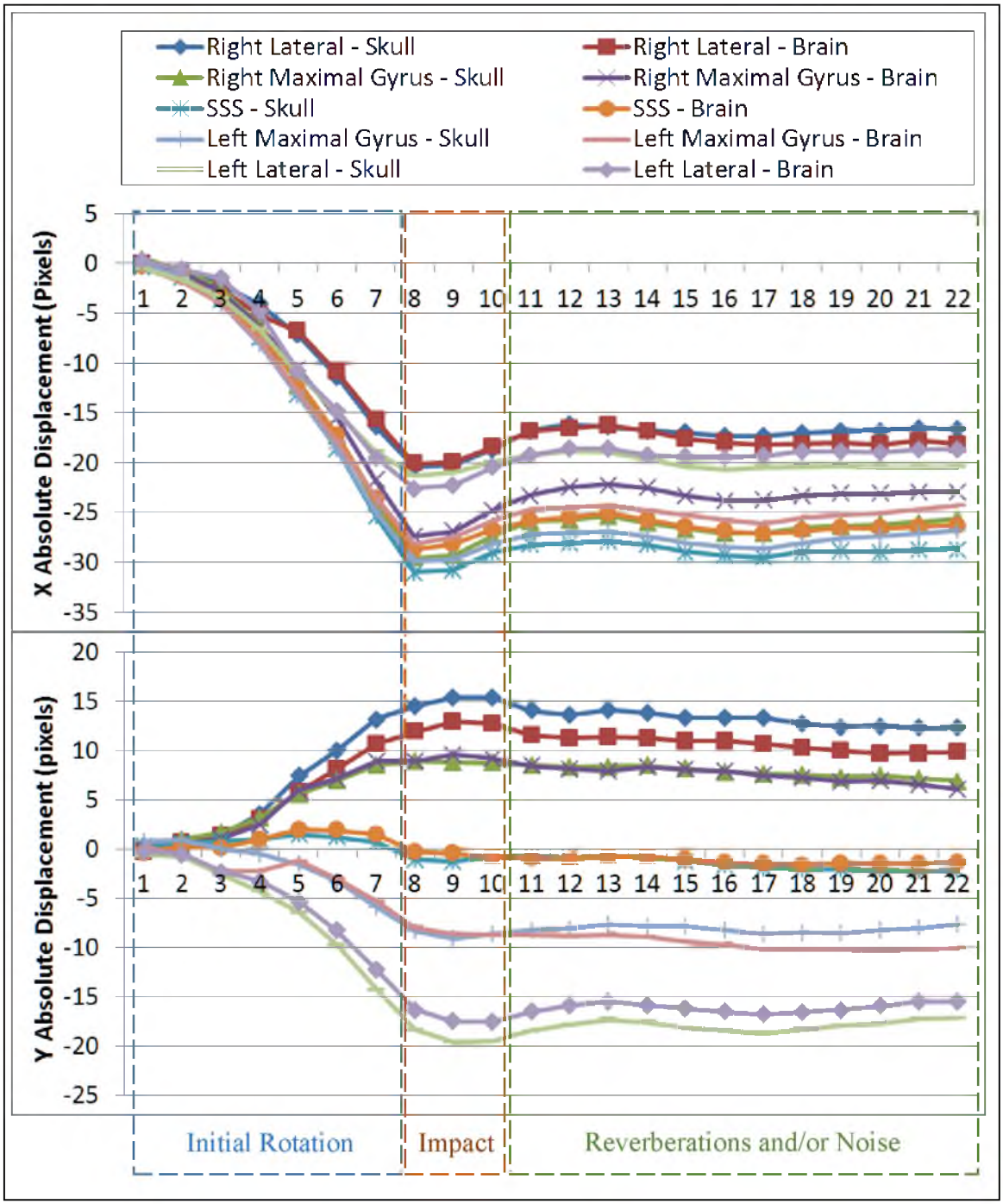

Figure 53: Total displacement of 5 pairs of brain and skull points for animal P14-007's pre-injury scan. The basal pair points are excluded for graph clarity, as they contained minimal deflection.

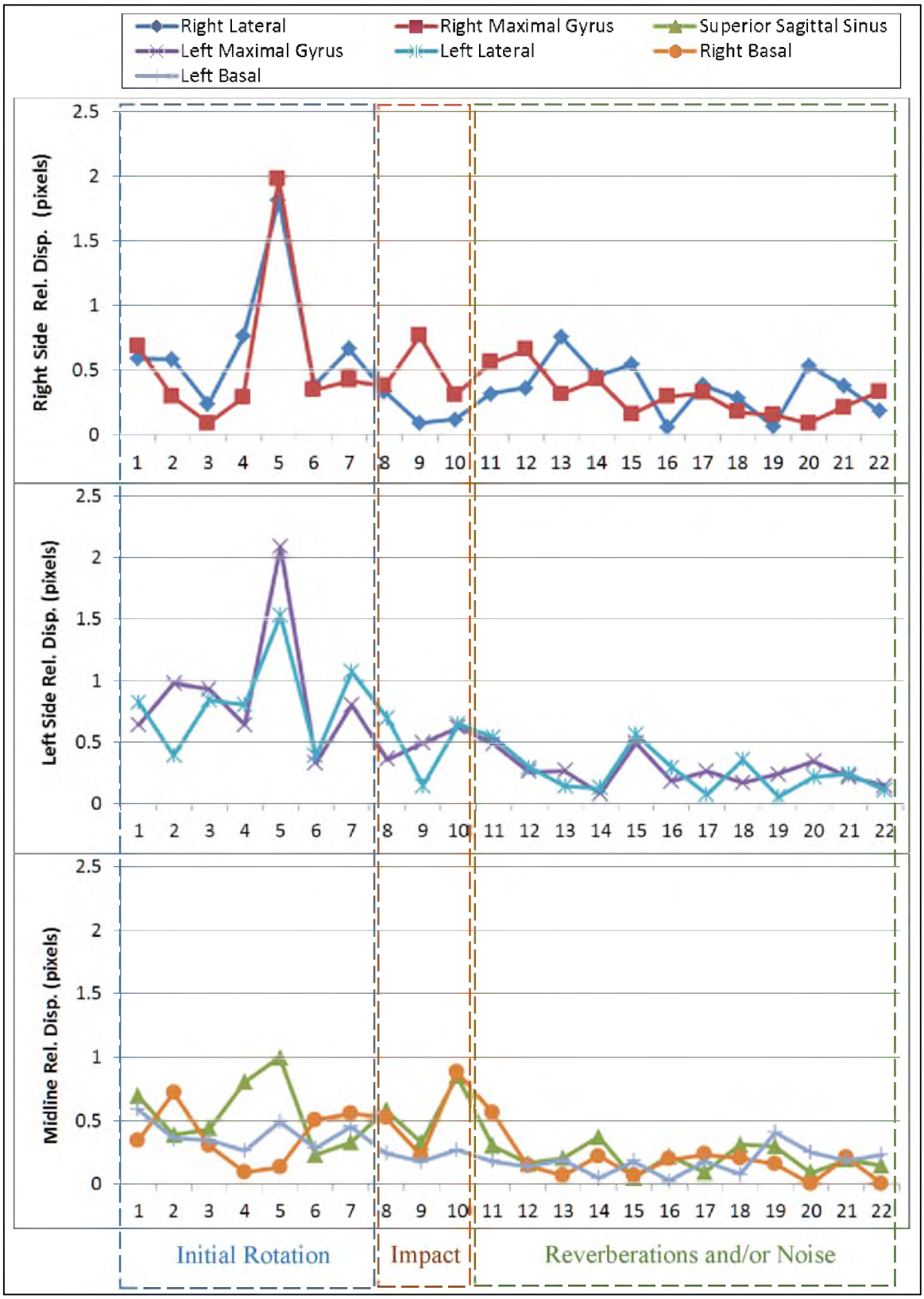

Figure 54: Relative brain-skull displacement for all 7 pairs of points. Data is from animal P14-007, pre-injury.

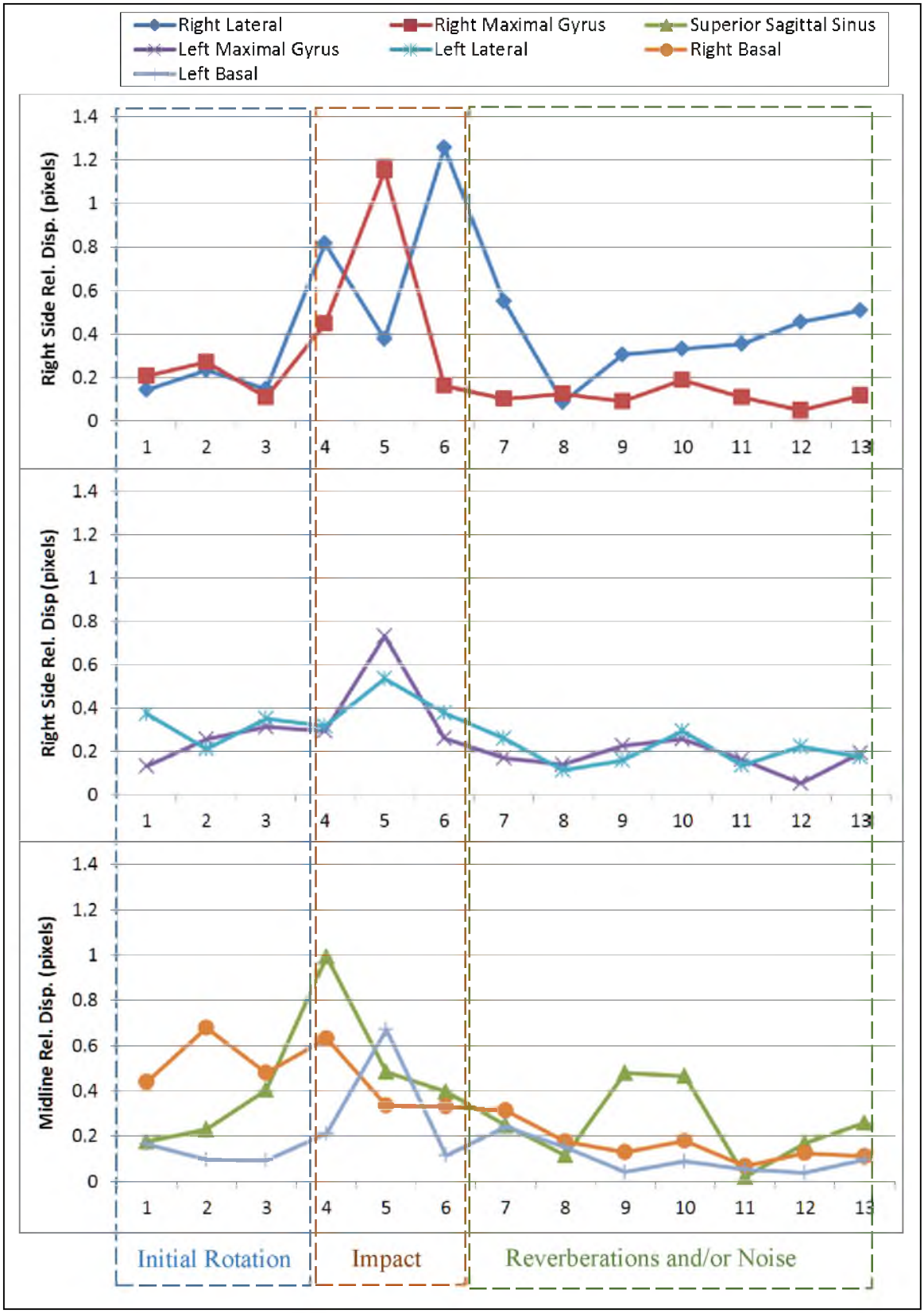

Figure 55: Relative brain-skull displacement for all 7 pairs of points. Data are from animal P14-007, postinjury.

measure gross displacement of the brain and skull, but were unable to confidently resolve brain-skull displacement. Higher resolution images will be required to increase confidence in differences between pre- and postinjury brain/skull displacement.

4.3.4 Effect of Induced Mild TBI on PAC Volume Fraction

No significant differences were discovered when comparing OCT-measured arachnoid trabeculae VF between injury and control animals (Figure 56 and Figure 57). As shown in Chapter 1, there is a large amount of variability within each animal. This large variability diminishes statistical power when grouping animals for evaluation. Furthermore, the sample size only includes 3 injured and 5 uninjured brains. Looking at the individual trends in Figure 57, there is a decrease in VF after injury in the LLO, RLP, and RMP subregions. This might be indicative of PAC injury since less AT are present.

4.4 Discussion

Correlating biomarkers that are MRI obtainable to PAC damage could benefit TBI research greatly. Invasive measurements that require surgery such as the OCT imaging presented in Chapter 1 provide insight into the microstructures of the PAC, but these measures could never be made *in-vivo* in a human population. The work presented in this chapter represents our attempt to find MRI modalities which correlate to PAC damage. Due to the small sample size of the pilot study, no significant conclusions can be made about any of these biomarkers; however, this should not downplay their potential impact. Several of the images had potentially relevant findings. Improvements in image resolution and sample size will clarify their potential as a clinical biomarker

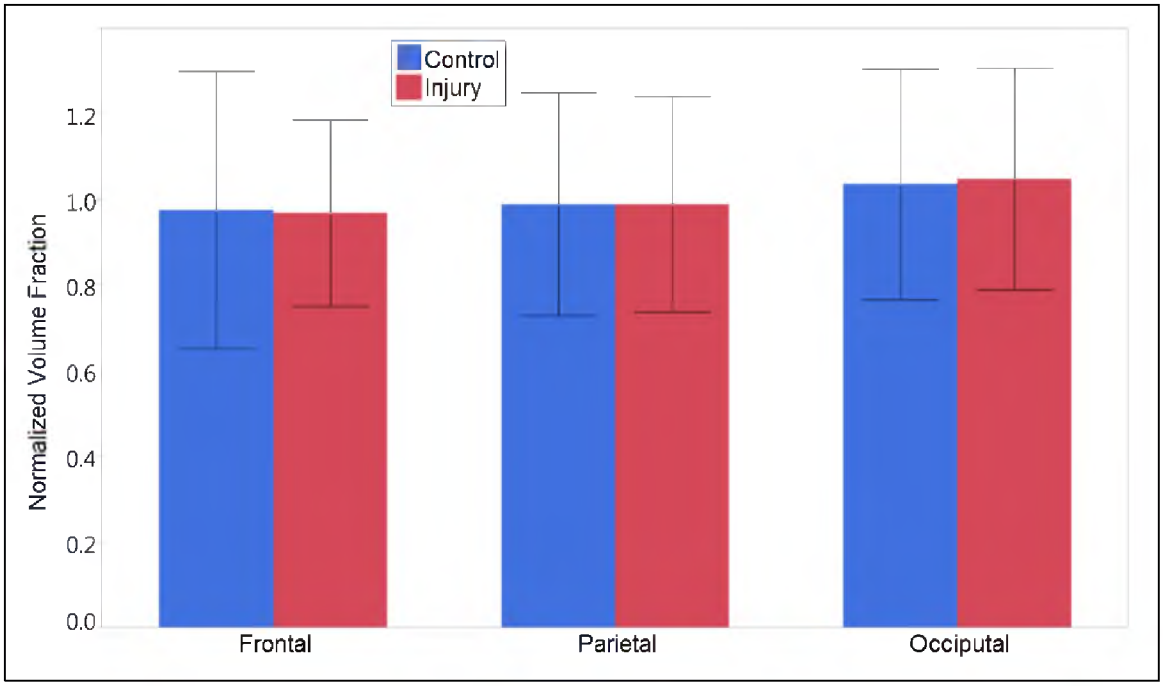

Figure 56: Means (with standard deviation) of the measured volume fractions in all uninflated control (N=5), and uninflated injury (N=3) brains, categorized by 3 major lobes of the brain.

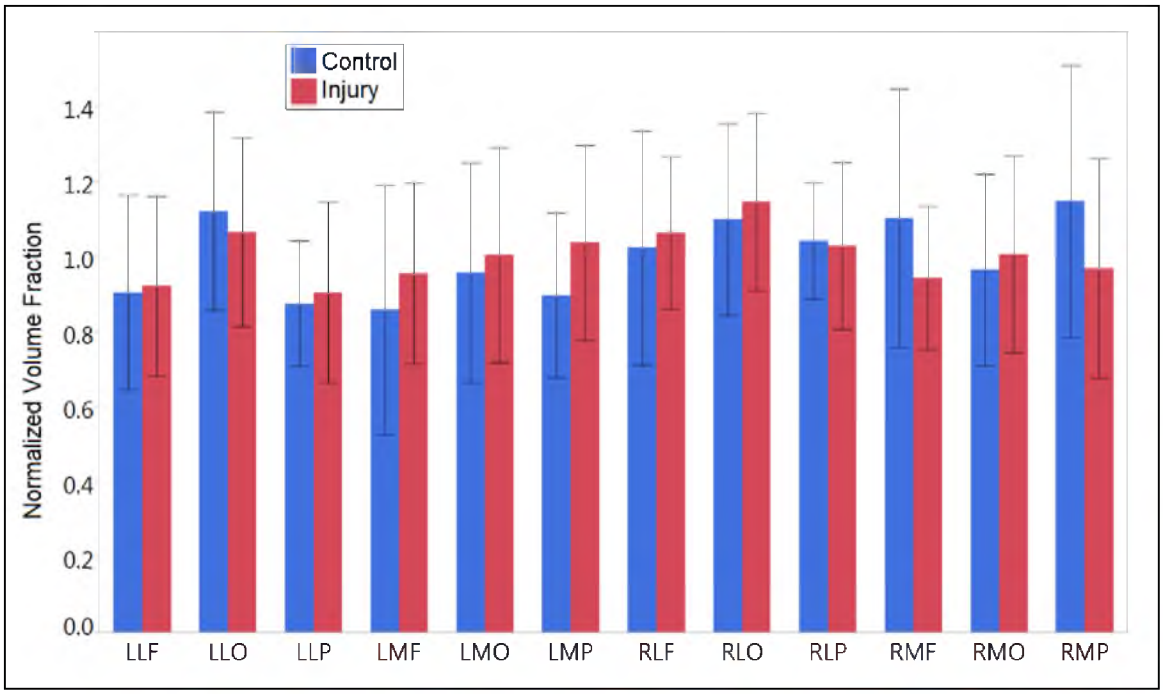

Figure 57: Means (with standard deviation) of the calculated volume fractions in all uninflated control (N=5), and uninflated injury (N=3) brains, categorized by 12 anatomical subregions (1st letter: left or right, 2nd letter: laterial or medial, 3rd letter: frontal, parietal or occiputal).

We have demonstrated in this paper a method of analyzing the volume of CSF in T2 MRI images on a quantitative level. This is of great benefit to the TBI research community as it provides numerical data that can be correlated to healthy or injured populations. These numerical data may allow trends to be seen that otherwise would go unnoticed in routine qualitative medical examinations of patients. When analyzing the brains, it appeared that whole-brain CSF measurements yielded more useful results. Individual anatomical regions were highly variable due to the large differences in gyral morphology from animal to animal. A singular anatomical comparison would, however, be a reasonable measure to evaluate CSF, before and after some form of insult in a single patient. When comparing the pre- and postinjury states, animals P14-001 and P14-002 appeared to show increases in CSF volume postinjury. This finding, however, may be a false positive as postinjury scans had increased resolution and increased sensitivity to identifying CSF. In future studies, the scans parameters should be set identical for pre- and postinjury scans.

A novel method of assessing CSF flow parameters in the subarachnoid space was demonstrated in this chapter. This method, originally created to measure stroke volume in the cerebral aqueduct of hydrocephalus patients, has proven quite robust and able to work for the markedly different geometries and flow regimes. It remains to be seen if this biomarker can be correlated to PAC damage. One limitation of this method is the high operator-to-operator variability. While it is quite repeatable within operator, the significant differences found in measurements across operators in this study are concerning. Future implementations of this algorithm may require a fixed ROI geometry, only allowing the user to translate or rotate the ROI. Stroke volumes were normalized by

ROI area to alleviate some of the variability, but velocity waveforms were not able to be normalized. Higher scan resolution and signal-to-noise ratio may also help make these scans more accurate as an injury biomarker.

The FLASH cine scans of coronal rotations in this study were the most likely to be directly linked to PAC damage. In our present study, we have shown we are able to capture the motion of the brain and skull *in-vivo* during a subinjury coronal rotation. We also demonstrate we are able to track the gross motion of the brain and skull quite well with an application of the Demon's algorithm. The major limitation of these current studies was that the limited resolution diminished confidence in the predictions of brain-skull displacement. Given a higher resolution scan or lower noise content, finer differences between the brain and skull displacement can be ascertained. An additional alternative would be the implementation of a different image registration algorithm, in which material stiffnesses are defined. This could aid the algorithm in estimating which areas are likely be to be moving and which are not [120]. However, these proposed changes to the algorithm would require more user input and could potentially pose many computational problems and user variation. Regardless of the postprocessing algorithm, brain-skull displacement was successfully created using the custom bed and the appropriate FLASH imaging sequence. These values of brain-skull displacement, when correlated to changes in PAC volume fraction could be very valuable to the TBI research community.

The OCT imaging results presented in this section do not instill a lot of confidence that any damage actually occurred to the PAC. This could be due to small sample sizes, but was also thought to be due to the study design itself. The team had to

re-evaluate the methods of measuring volume fraction to see if it was even sensitive to injury, and came to the conclusion that it is not. The arachnoid trabeculae (AT) and subarachnoid vasculature (SAV) act as tethers in the PAC, and are quantified using a volume fraction. If all of the AT and SAV were severed in the PAC, they may still occupy the same space, despite now being structurally deficient. If severed near the top of the PAC, the structures would likely fall down and blend in with the pial membrane. The resulting VF would be smaller, and PAC damage would correctly be identified. However, if the AT and SAV were severed at the bottom, they would likely still hang in the subarachnoid space and be counted. This poses a problem, as the VF measured tells us what is in the area, not the mechanical integrity of the structure. In order to assess the true structural state of the AT/SAV before and after injury, a more robust and sensitive computational algorithm would need to be employed (such as one measuring structural connectivity of the volumetric images).

One other possibility for not identifying PAC damage is that there truly wasn't any. In previous studies which utilized the same animal model of mild TBI (3-5-day-old piglets, subjected to rapid sagittal head rotations), only mild axonal injury was found. Perhaps more severe head rotations need to occur before there is any PAC damage that is identifiable in our MRI examinations or OCT imaging.

4.5 Conclusion

This study presents a series of explorations into correlating MRI biomarkers to PAC damage. However, due to small sample sizes and low scan resolutions, no strong correlations were found in any imaging modality. This by no means suggests any of these

biomarkers are not valid. It does suggest the biomarkers are subtle and sensitive to signal-to-noise ratio and scan resolution. Higher sample sizes and improved imaging parameters will be needed to see any distinct trends. Future studies taking care to address these issues have a high chance of providing correlations between these noninvasive scans to invasively obtained OCT data. If a strong correlation is found between PAC damage and *in-vivo* MRI biomarkers, the way clinicians diagnose mild TBI could be greatly improved.

CONCLUSIONS AND FUTURE WORK

A novel method of imaging the *in-situ* PAC postmortem utilizing optical coherence tomography (OCT) was developed in Chapter 1. This is the first study of its kind to utilize OCT imaging to create high-resolution photographs of the *in-situ* PAC; a structure previously only imaged *ex-vivo* with microscopy methods. The volume fractions (VF) presented here are the first of their kind and quantitatively measure the amount of arachnoid trabeculae (AT) present in the PAC. The results of these measurements show that a high variability of VF exists within brains, yet no significant trends existed across specific regions of the brain, or across different animals. This suggests that there may be mechanical "weak spots" across the cortical surface, increasing the chance for subdural or subarachnoid hemorrhaging (SDH/SAH) in those regions after a traumatic head rotation. This variability affects brain mechanics by virtue of these weakened regions allowing more strain in certain regions. Previous metrics which looked for a cutoff threshold of brain strain in simulations with homogenous PAC properties may underestimate injury when compared to a variable PAC model, which accounts for more weakened points and thus more areas of large strains.

A few limitations were encountered during these studies, the first of which was PAC collapse upon imaging. Because of this, measured values of VF were not easily correlated to the animal's *in-vivo* state. Performing craniotomies on live, anesthetized animals, and performing imaging *in-vivo* would overcome this. *In-vivo* imaging, however, would be challenged by the motion artifacts resulting from animal breathing

and the cardiac pulsatility of the brain.

Another limitation was the current OCT imaging system. Image resolution was not maximized and scan windows were fairly small, limiting the coverage of the cortical surface when imaging. The stereotactic positioning system does not provide any locational feedback, and there was no way of spatially registering all of the scans together. Future studies should include upgrades to the OCT imaging system, which would result in higher resolution and larger scan windows. Additionally, a redesign of the stereotactic positioning system may allow for better locational awareness during scans. These upgrades would allow for a more accurate mapping of the brain surface, with less doubt of having missed or repeated scans along the brain.

A third limitation of the studies was that of postprocessing. Manual segmentation of single frames representing the whole image volume, although adequate, is not ideal. Future work should develop robust algorithms to automatically segment and measure full OCT image volumes. Separate from measuring VF, there is still a need to measure directionality and/or connectivity of the AT, in an attempt to quantify damage (which could not be quantified with VF alone). Additional algorithms would also need to be developed to measure these metrics as well.

A microscale model of the PAC was developed and utilized in two parametric studies in Chapter 2. Aside from one other model presented in the literature [32], this is the first anatomically detailed FE model of the PAC available. Our first parametric study showed that the moduli of the AT and pia had a nonlinear relationship with vessel strain and brain-skull displacement. Our second parametric study showed that differing VFs of AT also had a similar nonlinear relationship. These two results show that the PAC,

although historically overlooked and simplified, can have a very large effect on injury prediction metrics.

Although these simulations presented some very insightful qualitative results, the linear elastic material models utilized limited the quantitative accuracy or physiological relevance greatly. Future studies will be conducted which take into account more physiologically realistic material models including strain-dependent, rate-dependent, and anisotropic behaviors.

In Chapter 3, the microscale PAC model was reconstructed to represent that of a 3-5-day-old porcine PAC, and incorporated into a porcine macroscale model of TBI which simulated rapid head rotation. The porcine PAC model simulated tensile tests in the in-plane and out-of-plane directions to determine properties for a representative solid element (RSE) to be implemented in the macroscale model. Volume fraction variance was then introduced into the macroscale model by way implementing RSE's with different material properties. This was performed for two sets of OCT data, resulting in two subject-specific multiscale models. These two multiscale models showed significant differences in brain-skull displacement in all measured regions when compared with a Kolmogorov-Smirnov goodness-of-fit test. The multiscale simulations were better predictors of regional intracranial hemorrhage than the previous models proposed by Coats et al. [23] in all regions except for midline. Future work will address the disagreement between the FE models and measured hemorrhage in the midline region. The major finding of this chapter is that including VF variability in the multiscale models appeared to allow for better regional prediction of intranasal hemorrhage when compared to the previous models which assumed homogenous properties of the PAC.

Just as in Chapter 2, one major limiting factor in these studies was that of material properties. In this case, the macroscale model featured very realistic material models, taking into account the strain and rate dependencies of brain tissue. However, the PAC elements were still linear-elastic, potentially causing some inaccuracies in the simulations. These inaccuracies are not expected to change our qualitative behavior drastically in terms of our rate-response, since the high rate modulus was used for all structures anyways. The absence of a strain-dependent material properties in the model may cause over prediction of PAC strain earlier on (where it should be weaker, in an initial toe region), and under prediction of PAC strain at high levels of stress (where the moduli exponentially increases). In the future, more advanced material models involving strain and rate dependence will be implemented, bringing the simulations closer to physiological accuracy. Separate from the issue of material model choices, a huge hurdle in accurately modeling the PAC is simply a lack of material property data. Material constants in the PAC model were estimated from bovine, human, and porcine data. An experimental study of the material properties of the PAC could yield very useful data for future studies. These studies could be conducted in a similar fashion to those done by Jin et al. on adult bovine tissue [57-59], or conducted with a form of inflation or peel testing, capitalizing on the OCT system as an optical strain measuring device.

The final chapter of this study showcased the use of a 3-5-day-old piglet model of mild TBI from rapid cyclic head rotations. Magnetic resonance imaging (MRI) was introduced as a means to collect biomarkers of PAC damage, and OCT imaging of the PAC was performed postmortem to tie back to those biomarkers. No strong correlations were seen in any of the MRI modalities or OCT imaging sequences. This, however, does

not hinder the impact of the study as much was learned about the imaging parameters required to properly capture PAC damage biomarkers of interest. This study was the first to capture the piglet brain in motion via MRI FLASH cine scans, thanks to the pneumatically controlled bed designed for this study. With some refinement to the motion-tracking algorithms and increases to scan resolution, brain-skull motion could be measured *in-vivo* in these animals. The other two imaging modalities tested (T2-weighted static images and phase contrast velocity imaging of CSF flow) did not show any significant trends due to low resolution, but there were several points of interest among the data. All imaging modalities would be improved with higher resolution. This resolution comes at a price, however, with longer imaging times (restricted by animal anesthesia time allotments) and lower signal-to-noise ratios (which could corrupt post-processing algorithms). Work is underway to refine the imaging parameters to optimum levels in order to get the best possible images in future studies. Future work will also include experimentation with alternative algorithms used for the postprocessing phases of these studies. In particular, a more refined motion-tracking algorithm could yield more accurate tracking of brain-skull displacement measurements from the FLASH cine scans. As mentioned previously, OCT imaging parameters will also be refined in the future, and new algorithms will be developed to measure alternative measures of AT integrity (such as connectivity and directionality). These higher resolution scans and new analysis algorithms may provide new insight into the PAC of the injured and uninjured animals (which currently show no significant differences).

Future work may also involve modifications to the animal model. Cyclic loading (shaking) alone does not appear to cause very large amounts of injury in these animals. In

many cases, only minor axonal injury and little to no hemorrhaging occurs. Animals that have undergone the same cyclic loading, but with an induced state of increased intracranial pressure (simulating crying), showed markedly more injury [121]. Conducting MRI and OCT imaging in these animals may elucidate the effects of injury more clearly (since more injury is innately produced).

Overall, in all studies except for the computational FE work, small sample sizes were a limitation. Predictive ability was greatly decreased when dealing with small numbers, especially for new, untested methodologies. Now that the pilot studies have helped identify areas for improvement, upcoming studies that incorporate several of these recommended changes are being implemented. Along with these improvements will also come appropriate sample sizes for our future work (n=24). With larger sample sizes, significant trends will be easier to discern in the MRI and OCT imaging data.

The work detailed in this thesis provides a great deal of new insight into the anatomical and biomechanical behavior of the pia arachnoid complex (PAC). As many of these studies have been the first of their kind, a multitude of new paths of research can stem from this work. These paths will all lead to more accurate models of the PAC, and in turn a more accurate understanding of TBI.

APPENDIX A

VOLUME FRACTION MEASUREMENT DATA

A.1 Volume Fraction Measurement Raw Data

Scan Name	Left or Right	Medial or Lateral	Frontal, Parietal or Occipital Lobe	Subregion (LMF, LLF, RMO, etc.)	AT Area (Pixels)	SAS Area (Pixels)	Area Fraction	Normalized Area Fraction	SAV Count
Animal P13-077 - 09-11-2013 - Control - Uninflated									
Left1	L	Lat	O	LLO	11866	38810	30.57%	0.902	2
Left2	L	Lat	O	LLO	3460	9010	38.40%	1.133	2
Left4	L	Lat	P	LLP	3489	12088	28.86%	0.852	0
Left5	L	Lat	F	LLF	15284	47259	32.34%	0.954	0
Left6	L	Lat	F	LLF	21592	52726	40.95%	1.208	0
Right1	R	M	O	RMO	2839	7650	37.11%	1.095	1
Right2	R	M	O	RMO	13713	36479	37.59%	1.109	3
Right3	R	M	P	RMP	19518	54682	35.69%	1.053	3
Right5	R	M	F	RMF	4068	7681	52.96%	1.563	2
Right7	R	M	F	RMF	9645	46535	20.73%	0.612	0
Right9	R	Lat	F	RLF	7105	21503	33.04%	0.975	0
Right10	R	Lat	P	RLP	9579	32298	29.66%	0.875	3
Right11	R	Lat	O	RLO	7205	23005	31.32%	0.924	1
Right12	R	Lat	O	RLO	3527	13954	25.28%	0.746	1
Animal P13-078 - 09-11-2013 - Control - Uninflated									
Left1	L	Lat	O	LLO	4409	15843	27.83%	0.802	0
Left2	L	Lat	O	LLO	5734	14750	38.87%	1.121	0
Left4	L	Lat	F	LLF	6704	26448	25.35%	0.731	4
Left5	L	M	F	LMF	4749	12124	39.17%	1.129	0
Right1	R	Lat	O	RLO	10269	33465	30.69%	0.885	2
Right2	R	Lat	P	RLP	6124	14953	40.95%	1.181	0
Right3	R	Lat	F	RLF	3717	10295	36.10%	1.041	0
Right5	R	M	F	RMF	9152	20128	45.47%	1.311	0
Right7	R	M	P	RMP	3341	11933	28.00%	0.807	0
Right9	R	M	O	RMO	1512	4398	34.38%	0.991	1
Animal P13-098 - 10-17-2013 - Control - Uninflated									
L1-0	L	M	O	LMO	6517	13678	47.65%	1.557	0
L1-1	L	M	O	LMO	18693	51200	36.51%	1.193	4
L1-2	L	M	O	LMO	9468	40595	23.32%	0.762	1
L1-4	L	M	P	LMP	2882	17546	16.43%	0.537	1
L1-6	L	M	P	LMP	8680	30882	28.11%	0.918	1
L1-7	L	M	F	LMF	9483	37685	25.16%	0.822	2
L1-8	L	M	F	LMF	8693	25606	33.95%	1.109	1
L1-11	L	M	F	LMF	2233	9133	24.45%	0.799	0
L1-12	L	M	F	LMF	7066	25169	28.07%	0.917	0

Scan Name	Left or Right	Medial or Lateral	Frontal, Parietal or Occipital Lobe	Subregion (LMF, LLF, RMO, etc.)	AT Area (Pixels)	SAS Area (Pixels)	Area Fraction	Normalized Area Fraction	SAV Count
L2-01	L	Lat	F	LLF	5638	23952	23.54%	0.769	1
L2-03	L	Lat	P	LLP	2890	12413	23.28%	0.761	1
L2-04	L	Lat	P	LLP	1395	4598	30.34%	0.991	0
L2-06	L	Lat	O	LLO	7294	16869	43.24%	1.413	2
R1-01	R	M	O	RMO	6830	21970	31.09%	1.016	0
R1-02	R	M	O	RMO	3731	16044	23.25%	0.760	0
R1-06	R	M	P	RMP	3805	11014	34.55%	1.129	1
R1-09	R	M	F	RMF	2626	8940	29.37%	0.960	0
R1-12	R	M	F	RMF	1906	5184	36.77%	1.201	0
R2-02	R	Lat	F	RLF	2410	7006	34.40%	1.124	0
R2-03	R	Lat	P	RLP	2712	8240	32.91%	1.075	0
R2-04	R	Lat	P	RLP	2888	7991	36.14%	1.181	0
R2-05	R	Lat	O	RLO	7203	23374	30.82%	1.007	1
Animal P13-102 - 10-23-2013 - Control - Uninflated									
L1-1	L	M	O	LMO	5240	23938	21.89%	0.733	1
L1-2	L	M	O	LMO	9620	25181	38.20%	1.279	1
L1-3	L	M	P	LMP	6306	28163	22.39%	0.750	1
L1-4	L	M	P	LMP	5607	21035	26.66%	0.892	1
L1-6	L	M	P	LMP	8818	37683	23.40%	0.783	1
L1-7	L	M	F	LMF	5315	22459	23.67%	0.792	0
L1-8	L	M	F	LMF	14076	44471	31.65%	1.060	0
L1-9	L	M	F	LMF	12073	43733	27.61%	0.924	0
L2-1	L	Lat	F	LLF	6300	25763	24.45%	0.819	1
L2-2	L	Lat	F	LLF	6304	24420	25.81%	0.864	0
L2-3	L	Lat	P	LLP	12640	41722	30.30%	1.014	1
L2-4	L	Lat	P	LLP	6379	18427	34.62%	1.159	0
L2-5	L	Lat	O	LLO	4324	16076	26.90%	0.901	0
L2-6	L	Lat	O	LLO	4847	14598	33.20%	1.112	0
L2-7	L	Lat	O	LLO	5070	12138	41.77%	1.398	1
R1-1	R	M	O	RMO	5070	17949	28.25%	0.946	0
R1-2	R	M	O	RMO	4089	11084	36.89%	1.235	0
R1-3	R	M	O	RMO	16678	75298	22.15%	0.742	0
R1-4	R	M	P	RMP	17163	70395	24.38%	0.816	0
R1-5	R	M	P	RMP	7577	24528	30.89%	1.034	0
R1-6	R	M	P	RMP	5917	14352	41.23%	1.380	0
R1-7	R	M	F	RMF	8544	26904	31.76%	1.063	2
R1-10	R	M	F	RMF	23598	78498	30.06%	1.006	0
R1-12	R	M	F	RMF	18390	63826	28.81%	0.965	2

Scan Name	Left or Right	Medial or Lateral	Frontal, Parietal or Occipital Lobe	Subregion (LMF, LLF, RMO, etc.)	AT Area (Pixels)	SAS Area (Pixels)	Area Fraction	Normalized Area Fraction	SAV Count
R2-1	R	Lat	F	RLF	13756	51593	26.66%	0.893	0
R1-2	R	Lat	F	RLF	4203	20673	20.33%	0.681	0
R2-3	R	Lat	F	RLF	10862	38249	28.40%	0.951	1
R2-6	R	Lat	P	RLP	4554	11364	40.07%	1.342	0
R2-9	R	Lat	O	RLO	12854	29356	43.79%	1.466	1
Animal P13-103 - 10-24-2013 - Control - Uninflated									
L1-2	L	M	O	LMO	9791	26454	37.01%	1.148	3
L1-3	L	M	O	LMO	14798	55989	26.43%	0.820	1
L1-4	L	M	P	LMP	8244	25295	32.59%	1.011	1
L1-6	L	M	P	LMP	7733	27595	28.02%	0.870	1
L1-8	L	M	F	LMF	2974	21615	13.76%	0.427	1
L1-9	L	M	F	LMF	4814	10427	46.17%	1.433	1
L2-1	L	Lat	F	LLF	17158	62079	27.64%	0.858	2
L2-2	L	Lat	F	LLF	16389	48743	33.62%	1.043	0
L2-4	L	Lat	P	LLP	1608	6096	26.38%	0.818	0
L2-6	L	Lat	O	LLO	3181	11472	27.73%	0.860	0
L2-7	L	Lat	O	LLO	3990	13159	30.32%	0.941	0
R1-1	R	M	O	RMO	11839	37274	31.76%	0.986	0
R1-2	R	M	O	RMO	11852	35960	32.96%	1.023	0
R1-3	R	M	P	RMP	14037	58259	24.09%	0.748	3
R1-4	R	M	P	RMP	19269	52593	36.64%	1.137	0
R1-7	R	M	F	RMF	18277	42783	42.72%	1.326	0
R1-8	R	M	F	RMF	2560	6763	37.85%	1.175	0
R1-9	R	M	F	RMF	4387	8411	52.16%	1.618	0
R2-1	R	Lat	F	RLF	7492	21986	34.08%	1.057	0
R2-2	R	Lat	F	RLF	7729	34543	22.38%	0.694	2
R2-3	R	Lat	F	RLF	7172	19248	37.26%	1.156	1
R2-4	R	Lat	P	RLP	16599	59676	27.82%	0.863	3
R2-6	R	Lat	P	RLP	10889	32219	33.80%	1.049	0
R2-8	R	Lat	O	RLO	13810	45620	30.27%	0.939	0
Animal P13-110 - 10-24-2013 - Injury - Uninflated									
L1-5_1	L	M	O	LMO	1419	5172	27.44%	0.844	1
L1-5_2	L	M	O	LMO	8069	27718	29.11%	0.895	2
L1-6	L	M	P	LMP	1837	4107	44.73%	1.375	0
L1-7	L	M	P	LMP	3643	9040	40.30%	1.239	0
L1-8	L	M	F	LMF	6893	28221	24.43%	0.751	2
L2-1	L	Lat	F	LLF	666	2391	27.85%	0.856	0
L2-2	L	Lat	F	LLF	1483	3048	48.65%	1.496	0

Scan Name	Left or Right	Medial or Lateral	Frontal, Parietal or Occipital Lobe	Subregion (LMF, LLF, RMO, etc.)	AT Area (Pixels)	SAS Area (Pixels)	Area Fraction	Normalized Area Fraction	SAV Count
L2-3	L	Lat	P	LLP	2317	13652	16.97%	0.522	0
L2-5	L	Lat	O	LLO	4014	11353	35.36%	1.087	0
R1-1	R	M	O	RMO	1228	3484	35.25%	1.084	0
R1-3	R	M	O	RMO	11293	36212	31.19%	0.959	0
R1-4	R	M	P	RMP	5694	13290	42.84%	1.317	0
R1-5	R	M	P	RMP	6487	21992	29.50%	0.907	1
R1-7	R	M	P	RMP	18188	69555	26.15%	0.804	4
R1-8	R	M	F	RMF	8777	32276	27.19%	0.836	2
R1-9	R	M	F	RMF	4903	14390	34.07%	1.048	1
R1-9_2	R	M	F	RMF	2979	8505	35.03%	1.077	1
R1-10	R	M	F	RMF	2176	8347	26.07%	0.802	1
R2-1	R	Lat	F	RLF	17445	51529	33.85%	1.041	5
R2-2	R	Lat	F	RLF	2957	8398	35.21%	1.083	1
R2-3	R	Lat	P	RLP	4802	13028	36.86%	1.133	0
R2-4	R	Lat	P	RLP	8354	26264	31.81%	0.978	1
R2-5	R	Lat	O	RLO	2749	9967	27.58%	0.848	0
R2-7	R	Lat	O	RLO	1089	3284	33.16%	1.020	0
Animal P13-121 - 12-18-2013 - Control - Inflated									
L1-1	R	M	O	RMO	10757	52268	20.58%	1.015	0
L1-2	R	M	O	RMO	13229	140775	9.40%	0.463	0
L1-3	R	M	P	RMP	4177	10002	41.76%	2.059	0
L1-4	R	M	P	RMP	18320	74058	24.74%	1.219	0
L1-5	R	M	F	RMF	5239	21551	24.31%	1.198	3
L1-6	R	M	F	RMF	9272	30939	29.97%	1.477	2
L1-7	R	M	F	RMF	15105	110473	13.67%	0.674	0
L2-1	R	Lat	F	RLF	16056	43934	36.55%	1.802	2
L2-2	R	Lat	F	RLF	5345	24517	21.80%	1.075	1
L2-3	R	Lat	P	RLP	8529	46153	18.48%	0.911	3
L2-4	R	Lat	P	RLP	4799	24931	19.25%	0.949	2
L2-5	R	Lat	O	RLO	3448	13999	24.63%	1.214	1
L2-6	R	Lat	O	RLO	8709	31092	28.01%	1.381	2
R1-1	L	M	O	LMO	6717	42401	15.84%	0.781	1
R1-2	L	M	O	LMO	13093	91306	14.34%	0.707	0
R1-3	L	M	P	LMP	3965	14464	27.41%	1.351	2
R1-4	L	M	P	LMP	12398	59177	20.95%	1.033	2
R1-5	L	M	P	LMP	2150	12260	17.54%	0.864	0
R1-6	L	M	F	LMF	11261	142453	7.91%	0.390	2
R1-7	L	M	F	LMF	9088	69042	13.16%	0.649	0

Scan Name	Left or Right	Medial or Lateral	Frontal, Parietal or Occipital Lobe	Subregion (LMF, LLF, RMO, etc.)	AT Area (Pixels)	SAS Area (Pixels)	Area Fraction	Normalized Area Fraction	SAV Count
R1-8	L	M	F	LMF	7779	65192	11.93%	0.588	0
R2-1	L	Lat	F	LLF	14661	78624	18.65%	0.919	2
R2-2	L	Lat	F	LLF	4858	51437	9.44%	0.466	0
R2-3	L	Lat	P	LLP	6858	50559	13.56%	0.669	2
R2-4	L	Lat	P	LLP	7838	37643	20.82%	1.026	1
R2-5	L	Lat	P	LLP	10659	62294	17.11%	0.843	0
R2-6	L	Lat	O	LLO	13620	70243	19.39%	0.956	4
R2-8	L	Lat	O	LLO	11800	44027	26.80%	1.321	1
Animal P13-122 - 12-18-2013 - Control - Inflated									
L1-1	L	M	O	LMO	10013	60876	16.45%	0.637	0
L1-2	L	M	O	LMO	10522	43208	24.35%	0.943	0
L1-3	L	M	P	LMP	22881	94015	24.34%	0.942	2
L1-4	L	M	P	LMP	1294	8631	14.99%	0.580	0
L1-5	L	M	P	LMP	9290	30951	30.02%	1.162	3
L1-6	L	M	F	LMF	12012	106199	11.31%	0.438	2
L1-7	L	M	F	LMF	17127	46476	36.85%	1.427	3
L2-1	L	Lat	F	LLF	14675	75462	19.45%	0.753	2
L2-2	L	Lat	F	LLF	8636	22330	38.67%	1.497	2
L2-4	L	Lat	P	LLP	13693	82717	16.55%	0.641	5
L2-5	L	Lat	O	LLO	5240	11662	44.93%	1.739	3
L2-6	L	Lat	O	LLO	5625	19152	29.37%	1.137	1
R1-1	R	M	O	RMO	4837	12481	38.75%	1.500	1
R1-2	R	M	O	RMO	4005	23742	16.87%	0.653	1
R1-4	R	M	P	RMP	8385	25590	32.77%	1.268	1
R1-7	R	M	F	RMF	7142	64080	11.15%	0.431	2
R2-1	R	Lat	F	RLF	6710	44672	15.02%	0.581	2
R2-2	R	Lat	F	RLF	5305	15739	33.71%	1.305	2
R2-3	R	Lat	P	RLP	6547	24903	26.29%	1.018	2
R2-5	R	Lat	O	RLO	3423	9839	34.79%	1.347	2
Animal P14-001 - 01-08-2014 - Injury - Uninflated									
L1-2	L	M	O	LMO	9573	45730	20.93%	0.673	2
L1-4	L	M	F	LMF	2336	7318	31.92%	1.027	0
L1-5	L	M	F	LMF	5110	14342	35.63%	1.146	0
L2-1	L	Lat	F	LLF	2658	6960	38.19%	1.228	0
L2-2	L	Lat	F	LLF	12970	58972	21.99%	0.707	1
L2-3	L	Lat	P	LLP	4133	11861	34.85%	1.121	0
L2-4	L	Lat	O	LLO	11160	27025	41.30%	1.328	1
R1-3	R	M	P	RMP	3702	13591	27.24%	0.876	0

Scan Name	Left or Right	Medial or Lateral	Frontal, Parietal or Occipital Lobe	Subregion (LMF, LLF, RMO, etc.)	AT Area (Pixels)	SAS Area (Pixels)	Area Fraction	Normalized Area Fraction	SAV Count
R1-4	R	M	F	RMF	5410	29664	18.24%	0.587	0
R1-5	R	M	F	RMF	4758	11457	41.53%	1.336	0
R1-6	R	M	F	RMF	7038	31251	22.52%	0.724	0
R2-1	R	Lat	F	RLF	3894	11580	33.63%	1.082	0
R2-2	R	Lat	P	RLP	3895	10766	36.18%	1.164	1
Animal P14-002 - 01-08-2014 - Injury - Uninflated									
L1-1	L	M	O	LMO	3180	14496	21.94%	0.708	1
L1-2	L	M	O	LMO	4925	17653	27.90%	0.901	4
L1-3	L	M	O	LMO	10260	25928	39.57%	1.278	1
L1-4	L	M	P	LMP	15156	73414	20.64%	0.667	1
L1-5	L	M	P	LMP	20847	60309	34.57%	1.116	1
L1-6	L	M	F	LMF	10382	37831	27.44%	0.886	0
L1-7	L	M	F	LMF	10018	28371	35.31%	1.140	0
L1-8	L	M	F	LMF	10244	43975	23.30%	0.752	0
L2-1	L	Lat	F	LLF	6624	21571	30.71%	0.992	0
L2-2	L	Lat	F	LLF	11355	40944	27.73%	0.896	0
L2-3	L	Lat	P	LLP	6823	30136	22.64%	0.731	0
L2-4	L	Lat	P	LLP	10093	25718	39.24%	1.267	1
L2-5	L	Lat	O	LLO	12745	43299	29.43%	0.951	0
L2-6	L	Lat	O	LLO	20181	73838	27.33%	0.883	1
L2-8	L	Lat	O	LLO	3225	11401	28.29%	0.914	1
R1-1	R	M	O	RMO	1803	5757	31.32%	1.011	0
R1-2	R	M	O	RMO	12992	55142	23.56%	0.761	1
R1-3	R	M	P	RMP	13494	66658	20.24%	0.654	0
R1-4	R	M	P	RMP	3690	9263	39.84%	1.286	0
R1-5	R	M	F	RMF	3458	11506	30.05%	0.971	0
R1-6	R	M	F	RMF	4256	11447	37.18%	1.201	1
R1-7	R	M	F	RMF	697	2239	31.13%	1.005	0
R2-1	R	Lat	F	RLF	9521	25131	37.89%	1.223	0
R2-2	R	Lat	F	RLF	13588	31974	42.50%	1.372	1
R2-4	R	Lat	P	RLP	2673	6694	39.93%	1.290	0
R2-5	R	Lat	P	RLP	13616	38432	35.43%	1.144	1
R2-6	R	Lat	O	RLO	10911	35265	30.94%	0.999	1
Animal P14-006 - 01-16-2014 - Injury - Inflated									
L1-1	L	M	O	LMO	2742	6561	41.79%	1.537	0
L1-2	L	M	O	LMO	23111	59506	38.84%	1.428	1
L1-3	L	M	O	LMO	19264	91625	21.02%	0.773	1
L1-4	L	M	P	LMP	5793	16933	34.21%	1.258	1

Scan Name	Left or Right	Medial or Lateral	Frontal, Parietal or Occipital Lobe	Subregion (LMF, LLF, RMO, etc.)	AT Area (Pixels)	SAS Area (Pixels)	Area Fraction	Normalized Area Fraction	SAV Count
L1-5	L	M	P	LMP	6734	19939	33.77%	1.242	1
L1-7	L	M	F	LMF	4231	10685	39.60%	1.456	1
L1-8	L	M	F	LMF	19710	69521	28.35%	1.043	0
L1-9	L	M	F	LMF	21405	131986	16.22%	0.596	0
L2-1	L	Lat	F	LLF	9253	43050	21.49%	0.790	1
L2-2	L	Lat	F	LLF	17067	70374	24.25%	0.892	2
L2-3	L	Lat	P	LLP	15633	66161	23.63%	0.869	1
L2-4	L	Lat	P	LLP	15375	55234	27.84%	1.024	1
L2-6	L	Lat	O	LLO	2589	6241	41.48%	1.526	2
L2-7	L	Lat	O	LLO	9634	51155	18.83%	0.693	0
R1-1	R	M	O	RMO	6053	30839	19.63%	0.722	0
R1-2	R	M	O	RMO	21533	112427	19.15%	0.704	0
R1-4	R	M	O	RMO	21696	93787	23.13%	0.851	0
R1-5	R	M	P	RMP	12909	36970	34.92%	1.284	0
R1-6	R	M	P	RMP	8961	73291	12.23%	0.450	1
R1-7	R	M	P	RMP	21205	82025	25.85%	0.951	3
R1-8	R	M	F	RMF	7217	25656	28.13%	1.034	3
R1-9	R	M	F	RMF	16118	59683	27.01%	0.993	0
R1-10	R	M	F	RMF	13459	50816	26.49%	0.974	1
R2-1	R	Lat	F	RLF	31324	132656	23.61%	0.868	0
R2-2	R	Lat	F	RLF	5522	15755	35.05%	1.289	2
R2-3	R	Lat	P	RLP	17157	84342	20.34%	0.748	2
R2-4	R	Lat	P	RLP	21984	103795	21.18%	0.779	0
R2-5	R	Lat	P	RLP	12466	67500	18.47%	0.679	5
R2-6	R	Lat	O	RLO	15020	41545	36.15%	1.330	1
R2-7	R	Lat	O	RLO	19168	57878	33.12%	1.218	0
Animal P14-007 - 01-16-2014 - Injury - Inflated									
L1-1	L	M	O	LMO	20116	90931	22.12%	1.046	2
L1-2	L	M	O	LMO	9593	54625	17.56%	0.830	1
L1-3	L	M	O	LMO	16637	66709	24.94%	1.179	1
L1-4	L	M	P	LMP	9312	49385	18.86%	0.892	0
L1-5	L	M	P	LMP	6044	35230	17.16%	0.811	0
L1-6	L	M	P	LMP	14454	90451	15.98%	0.756	1
L1-8	L	M	F	LMF	11790	70936	16.62%	0.786	0
L1-9	L	M	F	LMF	20344	101167	20.11%	0.951	0
L2-1	L	Lat	F	LLF	9097	58664	15.51%	0.733	3
L2-2	L	Lat	F	LLF	13522	84841	15.94%	0.754	2
L2-3	L	Lat	F	LLF	10579	61366	17.24%	0.815	3

Scan Name	Left or Right	Medial or Lateral	Frontal, Parietal or Occipital Lobe	Subregion (LMF, LLF, RMO, etc.)	AT Area (Pixels)	SAS Area (Pixels)	Area Fraction	Normalized Area Fraction	SAV Count
L2-4	L	Lat	P	LLP	13886	88842	15.63%	0.739	1
L2-5	L	Lat	P	LLP	15104	72717	20.77%	0.982	1
L2-6	L	Lat	O	LLO	10293	46552	22.11%	1.045	0
L2-7	L	Lat	O	LLO	8908	35386	25.17%	1.190	0
R1-1	R	M	O	RMO	15793	56663	27.87%	1.318	2
R1-2	R	M	O	RMO	10442	33829	30.87%	1.459	0
R1-3	R	M	O	RMO	11090	42696	25.97%	1.228	0
R1-4	R	M	P	RMP	21198	76874	27.57%	1.304	2
R1-5	R	M	P	RMP	7837	43348	18.08%	0.855	3
R1-6	R	M	F	RMF	18082	108165	16.72%	0.790	4
R1-7	R	M	F	RMF	18311	106615	17.17%	0.812	3
R1-1	R	Lat	F	RLF	17344	88557	19.59%	0.926	3
R2-2	R	Lat	F	RLF	12891	88522	14.56%	0.689	3
R2-3	R	Lat	F	RLF	6804	29550	23.03%	1.089	0
R2-4	R	Lat	P	RLP	10648	44474	23.94%	1.132	3
R2-5	R	Lat	P	RLP	7812	29187	26.77%	1.266	1
R2-6	R	Lat	O	RLO	6937	21138	32.82%	1.552	2
R2-8	R	Lat	O	RLO	1826	8054	22.67%	1.072	0

A.2 Volume Fraction Measurement Averaged Data

Left	Right	Medial	Lateral	Frontal	Parietal	Occipital	Whole Brain
Animal P13-077 - 09-11-2013 - Control - Uninflated							
34.23%	33.71%	36.82%	32.27%	36.00%	31.41%	33.38%	33.89%
(5.20%)	(9.11%)	(11.42%)	(4.80%)	(11.91%)	(3.74%)	(5.19%)	(7.71%)
Animal P13-078 - 09-11-2013 - Control - Uninflated							
32.81%	35.93%	36.75%	33.30%	36.52%	34.48%	32.53%	34.68%
(7.25%)	(6.47%)	(7.40%)	(6.29%)	(8.41%)	(9.16%)	(2.61%)	(6.59%)
Animal P13-098 - 10-17-2013 - Control - Uninflated							
29.54%	32.14%	29.91%	31.83%	29.46%	28.82%	33.70%	30.61%
(8.75%)	(4.16%)	(7.71%)	(6.56%)	(5.05%)	(6.96%)	(9.36%)	(7.22%)
Animal P13-102 - 10-23-2013 - Control - Uninflated							
28.83%	30.98%	28.82%	31.36%	27.20%	30.44%	32.56%	29.87%
(5.99%)	(7.13%)	(5.84%)	(7.41%)	(3.50%)	(7.00%)	(8.18%)	(6.53%)
Animal P13-103 - 10-24-2013 - Control - Uninflated							
29.97%	34.14%	34.01%	30.12%	34.76%	30.44%	30.93%	32.23%
(7.97%)	(7.80%)	(9.97%)	(4.29%)	(11.35%)	(7.00%)	(3.49%)	(7.99%)
Animal P13-110 - 10-24-2013 - Injury - Uninflated							
32.76%	32.38%	32.38%	32.73%	34.76%	33.64%	31.30%	32.52%
(10.27%)	(4.61%)	(6.54%)	(8.06%)	(11.35%)	(9.39%)	(3.39%)	(7.05%)
Animal P13-121 - 12-18-2013 - Control - Inflated							
16.99%	24.09%	19.57%	21.12%	18.74%	22.16%	19.87%	20.29%
(5.63%)	(8.73%)	(9.00%)	(6.83%)	(9.37%)	(7.92%)	(6.48%)	(7.96%)
Animal P13-122 - 12-18-2013 - Control - Inflated							
25.61%	26.17%	23.44%	28.75%	23.74%	24.16%	29.36%	25.83%
(10.57%)	(10.49%)	(10.04%)	(10.32%)	(12.26%)	(7.14%)	(10.86%)	(10.26%)
Animal P14-001 - 01-08-2014 - Injury - Uninflated							
32.12%	29.89%	28.29%	34.35%	30.46%	32.75%	31.11%	31.09%
(7.84%)	(8.79%)	(8.48%)	(6.63%)	(8.50%)	(4.82%)	(14.40%)	(8.01%)
Animal P14-002 - 01-08-2014 - Injury - Uninflated							
29.07%	33.33%	29.60%	32.67%	32.32%	31.57%	28.92%	30.96%
(5.93%)	(6.76%)	(6.73%)	(6.16%)	(5.80%)	(8.85%)	(5.06%)	(6.55%)
Animal P14-006 - 01-16-2014 - Injury - Inflated							
29.38%	25.28%	27.67%	26.57%	27.02%	25.24%	29.32%	27.19%
(8.84%)	(6.91%)	(8.57%)	(7.49%)	(6.60%)	(7.54%)	(9.83%)	(8.00%)
Animal P14-007 - 01-16-2014 - Injury - Inflated							
19.05%	23.40%	21.17%	21.12%	17.65%	20.53%	25.21%	21.15%
(3.31%)	(5.58%)	(4.98%)	(5.18%)	(2.54%)	(4.54%)	(4.49%)	(4.99%)

A.3 Statistical Analyses Summary

One-Way ANOVA of Normalized Means across Lobe			
Lobe	Number	Normalized Mean	Prob. > F
Frontal	38	1.00079	0.5495
Parietal	28	0.96521	
Occipital	33	1.02864	

One-Way ANOVA of Normalized Means across Subregion			
Subregion	Number	Normalized Mean	Prob. > F
LLF	8	0.90575	0.1460
LLO	10	1.05830	
LLP	6	0.93250	
LMF	10	0.94120	
LMO	7	1.07029	
LMP	7	0.82300	
RLF	9	0.95244	
RLO	6	0.99450	
RLP	7	1.08086	
RMF	11	1.16364	
RMO	10	0.99030	
RMP	8	1.01300	

One-Way ANOVA of Normalized Means across Animal			
Animal #	Number	Normalized Mean	Prob. > F
P13-077	14	1.00007	1.000
P13-078	10	0.99990	
P13-098	22	1.00005	
P13-102	29	1.00000	
P13-103	24	1.00000	

APPENDIX B

MICROSCALE MODEL SUBSTRUCTURE

RANDOMIZATION CODES

B.1 MATLAB Randomization Script

```
%Greg Scott - University of Utah - 5-12-14
%This script generates randomized locations for the arachnoid
%trabeculae in a FE Model of the pia-arachnoid complex. The cross-
%section of the PAC modeled is 1.5mm x 1.5mm, as such the random
%variables are restricted to this space.
clc;
clear;
close all;

%set up variables (maybe change later for user-inputs)
L = 1.5; %length of cross-section (mm)
mult = 3; %multiplier of 10-structure base to create requested vol.
fract. (only choose whole numbers or code will not work)
vf = mult*2.7666099; %This is what the volume fraction turns out to be
based on our 10:6:3:1 ratio.

%Based on Excel calculations (Porcine Model Properties.xlsx) these are
%the multiplier to volume fraction relations:
% Mult  Vf          Vf (with only 2 BVs)
%  1    2.77        3.03
%  2    5.53        5.04
%  3    8.30        7.06
%  4    11.07       9.07
%  5    13.83       11.09
%  6    16.60       13.10
%  7    19.37       15.12
%  8    22.13       17.13
%  9    24.90       19.15
%  10   27.67       21.16
%  11   30.43       23.18
%  12   33.20       25.19
%  13   35.97       27.21
%  14   38.73       29.22
%  15   41.50       31.24

%We assume there are 10 chords, 6 short sheets, 3 long sheets, and 1
%sheet /w/ bridging vessel per each basic unit, Note that we increased
%the AT structures from the previous 4:3:2:1 ratio in old models based
%what we saw in OCT images.
%
%Also note that Sheet with BV structures are manually deleted after 2
%are present in model.
c_total = 10*mult; %total # of chords
ss_total = 6*mult; %total # of short sheets
ls_total = 3*mult; %total # of long sheets
swbv_total = 1*mult; %total # of sheets /w/ BVs

%geometry
trab_diam = 0.018; %mm
ss_length = 0.150; %mm
ls_length = 0.450; %mm
swbv_length = 0.450; %mm
```

```
%initialize vectors
c_good = zeros(c_total,2);
ss_good = zeros(ss_total,2);
ang_ss = zeros(ss_total,1);
ang_ssdeg = zeros(ss_total,1);
ss_endpt = zeros(ss_total,2);
ls_good = zeros(ls_total,2);
ang_lsdeg = zeros(ls_total,1);
ang_ls = zeros(ls_total,1);
ls_endpt = zeros(ls_total,2);
swbv_good = zeros(swbv_total,2);
ang_swbv = zeros(swbv_total,1);
ang_swbvdeg = zeros(swbv_total,1);
swbv_endpt = zeros(swbv_total,2);
num_retries = 0;
cgc = 1;
cgss = 1;
cgls = 1;
cgswbv = 1;

%Generate pool of random values to choose from, as well as first points
c_possible = L.*rand(c_total*2,2);
c_good(1,1) = c_possible(1,1);
c_good(1,2) = c_possible(1,2);
ss_possible = L.*rand(ss_total*2,2);
ss_good(1,1) = ss_possible(1,1);
ss_good(1,2) = ss_possible(1,2);
ls_possible = L.*rand(ls_total*2,2);
ls_good(1,1) = ls_possible(1,1);
ls_good(1,2) = ls_possible(1,2);
swbv_possible = L.*rand(swbv_total*2,2);
swbv_good(1,1) = swbv_possible(1,1);
swbv_good(1,2) = swbv_possible(1,2);
sprintf('AT-CHORD CODE')
formatSpec = ['    a.Instance(name=''Trabeculae Chord-%1.0f'', part=p,
dependent=ON)\n','    a = mdb.models[''Model-1''].rootAssembly\n','
a.translate(instanceList=(''Trabeculae Chord-%1.0f'', ), vector=(%2.8f,
0.0, -%2.8f))\n'];
fprintf(formatSpec,cgc,cgc,c_good(cgc,1),c_good(cgc,2))

%1) CHORD SHAPE TRABECULAE LOCATIONS ARE GENERATED & ERORR-CHECKED TO
%CREATE OUR RANDOM DISTRIBUTION OF CHORD LOCATIONS FOR THE FE MODEL
for ic = 2:length(c_possible)
    nextxc = c_possible(ic,1);
    nextyc = c_possible(ic,2);
    for jc = 1:cgc
        currentgoodxc = c_good(jc,1);
        currentgoodyc = c_good(jc,2);
        c_dist = sqrt((nextxc - currentgoodxc)^2 + (nextyc -
currentgoodyc)^2);
        %Error-checking loop prevents trabeculae positions from being
        %too close (resulting in overlapping radii and bad geometry),
        %also checks positions from being too close to boundaries
        %(causing trabeculae to "spill out" of cross-section's
        %boundaries
        ChordTooClose = false; %will switch to true if bad point is
```

```
        found
        if c_dist < 2.1*trab_diam ||...
           nextxc <= trab_diam || nextxc >= (L-trab_diam) || ...
           nextyc <= trab_diam || nextyc >= (L-trab_diam)
           ChordTooClose = true;
           num_retries = num_retries+1; %counter to see if working
          break; %since point is bad, leave loop, do not store, and
redo
        end
    end
      %Populates "good" vector with trabeculae positions that do not
      %break any of the aforementioned geometry criterion
    if ~ChordTooClose %~ means false (aka our points are good/not
interfering)
        if cgc < c_total
            cgc = cgc + 1;
            c_good(cgc,1) = nextxc;
            c_good(cgc,2) = nextyc;
            %plot
            plot(c_good(1,1),c_good(1,2),'bo')
            plot(c_good(cgc,1),c_good(cgc,2),'bo')
            grid on;
            set(gca, 'GridLineStyle', '-');
%           grid(gca,'minor')
            axis square
            hold on
            %Print AT-Chord instancing Code
            formatSpec = ['    a.Instance(name=''Trabeculae Chord-
%1.0f'', part=p, dependent=ON)\n','    a = mdb.models[''Model-
1''].rootAssembly\n','    a.translate(instanceList=(''Trabeculae Chord-
%1.0f'', ), vector=(%2.8f, 0.0, -%2.8f))\n'];
            fprintf(formatSpec,cgc,cgc,c_good(cgc,1),c_good(cgc,2))
        end
    end

end
%split up "good" matrix into 2 peices (3/4 of size) so step 2 can
%error-check against it as well, without havign to change loop sizes
ss_vs_c_1 = c_good((1:0.75*cgc),:);
ss_vs_c_2 = c_good((0.25*cgc:(cgc-1)),:); %technically overlaps but
checking twice never hurt
sprintf('AT-SHORT SHEET CODE')
formatSpec = ['    a.Instance(name=''Trabeculae Short Sheet-%1.0f'',
part=p, dependent=ON)\n','    a = mdb.models[''Model-
1''].rootAssembly\n','    a.translate(instanceList=(''Trabeculae Short
Sheet-%1.0f'', ), vector=(%2.8f, 0.0, -%2.8f))\n'];
fprintf(formatSpec,cgss,cgss,ss_good(cgss,1),ss_good(cgss,2))

%2) SHEET SHAPE TRABECULAE START POINTS ARE GENERATED, ERROR-CHECKED
%TO CREATE OUR FINAL LOCATIONS FOR THESE STRUCTURES
for iss = 2:length(ss_possible)
    nextxss = ss_possible(iss,1);
    nextyss = ss_possible(iss,2);
    for jss = 1:cgss
        currentgoodxss = ss_good(jss,1);
        currentgoodyss = ss_good(jss,2);
```

```
        ss_dist = sqrt((nextxss - currentgoodxss)^2 + (nextyss -
currentgoodyss)^2);
        ss_c_dist_1 = sqrt((nextxss - ss_vs_c_1(jss,1))^2 + (nextyss -
ss_vs_c_1(jss,2))^2);
        ss_c_dist_2 = sqrt((nextxss - ss_vs_c_2(jss,1))^2 + (nextyss -
ss_vs_c_2(jss,2))^2);
        %Error-checking loop prevents trabeculae-sheet starting
        %positions  from being too close to eachother or too close to
        %the previously found chord locations in step 1.
        SSheetTooClose = false; %will switch to true if bad point is
        found
        if ss_dist < 2.1*trab_diam || ss_c_dist_1 < 2.1*trab_diam||...
           ss_c_dist_2 < 2.1*trab_diam || ...
           nextxss <= trab_diam || nextxss >= (L-trab_diam) || ...
           nextyss <= trab_diam || nextyss >= (L-trab_diam)
              SSheetTooClose = true;
              num_retries = num_retries+1; %counter to see if working
              break; %since point is bad, leave loop, do not store, and
            redo
        end
    end
      %Populates "good" vector with trabeculae positions that do not
      %break any of the aforementioned geometry criterion
    if ~SSheetTooClose %~ means false (aka our points are good/not
    interfering)
        if cgss < ss_total
            cgss = cgss + 1;
            ss_good(cgss,1) = nextxss;
            ss_good(cgss,2) = nextyss;
            %plot
            plot(ss_good(1,1),ss_good(1,2),'go')
            plot(ss_good(cgss,1),ss_good(cgss,2),'go')
            grid on;
            set(gca, 'GridLineStyle', '-');
%           grid(gca,'minor')
            axis square
            hold on
            %Print AT-Short Sheet instancing Code
            formatSpec = ['    a.Instance(name=''Trabeculae Short
Sheet-%1.0f'', part=p, dependent=ON)\n','    a = mdb.models[''Model-
1''].rootAssembly\n','    a.translate(instanceList=(''Trabeculae Short
Sheet-%1.0f'', ), vector=(%2.8f, 0.0, -%2.8f))\n'];

fprintf(formatSpec,cgss,cgss,ss_good(cgss,1),ss_good(cgss,2))
        end
    end

end
%now break up good_c matrix and ss_matrix into 2 parts again so they
can be
%error-checked in step 3
ls_vs_c_1 = c_good((1:0.5*cgc),:);
ls_vs_c_2 = c_good((0.5*cgc:(cgc-1)),:);
ls_vs_ss_1 = ss_good((1:(2/3)*cgss),:);
ls_vs_ss_2 = ss_good(((1/3)*cgss:(cgss-1)),:);
sprintf('AT-LONG SHEET CODE')
formatSpec = ['    a.Instance(name=''Trabeculae Long Sheet-%1.0f'',
```

```
part=p, dependent=ON)\n','    a = mdb.models[''Model-
1''].rootAssembly\n','    a.translate(instanceList=(''Trabeculae Long
Sheet-%1.0f'', ), vector=(%2.8f, 0.0, -%2.8f))\n'];
fprintf(formatSpec,cgls,cgls,ls_good(cgls,1),ls_good(cgls,2))

%3) LONG SHEET SHAPE TRABECULAE START POINTS ARE GENERATED, ERROR-
CHECKED
%TO CREATE OUR FINAL LOCATIONS FOR THESE STRUCTURES
for ils = 2:length(ls_possible)
    nextxls = ls_possible(ils,1);
    nextyls = ls_possible(ils,2);
    for jls = 1:cgls
        currentgoodxls = ls_good(jls,1);
        currentgoodyls = ls_good(jls,2);
        ls_dist = sqrt((nextxls - currentgoodxls)^2 + (nextyls -
currentgoodyls)^2);
        ls_c_dist_1 = sqrt((nextxls - ls_vs_c_1(jls,1))^2 + (nextyls -
ls_vs_c_1(jls,2))^2);
        ls_c_dist_2 = sqrt((nextxls - ls_vs_c_2(jls,1))^2 + (nextyls -
ls_vs_c_2(jls,2))^2);
        ls_ss_dist_1 = sqrt((nextxls - ls_vs_ss_1(jls,1))^2 + (nextyls
- ls_vs_ss_1(jls,2))^2);
        ls_ss_dist_2 = sqrt((nextxls - ls_vs_ss_2(jls,1))^2 + (nextyls
- ls_vs_ss_2(jls,2))^2);
        %Error-checking loop prevents trabeculae-sheet starting
        %positions from being too close to eachother or too close to
        %the previously found chord locations in step 1.
        LSheetTooClose = false; %will switch to true if bad point is
      found
        if ls_dist < 2.1*trab_diam || ...
           ls_c_dist_1 < 2.1*trab_diam || ls_c_dist_2 < 2.1*trab_diam
|| ls_ss_dist_1 < 2.1*trab_diam || ls_ss_dist_2 < 2.1*trab_diam ||
           nextxls <= trab_diam || nextxls >= (L-trab_diam) ||
           nextyls <= trab_diam || nextyls >= (L-trab_diam)
              LSheetTooClose = true;
              num_retries = num_retries+1; %counter to see if working
              break; %since point is bad, leave loop, do not store, and
            redo
        end
    end
      %Populates "good" vector with trabeculae positions that do not
      %break any of the aforementioned geometry criterion
    if ~LSheetTooClose %~ means false (aka our points are good/not
    interfering)
        if cgls < ls_total
            cgls = cgls + 1;
            ls_good(cgls,1) = nextxls;
            ls_good(cgls,2) = nextyls;
            %plot
            plot(ls_good(1,1),ls_good(1,2),'ro')
            plot(ls_good(cgls,1),ls_good(cgls,2),'ro')
            grid on;
            set(gca, 'GridLineStyle', '-');
%           grid(gca,'minor')
            axis square
            hold on
            formatSpec = ['    a.Instance(name=''Trabeculae Long Sheet-
```

```
%1.0f'', part=p, dependent=ON)\n','    a = mdb.models[''Model-
1''].rootAssembly\n','    a.translate(instanceList=(''Trabeculae Long
Sheet-%1.0f'', ), vector=(%2.8f, 0.0, -%2.8f))\n'];

fprintf(formatSpec,cgls,cgls,ls_good(cgls,1),ls_good(cgls,2))
        end
    end

end
%now break up good_c matrix into 4 parts, ss_matrix into 3 parts, and
%ls_matrix into 2 parts again so they can be error-checked in step 4
ls_vs_c_1 = c_good((1:0.5*cgc),:);
ls_vs_c_2 = c_good((0.5*cgc:(cgc-1)),:);
ls_vs_ss_1 = ss_good((1:(2/3)*cgss),:);
ls_vs_ss_2 = ss_good(((1/3)*cgss:(cgss-1)),:);
sprintf('AT-WITH-BV CODE')
formatSpec = ['    a.Instance(name=''Trabeculae with BV-%1.0f'',
part=p, dependent=ON)\n','    a = mdb.models[''Model-
1''].rootAssembly\n','    a.translate(instanceList=(''Trabeculae with
BV-%1.0f'', ), vector=(%2.8f, 0.0, -%2.8f))\n'];
fprintf(formatSpec,cgswbv,cgswbv,swbv_good(cgswbv,1),swbv_good(cgswbv,2
))

%4) SHEETS WITH BRIDGING VEINS START POINTS ARE GENERATED, ERROR-
CHECKED
%TO CREATE OUR FINAL LOCATIONS FOR THESE STRUCTURES
for iswbv = 2:length(swbv_possible)
    nextxswbv = swbv_possible(iswbv,1);
    nextyswbv = swbv_possible(iswbv,2);
    for jswbv = 1:cgswbv
        currentgoodxswbv = swbv_good(jswbv,1);
        currentgoodyswbv = swbv_good(jswbv,2);
        swbv_dist = sqrt((nextxswbv - currentgoodxswbv)^2 + (nextyswbv
- currentgoodyswbv)^2);
        %Error-checking loop prevents trabeculae positions from being
        %too close (resulting in overlapping radii and bad geometry),
        %also checks positions from being too close to boundaries
        %(causing trabeculae to "spill out" of cross-section's
        %boundaries
        SWBVTooClose = false; %will switch to true if bad point is
        found
        if swbv_dist < 2.1*trab_diam ||...
           nextxswbv <= trab_diam || nextxswbv >= (L-trab_diam) || ...
           nextyswbv <= trab_diam || nextyswbv >= (L-trab_diam)
           SWBVTooClose = true;
           num_retries = num_retries+1; %counter to see if working
            break; %since point is bad, leave loop, do not store, and
            redo
        end
    end
      %Populates "good" vector with trabeculae positions that do not
      %break any of the aforementioned geometry criterion
    if ~SWBVTooClose %~ means false (aka our points are good/not
    interfering)
        if cgswbv < swbv_total
            cgswbv = cgswbv + 1;
```

```
            swbv_good(cgswbv,1) = nextxswbv;
            swbv_good(cgswbv,2) = nextyswbv;
            %plot
            plot(swbv_good(1,1),swbv_good(1,2),'ko')
            plot(swbv_good(cgswbv,1),swbv_good(cgswbv,2),'ko')
            grid on;
            set(gca, 'GridLineStyle', '-');
            axis([0 1.5 0 1.5])
            hold on
            formatSpec = ['    a.Instance(name=''Trabeculae with BV-
%1.0f'', part=p, dependent=ON)\n','    a = mdb.models[''Model-
1''].rootAssembly\n','    a.translate(instanceList=(''Trabeculae with
BV-%1.0f'', ), vector=(%2.8f, 0.0, -%2.8f))\n'];

fprintf(formatSpec,cgswbv,cgswbv,swbv_good(cgswbv,1),swbv_good(cgswbv,2
))
        end
    end

end
%5) ENDPOINTS AND CONNECTING LINES ARE GENERATED FOR THE "SHEET" STYLE
%SHAPES (CLOSES THE START POINTS OF STEPS 2,3,& 4)
sprintf('SHORT SHEET ROTATION CODE')
for iss2 = 1:ss_total %short sheet loop
    ang_ss(iss2,1) = 2*pi*rand(1,1);
    ang_ssdeg(iss2,1) = ang_ss(iss2,1).*(180/pi);
    ss_endpt(iss2,1) = ss_good(iss2,1) + ss_length*cos(ang_ss(iss2,1));
    ss_endpt(iss2,2) = ss_good(iss2,2) + ss_length*sin(ang_ss(iss2,1));
    line([ss_good(iss2,1) ss_endpt(iss2,1)],[ss_good(iss2,2)
ss_endpt(iss2,2)],'Color',[0 1 0])
    plot(ss_endpt(:,1),ss_endpt(:,2),'go')
    hold on
    formatSpec = ['    a = mdb.models[''Model-1''].rootAssembly\n','
a.rotate(instanceList=(''Trabeculae Short Sheet-%1.0f'', ),
axisPoint=(%2.8f, 0.0, -%2.8f), axisDirection=(0.0, 0.8, 0.0),
angle=%3.8f)\n'];

fprintf(formatSpec,iss2,ss_good(iss2,1),ss_good(iss2,2),ang_ssdeg(iss2,
1))
end
sprintf('LONG SHEET ROTATION CODE')
for ils2 = 1:ls_total %long sheet loop
    ang_ls(ils2,1) = 2*pi*rand(1,1);
    ang_lsdeg(ils2,1) = ang_ls(ils2,1).*(180/pi);
    ls_endpt(ils2,1) = ls_good(ils2,1) + ls_length*cos(ang_ls(ils2,1));
    ls_endpt(ils2,2) = ls_good(ils2,2) + ls_length*sin(ang_ls(ils2,1));
    line([ls_good(ils2,1) ls_endpt(ils2,1)],[ls_good(ils2,2)
ls_endpt(ils2,2)],'Color',[1 0 0])
    plot(ls_endpt(:,1),ls_endpt(:,2),'ro')
    hold on
    formatSpec = ['    a = mdb.models[''Model-1''].rootAssembly\n','
a.rotate(instanceList=(''Trabeculae Long Sheet-%1.0f'', ),
axisPoint=(%2.8f, 0.0, -%2.8f), axisDirection=(0.0, 0.8, 0.0),
angle=%3.8f)\n'];

fprintf(formatSpec,ils2,ls_good(ils2,1),ls_good(ils2,2),ang_lsdeg(ils2,
1))
```

```
end
sprintf('AT WITH BV ROTATION CODE')
for iswbv2 = 1:swbv_total %sheet with bridging vein loop
    ang_swbv(iswbv2,1) = 2*pi*rand(1,1);
    ang_swbvdeg(iswbv2,1) = ang_swbv(iswbv2,1).*(180/pi);
    swbv_endpt(iswbv2,1) = swbv_good(iswbv2,1) +
swbv_length*cos(ang_swbv(iswbv2,1));
    swbv_endpt(iswbv2,2) = swbv_good(iswbv2,2) +
swbv_length*sin(ang_swbv(iswbv2,1));
    line([swbv_good(iswbv2,1)
swbv_endpt(iswbv2,1)],[swbv_good(iswbv2,2)
swbv_endpt(iswbv2,2)],'Color',[0 0 0])
    plot(swbv_endpt(:,1),swbv_endpt(:,2),'ko')
    hold on
    formatSpec = ['    a = mdb.models[''Model-1''].rootAssembly\n','
a.rotate(instanceList=(''Trabeculae with BV-%1.0f'', ),
axisPoint=(%2.8f, 0.0, -%2.8f), axisDirection=(0.0, 0.8, 0.0),
angle=%3.8f)\n'];

fprintf(formatSpec,iswbv2,swbv_good(iswbv2,1),swbv_good(iswbv2,2),ang_s
wbvdeg(iswbv2,1))
end
```

B.2 Python Script for ABAQUS Model Creation

```
# Do not delete the following import lines
from abaqus import *
from abaqusConstants import *
import __main__

def PorcineMult3():   #Stuff that ABAQUS needs to work (common to all
macros)
    import section
    import regionToolset
    import displayGroupMdbToolset as dgm
    import part
    import material
    import assembly
    import step
    import interaction
    import load
    import mesh
    import optimization
    import job
    import sketch
    import visualization
    import xyPlot
    import displayGroupOdbToolset as dgo
    import connectorBehavior
#Pia-Arachnoid Membrane Steps
    step =
mdb.openStep('D:\Abaqus_Working_Directory\CAD\Porcine_Pia.STEP',
scaleFromFile=OFF)#Imports membrane part
    mdb.models['Model-1'].PartFromGeometryFile(name='Pia',
geometryFile=step, combine=False, dimensionality=THREE_D,
type=DEFORMABLE_BODY)
    p = mdb.models['Model-1'].parts['Pia']
#Creates Part in abaqus? (referenced as "p")
    a = mdb.models['Model-1'].rootAssembly
#Creates assembly in abaqus? (referenced as "a")
    a = mdb.models['Model-1'].rootAssembly
    a.DatumCsysByDefault(CARTESIAN)
    p = mdb.models['Model-1'].parts['Pia']
    a.Instance(name='Pia-1', part=p, dependent=ON)
#Creates instance within assembly module? (p1 is new reference for
dependent instance?)

#Arachnoid Trabeculae Chord Steps
    step = mdb.openStep('D:\Abaqus_Working_Directory\CAD\Porcine AT
Chord.STEP', scaleFromFile=OFF)#imports part as 3D, deformable body
    mdb.models['Model-1'].PartFromGeometryFile(name='Trabeculae Chord',
geometryFile=step, combine=False, dimensionality=THREE_D,
type=DEFORMABLE_BODY)
    p = mdb.models['Model-1'].parts['Trabeculae Chord']
#creates part - now references this as "p" (pia-arachnoid membrane is
no longer p?)
    a = mdb.models['Model-1'].rootAssembly
    a = mdb.models['Model-1'].rootAssembly
    p = mdb.models['Model-1'].parts['Trabeculae Chord']
```

```
    #Instancing starts here
    a.Instance(name='Trabeculae Chord-1', part=p, dependent=ON)
    a = mdb.models['Model-1'].rootAssembly
    a.translate(instanceList=('Trabeculae Chord-1', ),
vector=(0.52156901, 0.0, -1.27606901))
    a.Instance(name='Trabeculae Chord-2', part=p, dependent=ON)
    a = mdb.models['Model-1'].rootAssembly
    a.translate(instanceList=('Trabeculae Chord-2', ),
vector=(0.22499588, 0.0, -0.84083929))
    a.Instance(name='Trabeculae Chord-3', part=p, dependent=ON)
    a = mdb.models['Model-1'].rootAssembly
    a.translate(instanceList=('Trabeculae Chord-3', ),
vector=(0.87913810, 0.0, -1.39441330))
    # And this is repeated for all Trabeculae Chords...

#Arachnoid Trabeculae Short Sheet Step
    step = mdb.openStep('D:\Abaqus_Working_Directory\CAD\Porcine AT
Short Sheet.STEP', scaleFromFile=OFF)          #import short sheet as 3d
deformable
    mdb.models['Model-1'].PartFromGeometryFile(name='Trabeculae Short
Sheet', geometryFile=step, combine=False, dimensionality=THREE_D,
type=DEFORMABLE_BODY)
    p = mdb.models['Model-1'].parts['Trabeculae Short Sheet']
#re-references part as "p"
    a = mdb.models['Model-1'].rootAssembly
#re-references assembly as "a"a = mdb.models['Model-1'].rootAssembly
    p = mdb.models['Model-1'].parts['Trabeculae Short Sheet']
    #instance
    a.Instance(name='Trabeculae Short Sheet-1', part=p, dependent=ON)
    a = mdb.models['Model-1'].rootAssembly
    a.translate(instanceList=('Trabeculae Short Sheet-1', ),
vector=(0.18589842, 0.0, -0.70060228))
    a.Instance(name='Trabeculae Short Sheet-2', part=p, dependent=ON)
    a = mdb.models['Model-1'].rootAssembly
    a.translate(instanceList=('Trabeculae Short Sheet-2', ),
vector=(0.73553594, 0.0, -0.97229761))
    a.Instance(name='Trabeculae Short Sheet-3', part=p, dependent=ON)
    a = mdb.models['Model-1'].rootAssembly
    a.translate(instanceList=('Trabeculae Short Sheet-3', ),
vector=(1.27949723, 0.0, -0.03784227))
# And this is repeated for all Trabeculae Short Sheets...

#Arachnoid Trabeculae Long Sheet Step
    step = mdb.openStep('D:\Abaqus_Working_Directory\CAD\Porcine AT
Long Sheet.STEP', scaleFromFile=OFF)
    mdb.models['Model-1'].PartFromGeometryFile(name='Trabeculae Long
Sheet', geometryFile=step, combine=False, dimensionality=THREE_D,
type=DEFORMABLE_BODY)
    p = mdb.models['Model-1'].parts['Trabeculae Long Sheet']
    a = mdb.models['Model-1'].rootAssembly
    a = mdb.models['Model-1'].rootAssembly
    p = mdb.models['Model-1'].parts['Trabeculae Long Sheet']
    #instance
    a.Instance(name='Trabeculae Long Sheet-1', part=p, dependent=ON)
    a = mdb.models['Model-1'].rootAssembly
    a.translate(instanceList=('Trabeculae Long Sheet-1', ),
vector=(1.11831911, 0.0, -0.68408650))
```

```
    a.Instance(name='Trabeculae Long Sheet-2', part=p, dependent=ON)
    a = mdb.models['Model-1'].rootAssembly
    a.translate(instanceList=('Trabeculae Long Sheet-2', ),
vector=(1.00440118, 0.0, -0.21250409))
    a.Instance(name='Trabeculae Long Sheet-3', part=p, dependent=ON)
    a = mdb.models['Model-1'].rootAssembly
    a.translate(instanceList=('Trabeculae Long Sheet-3', ),
vector=(0.27629115, 0.0, -0.49813925))
    # And this is repeated for all Trabeculae Long Sheets...

#Arachnoid Trabeculae /w/ Bridging Vein Step
    step = mdb.openStep('D:\Abaqus_Working_Directory\CAD\Porcine AT for
BV.STEP', scaleFromFile=OFF)
    mdb.models['Model-1'].PartFromGeometryFile(name='Trabeculae with
BV', geometryFile=step, combine=False, dimensionality=THREE_D,
type=DEFORMABLE_BODY)
    p = mdb.models['Model-1'].parts['Trabeculae with BV']
    a = mdb.models['Model-1'].rootAssembly
    a = mdb.models['Model-1'].rootAssembly
    p = mdb.models['Model-1'].parts['Trabeculae with BV']
    #instances
    a.Instance(name='Trabeculae with BV-2', part=p, dependent=ON)
    a = mdb.models['Model-1'].rootAssembly
    a.translate(instanceList=('Trabeculae with BV-2', ),
vector=(0.44095958, 0.0, -0.78915370))
    a.Instance(name='Trabeculae with BV-3', part=p, dependent=ON)
    a = mdb.models['Model-1'].rootAssembly
    a.translate(instanceList=('Trabeculae with BV-3', ),
vector=(1.11947014, 0.0, -1.09456417))
#Rotating Step for SS
    a = mdb.models['Model-1'].rootAssembly
    a.rotate(instanceList=('Trabeculae Short Sheet-1', ),
axisPoint=(0.18589842, 0.0, -0.70060228), axisDirection=(0.0, 0.8,
0.0), angle=249.31151510)
    a = mdb.models['Model-1'].rootAssembly
    a.rotate(instanceList=('Trabeculae Short Sheet-2', ),
axisPoint=(0.73553594, 0.0, -0.97229761), axisDirection=(0.0, 0.8,
0.0), angle=200.40114059)
    a = mdb.models['Model-1'].rootAssembly
    a.rotate(instanceList=('Trabeculae Short Sheet-3', ),
axisPoint=(1.27949723, 0.0, -0.03784227), axisDirection=(0.0, 0.8,
0.0), angle=142.74748533)
# And this is repeated to rotate all Short Sheets...

#Rotating Step for LS
    a = mdb.models['Model-1'].rootAssembly
    a.rotate(instanceList=('Trabeculae Long Sheet-1', ),
axisPoint=(1.11831911, 0.0, -0.68408650), axisDirection=(0.0, 0.8,
0.0), angle=287.40631108)
    a = mdb.models['Model-1'].rootAssembly
    a.rotate(instanceList=('Trabeculae Long Sheet-2', ),
axisPoint=(1.00440118, 0.0, -0.21250409), axisDirection=(0.0, 0.8,
0.0), angle=339.48293025)
    a = mdb.models['Model-1'].rootAssembly
    a.rotate(instanceList=('Trabeculae Long Sheet-3', ),
axisPoint=(0.27629115, 0.0, -0.49813925), axisDirection=(0.0, 0.8,
0.0), angle=246.13760607)
```

```
# And this is repeated to rotate all Long Sheets...

#Rotating Step for SWBV
    a = mdb.models['Model-1'].rootAssembly
    a.rotate(instanceList=('Trabeculae with BV-2', ),
axisPoint=(0.44095958, 0.0, -0.78915370), axisDirection=(0.0, 0.8,
0.0), angle=269.68732672)
    a = mdb.models['Model-1'].rootAssembly
    a.rotate(instanceList=('Trabeculae with BV-3', ),
axisPoint=(1.11947014, 0.0, -1.09456417), axisDirection=(0.0, 0.8,
0.0), angle=209.94686332)
```

APPENDIX C

MICROSCALE MODEL CONVERGENCE STUDY RESULTS

C.1 Arachnoid Trabeculae Chord Convergence

The first substructure tested was the chord shape structures. The same surface traction of 4 kPa was applied to the bottom surface of the chord in all cases to cause the shearing. Three element types were tested: quadratic hexahedral (C3D20R), linear tetrahedral (C3D4), and quadratic tetrahedral (C3D10). Linear hexahedral elements were not considered due to their known limitations at representing curved geometries, as well as their tendency to cause shear-locking errors in shear and bending problems. The chords were seeded by specifying a number of circumferential seed points and selecting a radially symmetric meshing strategy.

To ensure consistency in our convergence study, the furthest point in the direction of the shear, at the bottom surface of the structure was sampled for maximum deflection each time (Figure14A). Figure 58 shows the results for all three element types, and one can clearly see that the linear tetrahedral (C3D4) elements exhibited artificial over stiffening of the structure. The C3D4 elements were removed from consideration and our selection was based only on the remaining quadratic elements (Figure 59).

Since all of these trabecular structures are repeated multiple times in our final models, simulation run time is largely dependent on the number of nodes the substructure introduce to the model. The chosen final mesh was seeded with 10 seeds around the circumference of the cylinder, resulting in a mesh with 676 elements and 3638 nodes (Figure 16A).

This mesh density was chosen as it minimized number of elements while keeping our error below 0.001mm in deflection, which was 0.5% of the accepted value (0.21825mm).

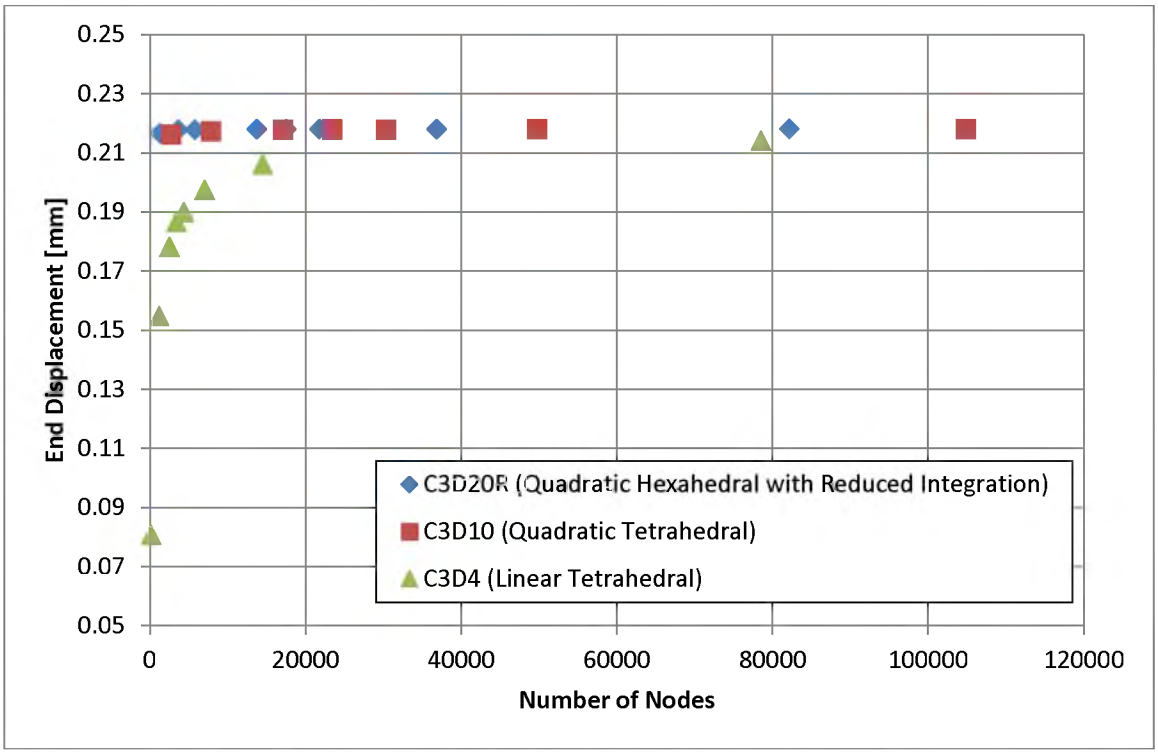

Figure 58: AT chord structure convergence study results (all three element types shown).

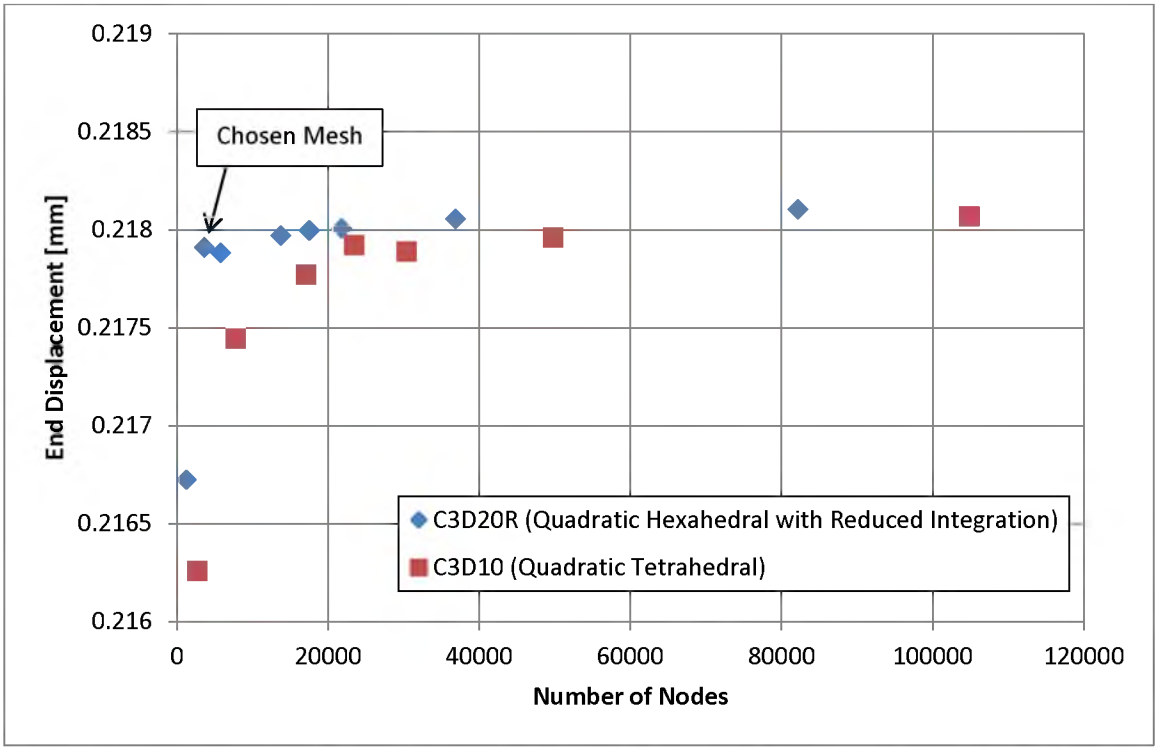

Figure 59: AT chord structure convergence study results (only quadratic element types shown)

C.2 Arachnoid Trabeculae Sheet Convergence

Since both sheet structures had identical geometry (with the exception of length), only the short sheet was tested for convergence. The convergence variable in these tests was also the maximum deflection on the bottom surface (Figure 14B). Only quadratic elements were tested for these structures due to the poor performance the linear hexahedral elements had in the chord studies. The same node position (of maximum deflection) was sampled for all tests and the same shear traction (4 kPa) was applied during each test. In these studies, the tetrahedral elements converged much smoother and quicker than the hexahedral elements (Figure 60). The tetrahedral (C3D10) mesh was chosen as our element type. The chosen mesh had a semicircumferential seed of 4 nodes (i.e., 4 nodes per semicircular end of each sheet), resulting in a mesh with 26,814 nodes for the short sheet and 33,588 nodes for the long sheet (Figure 16B-C).

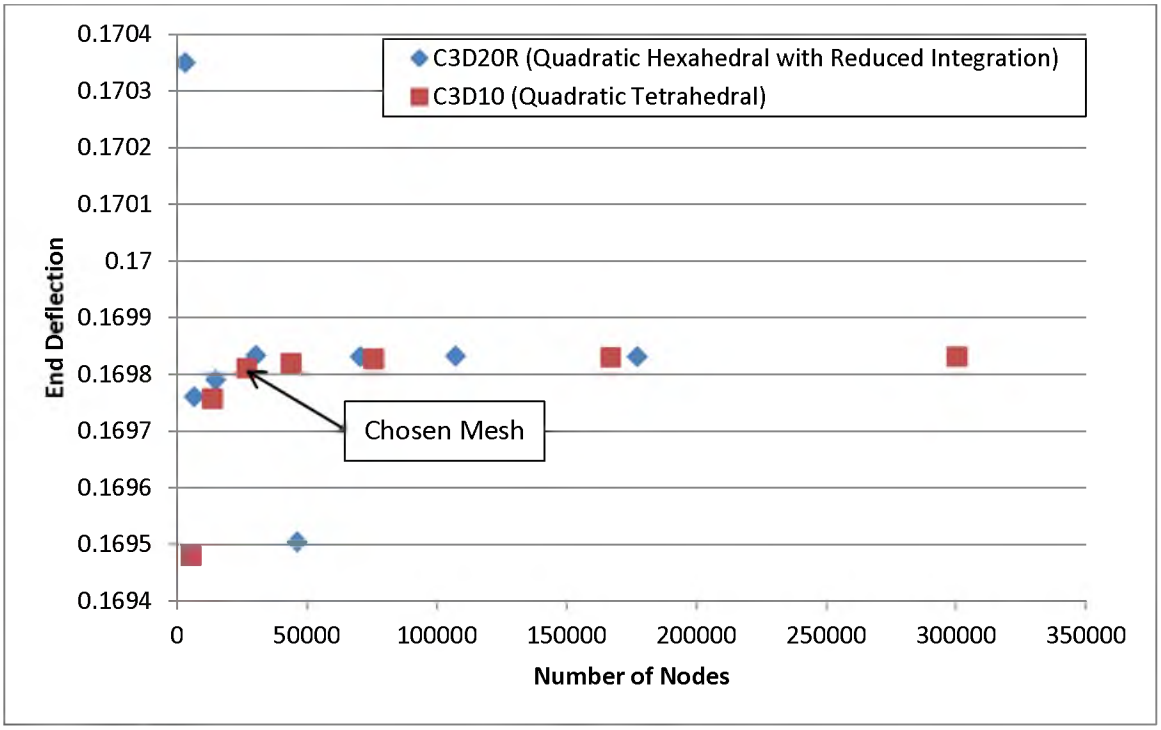

Figure 60: Sheet structure convergence study results

No additional mesh controls were needed as the mesh in the middle of the sheets was simply driven by these semicircumference seeds at the ends. This mesh minimized the number of nodes and was within a deflection error of 0.0001mm, which was well within our error tolerance (Figure 16B-C). The average element aspect ratio was 1.54 for the short sheet and 1.43 for the long sheet. The average shape factor for the short sheet was 0.7012 and 0.7573 for the long sheet.

C.3 Arachnoid Trabeculae Enveloping Subarachnoid Vasculature Convergence

Convergence of the AT sheets which enveloped subarachnoid vessels proved more difficult than the chord and sheet shapes. The AT sheet was meshed with quadratic tetrahedral elements and the vessel was meshed with quadratic hexahedral elements due to prior observations on which elements performed best. For this study, a moderately dense mesh with good mesh quality metrics close to our final mesh size for the previous sheet studies was chosen as our baseline mesh for the AT sheet. Then, we varied the mesh density of the vessel until vessel strain (our criterion) was within 0.5% error from the assumed true value. As before, a shear load of 4kPa was applied to the SAV/AT structure (Figure 14C-D). Convergence was difficult to determine, however, because vessel strain oscillated above and below a logarithmic decay towards our "true" value (Figure 61). This oscillation is likely due to the influence of mesh density on the master-slave relationship between the AT sheet and the SAV. If the mesh of the AT sheet lines up with the mesh of the SAV very well (i.e., even mesh ratios such as 1:1, 1:2, 1:4), the slave nodes of the SAV do not need to adjust very far to tie with the master nodes of the

AT sheet. However, if the AT mesh is mismatched with the SAV mesh (i.e., non-normal mesh ratios such as 1:5, 2:3, etc.) the slave nodes must be adjusted further, and may affect the final strain. At higher densities, the oscillation decreased, and a logarithmic decay was observed in the data. A logarithmic trend line was fit to the data, and a mesh density was chosen that was within 0.5% of the assumed true value (0.02925). To choose our final mesh, we ensured we had a good matchup between our master and slave node pair, as to avoid the aforementioned oscillations. The final mesh had 42 nodes around the circumference of the vessel, resulting in 32164 nodes, with an average element aspect ratio of 1.25 (Figure 16D). Shape factor was not reported as it does not apply to hexahedral elements.

After the final mesh was chosen for the SAV, the AT membrane was iterated to a converged value while keeping the SAV mesh constant. End-tip deflection was used as the convergence parameter as in the other AT convergence studies. The membrane converged well and did not exhibit the oscillation from the master-slave pairing (Figure 62). The final mesh had a global element length of 0.03mm and contained 30651 nodes (Figure 16E). The average element aspect ratio was 1.43 and the average shape factor was 0.78.

C.4 Dura, Upper Arachnoid, and Pia Membranes Convergence

The final convergence study was performed on the entire assembled model, utilizing all of the aforementioned chosen meshes for the subcomponenents. The dura, pia, and arachnoid membranes were each meshed with linear hexahedral (C3D4R) elements. Shear traction was applied to the model and it was sampled for maximum pial

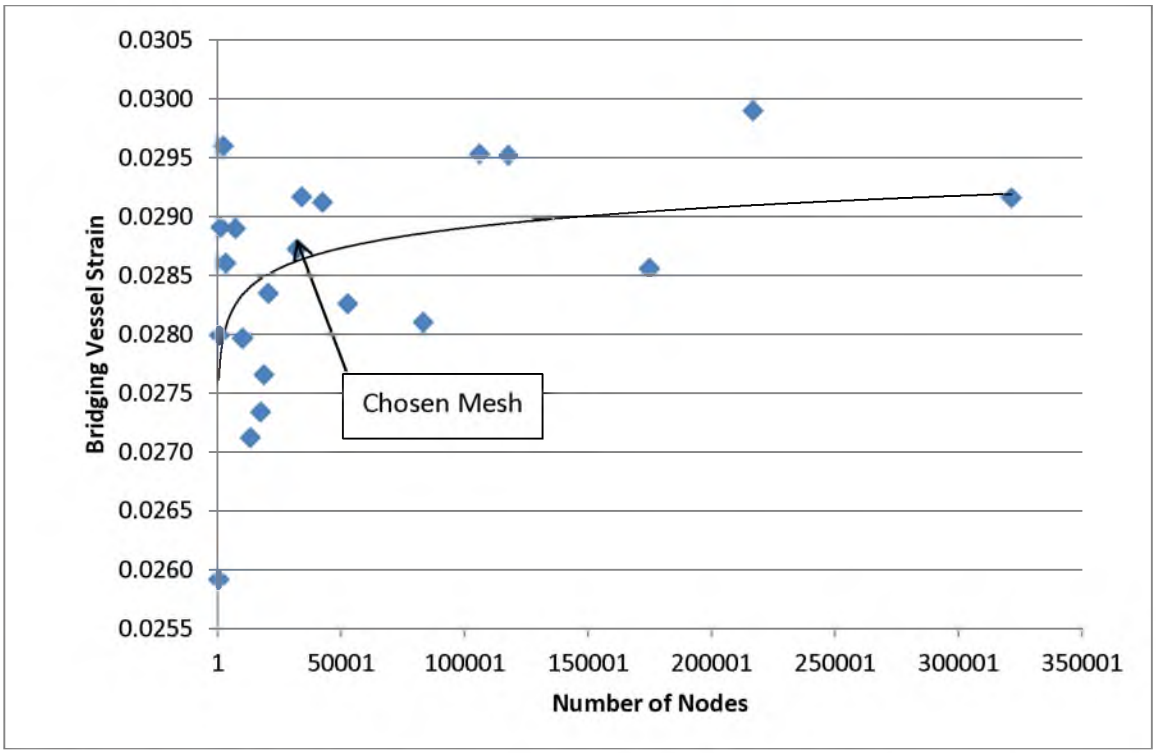

Figure 61: Subarachnoid vessel (SAV) convergence study results

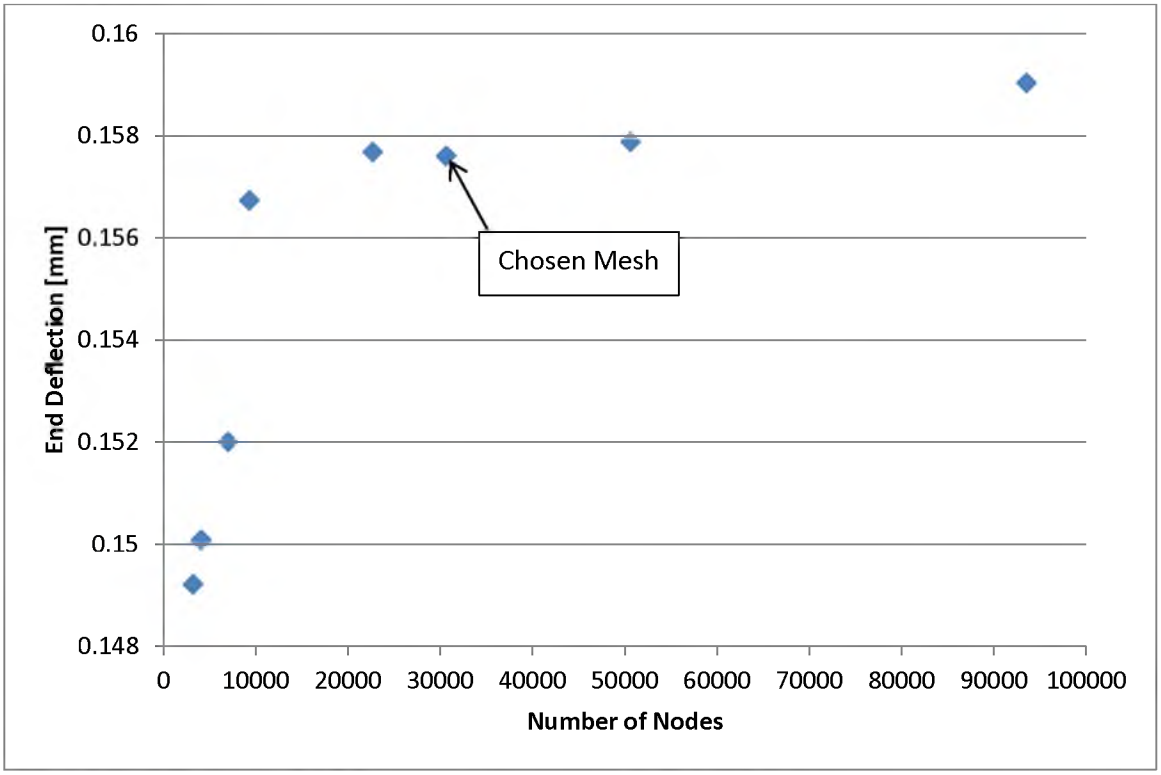

Figure 62: AT vessel membrane convergence study results

deflection and maximum strain in each SAV; these two variables were our convergence criterion. Since multiple SAV structures existed in the model, the average of each structure's maximum strain value was reported. The membranes were seeded with global element edge lengths of decreasing size until an acceptable convergence was observed in both variables (Figure 63 and Figure 64). The dura and upper arachnoid contributed very little to the deflection of the model due to their relatively high moduli, as such it was not deemed necessary to perform separate convergence studies for them. Instead, the dura and upper arachnoid were seeded at twice the edge length of the pia each time (resulting in a twice as course mesh, which did not introduce any problems). Note that in addition to the global element size, edge seeds had to be applied across the thickness of the membrane in order to allow for more than one element to exist across the thickness. This eliminated some early hour-glassing and shear-locking errors found in courser meshes. The final mesh for the dura and upper arachnoid was seeded with a global seed size of 0.1mm and an edge seed of 2, resulting in 3200 nodes total (Figure 16F). The final chosen mesh for the pia was seeded with a global seed size of 0.05mm and an edge seed of 3, resulting in 26244 nodes total (Figure 16G).

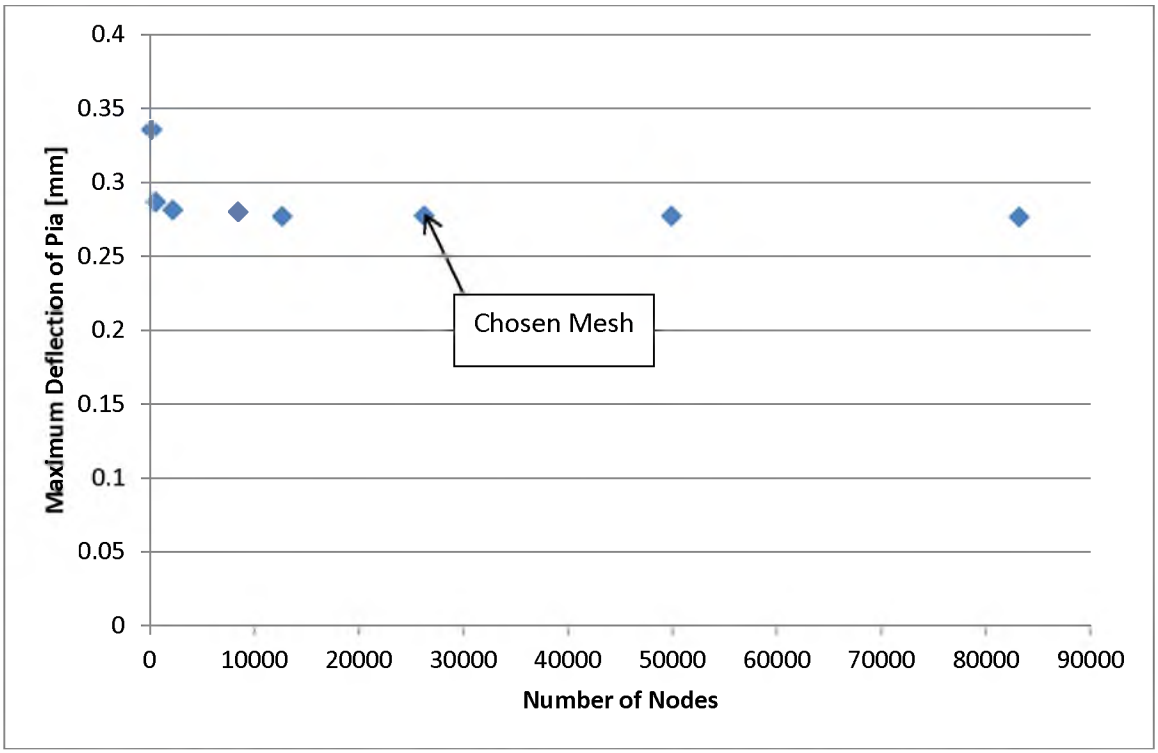

Figure 63: Pia, dura, and upper arachnoid membrane convergence study results

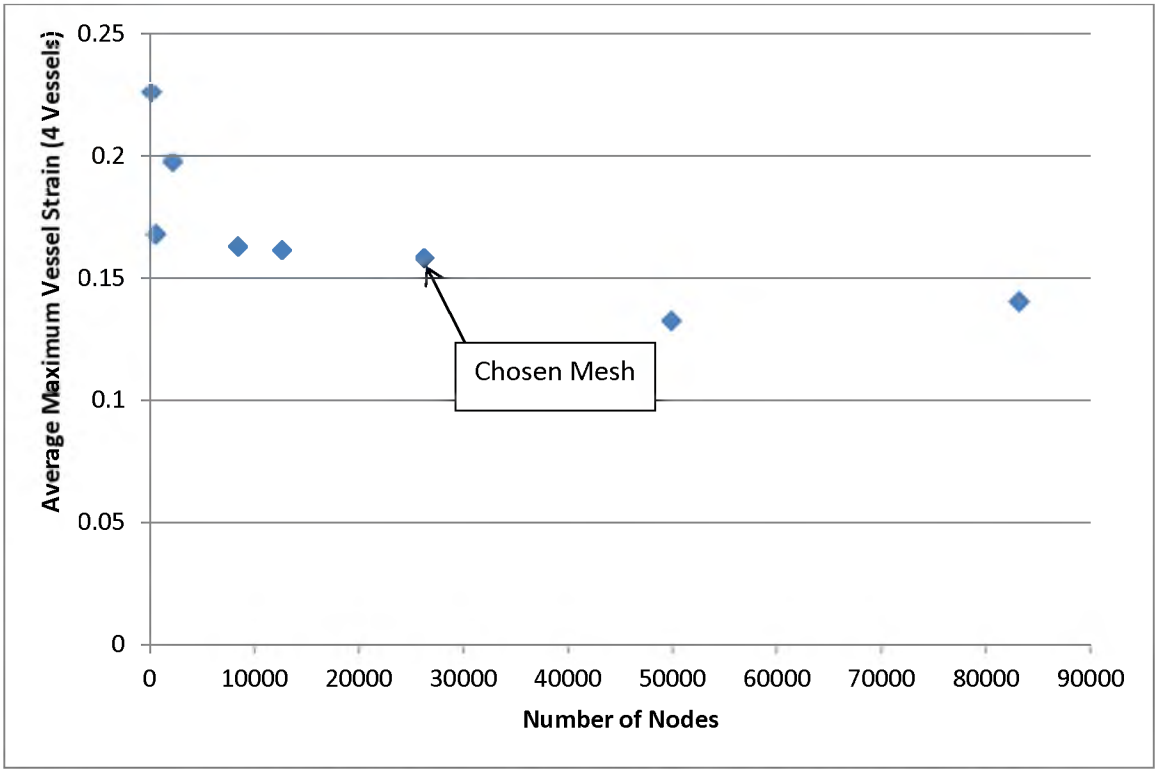

Figure 64: Pia, dura, and upper arachnoid membrane convergence study results

APPENDIX D

MACROSCALE MODEL ABAQUS AND MATLAB CODES

D.1 Multiscale Model Input Files

Input file for P13-121:

```
*HEADING
Modeling for 5 day old piglet axial rotation, ABAQUS job created on 27-Mar-08 at
09:51:58
** units: mm, kg, mN, KPa, rad/sec
**
** Uses 50%laplacian, 50%isomesh parameters for mesh,
**      frictional sliding for all brain-skull & brain-plexiglass plate contacts,
**      tracer points on entire sliced brain surfact & 2 front of skull points
**
*RESTART, WRITE, NUMBER INTERVAL=10
**
** ----------------------------------------------------------
** Define Center of Rotation
** ----------------------------------------------------------
** define rigid reference node for skull rigid body
*Node
 999999, 67.195000, 69.063995, -52.51
*NSET, NSET=CENTER_ROTATION
 999999
**
** measured on 5d piglet from front of eye socket to C5 spine
**   and scaled from same on 4wk piglet (by 0.89)
**
** ----------------------------------------------------------
** Define Skull
** ----------------------------------------------------------
** define nodes in skull
*INCLUDE,INPUT=skull_nodes_70830.inp
** define elements in skull
*INCLUDE,INPUT=skull_elem_finer_mesh.inp
**
** uses R3D4 (rigid body quadrilateral elements) elements
**   governed by motion of rigid reference node 999999,
**   elems set BCs of brain rotation deformation
**
** ----------------------------------------------------------
** define skull as rigid body
*RIGID BODY, REF NODE=999999, ELSET=SKULL_ELEM
**
** ----------------------------------------------------------
** Define CSF
** ----------------------------------------------------------
**
```

```
*INCLUDE, INPUT=CSF_elem.inp
*INCLUDE, INPUT=CSF_nodes.inp
**
**include new node sets
*INCLUDE, INPUT=CSF_Bottom_Nodes.inp
*INCLUDE, INPUT=CSF_LLF_Nodes.inp
*INCLUDE, INPUT=CSF_LLP_Nodes.inp
*INCLUDE, INPUT=CSF_LLO_Nodes.inp
*INCLUDE, INPUT=CSF_LMF_Nodes.inp
*INCLUDE, INPUT=CSF_LMP_Nodes.inp
*INCLUDE, INPUT=CSF_LMO_Nodes.inp
*INCLUDE, INPUT=CSF_RLF_Nodes.inp
*INCLUDE, INPUT=CSF_RLP_Nodes.inp
*INCLUDE, INPUT=CSF_RLO_Nodes.inp
*INCLUDE, INPUT=CSF_RMF_Nodes.inp
*INCLUDE, INPUT=CSF_RMP_Nodes.inp
*INCLUDE, INPUT=CSF_RMO_Nodes.inp
**element  new element sets
*INCLUDE, INPUT=CSF_Bottom_Elements.inp
*INCLUDE, INPUT=CSF_LLF_Elements.inp
*INCLUDE, INPUT=CSF_LLP_Elements.inp
*INCLUDE, INPUT=CSF_LLO_Elements.inp
*INCLUDE, INPUT=CSF_LMF_Elements.inp
*INCLUDE, INPUT=CSF_LMP_Elements.inp
*INCLUDE, INPUT=CSF_LMO_Elements.inp
*INCLUDE, INPUT=CSF_RLF_Elements.inp
*INCLUDE, INPUT=CSF_RLP_Elements.inp
*INCLUDE, INPUT=CSF_RLO_Elements.inp
*INCLUDE, INPUT=CSF_RMF_Elements.inp
*INCLUDE, INPUT=CSF_RMP_Elements.inp
*INCLUDE, INPUT=CSF_RMO_Elements.inp
**
** ----------------------------------------------------------
** Define Falx Cerebri
** ----------------------------------------------------------
** define nodes in falx
*INCLUDE,INPUT=falx_node_70830.inp
** define elements in falx
*INCLUDE,INPUT=falx_solid_elem_input.inp
**
** uses M3D4 (rigid body quadrilateral elements) elements
**
** ----------------------------------------------------------
** Define Brain
** ----------------------------------------------------------
** define nodes in brain
```

```
**   combine new p2 w p3 regions == p2
*INCLUDE,INPUT=brain_node_70830.inp
*NSET, NSET=BRAIN_NODE
 BRAIN_NODE_1
**
** define elements in brain
*INCLUDE,INPUT=brain_elem_brainstem_13018.inp
*ELSET, ELSET=BRAIN_ELEM
 BRAIN_ELEM_1
**
** uses C3D8R (reduced integration hexahedral) elements 2/2
**   hex elems are less stiff (better for stress analysis)
**   & ABAQUS/Explicit requires R for hex elems
** replaces C3D4 (tetrahedral) elements in p2 (transitional zone)
**   with new p2 closer to p3, combined w p3
**
** ----------------------------------------------------------
** Define Node Set for Output
** ----------------------------------------------------------
*NSET, NSET=ALL_NODE
 BRAIN_NODE, SKULL_NODE, CENTER_ROTATION, FALX_NODE, CSF_NODE,
CSF_BOTTOM_NODES, CSF_LLF, CSF_LLP,
 CSF_LLO, CSF_LMF, CSF_LMP, CSF_LMO, CSF_RLF, CSF_RLP, CSF_RLO,
 CSF_RMF, CSF_RMP, CSF_RMO
**
** ----------------------------------------------------------
** Define Brain Material Properties
** ----------------------------------------------------------
** define brain element properties (mixed gray-white matter)
*SECTION CONTROLS, NAME=BRAIN_HOURGLASS, HOURGLASS=VISCOUS,
DISTORTION CONTROL=YES, LENGTH RATIO = 0.25
*SOLID SECTION, ELSET=BRAIN_ELEM_1, MATERIAL=MIXED_GRAYWHITE,
CONTROLS=BRAIN_HOURGLASS
*MATERIAL, NAME=MIXED_GRAYWHITE
*DENSITY
 1.04E-6,
*HYPERELASTIC, N=1, OGDEN
  0.79035, 0.0100, 5.0611E-5
** use 1p5x stiffness
*VISCOELASTIC, TIME=PRONY
 0.3322, 0.0, 2.9572
 0.3890, 0.0, 0.1813
**
** specifies dissipative behavior for use with elasticity
**   for a linear, isotropic, viscoelastic material by giving
**   parameters of the Prony series representation of
```

```
**   relaxation moduli
** data input lines: g1P (modulus ratio in 1st term of
**   Prony series expansion of shear relaxation modulus),
**   k1P (modulus ratio in 1st term Prny s exp of bulk rlx mod),
**   tau1 (relaxation time for 1st term Prny s exp)
**   --> repeat this data line to define 2nd, 3rd, etc terms
**   (from data for Prange 2002 -- primary source?)
**
** ----------------------------------------------------------
** Define Falx Cerebri Material Properties
** ----------------------------------------------------------
** falx
**
*SOLID SECTION, ELSET=FALX_ELEM, MATERIAL=FALX
**       0.57,
**
*MATERIAL, NAME=FALX
**
*DENSITY
  1.130E-6,
**
*ELASTIC, TYPE=ISOTROPIC
    15E+3,        0.45
**
** ----------------------------------------------------------
** Define PAC Material Properties
** ----------------------------------------------------------
**
**Set Hourglass Controls for All Element Sets
*SECTION CONTROLS, NAME=CSF, HOURGLASS=VISCOUS
**Orientation for all Elements
*ORIENTATION, NAME=AllCSF, DEFINITION=OFFSET TO NODES,
SYSTEM=RECTANGULAR
6,5,8
**
**Properties for All Unscanned CSF Regions
*SOLID SECTION, ELSET=CSF_BOTTOM_ELEM, MATERIAL=RSE_AVG,
CONTROLS=CSF, ORIENTATION=AllCSF
*MATERIAL, NAME=RSE_AVG
*DENSITY
1E-6
*ELASTIC, TYPE=ENGINEERING CONSTANTS
**E1,E2,E3,v12,v13,v23,G12,G13,G23
14.43E+3,14.43E+3,70.108,0.45,0.002186,0.002186,4.976E+3,22.37
22.37
**
```

```
**Properties for LLF Region
*SOLID SECTION, ELSET=CSF_LLF_ELEM, MATERIAL=RSE_AVG,
CONTROLS=CSF, ORIENTATION=AllCSF
*MATERIAL, NAME=RSE_LLF
*DENSITY
1E-6
*ELASTIC, TYPE=ENGINEERING CONSTANTS
**E1,E2,E3,v12,v13,v23,G12,G13,G23
14.43E+3,14.43E+3,48.542,0.45,0.001514,0.001514,4.976E+3,22.37
22.37
**
**Properties for LLP Region
*SOLID SECTION, ELSET=CSF_LLP_ELEM, MATERIAL=RSE_AVG,
CONTROLS=CSF, ORIENTATION=AllCSF
*MATERIAL, NAME=RSE_LLP
*DENSITY
1E-6
*ELASTIC, TYPE=ENGINEERING CONSTANTS
**E1,E2,E3,v12,v13,v23,G12,G13,G23
14.43E+3,14.43E+3,59.325,0.45,0.001850,0.001850,4.976E+3,22.37
22.37
**
**Properties for LLO Region
*SOLID SECTION, ELSET=CSF_LLO_ELEM, MATERIAL=RSE_AVG,
CONTROLS=CSF, ORIENTATION=AllCSF
*MATERIAL, NAME=RSE_LLO
*DENSITY
1E-6
*ELASTIC, TYPE=ENGINEERING CONSTANTS
**E1,E2,E3,v12,v13,v23,G12,G13,G23
14.43E+3,14.43E+3,79.819,0.45,0.002489,0.002489,4.976E+3,22.37
22.37
**
**Properties for LMF Region
*SOLID SECTION, ELSET=CSF_LMF_ELEM, MATERIAL=RSE_AVG,
CONTROLS=CSF, ORIENTATION=AllCSF
*MATERIAL, NAME=RSE_LMF
*DENSITY
1E-6
*ELASTIC, TYPE=ENGINEERING CONSTANTS
**E1,E2,E3,v12,v13,v23,G12,G13,G23
14.43E+3,14.43E+3,38.017,0.45,0.001186,0.001186,4.976E+3,22.37
22.37
**
**Properties for LMP Region
*SOLID SECTION, ELSET=CSF_LMP_ELEM, MATERIAL=RSE_AVG,
```

```
CONTROLS=CSF, ORIENTATION=AllCSF
*MATERIAL, NAME=RSE_LMP
*DENSITY
1E-6
*ELASTIC, TYPE=ENGINEERING CONSTANTS
**E1,E2,E3,v12,v13,v23,G12,G13,G23
14.43E+3,14.43E+3,75.917,0.45,0.002367,0.002367,4.976E+3,22.37
22.37
**
**Properties for LMO Region
*SOLID SECTION, ELSET=CSF_LMO_ELEM, MATERIAL=RSE_AVG,
CONTROLS=CSF, ORIENTATION=AllCSF
*MATERIAL, NAME=RSE_LMO
*DENSITY
1E-6
*ELASTIC, TYPE=ENGINEERING CONSTANTS
**E1,E2,E3,v12,v13,v23,G12,G13,G23
14.43E+3,14.43E+3,52.153,0.45,0.001626,0.001626,4.976E+3,22.37
22.37
**
**Properties for RLF Region
*SOLID SECTION, ELSET=CSF_RLF_ELEM, MATERIAL=RSE_AVG,
CONTROLS=CSF, ORIENTATION=AllCSF
*MATERIAL, NAME=RSE_RLF
*DENSITY
1E-6
*ELASTIC, TYPE=ENGINEERING CONSTANTS
**E1,E2,E3,v12,v13,v23,G12,G13,G23
14.43E+3,14.43E+3,100.823,0.45,0.003144,0.003144,4.976E+3,22.37
22.37
**
**Properties for RLP Region
*SOLID SECTION, ELSET=CSF_RLP_ELEM, MATERIAL=RSE_AVG,
CONTROLS=CSF, ORIENTATION=AllCSF
*MATERIAL, NAME=RSE_RLP
*DENSITY
1E-6
*ELASTIC, TYPE=ENGINEERING CONSTANTS
**E1,E2,E3,v12,v13,v23,G12,G13,G23
14.43E+3,14.43E+3,65.196,0.45,0.002033,0.002033,4.976E+3,22.37
22.37
**
**Properties for RLO Region
*SOLID SECTION, ELSET=CSF_RLO_ELEM, MATERIAL=RSE_AVG,
CONTROLS=CSF, ORIENTATION=AllCSF
*MATERIAL, NAME=RSE_RLO
```

```
*DENSITY
1E-6
*ELASTIC, TYPE=ENGINEERING CONSTANTS
**E1,E2,E3,v12,v13,v23,G12,G13,G23
14.43E+3,14.43E+3,90.963,0.45,0.002837,0.002837,4.976E+3,22.37
22.37
**
**Properties for RMF Region
*SOLID SECTION, ELSET=CSF_RMF_ELEM, MATERIAL=RSE_AVG,
CONTROLS=CSF, ORIENTATION=AllCSF
*MATERIAL, NAME=RSE_RMF
*DENSITY
1E-6
*ELASTIC, TYPE=ENGINEERING CONSTANTS
**E1,E2,E3,v12,v13,v23,G12,G13,G23
14.43E+3,14.43E+3,78.280,0.45,0.002441,0.002441,4.976E+3,22.37
22.37
**
**Properties for RMP Region
*SOLID SECTION, ELSET=CSF_RMP_ELEM, MATERIAL=RSE_AVG,
CONTROLS=CSF, ORIENTATION=AllCSF
*MATERIAL, NAME=RSE_RMP
*DENSITY
1E-6
*ELASTIC, TYPE=ENGINEERING CONSTANTS
**E1,E2,E3,v12,v13,v23,G12,G13,G23
14.43E+3,14.43E+3,114.910,0.45,0.003583,0.003583,4.976E+3,22.37
22.37
**
**Properties for RMO Region
*SOLID SECTION, ELSET=CSF_RMO_ELEM, MATERIAL=RSE_AVG,
CONTROLS=CSF, ORIENTATION=AllCSF
*MATERIAL, NAME=RSE_RMO
*DENSITY
1E-6
*ELASTIC, TYPE=ENGINEERING CONSTANTS
**E1,E2,E3,v12,v13,v23,G12,G13,G23
14.43E+3,14.43E+3,51.802,0.45,0.001615,0.001615,4.976E+3,22.37
22.37
**
**
** ----------------------------------------------------------
** Define Connection between Brain and Skull
** ----------------------------------------------------------
** define connector elements between brain surface & skull
*INCLUDE,INPUT=connector_elem_falx_solid_brain.inp
```

```
***INCLUDE,INPUT=connector_elem_cort.inp
***INCLUDE,INPUT=connector_elem_BV.inp
**
**   Bridging Veins
**
*CONNECTOR SECTION, ELSET=CONNECT_BV, BEHAVIOR=BV_TIE
 AXIAL,
*CONNECTOR BEHAVIOR, NAME=BV_TIE
***CONNECTOR FAILURE, COMPONENT=1, RELEASE=ALL
** ,,,1210
**
**   Bridging vein stiffness
**
*CONNECTOR ELASTICITY, COMPONENT=1
 6430,,
**
**   Cortical veins
**
***CONNECTOR SECTION, ELSET=CONNECT_CORT,
BEHAVIOR=CORTEX_TIE
** AXIAL,
***CONNECTOR BEHAVIOR, NAME=CORTEX_TIE
***CONNECTOR FAILURE, COMPONENT=1, RELEASE=ALL
** ,,,515
**
**   Cortical vein stiffness
**
***CONNECTOR ELASTICITY, COMPONENT=1
** 3460,,
**
**
** ----------------------------------------------------------
** Define Contact Surfaces
** ----------------------------------------------------------
** define outer braiN, inner skull, and falx surfaces for contact
**
**Generates the "exterior (free) faces" of the brain elements
**
*SURFACE, NAME=BRAINFACE_1, TYPE=ELEMENT, REGION TYPE=SLIDING
 BRAIN_ELEM_1,
**
*SURFACE, NAME=SKULLINNER, TYPE=ELEMENT
 SKULL_ELEM, SPOS
**
*SURFACE, NAME=FALX, TYPE=ELEMENT
 FALX_ELEM,
```

```
**
*SURFACE, NAME=CSF_SURF, TYPE=ELEMENT
CSF_ELM
**
**
** ----------------------------------------------------------
** Tie falx to skull
** ----------------------------------------------------------
**
*INCLUDE, INPUT=falx_tie_nodes.inp
**
***TIE, NAME=FALX_SKULL_TIE, POSITION TOLERANCE=0.0080
*TIE, NAME=FALX_SKULL_TIE, TIED NSET=FALX_TIE
 FALX, SKULLINNER
*TIE, NAME=CSF, POSITION TOLERANCE=0.1, ADJUST=NO
CSF_SURF, BRAINFACE_1
CSF_SURF, SKULLINNER
CSF_SURF, FALX
**
** ----------------------------------------------------------
** Define Boundary Conditions
** ----------------------------------------------------------
** define degree of freedom constraints for center of rotation
*BOUNDARY, TYPE=DISPLACEMENT
 CENTER_ROTATION, 1, , 0.
 CENTER_ROTATION, 2, , 0.
 CENTER_ROTATION, 3, , 0.
 CENTER_ROTATION, 5, , 0.
 CENTER_ROTATION, 6, , 0.
**
** constrains center of rotation of model to motion only in
**   degree of freedom 4 (sagittal rotation)
**
** ----------------------------------------------------------
** define initial conditions
***INITIAL CONDITIONS, TYPE=ROTATING VELOCITY
** BRAIN_NODE, , , ,
** 60, 69.063995, -52.51, 70, 69.063995, -52.51
**
** axis of rotation at CENTER_ROTATION along x-axis
**
**
*SURFACE INTERACTION, NAME=DURA_CSF
*FRICTION
 0.2
**
```

```
** ----------------------------------------------------------
** Begin Step Definition for Analysis
** ----------------------------------------------------------
*STEP, NLGEOM=YES
*DYNAMIC, EXPLICIT, ELEMENT BY ELEMENT
 , 24E-3
**
** uses large-displacement formulation of element calculations
** uses element-by-element stable time increment estimates
**   generated by abaqus
** runs 10ms longer than end of velocity trace
**
** ----------------------------------------------------------
** Define Loading Conditions
** ----------------------------------------------------------
** define rotational velocity trace
*INCLUDE,INPUT=velocity_70830.inp
*BOUNDARY, AMPLITUDE=HYGEDATA, TYPE=VELOCITY
 CENTER_ROTATION, 4, , 1.
**
** rotational load prescribed by listed amplitudes from
**   recorded angular velocity trace is applied to
**   center of rotation about x-axis for rigid body skull motion
**
*DLOAD
BRAIN_ELEM_1, GRAV, 9.81, 0, .259, -.966
**
**
**   Addition of gravity
**
** ----------------------------------------------------------
** Define Contact Interactions
** ----------------------------------------------------------
** Define contact interaction between outer brain and inner skull surfaces (including
plexi plate)
** This is impact aread where connectors are not already determining this interaction.
**
***CONTACT PAIR, INTERACTION=DURA_CSF, CPSET=BRAIN_SKULL,
MECHANICAL CONSTRAINT=PENALTY
** BRAINFACE_1, SKULLINNER
***CONTACT CONTROLS, CPSET=BRAIN_SKULL, WARP CUT OFF=45,
GLOBTRKINC=5, FASTLOCALTRK=NO, SCALE PENALTY=5
***CONTACT PAIR, INTERACTION=DURA_CSF, CPSET=BRAIN_FALX,
MECHANICAL CONSTRAINT=PENALTY
** BRAINFACE_1, FALX
***CONTACT CONTROLS, CPSET=BRAIN_FALX, WARP CUT OFF=45,
```

```
GLOBTRKINC=5, FASTLOCALTRK=NO, SCALE PENALTY=2
**
*CONTACT
*CONTACT INCLUSIONS
 BRAINFACE_1, SKULLINNER
 BRAINFACE_1, FALX
 CSF_SURF, FALX
** defines surface interaction between outer brain & inner skull/plexi plate
**   as frictional sliding (mu=0.2) contact representing dura & CSF,
**   does global search every 10 increments for master-slave node matching
**   & uses conservative local searches between global searches
**
*INCLUDE,INPUT=5L_tracers.inp
*INCLUDE,INPUT=6L_tracers.inp
*INCLUDE,INPUT=7L_tracers.inp
*INCLUDE,INPUT=8L_tracers.inp
*INCLUDE,INPUT=9L_tracers.inp
*INCLUDE,INPUT=5R_tracers.inp
*INCLUDE,INPUT=6R_tracers.inp
*INCLUDE,INPUT=7R_tracers.inp
*INCLUDE,INPUT=8R_tracers.inp
*INCLUDE,INPUT=9R_tracers.inp
*INCLUDE,INPUT=midline_tracers.inp
**
***TRACER PARTICLE, TRACER SET=TRACER_NODES
** L5, L6, L7, L8, L9, R5, R6, R7, R8, R9, MIDLINE
**
** The above tracer nodse are to match to Stephanie's
** pathology
**
**
*INCLUDE, INPUT=brain_surf_nodes.inp
*INCLUDE, INPUT=skull_conn_nodes.inp
**
***TRACER PARTICLE, TRACER SET=DISPLACEMENT
**BNODES
**
** The above input files will create the node sets to
** calculate brain/skull displacment.
**
** ----------------------------------------------------------
** Define Output Conditions
** ----------------------------------------------------------
*OUTPUT, HISTORY, TIME INTERVAL=0.0001
*NODE OUTPUT, NSET=BNODES
COORD
```

```
***NODE OUTPUT, NSET=SNODES
**COORD
***ELEMENT OUTPUT, TRACER SET=TRACER_NODES
**SP3, NEP1, NEP3
**
*OUTPUT, FIELD, NUMBER INTERVAL=250
*ELEMENT OUTPUT, ELSET=BRAIN_ELEM
 S
*NODE OUTPUT, NSET=ALL_NODE
U
**
** ----------------------------------------------------------
** End Step Definition
** ----------------------------------------------------------
*END STEP
```

Input file for P13-122:

```
**NOTE ONLY THE PAC PROPERTIES LINES ARE SHOWN, ASIDE FROM THIS
**SECTION, EVERYTHING IN THIS CODE IS IDENTICAL TO P13-121'S CODE
** ----------------------------------------------------------
** Define PAC Material Properties
** ----------------------------------------------------------
**
**Set Hourglass Controls for All Element Sets
*SECTION CONTROLS, NAME=CSF, HOURGLASS=VISCOUS
**Orientation for all Elements
*ORIENTATION, NAME=AllCSF, DEFINITION=OFFSET TO NODES,
SYSTEM=RECTANGULAR
6,5,8
**
**Properties for All Unscanned CSF Regions
*SOLID SECTION, ELSET=CSF_BOTTOM_ELEM, MATERIAL=RSE_AVG,
CONTROLS=CSF, ORIENTATION=AllCSF
*MATERIAL, NAME=RSE_AVG
*DENSITY
1E-6
*ELASTIC, TYPE=ENGINEERING CONSTANTS
**E1,E2,E3,v12,v13,v23,G12,G13,G23
14.43E+3,14.43E+3,89.273,0.45,0.002784,0.002784,4.976E+3,22.37
22.37
**
**Properties for LLF Region
*SOLID SECTION, ELSET=CSF_LLF_ELEM, MATERIAL=RSE_AVG,
CONTROLS=CSF, ORIENTATION=AllCSF
*MATERIAL, NAME=RSE_LLF
*DENSITY
1E-6
```

```
*ELASTIC, TYPE=ENGINEERING CONSTANTS
**E1,E2,E3,v12,v13,v23,G12,G13,G23
14.43E+3,14.43E+3,100.434,0.45,0.003132,0.003132,4.976E+3,22.37
22.37
**
**Properties for LLP Region
*SOLID SECTION, ELSET=CSF_LLP_ELEM, MATERIAL=RSE_AVG,
CONTROLS=CSF, ORIENTATION=AllCSF
*MATERIAL, NAME=RSE_LLP
*DENSITY
1E-6
*ELASTIC, TYPE=ENGINEERING CONSTANTS
**E1,E2,E3,v12,v13,v23,G12,G13,G23
14.43E+3,14.43E+3,57.211,0.45,0.001784,0.001784,4.976E+3,22.37
22.37
**
**Properties for LLO Region
*SOLID SECTION, ELSET=CSF_LLO_ELEM, MATERIAL=RSE_AVG,
CONTROLS=CSF, ORIENTATION=AllCSF
*MATERIAL, NAME=RSE_LLO
*DENSITY
1E-6
*ELASTIC, TYPE=ENGINEERING CONSTANTS
**E1,E2,E3,v12,v13,v23,G12,G13,G23
14.43E+3,14.43E+3,128.395,0.45,0.004004,0.004004,4.976E+3,22.37
22.37
**
**Properties for LMF Region
*SOLID SECTION, ELSET=CSF_LMF_ELEM, MATERIAL=RSE_AVG,
CONTROLS=CSF, ORIENTATION=AllCSF
*MATERIAL, NAME=RSE_LMF
*DENSITY
1E-6
*ELASTIC, TYPE=ENGINEERING CONSTANTS
**E1,E2,E3,v12,v13,v23,G12,G13,G23
14.43E+3,14.43E+3,83.224,0.45,0.002595,0.002595,4.976E+3,22.37
22.37
**
**Properties for LMP Region
*SOLID SECTION, ELSET=CSF_LMP_ELEM, MATERIAL=RSE_AVG,
CONTROLS=CSF, ORIENTATION=AllCSF
*MATERIAL, NAME=RSE_LMP
*DENSITY
1E-6
*ELASTIC, TYPE=ENGINEERING CONSTANTS
**E1,E2,E3,v12,v13,v23,G12,G13,G23
```

```
14.43E+3,14.43E+3,79.886,0.45,0.002491,0.002491,4.976E+3,22.37
22.37
**
**Properties for LMO Region
*SOLID SECTION, ELSET=CSF_LMO_ELEM, MATERIAL=RSE_AVG,
CONTROLS=CSF, ORIENTATION=AllCSF
*MATERIAL, NAME=RSE_LMO
*DENSITY
1E-6
*ELASTIC, TYPE=ENGINEERING CONSTANTS
**E1,E2,E3,v12,v13,v23,G12,G13,G23
14.43E+3,14.43E+3,70.503,0.45,0.002199,0.002199,4.976E+3,22.37
22.37
**
**Properties for RLF Region
*SOLID SECTION, ELSET=CSF_RLF_ELEM, MATERIAL=RSE_AVG,
CONTROLS=CSF, ORIENTATION=AllCSF
*MATERIAL, NAME=RSE_RLF
*DENSITY
1E-6
*ELASTIC, TYPE=ENGINEERING CONSTANTS
**E1,E2,E3,v12,v13,v23,G12,G13,G23
14.43E+3,14.43E+3,84.200,0.45,0.002626,0.002626,4.976E+3,22.37
22.37
**
**Properties for RLP Region
*SOLID SECTION, ELSET=CSF_RLP_ELEM, MATERIAL=RSE_AVG,
CONTROLS=CSF, ORIENTATION=AllCSF
*MATERIAL, NAME=RSE_RLP
*DENSITY
1E-6
*ELASTIC, TYPE=ENGINEERING CONSTANTS
**E1,E2,E3,v12,v13,v23,G12,G13,G23
14.43E+3,14.43E+3,90.858,0.45,0.002833,0.002833,4.976E+3,22.37
22.37
**
**Properties for RLO Region
*SOLID SECTION, ELSET=CSF_RLO_ELEM, MATERIAL=RSE_AVG,
CONTROLS=CSF, ORIENTATION=AllCSF
*MATERIAL, NAME=RSE_RLO
*DENSITY
1E-6
*ELASTIC, TYPE=ENGINEERING CONSTANTS
**E1,E2,E3,v12,v13,v23,G12,G13,G23
14.43E+3,14.43E+3,120.235,0.45,0.003750,0.003750,4.976E+3,22.37
22.37
```

```
**
**Properties for RMF Region
*SOLID SECTION, ELSET=CSF_RMF_ELEM, MATERIAL=RSE_AVG,
CONTROLS=CSF, ORIENTATION=AllCSF
*MATERIAL, NAME=RSE_RMF
*DENSITY
1E-6
*ELASTIC, TYPE=ENGINEERING CONSTANTS
**E1,E2,E3,v12,v13,v23,G12,G13,G23
14.43E+3,14.43E+3,38.519,0.45,0.001201,0.001201,4.976E+3,22.37
22.37
**
**Properties for RMP Region
*SOLID SECTION, ELSET=CSF_RMP_ELEM, MATERIAL=RSE_AVG,
CONTROLS=CSF, ORIENTATION=AllCSF
*MATERIAL, NAME=RSE_RMP
*DENSITY
1E-6
*ELASTIC, TYPE=ENGINEERING CONSTANTS
**E1,E2,E3,v12,v13,v23,G12,G13,G23
14.43E+3,14.43E+3,113.242,0.45,0.003531,0.003531,4.976E+3,22.37
22.37
**
**Properties for RMO Region
*SOLID SECTION, ELSET=CSF_RMO_ELEM, MATERIAL=RSE_AVG,
CONTROLS=CSF, ORIENTATION=AllCSF
*MATERIAL, NAME=RSE_RMO
*DENSITY
1E-6
*ELASTIC, TYPE=ENGINEERING CONSTANTS
**E1,E2,E3,v12,v13,v23,G12,G13,G23
14.43E+3,14.43E+3,96.118,0.45,0.002997,0.002997,4.976E+3,22.37
22.37
**
```

D.2 Post-Processing MATLAB Code

```
%This code was adapated from a larger code originally written by By
%Brittany Coats for the publication:
%Coats B. et al., "Finite element model predictions of intracranial
%hemorrhage from non-impact rapid head rotations in the piglet" Int. J.
%Dev. Neurosi. (2012) doi:10.1016/j.ijdevneu.2011.12.009
%
%% This analysis file is specific to the CSF model.
% This code loads FEM data and calculates the distribution of cortical
% strain (NEP3), cortical stress (SP3) and brain-skull displacement
(COORD1-3).
% The distribution of these parameters will be divided up into 5
regions
% Anterior Left (AntL), Posterior left (PostL), Anterior Right (AntR),
% Posterior Right (PostR) and midline.  The pop1, 10, 50 and 90 of
these
% regions will be calculated at the end.

%File is organized according to input (SP3, NEP3, etc) so that entire
%sections can be commented out if the input is absent (or not wanted).

clear all
close all

%% Tracers file
% List of all nodes or connectors in each of the slices.  Used to
divide up
% the regions.  In addition to cortical surface nodes, CSF elements
were
% also analyzed.

load surf_nodes_by_slice.mat   %for SP3, NEP1/3 for brain surface
% load CSF_regions   %for NEP1/3 for CSF
load csurf_nodes_by_slice.mat %for brain/skull displacement

%% Matched nodes file
% File containing the skull node closest to each brain surface node.

load whole_brain_CSF_matched_nodes.mat

%% load data from FEM
%Each data file could contain NEP1, NEP3, brain_coord1/2/3, and
%skull_coord1/2/3. All elements and nodes will be in numerical order

load 121BSdisp.mat

%% Brain/Skull Displacement
%Requires brain_coord 1/2/3 & skull_coord 1/2/3

%Sorting
[nfe,mfe]=size(brain_coord1);

% nfe=number of history data timepoints
```

```
% mfe=number of tracer nodes +1(1st column=time column)

total_tr_fem=mfe-1;          % total # tracers in all regions

cAntL=[];
cAntR=[];
for i=1:cutoff-4
    cAntL=[cAntL; nonzeros(cleft_regions(:,i))];
    cAntR=[cAntR; nonzeros(cright_regions(:,i))];
end

cPostL=[];
cPostR=[];
for i=cutoff-3:5
    cPostL=[cPostL; nonzeros(cleft_regions(:,i))];
    cPostR=[cPostR; nonzeros(cright_regions(:,i))];
end

ncAntL=length(cAntL);      % # tracers AntL
ncAntR=length(cAntR);      % # tracers AntR
ncPostL=length(cPostL);    % # tracers PostL
ncPostR=length(cPostR);    % # tracers PostR
ncmidline=length(cmidline(:,1)); % # tracers along midline

% Note: No file size check is created because we have connectors along
the
% brainstem, but we don't want to include those in our analysis.

%Put each region into a column of the connectors file.

maxheight=max([ncAntL ncPostL ncAntR ncPostR ncmidline]);  %ncAntmid
ncPostmid]);
conns=zeros(maxheight,5);

conns(1:ncAntL,2)=cAntL;
conns(1:ncPostL,4)=cPostL;
conns(1:ncAntR,1)=cAntR;
conns(1:ncPostR,3)=cPostR;
conns(1:ncmidline,5)=cmidline(:,1);

conns_ordered=[cAntR; cAntL; cPostR; cPostL; cmidline(:,1)];
conns_ordered=sortrows(conns_ordered);
conns_ordered=unique(conns_ordered);

% Calculate displacement for each brain node

load skull_connect_nodes.mat

for i=1:length(matching)
    bnode=matching(i,2);
    snode=matching(i,3);
    locb=i+1;
    locs=find(connect_nodes==snode)+1;
    if isempty(locb)||isempty(locs)
```

```
        disp('You have a node that doesnt match. Check code');
        break
    else
        distance(:,i)=((brain_coord1(:,locb)-skull_coord1(:,locs)).^2+
(brain_coord2(:,locb)-skull_coord2(:,locs)).^2 + (brain_coord3(:,locb)-
skull_coord3(:,locs)).^2).^(1/2);
        displacement(:,i)=distance(:,i)-distance(1,i);
    end
end

% Find Peak Brain/Skull Displacement across all timepoints in FEM

PeakDisp=zeros(maxheight,5);

for i=1:5
    for j=1:length(nonzeros(conns(:,i)))
    loc=find(conns_ordered==conns(j,i));
    PeakDisp(j,i)=max(displacement(:,loc+1));
    end
end

% Cumulative Brain/Skull displacement distribution in each FEM Region
% (each region is in a column: [AntL, PostL, AntR, PostR, midline]).

dispincrement=0.001;
disptop=1.845;
counterdisp=zeros(ceil(disptop/dispincrement),5);
dispvector=zeros(ceil(disptop/dispincrement),5);

d=0;
k=1;
for i=1:5
    while k<length(counterdisp)+1
    dispvector(k,i)=d;

    for j=1:length(nonzeros(conns(:,i)))

        if PeakDisp(j,i)>d
        counterdisp(k,i)=counterdisp(k,i)+1;
        end
    end

    k=k+1;
    d=d+dispincrement;
    end
    d=0;
    k=1;
end

% Plot brain/skull displacement cumulative distribution
displacement=dispvector;

for i=1:5
    counter_disp(:,i)=counterdisp(:,i)./length(nonzeros(conns(:,i)));
end
```

```
figure()
for i=1:5
hold all;
    plot(displacement(:,i),counter_disp(:,i),'');
    xlabel('Peak Displacement')
    ylabel('Fraction of Nodes above Peak Displacement')
    title('FEM Brain/Skull Displacement:  Animal________')
end
legend('AntR', 'AntL', 'PostR', 'PostL', 'midline')
hold off

% Identify the 90, 50, 10 & 1 populations for principal stress.
% This will interpolate between two values to get the value more
% accurately representing those populations.

for i=1:5
    for j=1:length(counter_disp(:,i))-1
        if (counter_disp(j,i))==0.05
            pop5d(i)=displacement(j,i);
        elseif (counter_disp(j,i)>0.05)&&(counter_disp(j+1,i)<0.05)
            pop5d(i)=(displacement(j,i)+displacement(j+1,i))/2;
        end
        if (counter_disp(j,i))==0.5
            pop50d(i)=displacement(j,i);
        elseif (counter_disp(j,i)>0.5)&&(counter_disp(j+1,i)<0.5)
            pop50d(i)=(displacement(j,i)+displacement(j+1,i))/2;
        end
        if (counter_disp(j,i))==0.1
            pop10d(i)=displacement(j,i);
        elseif (counter_disp(j,i)>0.1)&&(counter_disp(j+1,i)<0.1)
            pop10d(i)=(displacement(j,i)+displacement(j+1,i))/2;
        end
        if (counter_disp(j,i))==0.01
            pop1d(i)=displacement(j,i);
        elseif (counter_disp(j,i)>0.01)&&(counter_disp(j+1,i)<0.01)
            pop1d(i)=(displacement(j,i)+displacement(j+1,i))/2;
        end
    end
end

%% Outputs
pop=[pop50d' pop10d' pop5d' pop1d'];
```

D.3 Kolmogorov-Smirnov Goodness of Fit MATLAB Code

```
%This code was adapated from a larger code originally written by By
%Brittany Coats for the publication:
%Coats B. et al., "Finite element model predictions of intracranial
%hemorrhage from non-impact rapid head rotations in the piglet" Int. J.
%Dev. Neurosi. (2012) doi:10.1016/j.ijdevneu.2011.12.009
%
%Important variables the user needs to define:
%upperm = maximum value of your distribution curves (whichever one is
%larger)
%pmagEXP = Displacements for one of your simulations (preferably longer
one)
%pmagFEM = Displacements for the other simulation.
%inc = increment you want on your x-axis. (I've done 0.01 before).

load 121DispForKS.mat
load 122DispForKS.mat
pmagEXP = fractPostR121; %Input region you want to analyze for 121
(more defl)
pmagFEM = fractPostR122; %Input region you want to analyze for 122
inc = 0.01;
upperm = 1.844;
displace=0;
k=1;
pdispm=[];
counter_EXP = 0;
counter_FEM = 0;
while displace<upperm
    pdispm(k)=displace;
    for i=1:length(pmagEXP)
        if pmagEXP(i)>displace
        counter_EXP=counter_EXP+1;
        end
        if pmagFEM(i)>displace
        counter_FEM=counter_FEM+1;
        end
    end
    FEMmag(k)=counter_FEM/length(pmagFEM);
    EXPmag(k)=counter_EXP/length(pmagEXP);
    counter_EXP=0;
    counter_FEM=0;
    k=k+1;
    displace=displace+inc;
end

%Statistics for mag displacement
for i=1:length(pdispm)
    if i==1
        Dim(i)=abs(EXPmag(i)-FEMmag(i));
        Diprimem(i)=0;
    else
        Dim(i)=abs(EXPmag(i)-FEMmag(i));
        Diprimem(i)=abs(EXPmag(i-1)-FEMmag(i));
    end
end
```

```
maxDi=max(Dim);
maxDiprime=max(Diprimem);

D=max([maxDi maxDiprime]);
n=length(pdispm);
%b = number of brain-skull displacements

% Look up these values in the D-distribution table (Table B.9, page 741
in
% Zars - Biostatistical Analysis, 5th Ed.
disp(['Your evaluated D-value is:  ' num2str(D)])
disp(['Your sample size is:  ' num2str(n)])
disp(' ')
disp('Look at the D-distribution table B.9 in the appendix of Zars')
disp('and enter the following information from that table.')
disp(' ')
upperD=input('Enter D-crit above D.  Upper D-crit =   ');
lowerD=input('Enter D-crit below D.  Lower D-crit =   ');
uppera=input('Enter alpha associated with upper D-crit:  ');
lowera=input('Enter alpha associated with lower D=-crit: ');
pvaluem=(lowera*(upperD-D)+uppera*(D-lowerD))/(upperD-lowerD);
disp(['The p-value for the mag-displacement is:  ' num2str(pvaluem)])
```

APPENDIX E

MRI POSTPROCESSING MATLAB CODES

E.1 T2 Image Processing MATLAB Code

```
%T2 Image Analysis Code
%This code allows the user to select ROIs in an image and reports the
%amount of pixels above a certain threshold. In this case the threshold
%represents CSF.
clear all
close all
clc

%%%%%%Section 1: Set Thesholding Parameters (will alter for each image)
use in conjunction with section 2 to visualize each attempt%%%%%%%%%%
%Input format is: ('Single-file Stacked 8-bit .tif',Frame number)
A = imread('P14-007-Post_1Denoise8bit.tif',28);
A2 = im2double(A); %matlab likes double for image manipulation
B = imadjust(A2,[0.30 0.60],[0.025 0.99]); %contrast adjust
C = im2bw(B,0.45); %make image binary
se = strel('disk',3);
D = imclose(C,se); %slight hole/gap smoothing operation

% %%%%%%Section 2: Contrast Adjustment Test Plotting (Comment Out when
Done)%%%%%%%%%
% %Compile Images for Montage plotting
% Z(:,:,1,1) = A2;
% Z(:,:,1,2) = B;
% Z(:,:,1,3) = C;
% Z(:,:,1,4) = D;
% %plot montage of image filtering views
% figure
% montage(Z,'size',[2 2])
% title({'1 - Initial, 2-4 - Contast Adjusts'})

%%%%%%%%%Section 3: User Tracing ROIs (Uncomment when ready)%%%%%%%%%%
%User Traces an ROI for the program to analyze in this section.
figure
subplot(1,2,1)
imshow(A2) %plot original image for reference
title('original T2 image')
subplot(1,2,2)
imshow(D) %plot altered b&w image for trabeculae counting
title('filtered, binary image')
set(gcf, 'Position', get(0,'Screensize')); %Maximize Figure Window)
hFH = imfreehand(); %sets up a tool for user to trace the ROI
mask = hFH.createMask(); %isolates the region the user traced out

%get histogram of traced region of binary image
imageinmask = D(mask);
[pixelcounts levels] = imhist(imageinmask);
%get CSF area and total ROI area values
blackcount = pixelcounts(1);
whitecount = pixelcounts(2);
total = blackcount + whitecount;

%print out CSF area and total area values for user to record
fprintf('CSF Area %f - Total Area %f',whitecount,total);
```

E.2 T2 Image Processing Raw Data Tables

Four Anatomical Regions Measurement Data:

		P14-001		P14-002		P14-006		P14-007	
		Pre	Post	Pre	Post	Pre	Post	Pre	Post
Region 1	Frame #	9	9	9	8	10	9	9	9
	CSF Pixels	2156	12233	4315	7698	5136	9768	8762	6477
Region 2	Frame #	17	17	16	16	18	16	17	17
	CSF Pixels	1812	3191	2483	1974	5631	6342	1273	1666
Region 3	Frame #	20	19	19	19	20	20	18	18
	CSF Pixels	1671	719	302	1229	1708	1279	2089	2579
Region 4	Frame #	25	25	24	24	26	25	23	23
	CSF Pixels	2528	3354	3182	2826	4114	3203	509	786

Whole Brain Measurement Data (All Data in Pixels):

	P14-001		P14-002		P14-006		P14-007	
Frame #	**Pre**	**Post**	**Pre**	**Post**	**Pre**	**Post**	**Pre**	**Post**
1	0	0	0	0	0	0	0	0
2	0	4812	0	5196	0	4071	4649	4580
3	2548	5402	5476	7295	3512	7435	15790	15171
4	4844	14176	13948	16314	5958	23226	21912	18693
5	6691	13472	11134	16364	14197	18790	11878	10988
6	4697	9477	10028	21341	18065	12362	13810	11175
7	7680	19827	12743	19735	20826	12363	17635	18152
8	6714	23449	6208	14631	20221	18290	15667	17556
9	3368	20050	9291	19543	13267	31321	31777	23234
10	9514	14356	6874	12221	15998	18795	6027	8520
11	6522	12078	9771	21412	32288	11963	11656	14060
12	4352	12058	6949	12658	21353	13674	19121	18538
13	4076	12045	4469	11739	24012	16970	20341	19148
14	2016	7633	2773	8275	21116	16486	12348	9432
15	2743	5429	4239	17195	17464	17849	8699	8580
16	5927	10791	7906	17469	23949	12613	11609	13004
17	8203	15356	4842	11156	22652	11680	16044	11259
18	5799	8465	3241	8347	22299	8130	8882	9201
19	4855	7422	5894	10831	12717	7986	7500	7345
20	7367	8038	5919	10517	18254	6306	3524	3579
21	7099	8785	3776	4387	12440	5134	2086	2403
22	4642	6425	1050	7701	9561	2087	2150	3533
23	2845	4202	4729	9275	3953	4207	1866	2429
24	2541	4697	7095	9129	5392	4436	592	1383
25	11473	9920	7464	15270	7966	6580	705	1077
26	10995	13068	13123	12126	7989	4758	4940	5681
27	17094	14858	10926	0	5634	7205	6976	8481
28	18025	0	0	0	10356	8387	5176	5579
29	0	0	0	0	12608	8958	0	0
30	0	0	0	0	7890	0	0	0
31	0	0	0	0	0	0	0	0
32	0	0	0	0	0	0	0	0
Total	172630	286291	179868	320127	411937	322062	283360	272781

E.3 CSF Flow Measurement MATLAB Codes

1. Main Script

```
% Main Script: main_velocity_Final_012814.m
% Author: Osama Abdullah
%
clear all
close all
clc

path1 = 'D:\Coats_FullData\Raw\Coats13.nJ1\19'
% Change path for each individual image

cd(path1)
% path1 = pwd % path for the phase contrast scan folder
param = get_dti_method_param
filename=['profile']
separtor = '\'; %change to \ for Windows system

[mag_im1, velocity1] =
process_PC_velocity_bruker_012814(path1,separtor);
mag_im = squeeze(mean(mag_im1,4)); %average magnitude images to improve
SNR
for ii=1:size(velocity1,3)
%     for jj=1:size(mag_im1,4)
        velocity(:,:,ii) = squeeze(velocity1(:,:,ii));
          im(:,:,ii) = squeeze(mag_im(:,:,ii));
end

%% plot velocity profile
zoomFact = [0 0 0 0];

[rr ttstd BW zoomFact] = draw_roi_zoom(mag_im(:,:,5),'freehand',
zoomFact);
[rr2 ttstd2 BW2 zoomFact] = draw_roi_zoom(mag_im(:,:,5),'freehand',
zoomFact);

for ii=1:param.NumMovieFrames
    roi_mean(ii) = sum(sum(velocity(:,:,ii).*BW)); %sum of collected
velocities
    roi_mean2(ii) = sum(sum(velocity(:,:,ii).*BW2));
end
roi_mean = roi_mean - roi_mean2*sum(sum(BW))/sum(sum(BW2));
roi_mean = roi_mean - mean(roi_mean(:));
stroke_volume =
sum(roi_mean(roi_mean>0))*(param.TR*.001)*(param.Resolution(1)*param.Re
solution(2) * 0.01) * 1e6 % calculates final stroke volume (in nano-L)
figure, plot(roi_mean)
```

2. Image zoom and ROI creation subfunction:

```
function [roi_mean, std1, BW, zoomFact] = draw_roi(im, mode, zoomFact)
%MATLAB FUNCTION USED TO DRAW ROIS IN THE IMAGE IM
if nargin == 1
    mode = 'freehand'; %default
end
figure(51)
    switch mode
        case 'freehand'
%             h_im=imagesc(max(im,[],3)-min(im,[],3),[-0.5 0.5]),axis
image, colormap gray
            h_im = imagesc(im),axis image, colormap gray
            zoom(2)
            if (sum(zoomFact)>0),axis(zoomFact),end
            h = imfreehand
            BW = createMask(h,h_im);
            ind = find(im(:,:,1).*BW>0)
            size(ind)
            roi_mean = mean(im(ind));std1=std(im(ind));
        case 'rect'
           imagesc((im')), colormap gray, axis image, axis off % 1c
            roi_c=getrect;
            roi_c=round(roi_c);
            rc1=roi_c(1); rc2=roi_c(2);
            rc3=rc1+roi_c(3); rc4=rc2+roi_c(4);
            roi_im=im(rc1:rc3,rc2:rc4);
            roi_mean=mean(roi_im(:));std1=std(roi_im(:));
    end
    zoomFact = axis;
return
```

3. MRI parameter gathering subfunction

```
% Function that extracts paramters from method file

function param = get_dti_method_param(path)
if nargin == 1
    acqp=fopen(path,'r');
else
acqp=fopen('method','r');
end
BRUKERvar = {'Method='; 'PVM_EchoTime='; 'PVM_RepetitionTime=';
'PVM_RareFactor='; 'PVM_DwGradDur='; ...
    'PVM_DwGradSep=';
'PVM_DwNDiffDir=';'PVM_DwNDiffExpEach=';'PVM_DwAoImages=';'#$PVM_DwBMat
';'$PVM_EncMatrix'...

;'$PVM_EncSteps1';'$PVM_DwDir';'$PVM_GradCalConst';'$PVM_DwGradAmp';'$P
VM_DwEffBval';'$PVM_Matrix'...

;'$PVM_ObjOrderList';'$PVM_SPackArrNSlices';'$PVM_NAverages=';'$PVM_NRe
petitions=';'$RECO_wordtype='...

;'$PVM_DwBvalEach';'$PVM_TeDwSliceSpoilGradDur=';'$PVM_TeDwSliceSpoilGr
```

```
ad=';'$PVM_DwRfcPulse=('...

;'$PVM_DwSpDir';'$PVM_SpatDimEnum=';'##$FlowRange=';'$FlowEncLoop=';'$M
inFlowRange='...
    ; '$PVM_NMovieFrames=';'$TimeForMovieFrames=';'$PVM_SpatResol='};
% 33 parameters
param = struct();

while(~feof(acqp))

    line = fgetl(acqp);

    for ii = 1:size(BRUKERvar,1)

        tmpvar = BRUKERvar{ii};

        if strfind(line, tmpvar) & ii == 1 % Method name
            pos = strfind(line,'=')+1; sz = size(line);
            param.method = line(pos:sz(2));

        elseif strfind(line,tmpvar) & ii == 2
            pos = strfind(line,'=')+1; sz = size(line); %Echo time ms
            param.TE = eval(line(pos:sz(2)));

        elseif strfind(line,tmpvar) & ii == 3
            pos = strfind(line,'=')+1; sz = size(line); %TR ms
            param.TR = eval(line(pos:sz(2)));


%
        elseif strfind(line,tmpvar) & ii == 4
            pos = strfind(line,'=')+1; sz = size(line);%RARE ETL
            param.etl = round(eval(line(pos:sz(2))));

        elseif strfind(line,tmpvar) & ii == 5
            line = fgetl(acqp)
%             pos = eval(line);
            param.small_delta = eval(line); %Small Delta (diffusion
gradient duration) ms

        elseif strfind(line,tmpvar) & ii == 6
            line = fgetl(acqp)
            param.big_delta = eval(line); %Big Delta (diffusion
gradients separation) ms

        elseif strfind(line,tmpvar) & ii == 7
        pos = strfind(line,'=')+1; sz = size(line);
        param.NDwDir = (eval(line(pos:sz(2)))); % Number of Diffusion
weighted gradients directions

        elseif strfind(line,tmpvar) & ii == 8
        pos = strfind(line,'=')+1; sz = size(line);
        param.Nbvalues_per_dir = (eval(line(pos:sz(2)))); %Number of b-
values per direction
```

```
        elseif strfind(line,tmpvar) & ii == 9
        pos = strfind(line,'=')+1; sz = size(line);
        param.NB0 = (eval(line(pos:sz(2)))); % Number of NON-diffusion-
weighted images

        elseif strfind(line,tmpvar) & ii == 10
            line=fgetl(acqp);
            param.BMatrix = str2num(line);  % Effective B-matrix as
calculated by Bruker

            while  ~strcmp(line(1,1),'#')

             line=fgetl(acqp);
             if ~strcmp(line(1,1),'#')
                 param.BMatrix = [param.BMatrix, str2num(line)];
             end
            end


         param.NImages = param.NDwDir*param.Nbvalues_per_dir+param.NB0;
         param.BMatrix = reshape(param.BMatrix,3,3, param.NImages);


        elseif strfind(line,tmpvar) & ii == 11
            line=fgetl(acqp);
            param.EncodingMatrix = line; %Matrix size

        elseif strfind(line,tmpvar) & ii == 12
            line=fgetl(acqp);
            param.EncSteps1 = line; % Encoding Order (e.g., linear,
centric)

            while  ~strcmp(line(1,1),'#')

                line=fgetl(acqp);
                if ~strcmp(line(1,1),'#')
                    param.EncSteps1 = [param.EncSteps1, line];
                end
            end
            param.EncSteps1 = str2num(param.EncSteps1);

        elseif strfind(line,tmpvar) & ii == 13
            line=fgetl(acqp);
            param.DwDir = line; %Diffusion weigting gradients
directions

            while  ~strcmp(line(1,1),'#')

                line=fgetl(acqp);
                if ~strcmp(line(1,1),'#')
                    param.DwDir = [param.DwDir, line];
                end
            end
            param.DwDir = str2num(param.DwDir);
```

```
        elseif strfind(line, tmpvar) & ii == 14 %$PVM_GradCalConst
Hz/mm maximum gradient allowed by the system
            pos = strfind(line,'=')+1; sz = size(line);
            param.gradCalConst = eval(line(pos:sz(2)));

        elseif strfind(line, tmpvar) & ii == 15 %$PVM_DwGradAmp
diffusion gradient max amplitude (%)
            line=fgetl(acqp);
            param.DwGradAmp = str2num(line);
            while  ~strcmp(line(1,1),'#')

                line=fgetl(acqp);
                if ~strcmp(line(1,1),'#')
                    param.DwGradAmp = [param.DwGradAmp, str2num(line)];
                end
            end

        elseif strfind(line,tmpvar) & ii == 16
            line=fgetl(acqp);
            param.bvalue = str2num(line);  % Effective B-values as
calculated by Bruker

            while  ~strcmp(line(1,1),'#')

                line=fgetl(acqp);
                if ~strcmp(line(1,1),'#')
                    param.bvalue = [param.bvalue, str2num(line)];
                end
            end

        elseif strfind(line,tmpvar) & ii == 17
            line=fgetl(acqp);
            param.Matrix = str2num(line); %Matrix size

        elseif strfind(line,tmpvar) & ii == 18
            line=fgetl(acqp);
            param.ObjOrder = str2num(line); %Slice ordering

        elseif strfind(line,tmpvar) & ii == 19
            line=fgetl(acqp);
            param.NSlices = str2num(line); %Number of Slices

        elseif strfind(line,tmpvar) & ii == 20
            pos = strfind(line,'=')+1; sz = size(line); % Number of
averages
            param.NA = eval(line(pos:sz(2)));

        elseif strfind(line,tmpvar) & ii == 21
            pos = strfind(line,'=')+1; sz = size(line); % Number of
repetitions
            param.NR = eval(line(pos:sz(2)));

        elseif strfind(line, tmpvar) & ii == 22 % Reconstruction Data
```

```
Type
            pos = strfind(line,'=')+1; sz = size(line);
            param.DataType = line(pos:sz(2));

        elseif strfind(line,tmpvar) & ii == 23
            line=fgetl(acqp);
            param.BvalEach = str2num(line); % Selected b values


        elseif strfind(line,tmpvar) & ii == 24
             pos = strfind(line,'=')+1; sz = size(line); %Spoiler (or
crusher) Gradient duration
            param.SpoilerDur = eval(line(pos:sz(2))); %ms


        elseif strfind(line,tmpvar) & ii == 25
             pos = strfind(line,'=')+1; sz = size(line); %Spoiler (or
crusher) Gradient Amplitude
            param.SpoilerGradAmp = eval(line(pos:sz(2))); %percentage

        elseif strfind(line,tmpvar) & ii == 26
             pos1 = strfind(line,'(')+1;% sz = size(line);
            pos2 = strfind(line,',');
             param.RfcPulseDur = eval(line(pos1:pos2(1))); %ms


           elseif strfind(line,tmpvar) & ii == 27

            line=fgetl(acqp);
            param.SpoilerDirections = str2num(line);

            while  ~strcmp(line(1,1),'#')

             line=fgetl(acqp);
             if ~strcmp(line(1,1),'#')
                 param.SpoilerDirections = [param.SpoilerDirections,
str2num(line)];
             end
            end
         param.SpoilerDirections =
reshape(param.SpoilerDirections,3,param.NImages)';

        elseif strfind(line,tmpvar) & ii == 28
             pos = strfind(line,'=')+1; sz = size(line); % 3D vs 2D
acquisition
            param.AcqType = line(pos:sz(2)); %

            elseif strfind(line,tmpvar) & ii == 29
             pos = strfind(line,'=')+1; sz = size(line); % Vecn if
Phase Contrat is used (cm/s)
            param.Venc = eval(line(pos:sz(2))); %
            elseif strfind(line,tmpvar) & ii == 30
             pos = strfind(line,'=')+1; sz = size(line); % Number of
flow encoding steps
```

```
            param.FlowEncSteps = eval(line(pos:sz(2))); %

            elseif strfind(line,tmpvar) & ii == 31
             pos = strfind(line,'=')+1; sz = size(line); % Minimum flow
range (aka flow resolution) (cm/s)
            param.minVelocity = eval(line(pos:sz(2))); %

            elseif strfind(line,tmpvar) & ii == 32
             pos = strfind(line,'=')+1; sz = size(line); % number of
movie frames (if CINE turned ON)
            param.NumMovieFrames = eval(line(pos:sz(2))); %

            elseif strfind(line,tmpvar) & ii == 33
             pos = strfind(line,'=')+1; sz = size(line); % Time for all
movie frames (~ TR * NumMovieFrames) if CINE mode is ON
            param.TimeForMovieFrame = eval(line(pos:sz(2))); % ms

             elseif strfind(line,tmpvar) & ii == 34
            line=fgetl(acqp);
            param.Resolution = str2num(line); % Spatial Resolution (in
plane)
        end
    end
end
fclose(acqp);
end
```

E.4 CSF Flow Measurement Raw Data

Operator 1 Data:

Animal ID	Category	Right or Left	# of Pixels in L.V	L.V. Stroke Volume (nL)	L.V. Total Velocity In ROI (cm/s)	# of Pixels in SAS	SAS Stroke Volume (nL)	SAS Total Velocity in ROI (cm/s)
P14-001	Pre	left	17	72.785	-4.236	78	56.342	2.345
P14-001	Pre	left	17	115.636	-7.915	91	86.406	-4.145
P14-001	Pre	left	24	96.681	-5.928	61	90.904	-4.943
P14-001	Pre	right	19	106.866	-4.316	79	121.109	-5.741
P14-001	Pre	right	22	182.624	-6.252	81	8.841	3.812
P14-001	Pre	right	22	89.781	-4.077	102	133.630	6.086
P14-001	Post	left	19	95.085	-3.819	74	50.553	-2.002
P14-001	Post	left	21	80.372	-3.373	82	43.152	-1.847
P14-001	Post	left	20	76.967	-3.44	75	99.431	3.844
P14-001	Post	right	16	106.474	-4.583	77	82.012	3.76
P14-001	Post	right	11	59.907	-2.292	69	147.619	6.306
P14-001	Post	right	15	105.438	-4.541	73	141.308	5.391
P14-002	Pre	left	21	84.053	3.743	79	137.798	-8.344
P14-002	Pre	left	18	99.412	4.591	67	38.337	-1.779
P14-002	Pre	left	15	109.705	6.592	61	89.836	-3.934
P14-002	Pre	right	16	71.004	4.009	87	28.293	-2.121
P14-002	Pre	right	14	34.192	-1.573	70	22.332	-9.744
P14-002	Pre	right	16	44.897	2.875	111	53.606	-3.3
P14-002	Post	left	8	69.552	4.404	75	115.852	-4.94
P14-002	Post	left	19	84.928	3.979	81	112.343	4.171
P14-002	Post	left	14	84.554	4.484	89	92.491	4.479
P14-002	Post	right	20	107.516	-5.4	70	108.017	-7.662
P14-002	Post	right	11	72.682	-4.461	85	72.141	3.111
P14-002	Post	right	13	80.732	-4.44	71	69.208	-3.605
P14-007	Pre	left	27	63.118	-3.608	92	186.137	8.351
P14-007	Pre	left	32	87.341	-6.476	112	213.287	-9.218
P14-007	Pre	left	17	73.009	-3.867	73	196.498	-7.939
P14-007	Pre	right	13	111.368	-8.952	115	148.491	-8.219
P14-007	Pre	right	17	106.833	4.893	86	116.793	-10.47
P14-007	Pre	right	14	111.691	-7.75	80	142.045	-11.08

Animal ID	Category	Right or Left	# of Pixels in L.V	L.V. Stroke Volume (nL)	L.V. Total Velocity In ROI (cm/s)	# of Pixels in SAS	SAS Stroke Volume (nL)	SAS Total Velocity in ROI (cm/s)
P14-007	Post	left	25	142.115	9.199	103	173.931	16.61
P14-007	Post	left	29	130.169	8.411	90	231.000	16.86
P14-007	Post	left	25	111.197	6.208	92	101.173	10.22
P14-007	Post	right	17	79.504	-4.768	100	150.118	9.217
P14-007	Post	right	13	107.403	6.993	108	213.429	-10.29
P14-007	Post	right	12	139.425	-9.238	108	161.244	8.78

Operator 2 Data:

Animal ID	Category	Right or Left	# of Pixels in L.V	L.V. Stroke Volume (nL)	L.V. Total Velocity In ROI (cm/s)	# of Pixels in SAS	SAS Stroke Volume (nL)	SAS Total Velocity in ROI (cm/s)
P14-001	Pre	left	16	27.832	-2.222	14	64.012	2.482
P14-001	Pre	left	15	53.436	-4.302	27	41.300	1.354
P14-001	Pre	left	18	33.233	-2.621	36	46.841	1.869
P14-001	Pre	right	14	74.622	-3.405	32	35.386	2.422
P14-001	Pre	right	21	72.467	-3.203	42	30.122	1.628
P14-001	Pre	right	21	70.149	-2.035	34	32.897	2.326
P14-001	Post	left	18	48.622	-1.819	30	58.139	1.864
P14-001	Post	left	16	44.055	-1.759	21	55.256	1.947
P14-001	Post	left	19	53.166	-2.122	18	49.570	1.808
P14-001	Post	right	17	29.458	-1.051	37	60.595	2.92
P14-001	Post	right	15	75.529	-3.58	24	45.098	2.349
P14-001	Post	right	13	62.870	-2.698	32	31.599	3.147
P14-002	Pre	left	16	39.100	-1.716	23	48.623	2.343
P14-002	Pre	left	19	61.618	-1.421	34	57.950	3.574
P14-002	Pre	left	14	64.665	-2.195	36	47.057	2.543
P14-002	Pre	right	24	24.067	-1.049	45	41.042	1.844
P14-002	Pre	right	13	53.162	-1.793	52	34.341	1.852
P14-002	Pre	right	10	51.165	-1.773	54	35.751	1.362
P14-002	Post	left	15	50.434	-2.366	35	41.199	2.277
P14-002	Post	left	11	42.909	-2.088	48	28.995	1.525
P14-002	Post	left	14	39.393	-1.512	33	43.251	2.726

Animal ID	Category	Right or Left	# of Pixels in L.V	L.V. Stroke Volume (nL)	L.V. Total Velocity In ROI (cm/s)	# of Pixels in SAS	SAS Stroke Volume (nL)	SAS Total Velocity in ROI (cm/s)
P14-002	Post	right	10	57.432	-2.914	45	40.975	2.746
P14-002	Post	right	10	39.759	-2.117	30	45.217	2.697
P14-002	Post	right	9	63.710	-3.347	37	33.289	2.376
P14-007	Pre	left	27	39.455	-3.158	57	138.450	6.793
P14-007	Pre	left	27	21.249	-1.439	59	121.318	4.892
P14-007	Pre	left	20	33.976	-2.184	59	131.850	6.327
P14-007	Pre	right	13	41.973	-2.894	57	80.451	-6.768
P14-007	Pre	right	12	60.266	-3.862	74	106.747	5.566
P14-007	Pre	right	14	22.206	-1.672	63	52.324	-4.472
P14-007	Post	left	21	50.486	-2.519	54	67.385	3.314
P14-007	Post	left	15	54.996	-2.141	45	114.498	6.6006
P14-007	Post	left	9	46.994	-2.012	39	92.606	5.575
P14-007	Post	right	13	37.734	-2.981	67	54.353	2.659
P14-007	Post	right	12	62.057	-3.745	49	56.367	1.814
P14-007	Post	right	12	32.601	-2.514	65	57.133	3.296

E.5 CSF Flow Measurement Averaged and Normalized Data

Operator 1 Data:

Animal #	Category	Right/Left	# of Pixels in LV	LV Stroke Volume (pL)	LV Stroke Volume Per Pixel (pL/pixel)	LV Max Velocity (Absolute) (cm/s)	LV Avg Velocity (cm/s)	# of Pixels in SAS	SAS Stroke Volume (pL)	SAS Stroke Volume Per Pixel (pL/pixel)	SAS Max Velocity (Absolute) (cm/s)	SAS Avg Velocity (cm/s)
P14-001	Pre	left	19.33	95.034	5.037	6.026	0.312	76.67	77.884	1.054	3.811	0.050
	Pre	right	21.00	126.424	6.002	4.882	0.232	87.33	87.860	0.984	5.213	0.060
	Post	left	20.00	84.142	4.227	3.544	0.177	77.00	64.378	0.845	2.564	0.033
	Post	right	14.00	90.606	6.377	3.805	0.272	73.00	123.646	1.713	5.152	0.071
P14-002	Pre	left	18.00	97.724	5.613	4.975	0.276	69.00	88.657	1.263	4.686	0.068
	Pre	right	15.33	50.031	3.229	2.819	0.184	89.33	34.744	0.376	5.055	0.057
	Post	left	13.67	79.678	6.401	4.289	0.314	81.67	106.895	1.324	4.530	0.055
	Post	right	14.67	86.976	6.064	4.767	0.325	75.33	83.122	1.122	4.793	0.064
P14-007	Pre	left	25.33	74.489	3.121	4.650	0.184	92.33	198.641	2.206	8.503	0.092
	Pre	right	14.67	109.964	7.610	7.198	0.491	93.67	135.776	1.475	9.923	0.106
	Post	left	26.33	127.827	4.874	7.939	0.301	95.00	168.701	1.785	14.563	0.153
	Post	right	14.00	108.778	8.186	7.000	0.500	105.33	174.930	1.657	9.429	0.090

Operator 2 Data:

Animal #	Category	Right/Left	# of Pixels in LV	LV Stroke Volume (pL)	LV Stroke Volume Per Pixel (pL/pixel)	LV Max Velocity (Absolute) (cm/s)	LV Avg Velocity (cm/s)	# of Pixels in SAS	SAS Stroke Volume (pL)	SAS Stroke Volume Per Pixel (pL/pixel)	SAS Max Velocity (Absolute) (cm/s)	SAS Avg Velocity (cm/s)
P14-001	Pre	left	16.33	38.167	2.383	3.048	0.187	25.67	50.717	2.468	1.902	0.074
	Pre	right	18.67	72.413	4.040	2.881	0.154	36.00	32.801	0.930	2.125	0.059
	Post	left	17.67	48.614	2.751	1.900	0.108	23.00	54.322	2.441	1.873	0.081
	Post	right	15.00	55.953	3.868	2.443	0.163	31.00	45.764	1.501	2.805	0.090
P14-002	Pre	left	16.33	55.127	3.435	1.777	0.109	31.00	51.210	1.709	2.820	0.091
	Pre	right	15.67	42.798	3.403	1.538	0.098	50.33	37.045	0.745	1.686	0.033
	Post	left	13.33	44.245	3.359	1.989	0.149	38.67	37.815	1.031	2.176	0.056
	Post	right	9.67	53.634	5.599	2.793	0.289	37.33	39.827	1.106	2.606	0.070
P14-007	Pre	left	24.67	31.560	1.316	2.260	0.092	58.33	130.539	2.240	6.004	0.103
	Pre	right	13.00	41.482	3.279	2.809	0.216	64.67	79.841	1.228	5.602	0.087
	Post	left	15.00	50.825	3.764	2.224	0.148	46.00	91.496	2.056	5.163	0.112
	Post	right	12.33	44.131	3.597	3.080	0.250	60.33	55.951	0.947	2.590	0.043

Pre Injury Dataset for P14-007. X-Direction Displacement (Frames 8 to 19):

Point of Measurement	Frames across which displacement was calculated										
	8-9	9-10	10-11	11-12	12-13	13-14	14-15	15-16	16-17	17-18	18-19
	Displacement (in Pixels)										
Right Lateral Skull	-0.080	-0.657	-1.323	-2.052	-3.081	-4.137	-5.018	-4.099	0.215	1.529	1.941
Right Lateral Brain	0.083	-1.082	-1.532	-2.670	-1.606	-4.068	-4.812	-4.423	0.221	1.441	1.631
Right Maximal Gyrus Skull	0.483	-1.116	-1.870	-3.785	-5.844	-5.210	-6.620	-5.614	0.271	1.941	1.482
Right Maximal Gyrus Brain	-0.093	-0.879	-1.922	-3.504	-4.141	-4.918	-6.283	-5.602	0.488	2.095	1.516
SSS - Skull	-0.347	-1.170	-2.155	-3.815	-5.645	-5.470	-6.684	-5.711	0.240	1.710	0.800
SSS - Brain	-0.284	-1.045	-2.234	-3.563	-4.794	-5.275	-6.375	-5.131	0.564	1.385	0.944
Left Maximal Gyrus - Skull	-0.143	-1.093	-2.778	-4.086	-5.227	-5.219	-6.275	-5.042	0.175	1.524	0.933
Left Maximal Gyrus - Brain	-0.476	-1.308	-2.229	-3.771	-5.143	-4.961	-5.555	-4.719	0.656	1.699	1.146
Left Lateral Skull	-0.490	-1.147	-1.823	-3.206	-4.435	-3.924	-3.821	-2.420	0.272	1.101	0.664
Left Lateral Brain	0.260	-0.766	-0.980	-3.432	-5.967	-3.818	-4.748	-3.117	0.364	1.715	1.207
Right Basal - Skull	-0.036	-1.060	-1.061	-0.934	-1.090	-1.335	-1.632	-1.740	0.169	0.985	1.019
Right Basal - Brain	0.124	-0.370	-0.780	-1.007	-1.206	-1.821	-2.172	-2.261	-0.042	1.625	1.068
Left Basal - Skull	-0.100	-0.423	-0.296	-1.111	-1.247	-1.266	-1.109	-1.199	-0.067	0.958	0.806
Left Basal - Brain	-0.144	-0.780	0.009	-1.265	-1.728	-1.305	-1.527	-1.101	0.081	1.039	0.676

Pre Injury Dataset for P14-007, X-Direction Displacement Continued (Frames 19 to 30):

Point of Measurement	Frames across which displacement was calculated										
	19-20	20-21	21-22	22-23	23-24	24-25	25-26	26-27	27-28	28-29	29-30
	Displacement (in Pixels)										
Right Lateral Skull	0.653	-0.338	-0.306	-0.237	-0.363	0.011	0.313	0.184	0.087	0.234	-0.114
Right Lateral Brain	0.311	0.300	-0.660	-0.730	-0.344	-0.255	0.076	0.159	-0.254	0.394	-0.290
Right Maximal Gyrus Skull	0.136	0.364	-0.617	-0.640	-0.488	0.053	0.529	0.244	0.088	0.240	0.353
Right Maximal Gyrus Brain	0.777	0.270	-0.344	-0.796	-0.470	0.049	0.400	0.256	0.004	0.129	0.083
SSS - Skull	0.214	0.164	-0.347	-0.731	-0.384	-0.171	0.527	0.083	-0.090	0.218	0.093
SSS - Brain	0.352	0.364	-0.621	-0.683	-0.470	-0.265	0.246	0.336	-0.013	0.104	0.230
Left Maximal Gyrus - Skull	0.210	0.121	-0.500	-0.618	-0.461	-0.182	0.604	0.461	0.205	0.253	0.328
Left Maximal Gyrus - Brain	0.157	0.228	-0.537	-0.442	-0.462	-0.371	0.572	0.229	0.255	0.340	0.365
Left Lateral Skull	0.390	-0.081	-0.753	-0.709	-0.361	0.236	0.136	0.077	-0.215	-0.011	0.018
Left Lateral Brain	0.685	-0.003	-0.639	-0.160	-0.066	0.161	0.405	0.087	-0.097	0.232	0.032
Right Basal - Skull	0.653	-0.338	-0.306	-0.237	-0.363	0.011	0.313	0.184	0.087	0.234	-0.114
Right Basal - Brain	0.311	0.300	-0.660	-0.730	-0.344	-0.255	0.076	0.159	-0.254	0.394	-0.290
Left Basal - Skull	0.136	0.364	-0.617	-0.640	-0.488	0.053	0.529	0.244	0.088	0.240	0.353
Left Basal - Brain	0.777	0.270	-0.344	-0.796	-0.470	0.049	0.400	0.256	0.004	0.129	0.083

Pre Injury Dataset for P14-007, Y-Direction Displacement (Frames 8 to 19):

Point of Measurement	Frames across which displacement was calculated										
	8-9	9-10	10-11	11-12	12-13	13-14	14-15	15-16	16-17	17-18	18-19
	Displacement (in Pixels)										
Right Lateral Skull	0.315	0.532	0.562	2.152	3.809	2.671	3.179	1.297	0.913	-0.055	-1.285
Right Lateral Brain	-0.248	0.931	0.671	1.717	2.760	2.296	2.554	1.233	1.001	-0.133	-1.216
Right Maximal Gyrus Skull	0.162	0.811	0.663	1.533	2.457	1.373	1.542	0.381	-0.062	-0.101	-0.221
Right Maximal Gyrus Brain	-0.203	0.640	0.595	1.467	3.460	1.192	1.788	0.007	0.670	-0.368	-0.778
SSS - Skull	0.330	0.258	0.237	0.158	0.461	-0.228	-0.495	-1.804	-0.203	0.495	0.093
SSS - Brain	-0.358	0.622	-0.190	0.922	0.982	-0.112	-0.390	-1.774	-0.182	-0.290	-0.171
Left Maximal Gyrus - Skull	0.761	0.148	-0.870	-0.571	-1.057	-1.665	-2.633	-2.499	-0.709	0.434	0.447
Left Maximal Gyrus - Brain	0.209	-0.805	-1.625	-0.009	1.031	-1.877	-2.273	-2.658	-0.600	-0.162	0.009
Left Lateral Skull	-0.636	-0.141	-1.816	-1.739	-2.084	-3.349	-4.479	-4.128	-1.299	0.138	1.022
Left Lateral Brain	-0.300	-0.232	-1.770	-0.967	-2.081	-2.972	-3.936	-4.093	-1.184	-0.070	1.039
Right Basal - Skull	0.436	0.451	0.156	0.354	0.417	0.821	0.411	0.741	0.084	-0.106	-0.493
Right Basal - Brain	0.133	0.247	0.271	0.298	0.480	0.962	0.554	0.784	0.158	-0.714	-1.055
Left Basal - Skull	0.019	-0.036	-0.427	-0.908	-1.159	-1.152	-1.616	-0.569	0.189	0.324	0.489
Left Basal - Brain	-0.568	-0.033	-0.593	-0.693	-1.052	-0.873	-1.786	-0.348	0.287	0.580	0.614

Pre Injury Dataset for P14-007, Y-Direction Displacement Continued (Frames 19 to 30):

Point of Measurement	Frames across which displacement was calculated										
	19-20	20-21	21-22	22-23	23-24	24-25	25-26	26-27	27-28	28-29	29-30
	Displacement (in Pixels)										
Right Lateral Skull	-0.420	0.496	-0.355	-0.463	0.021	-0.051	-0.538	-0.347	0.130	-0.254	0.060
Right Lateral Brain	-0.308	0.095	-0.070	-0.241	-0.033	-0.328	-0.394	-0.291	-0.274	0.085	0.029
Right Maximal Gyrus Skull	-0.190	0.079	0.068	-0.310	-0.340	-0.189	-0.119	-0.192	0.091	-0.270	-0.239
Right Maximal Gyrus Brain	-0.318	-0.220	0.397	-0.283	-0.050	-0.509	-0.234	-0.341	0.070	-0.452	-0.428
SSS - Skull	-0.176	0.227	-0.232	-0.345	-0.406	-0.258	-0.167	-0.043	-0.043	-0.136	0.109
SSS - Brain	-0.090	0.240	0.018	-0.356	-0.203	-0.251	-0.029	0.113	0.003	0.015	0.156
Left Maximal Gyrus - Skull	0.146	0.398	-0.144	-0.081	-0.394	-0.338	0.142	-0.051	0.268	0.234	0.338
Left Maximal Gyrus - Brain	-0.110	0.152	-0.220	-0.541	-0.213	-0.524	-0.027	0.016	-0.074	0.037	0.194
Left Lateral Skull	0.679	0.454	-0.282	-0.463	-0.354	-0.285	0.432	0.359	0.161	0.495	0.093
Left Lateral Brain	0.665	0.334	-0.336	-0.348	-0.321	-0.262	0.195	0.306	0.342	0.498	-0.016
Right Basal - Skull	-0.248	0.026	-0.149	-0.192	-0.169	-0.368	-0.267	-0.293	-0.265	0.331	-0.224
Right Basal - Brain	-0.393	-0.016	-0.284	-0.257	-0.359	-0.577	-0.404	-0.432	-0.265	0.150	-0.224
Left Basal - Skull	0.296	0.173	-0.146	0.126	-0.210	0.016	-0.270	0.074	0.106	0.055	-0.118
Left Basal - Brain	0.353	-0.005	-0.132	-0.052	-0.194	-0.134	-0.286	-0.129	0.032	-0.133	0.110

Post Injury Dataset for P14-007, X-Direction Displacement (Frames 13 to 26):

Point of Measurement	Frames across which displacement was calculated												
	13-14	14-15	15-16	16-17	17-18	18-19	19-20	20-21	21-22	22-23	23-24	24-25	25-26
	Displacement (in Pixels)												
Right Lateral Skull	-2.002	-2.242	-1.579	-1.112	0.634	0.617	0.215	-0.231	-0.026	-0.158	0.087	0.063	0.251
Right Lateral Brain	-1.876	-2.018	-1.583	-1.928	0.893	-0.154	-0.199	-0.194	-0.298	-0.087	-0.140	-0.370	-0.251
Right Max. Gyrus Skull	-2.263	-2.313	-2.346	-1.960	0.355	0.470	0.152	-0.330	-0.249	-0.362	-0.246	-0.042	-0.227
Right Max. Gyrus Brain	-2.059	-2.321	-2.340	-2.091	1.262	0.420	0.119	-0.389	-0.165	-0.489	-0.286	-0.063	-0.308
SSS - Skull	-2.192	-2.348	-2.711	-2.351	0.687	0.356	0.037	-0.413	-0.103	-0.314	-0.411	-0.136	-0.304
SSS - Brain	-2.051	-2.221	-2.389	-1.956	0.510	0.107	-0.023	-0.397	-0.181	-0.094	-0.423	0.031	-0.279
Left Max. Gyrus - Skull	-2.529	-2.536	-2.926	-2.321	0.377	0.672	0.177	-0.568	0.229	-0.482	-0.405	-0.024	-0.397
Left Max. Gyrus - Brain	-2.403	-2.283	-2.647	-2.119	-0.128	0.499	0.181	-0.465	0.196	-0.255	-0.264	-0.031	-0.298
Left Lateral Skull	-2.359	-2.428	-2.204	-1.616	-0.007	0.796	-0.005	-0.114	-0.247	-0.296	-0.056	-0.052	-0.272
Left Lateral Brain	-2.370	-2.222	-2.406	-1.301	-0.104	0.731	0.218	-0.116	-0.138	-0.075	-0.177	0.162	-0.101
Right Basal - Skull	-0.580	-0.690	-0.162	-0.287	0.185	0.417	-0.248	-0.364	-0.136	-0.016	-0.169	-0.118	-0.026
Right Basal - Brain	-0.603	-0.547	-0.093	0.317	0.373	0.591	-0.228	-0.382	-0.132	0.049	-0.124	-0.098	-0.117
Left Basal - Skull	-0.814	-0.403	-0.254	0.239	0.304	0.622	0.045	0.033	-0.013	-0.102	-0.099	0.089	0.004
Left Basal - Brain	-0.652	-0.329	-0.283	0.026	0.204	0.549	0.045	-0.091	-0.015	-0.188	-0.143	0.053	-0.052

Post Injury Dataset for P14-007, Y-Direction Displacement (Frames 13 to 26):

Point of Measurement	Frames across which displacement was calculated												
	13-14	14-15	15-16	16-17	17-18	18-19	19-20	20-21	21-22	22-23	23-24	24-25	25-26
	Displacement (in Pixels)												
Right Lateral Skull	1.601	1.390	2.192	1.722	0.803	-0.890	-0.682	-0.365	-0.064	0.091	-0.213	-0.006	-0.043
Right Lateral Brain	1.531	1.328	2.045	1.760	0.528	0.107	-0.322	-0.443	-0.206	0.416	0.058	0.142	-0.108
Right Max. Gyrus Skull	1.174	1.008	1.269	1.620	0.603	-0.125	-0.170	-0.350	-0.050	0.279	0.090	0.025	0.126
Right Max. Gyrus Brain	1.139	0.738	1.159	1.193	1.311	-0.280	-0.265	-0.459	-0.017	0.142	-0.009	-0.019	0.043
SSS - Skull	0.695	0.728	0.605	0.462	0.248	0.049	-0.237	-0.297	-0.312	-0.195	0.006	0.026	-0.026
SSS - Brain	0.592	0.534	0.357	-0.447	0.697	-0.262	-0.479	-0.411	0.163	0.216	-0.013	-0.010	0.232
Left Max. Gyrus - Skull	-0.248	-0.312	-0.652	-0.699	0.157	-0.328	-0.177	-0.139	0.160	-0.105	-0.200	0.258	-0.113
Left Max. Gyrus - Brain	-0.283	-0.359	-0.793	-0.911	0.687	-0.134	-0.346	-0.230	-0.062	-0.223	-0.276	0.206	-0.277
Left Lateral Skull	-1.268	-1.196	-1.704	-1.616	-0.093	0.651	-0.284	-0.405	0.483	-0.285	-0.382	-0.018	-0.369
Left Lateral Brain	-0.896	-1.241	-1.415	-1.589	0.433	0.279	-0.418	-0.517	0.366	-0.483	-0.322	-0.080	-0.381
Right Basal - Skull	0.865	0.935	1.265	1.114	0.476	-0.419	-0.166	-0.051	-0.234	-0.025	0.038	-0.039	-0.047
Right Basal - Brain	0.425	0.270	0.790	0.930	0.198	-0.701	-0.481	-0.225	-0.364	0.143	-0.013	-0.165	-0.110
Left Basal - Skull	-0.628	-0.897	-0.545	-0.107	0.378	0.211	-0.279	-0.045	-0.097	0.210	0.070	-0.040	0.090
Left Basal - Brain	-0.658	-0.833	-0.633	-0.117	-0.286	0.122	-0.520	-0.134	-0.141	0.233	0.039	-0.056	0.009

REFERENCES

[1] M. Faul, L. Xu, M. M. Wald and V. G. Coronado, "Traumatic Brain Injury in the United States: Emergency Department Visits, Hospitalizations and Deaths 2002-2006.," Centers for Disease Control and Prevention, Atlanta, GA, 2010.

[2] M. E. Billmire and P. A. Myers, "Serious Head Injury in Infants: Accident or Abuse?," *Pediatrics,* vol. 75, no. 2, pp. 340-342, 1985.

[3] A.-C. Duhaime, T. A. Gennarelli, L. E. Thibault, D. A. Bruce, S. S. Margulies and R. Wiser, "The Shaken Baby Syndrome: A Clinical, Pathological, and Biomechanical Study," *Journal of Neurosurgery,* vol. 66, pp. 409-415, 1987.

[4] A.D.A.M. Health Solutions, Ebix, Inc., *Meninges of the Brain (Image),* Bethesda, MD: MedlinePlus, 2012.

[5] H. Gray, Gray's Anatomy, New York, NY: Churchill Livingstone, 1995.

[6] E. Takhounts, S. Ridella, V. Hasija, R. Tannous, J. Campbell, D. Malone, K. Danelson, J. Stitzel, S. Rowson and S. Duma, "Investigation of traumatic brain injuries using the next generation of simulated injury monitor (SIMon) finite element head model," *Stapp Car Crash Journal,* vol. 52, no. November 2008, pp. 1-31, 2008.

[7] L. Zhang, J. Bae, W. N. Hardy, K. L. Monson, G. T. Manley, W. Goldsmith, K. H. Yang and A. I. King, "Computational Study of the Contribution of the Vasculature on the Dynamic Response of the Brain," *Stapp Car Crash Journal,* vol. 46, pp. 145-164, November 2002.

[8] S. Roth, J.-S. Raul and R. Willinger, "Biofidelic child head FE model to simulate reasl world trauma," *Computer Methods and Programs in Biomedicine,* vol. 90, pp. 262-274, 2008.

[9] L. Zhang, K. H. Yang, R. Dwarampudi, K. Omori, T. Li, K. Chang, W. N. Hardy, T. B. Khalil and A. I. King, "Recet Advances in Brain Injury Research: A New Human Head Model Development and Validation," *Stapp Car Crash Journal,* vol. 45, no. November 2011, pp. 375-400, 2001.

[10] C. Giordano, R. Cloots, J. vanDommelen and K. S., "The influence of anisotropy on brain injury prediction," *Journal of Biomechanics,* vol. 47, no. 5, pp. 1052-1059,

2013.

[11] S. Ji, H. Ghadyani, R. Bolander, J. Beckwith, J. Ford, T. McAllister, L. Flashman, K. Paulsen, K. Ernstrom, S. Jain, R. Raman, L. Zhang and R. Greenwald, "Parametric Comparisons of Intracranial Mechanical Responses from Three Validated Finite Element Models of the Human Head," *Annals of Biomedical Engineering,* vol. 42, no. 1, pp. 11-24, 2014.

[12] T. McAllister, J. Ford, S. Ji, J. Beckwith, L. Flashman, K. Paulsen and R. Greenwald, "Maximum Principal Strain and Strain Rate Associated with Concussion Diagnosis Correlates with Changes in Corpus Callosum White Matter Indices," *Annals of Biomedical Engineering,* vol. 10, no. 1, pp. 127-140, 2011.

[13] L. Zhang, K. Yang, R. Dwarmpudi, K. Omori, T. Li, K. Chang, W. Hardy, T. Khalil and A. King, "Recent Advances in Brain Injury Research: A New Human Head Model Development and Validation," *Stapp Car Crash Journal,* vol. 45, no. November 2011, pp. 369-94, 2001.

[14] C. Bonnier, B. Mesplès, S. Carpentier, D. Henin and P. Gressens, "Delayed White Matter Injury in a Murine Model of Shaken Baby Syndrome," *Brain Pathology,* vol. 12, pp. 320-328, 2002.

[15] C. Bonnier, B. Mesples and P. Gressens, "Animal models of shaken baby syndrome: revisiting the pathopysiology of this devastating injury," *Pediatric Rehabilitation,* vol. 7, no. 3, pp. 165-171, 2004.

[16] J. Finnie, P. Blumbergs, J. Manavis, R. Turner, S. Helps, R. Vink, R. Byard, G. Chidlow, B. Sandoz, J. Dutschke and R. Anderson, "Neuropathological changes in a lamb model of non-accidental head injury (the shaken baby syndrome)," *Journal of Clinical Neuroscience,* vol. 19, pp. 1159-1164, 2012.

[17] J. W. Finnie, J. Manavis and P. C. Blumbergs, "Diffuse neuronal perikaryal amyloid precursor protein immunoreactivity in an ovine model of non-accidental head injury (the shaken baby syndrome)," *Journal of Clinical Neuroscience,* vol. 17, pp. 237-240, 2010.

[18] T. Lintern, N. Puhulwelle Gamage, A. Taberner, P. Nielsen, F. Bloomfield and M. Nash, "Neck stiffness properties in a lamb - an animal model of shaken baby syndrome," in *Proceedings of the 11th International Symposium, Computer Methods in Biomechanics and Biomedical Engineering*, Salt Lake City, UT, 2013.

[19] Y. Xiong, A. Mahmood and M. Chopp, "Animal models of traumatic brain injury," *Nature Reviews: Neuroscience,* vol. 14, no. February 2013, pp. 128-142, 2013.

[20] N. G. Ibrahim, J. Ralson, C. Smith and S. S. Margulies, "Physiological and

Pathological Responses to Head Rotations in Toddler Piglets," *Journal of Neurotrauma,* vol. 27, pp. 1021-1035, 2010.

[21] R. Raghupathi and S. S. Margulies, "Traumatic Axonal Injury after Closed Head Injury in the Neonatal Pig," *Journal of Neurotauma,* vol. 19, no. 7, pp. 843-853, 2002.

[22] R. Raghupathi, M. F. Mehr, M. A. Helfaer and S. S. Margulues, "Traumatic Axonal Injury Is Exacerbated Following Repetitive Closed Head Injury in the Neonatal Pig," *Journal of Neurotrauma,* vol. 21, no. 3, pp. 307-316, 2004.

[23] B. Coats, S. Eucker, S. Sullivan and S. Margulies, "Finite element model predictions of intracranial hemorrhage from non-impact, rapid head rotations in the piglet.," *International Journal of Developmental Neuroscience,* vol. 30, pp. 191-200, 2012.

[24] M. T. Prange, B. Coats, A.-C. Duhaime and S. S. Margulies, "Anthropomorphic simulations of falls, shakes, and inflicted impacts in infants," *Journal of Neurosurgery,* vol. 99, pp. 143-150, 2003.

[25] N. G. Ibrahim and S. S. Margulies, "Biomechanics of the toddler head during low-height falls: an anthropomorphic dummy analysis," *Journal of Neurosurgery: Pediatrics,* vol. 6, pp. 57-68, 2010.

[26] B. Paolini, K. Danelson, C. Geer and J. Stitzel, "A multiscale computational approach to estimating axonal damage under inertial loading of the head," *Journal of Neurotrauma,* vol. 30, pp. 102-118, 2013.

[27] R. Cloots, H. Gervaise, J. van Dommelen and M. Geers, "Biomechanics of traumatic brain injury: influences of the morphologic heterogeneities of the cerebral cortex.," *Annals of Biomedical Engineering,* vol. 36, pp. 1203-1215, 2008.

[28] Z. Couper and F. Albermani, "Infant brain subjected to oscillatory loading: material differentiation, properties, and interface conditions.," *Biomechanics and modeling in mechanobiology,* vol. 7, pp. 105-125, 2008.

[29] A. Kuijpers, M. Claessens and A. Sauren, "The influence of different boundary conditions on the response of the head to impact: a two-dimensional finite element study.," *Journal of Neurotrauma,* vol. 12, pp. 715-724, 1995.

[30] A. Wittek and K. Omori, "Parametric study of the effects of brain-skull boundary conditions and brain material properties on responses of simplified finite element brain model under angular acceleration impulse in the sagittal plane," *JSME International Journal Series C,* vol. 46, pp. 1388-1399, 2003.

[31] C. Ma, X. Jin, J. Zhang and S. Huang, "Development of the Pia-Arachnoid Complex Finite Element Model," in *The 2nd International Conference on Bioinformatics and Biomedical Engineering*, Shanghai, China, 2008.

[32] M. Zoghi-Moghadam and A. M. Sadegh, "Global/local head models to analyse cerebral blood vessel rupture leading to ASDH and SAH," *Computer Methods in Biomechanics and Biomedical Engineering,* vol. 12, no. 1, pp. 1-12, February 2009.

[33] B. Coats, G. Binenbaum, R. Peiffer, S. Sullivan, J. A. T. Ralston, C. Smith, A. Duhaime and S. Margulies, "Ocular and neuropathology from cyclic, low velocity head rotations in immature pigs," in *National Neurotrauma Symposium*, Fort Lauderdale, FL, 2011.

[34] S. Eucker, "PhD Dissertation: Effect of head rotation direction on closed head injury in neonatal piglets.," University of Pennsylvania, Philadelphia, 2009.

[35] R. Alcolado, R. Weller, E. Parrish and D. Garrod, "The Cranial Arachnoid And Pia Mater In Man: Anatomical And Ultrastructural Observations," *Neuropathology and Medical Oncology, Southampton University Medical School, UK,* vol. 14, pp. 1-17, 1987.

[36] S. Petroni, O. Tamega, L. Tirapelli and J. Soares, "Mesoscopy and Scanning Electron Microscopy of the Trabecular Projections in the Superior Sagittal Sinus," *Cells Tissues Organs,* vol. 173, pp. 122-126, 2002.

[37] R. Weller, "Microscopy Morphology and Histology of the Human Meninges," *Morphologie,* vol. 89, pp. 22-34, 2005.

[38] D. S. Nicholas and R. O. Weller, "The fine anatomy of the human spinal meninges: A light and scanning electron microscopy study," *Journal of Neurosurgery,* vol. 69, pp. 276-282, August 1988.

[39] H. Killer, H. Laeng and J. Flammer, "Architecture of arachnoid trabeculae, pillars, and septa in the subarachnoid space of the human optic nerve: anatomy and clinical considerations," *British Journal of Ophthalmology,* vol. 87, pp. 777-781, 12 November 2003.

[40] D. Huang, E. Swanson, C. Lin, J. Schuman, W. Stinson, W. Chang, M. Hee, T. Flotte, K. Gregory, C. Puliafito and J. Fujimoto, "Optical Coherence Tomography," *Science,* vol. 254, no. 5035, pp. 1178-1181, 22 Nov 1991.

[41] J. Schmitt, M. Yadlowsky and R. Bonner, "Subsurface imaging of living skin with optical coherence tomography," *Dermatology,* vol. 191, no. 2, pp. 93-98, 1995.

[42] J. A. Izatt, M. D. Kulkarni, H.-W. Wang, K. Kobayashi and M. V. Sivak Jr, "Optical Coherence Tomography and Microscopy in Gastrointestinal Tisues," *IEEE Journal o Selected Topics in Quantum Electronics,* vol. 2, no. 4, pp. 1017-1028, 1996.

[43] M. Brezinski, G. Tearney, N. Weissman, S. Boppart, B. Bouma, M. Hee, A. Weyman, E. Swanson, J. Southern and J. Fujimoto, "Assessing atherosclerotic plaque morphology: comparison of optical coherence tomography and high frequency intravascular ultrasound," *Heart,* vol. 77, pp. 397-403, 1997.

[44] S. A. Boppart, "Optical Coherence Tomography: Technology and Applications for neuroimaging," *Psychophysiology,* vol. 40, pp. 529-541, 2003.

[45] S. W. Jeon, M. A. Shure, K. B. Baker, D. Huang, A. M. Rollins, A. Chahlavi and A. R. Rezai, "A feasibility study of optical coherence tomography for guiding deep brain probes," *Journal of Neuroscience Methods,* vol. 154, no. 1-2, pp. 96-101, 30 June 2006.

[46] V. J. Srinivasan, J. Y. Jiang, M. A. Yaseen, H. Radhakrishnan, W. Wu, S. Barry, A. E. Cable and D. A. Boas, "Rapid volumetric angiography of cortical microvasculature with optical coherence tomography," *Optics Letters,* vol. 35, no. 1, pp. 43-45, 2010.

[47] V. J. Srinivasan, D. N. Atochin, H. Radhakrishnan, J. Y. Jiang, S. Ruvinskaya, W. Wu, S. Barry, A. E. Cable, C. Ayata, P. L. Huang and D. A. Boas, "Optical coherence tomography for the quantitative study of cerebrovascular physiology," *Journal of Cerebral Blood Flow & Metabolism,* vol. 31, pp. 1339-1345, 2011.

[48] H. Wang, A. J. Black, J. Zhu, T. W. Stigen, M. K. Al-Qaisi, T. I. Netoff, A. Abosch and T. Akkin, "Reconstructing micrometer-scale fiber pathways in the brain: multi-contrast optical coherence tomography based tractography," *Neuroimage,* vol. 58, no. 4, pp. 984-992, 15 October 2011.

[49] O. Assayag, K. Grieve, B. Devaux, F. Harms, J. Pallud, F. Chretien, C. Boccara and P. Varlet, "Imagin of non-tumorous and tumorous human brain tissues with full-field optical coherence tomography," *NeuroImage: Clinical,* vol. 2, pp. 549-557, 2013.

[50] Y. Damestani, C. L. Reynolds, J. Szu, M. S. Hsu, Y. Kodera, D. K. Binder, B. H. Park, J. E. Garay, M. P. Rao and G. Aguilar, "Transparent nanocrystalline yttria-stabilized-zirconia calvarium prosthesis," *Nanomedicine: Nanotechnology, Biology,and Medicine,* vol. 9, pp. 1135-1138, 2013.

[51] J. Szu, M. Eberle, C. Reynolds, M. Hsu, Y. Wang, C. Oh, M. Islam, B. Park and D. Binder, "Thinned-skull cortical window technique for in vivo optical coherence

tomography imaging," *Journal of Visualized Experiments,* vol. 69, p. e50053, 19 November 2012.

[52] M. Finke, S. Kantelhardt, A. Schlaefer, R. Bruder, E. Lankenau, A. Giese and A. Schweikard, "Automatic scanning of large tissue areas in neurosurgery using optical coherence tomography," *The International Journal of Medical Robotics and Computer Assisted Surgery,* vol. 8, pp. 327-336, 2012.

[53] A. Nahas, M. Tanter, T.-M. Nguyen, J.-M. Chassot, M. Fink and A. C. Boccara, "From supersonic shear wave imaging to full-field optical coherence shear wave elastography," *Journal of Biomedical Optics,* vol. 18, no. 12, p. Published Online, 19 December 2013.

[54] S. Lee, M. King, J. Sun, H. Xie, G. Subhash and M. Sarntinoranont, "Measurement of viscoelastic properties in multiple anatomical regions of acute rat brain tissue slices," *Journal of the Mechanical Behavior of Biomedical Materials,* vol. 29, pp. 213-224, 2014.

[55] Scientific Computing and Imaging Institute (SCI), *"Seg3D" Volumetric Image Segmentation and Visualization.,* University of Utah, 72 S Central Campus Drive Room 3750, Salt Lake City, UT 84112.

[56] K. Oka, A. L. Rhoton, M. Barry and R. Rodriquez, "Microsurgical Anatomy of the Superficial Veins of the Cerebrum," *Neurosurgery,* vol. 17, no. 5, pp. 711-748, 1985.

[57] X. Jin, J. B. Lee, L. Y. Leung, L. Zhang, K. H. Yang and A. I. King, "Biomechanical Response of the Bovine Pia-Arachnoid Complex to Tensile Loading at Varying Strain-Rates," *Stapp Car Crash Journal,* vol. 50, pp. 637-649, November 2006.

[58] X. Jin, C. Ma, L. Zhang, K. H. Yang and A. I. King, "Biomechanical Response of the Bovine Pia-Arachnoid Complex to Normal Traction Loading at Varying Strain Rates," *Stapp Car Crash Jounal,* vol. 51, pp. 115-126, October 2007.

[59] X. Jin, K. H. Yang and A. I. King, "Mechanical properties of bovine pia-arachnoid complex in shear," *Journal of Biomechanics,* vol. 44, pp. 467-474, 2011.

[60] J. McElhaney, J. Melvin, V. Roberts and H. Portnoy, "Dynamic Characteristics of the Tissues of the Head," *Perspectives in biomedical engineering,* pp. 215-222, 1973.

[61] C. Cha and J. Oh, "An optofluidic mechanical system for elasticity measurement of thin biological tissues," *Biotechnology Letters,* vol. Online , pp. 1-8, 2013.

[62] K. L. Monson, W. Goldsmith, N. M. Barbaro and G. T. Manley, "Significance of source and size in the mechanical response of human cerebral blood vessels," *Journal of Biomechanics,* vol. 38, pp. 737-744, 2005.

[63] Q. Pang, X. Lu, H. Gregersen, G. Oettingen and J. Astrup, "Biomechanical Properties of Porcine Cerebral Bridging Veins with Reference to the Zero-Stress State," *Journal of Vascular Research,* vol. 38, pp. 83-90, 2001.

[64] M. Schmidt, N. Langen, F. Nasirimanesh, P. Shirvanchi, N. Ondreka and M. Kramer, "A study of the comparative anatomy of the brain of domestic ruminants using magnetic resonance imaging," *The Veterinary Journal,* vol. 191, pp. 85-93, 2012.

[65] T. Harrigan, M. Jasty, R. Mann and W. Harris, "Limitations of the continuum assumption in cancellous bone," *Journal of Biomechanics,* vol. 21, no. 4, pp. 269-75, 1988.

[66] D. A. Frankel, D. P. Fessel and W. P. Wolfson, "High Resolution Sonographic Determination of the Normal Dimensions of the Intracranial Extraaxial Compartment in the Newborn Infant," *Journal of Ultrasound in Medicine,* vol. 17, pp. 411-415, 1998.

[67] D. Armstrong, C. Bagnall, J. Harding and R. Teele, "Measurement of the subarachnoid space by ultrasound in preterm infants," *Arch Dis Child Fetal Neonatal,* vol. 86, pp. F124-F126, 2002.

[68] C. Hagmann, N. Robertson, D. Acolet, N. Nyombi, S. Ondo, M. Nakekeeto and F. Cowan, "Cerebral measurements made using cranial ultrasound in term Ugandan newborns," *Early Human Development,* vol. 87, pp. 341-347, 2011.

[69] W. W. M. Lam, V. H. G. Ai, V. Wong and L. L. Y. Leong, "Ultrasonographic Measurement of Subarachnoid Space in Normal Infants and Children," *Pediatric Neurology,* vol. 25, no. 5, 2001.

[70] P. Aimedieu and R. Grebe, "Tensile Strength of Cranial Pia Mater: Preliminary Results," *Journal of Neurosurgery,* vol. 100, pp. 111-114, 2004.

[71] A. R. Tunturi, "Elasticity of the spinal cord, pia, and denticulate ligament in the dog," *Journal of Neurosurgery,* vol. 48, no. 6, pp. 975-979, 1978.

[72] J. E. Galford and J. H. McElhaney, "A Viscoelastic Study of Scalp, Brain, and Dura," *Journal of Biomechanics,* vol. 3, no. 2, pp. 211-221, 1970.

[73] R. van Noort, T. Martin, M. Black, A. Barker and C. Montero, "The mechanical properties of human dura mater and the effects of storage media," *Clinical Physics*

and Physiological Measurement, vol. 2, no. 3, pp. 197-203, 1981.

[74] M. G. Dunn and F. H. Silver, "Viscoelastic Behavior of Human Connective Tissues: Relative Contribution of Viscous and Elastic Components," *Connective Tissue Research,* vol. 12, pp. 59-70, 1983.

[75] M. Sacks, M. Jimenez Hamann, S. Otaño-Lata and T. Malinin, "Local Mechanical Anisotropy in Human Cranial Dura Mater Allografts," *Journal of Biomechanical Engineering,* vol. 120, no. 4, pp. 541-544, August 1998.

[76] L. Zhou, D. Song and Z. Ding, "Biomechanical study of human dura and its substitutes," *Chinese Medical Journal,* vol. 115, no. 11, pp. 1657-1659, 2002.

[77] T. Kriewall, N. Akkas, D. Bylski, J. Melvin and B. Work Jr., "Mechanical Behavior of Fetal Dura Mater Under Large Axisymmetric Inflation," *Journal of Biomechanical Engineering,* vol. 105, no. February 1983, pp. 71-76, 1983.

[78] D. I. Bylski, T. J. Kriewall, N. Akkas and J. W. Melvin, "Mechanical Behavior of Fetal Dura Mater Under Large Deformation Biaxial Tension," *Journal of Biomechanics,* vol. 19, no. 1, pp. 19-26, 1986.

[79] N. Adeeb, A. Deep, C. J. Griessenauer, M. M. Mortazavi, K. Watanabe, M. Loukas, R. S. Tubbs and A. A. Cohen-Gadol, "The intracranial arachnoid mater: A comprehensive review of its history, anatomy, imaging, and pathology," *Child's Nervous System,* vol. 29, no. 1, pp. 17-33, January 2013.

[80] N. Adeeb, M. M. Mortazavi, A. Deep, C. J. Griessenauer, K. Watanabe, M. M. Shoja, M. Loukas and R. S. Tubbs, "The pia mater: a comprehensive review of literature," *Childs Nervous System,* vol. February 2013, p. Epub, 2012.

[81] N. Adeeb, M. M. Mortazavi, R. S. Tubbs and A. A. Cohen-Gadol, "The cranial dura mater: a review of it's history, embryology, and anatomy," *Childs Nervous System,* vol. 28, pp. 827-837, 2012.

[82] K. L. Monson, W. Goldsmith, N. M. Barbaro and G. T. Manley, "Axial Mechanical Properties of Fresh Human Cerebral Blood Vessels," *Journal of Biomechanical Engineering,* vol. 125, no. 2, pp. 288-294, 2003.

[83] K. L. Monson, N. M. Barbaro and G. T. Manley, "Biaxial Response of Passive Human Cerebral Arteries," *Annals of Biomedical Engineering,* vol. 36, no. 12, pp. 2028-2041, December 2008.

[84] T. W. Barber, J. A. Brockway and L. S. Higgins, "The Density of Tissues in and About the Head," *Acta Neurologica Scandinavia,* vol. 46, pp. 85-92, 1970.

[85] R. Coots, J. van Dommelen, T. Nyberg, S. Kleiven and M. Geers, "Micromechanics of diffuse axonal injury: influence of axonal orientation and anisotropy," *Biomechanics and Modeling in Mechanobiology,* vol. 10, no. 3, pp. 413-422, 2011.

[86] R. Cloots, J. van Dommelen and M. Geers, "A tissue-level anisotropic criterion for brain injury based on microstructural axonal deformation," *Journal of the Mechanical Behavior of Biomedical Materials,* vol. 5, pp. 41-52, 2012.

[87] R. Cloots, J. van Dommelen and S. Kleiven, "Multi-scale mechanics of traumatic brain injury: predicting axonal strains from head loads," *Biomechanics and Modeling in Mechanobiology,* vol. 12, pp. 137-150, 2013.

[88] C. Persson, S. Evans, R. Marsh, J. L. Summers and R. M. Hall, "Poisson's Ratio and Strain Rate Dependency of the Constitutive Behavior of Spinal Dura Mater," *Annals of Biomedical Engineering,* vol. 38, no. 3, pp. 975-983, 2010.

[89] Dassault Systèmes, "Abaqus/CAE 6.12 Analysis User's Guide," Vélizy-Villacoublay, France, 2012.

[90] M. Meyers, Dynamic Behavior of Materials, New York: John Wiley & Sons, 1994.

[91] M. T. Prange and S. S. Margulies, "Regional, Directional, and Age-Dependent Properties of the Brain Undergoing Large Deformation," *Journal of Biomechanical Engineering,* vol. 124, no. April 2002, pp. 244-252, 2002.

[92] J. H. Zar, "Kolmogorov-Smirnov Goodness of Fit," in *Biostatistical Analysis*, 5th ed., Upper Saddle River, New Jersey, Pearson Prentice Hall, 2010, pp. 481-489.

[93] A. Holbourn, "Mechanics of Head Injuries," *The Lancet,* vol. 242, no. 6267, pp. 438-441, 9 October 1943.

[94] A. Holbourn, "The Mechanics of Brain Injuries," *British Medical Bulletin,* vol. 3, no. 6, pp. 147-149, 1945.

[95] L. C. H. Shelden, L. R. H. Pudenz, L. C. J. S. Restarski and C. W. M. Craig, "The Lucite Calvarium: A Method for Direct Observation of the Brain," *Journal of Neurosurgery,* vol. 1, no. 67, pp. 67-75, 19 December 1943.

[96] S. Shatsky, "Flash X-Ray Cinematography During Impact Injury," *Proceedings of the 17th Stapp Car Crash Conference,* pp. 361-376, 1973.

[97] V. Hodgson, E. Gurdjian and L. Thomas, "Experimental Skull Deformation and Brain Displacement Demonstrated by Flash X-Ray Technique," *Journal of*

Neursurgery, vol. 25, no. 5, pp. 549-552, 1966.

[98] W. Hardy, C. Foster, A. King and S. Tashman, "Investigation of Brain Injury Kinematics: Introduction of a New Technique," *Crashworthiness, Occupant Protection and Biomechanics in Transportation Systems,* vol. 225, pp. 241-254, 1997.

[99] E. Gurdjian, V. Hodgson, L. Thomas and L. Patrick, "Significance of Relative Movement of Scalp, Skull, and Intracranial Contents During Impact Injury of the Head," *Journal of Neurosurgery,* vol. 29, pp. 70-72, 1968.

[100] G. Nusholtz, P. Lux, P. Kaiker and M. Janicki, "Head Impact Response - Skull Deformation and Angular Accelerations," *Proceedings of the 28th Stapp Car Crash Conference,* pp. 41-74, 1984.

[101] P. Bayly, S. Ji, S. Song, R. Okamoto, P. Massouros and G. Genin, "Measurement of Strain in Physical Models of Brain Injury: A Method Based on HARP Analysis of Tagged Magnetic Resonance Images (MRI)," *Journal of Biomechanical Engineering,* vol. 126, pp. 523-528, August 2004.

[102] P. V. Bayly, E. E. Black, R. C. Pedersen, E. P. Leister and G. M. Genin, "In vivo imaging of rapid deformation and strain in an animal model of traumatic brain injury," *Journal of Biomechanics,* vol. 39, no. 6, pp. 1086-1095, 2006.

[103] S. M. Atay, C. D. Kroenke, A. Sabet and P. V. Bayly, "Measurement of the Dynamic Shear Modulus of Mouse Brain Tissue In Vivo by Magnetic Resonance Elastography," *Journal of Biomechanical Engineering,* vol. 130, no. 2, 2008.

[104] Y. Feng, E. Clayton, Y. Chang, R. Okamoto and P. Bayly, "Viscoelastic properties of the ferret brain measured in vivo at multiple frequencies by magnetic resonance elastography," *Journal of Biomechanics,* vol. 46, pp. 863-870, 2013.

[105] P. Bayly, T. Cohen, E. Leister, D. Ajo, E. Leuthardt and G. Genin, "Deformation of the human brain induced by mild acceleration," *Journal of Neurotrauma,* vol. 22, no. 8, pp. 845-856, 2005.

[106] A. A. Sabet, E. Christoforou, B. Zatlin, G. M. Genin and P. V. Bayly, "Deformation of the human brain induced by mild angular head acceleration," *Journal of Biomechanics,* vol. 41, pp. 307-315, 2008.

[107] Y. Feng, T. Abney, R. Okamoto, R. Pless, G. Genin and P. Bayly, "Relative brain displacement and deformation during constrained mild frontal head impact," *Journal of the Royal Society Interface,* vol. 7, pp. 1677-1688, 2010.

[108] P. V. Bayly, E. H. Clayton and G. M. Genin, "Quantitative Imaging Methods for the Development and Validation of Brain Biomechanics Models," *Annual Review of Biomedical Engineering,* vol. 14, pp. 369-96, 2012.

[109] B. Lee and A. Newberg, "Neuroimaging in Traumatic Brain Imaging," *NeuroRx,* vol. 2, no. 2, pp. 372-383, 2005.

[110] B. Mokri, "The Monro-Kellie hypothesis: Applications in CSF volume depletion," *Neurology,* vol. 56, pp. 1746-1748, 2001.

[111] F. Luisier, C. Vonesch, T. Blu and M. Unser, "Fast interscal wavelet denoising of Poisson-corrupted images," *Signal Processing,* vol. 90, pp. 415-427, 2010.

[112] M. E. Wagshul, J. J. Chen, M. R. Egnor, E. J. McCormack and P. E. Roche, "Amplitude and phase of cerebrospinal fluid pulsations: experimental studies and review of the literature," *Journal of Neurosurgery,* vol. 104, pp. 810-819, 2006.

[113] A. Haase, J. Frahm, D. Matthaei, W. Hanicke and K. Merboldt, "FLASH imaging. Rapid NMR imaging using low flip-angle pulses," *Journal of Magnetic Resonance,* vol. 67, no. 2, pp. 258-266, 1969.

[114] R. S. Naunheim, P. V. Bayly, J. Standeven, J. S. Neubauer, L. M. Lewes and G. M. Genin, "Linear and Angular Head Accelerations during Heading of a Soccer Ball," *Medicine & Science in Sports & Exercise,* vol. 35, no. 8, pp. 1406-1412, 2003.

[115] A. Holbourn, *Letter to Dr. Strich on Head Injury Scaling,* Old Aberdeen, UK, 1956.

[116] S. Margulies, L. Thibault and T. Gennarelli, "Physical model simulations of brain injury in the primate," *Journal of Biomechanics,* vol. 23, no. 8, pp. 823-836, 1990.

[117] S. M. Blinkov and I. I. Glezer, The Human Brain in Figures and Tables. A Quantitative Handbook, New York: Plenum Press, 1968.

[118] J. Thirion, "Image matching as a diffusion process: an analogy with Maxwell's demons," *Medical Image Analysis,* vol. 2, no. 3, pp. 243-260, 1998.

[119] X. Pennec, P. Cachier and N. Ayache, "Understanding the "Demon's Algorithm" 3D Non-Rigid registration by Gradient Descent," in *2nd Int. Conf on Medical Image Computing and Computer-Assisted Intervention*, Cambridge, UK, 1999.

[120] A. Varess, N. Phatak and J. Weiss, "Deformable Image Registration with Hyperelastic Warping," in *Handbook of Biomedical Image Analysis*, Springer, 2005, pp. 487-534.

[121] B. Coats, S. Evans and G. Scott, *In-House Communications,* Salt Lake City: University of Utah Pediatric Injury Biomechanics Laboratory, 2014.

[122] The MathWorks, Inc., *MATLAB and Image Processing Toolbox Release 2012b,* Natick, Massachusetts, United States.

[123] Adobe Systems Incorporated, *Adobe Photoshop Creative Suite 5,* 345 Park Avenue, San Jose, California, 95110, USA, 2010.

[124 SAS Institute Inc., *JMP Version 11,* Cary, NC, 1989-2014.

[125] Python Software Foundation, *Python v3.3,* 2013.

[126] U. S. National Institutes of Health, *ImageJ v1.47* Bethesda, MD, 1997-2014.